SCUOLA DI DOTTORATO
UNIVERSITÀ DEGLI STUDI DI MILANO-BICOCCA

Department of

Earth and Environmental Sciences

PhD program in: Chemical, Geological and Environmental Sciences   Cycle: XXXII

Curriculum: Geological Sciences

GEOCHRONOLOGY AND KINEMATICS OF CRUSTAL SCALE SHEAR ZONES IN THE HIMALAYAN COLLISIONAL BELT

MONTEMAGNI CHIARA

Registration number: 823005

Tutor: Prof. Igor M. Villa

Co-tutor: Prof. Chiara Montomoli
Prof. Rodolfo Carosi

Coordinator: Prof. Maria Luce Frezzotti

ACADEMIC YEAR   2018/2019

“Alla fine ci sono andato davvero in Himalaya.
Non per scalare le cime, come sognavo da bambino,
ma per esplorare le valli.”

(P. Cognetti, Senza mai arrivare in cima)

TABLE OF CONTENTS

ABSTRACT

The Himalaya is commonly regarded as a cylindrical belt from west to east due to the impressive lateral continuity of the main litho-tectonic units and faults/shear zones, which is a particular feature of this mountain range. The exhumation of the metamorphic core of the belt, the Greater Himalayan Sequence (GHS), was favored by two regional scale opposite-kinematics ductile to brittle shear zones: the contractional Main Central Thrust zone (MCTz) at the bottom and the normal-sense South Tibetan Detachment System (STDS) at the top of the GHS itself.

In this thesis, I investigated the structural and geochronological evolution of the STDS and the MCTz, with a particular focus on the latter, in two transects in the Indian Western Himalaya: the Alaknanda – Dhauli Ganga Valleys and the Bhagirathi – Gangotri Valley in the Garhwal region.

To this aim, I used a multidisciplinary approach, which combines microstructural, chemical and geochronological studies, as well as a kinematic estimate.

As micas are ubiquitous in many high strain shear zones, the $^{40}Ar/^{39}Ar$ geochronological method on biotite and muscovite has commonly been employed to constrain the ages of mylonitization. The $^{40}Ar/^{39}Ar$ step-heating approach, the most useful for the present study, is a key procedure for unravelling petrological and chemical complexities because of the recognition of different ages due to different steps of Ar release characterized by different Cl/K and Ca/K ratios. I applied this method, combined with a new methodological approach first developed in detail during this Ph.D. thesis work, to rocks coming from the bounding shear zones of the GHS. This new procedure, named Ar Differential Release Plot (DRP), that allows us to clearly identify the influence of the co-existence of phyllosilicates on the trend of Ar release during heating steps. This, in turn allows us to select the optimal steps corresponding to the degassing of micas *sensu stricto*, which leads to more reliable age determinations in such metamorphic multiply deformed rocks. Results of the $^{40}Ar/^{39}Ar$ method support the diachroneity of the MCTz and the STDS in the studied areas, suggesting that models of exhumation of the GHS should account for their lack of contemporaneity.

Moreover, a new three-dimensional approach based on the X-ray micro Computed Tomography (microCT) analytical method has been developed and applied to study of the kinematic flow vorticity within the MCTz using the stable porphyroclast method. A close examination of literature data shows that our study approach in the study of kinematic vorticity using the microCT has never been applied before. This method has been applied to MCTz rocks from the Bhagirathi valley and the results suggest that exhumation of the GHS has been affected by a shift of deformation within the MCTz from simple to pure shear dominated flow, consistent with previous published data all along the Himalaya.

In summary, combining meso- and micro-structural studies as well as chemical analyses and $^{40}Ar/^{39}Ar$ geochronology, my thesis results points out how MCTz and STDS are not coeval in the studied structural transects and that the MCTz shows a shift in deformation regime during its evolution.

RIASSUNTO

L'Himalaya è classicamente considerata una catena orogenica strutturalmente cilindrica per l'impressionante continuità laterale, da ovest ad est, delle principali unità lito-tettoniche e zone di taglio, caratteristica peculiare di questa catena collisionale. L'esumazione del cuore metamorfico della catena, il Greater Himalayan Sequence (GHS), è favorita dall'attività di due zone di taglio regionali a cinematica opposta: la Main Central Thrust zone (MCTz) a cinematica compressiva e il South Tibetan Detachment System (STDS) a cinematica normale, rispettivamente alla base e al tetto del GHS stesso.

In questa tesi ho studiato l'evoluzione strutturale e geocronologica del STDS e della MCTz, con particolare focus su quest'ultima, in due transetti nell'Himalaya indiana occidentale: le valli dell'Alaknanda – Dhauli Ganga e la valle del Bhagirathi – Gangotri nella regione del Garhwal.

A questo scopo, ho adottato un approccio multidisciplinare che combina studi microstrutturali, chimici e geocronologici e stime di vorticità cinematica.

Poiché le miche sono ubiquitarie nelle zone di taglio, il metodo geocronologico ^{40}Ar/^{39}Ar su biotitie e muscovite è stato ampiamente utilizzato in passato e viene utilizzato tutt'oggi per vincolare l'età della deformazione per taglio.

Il metodo ^{40}Ar/^{39}Ar *step-heating*, il più adatto per questo tipo di studi, è un metodo chiave per risolvere complessità petrologiche e chimiche grazie al riconoscimento di età differenti dovute a un differente rilascio dell'Ar caratterizzato da diversi rapporti Cl/K e Ca/K. Ho applicato questo metodo, combinato con una nuova procedura, l'*Ar Differential Release Plot* (DRP), che permette di identificare chiaramente l'influenza della coesistenza di fillosilicati nel trend di rilascio dell'Ar durante gli *step* di riscaldamento, permettendo di selezionare gli *step* ottimali che corrispondono al degassamento delle miche in senso stretto. Questa nuova procedura permette di determinare l'età in modo molto più accurato in rocce polideformate come quelle studiate. I risultati ottenuti con il metodo ^{40}Ar/^{39}Ar supportano la diacronicità della MCTz e del STDS nelle aree studiate, suggerendo che i modelli di esumazione del GHS dovrebbero tener conto della mancanza di contemporaneità tra queste due strutture.

Inoltre, è stato sviluppato un nuovo approccio tridimensionale basato sulla *X-ray micro Computed Tomography* (microCT) e applicato per lo studio della vorticità cinematica usando il metodo dei porfiroclasti stabili. Un esame dei dati di letteratura ha dimostrato che il nostro approccio nello studio di vorticità usando il metodo dei porfiroclasti stabili non era mai stato applicato prima. Questo metodo è stato applicato a rocce provenienti dalla MCTz nella valle del Bhagirathi e i risultati suggeriscono che l'esumazione del GHS sia stata guidata da una variazione di deformazione all'interno della MCTz da un deformazione dominata da taglio semplice a cui è seguita una deformazione dominata da taglio puro, coerentemente con i dati di letteratura lungo la catena.

Riassumendo, combinando studi meso e microstrutturali con analisi chimiche e geocronologia ^{40}Ar/^{39}Ar, i risultati della mia tesi indicano che la MCTz e il STDS non sono coevi nei transetti studiati e che la MCTz mostra una variazione di regime deformativo durante la sua evoluzione.

1. INTRODUCTION

The Himalaya is commonly regarded as a cylindrical belt from west to east due to the impressive lateral continuity of the main litho-tectonic units and faults/shear zones, which is a particular feature of this mountain range. From south to north these units are the Sub Himalaya, the Lesser Himalayan Sequence (LHS), the Greater Himalayan Sequence (GHS) and the Tethyan Himalayan Sequence (THS) separated by north dipping faults/shear zones that are the Main Boundary Thrust (MBT), the Main Central Thrust zone (MCTz) and the South Tibetan Detachment System (STDS).

Nevertheless, along-strike differences in geological structures, topography, convergence rates and geochronology have been described in the literature (Hodges, 2000; Robert et al., 2011). The occurrence of regional-scale shear zones makes the Himalaya the right place to investigate large-scale tectonics, kinematics and ages of these structures. The exhumation of the metamorphic core of the belt, the GHS, was facilitated reversal and normal sense motion on the MCt at the bottom (Hodges et al., 1996; Searle et al., 2008) and the STDS at the top of the GHS, respectively (Caby et al., 1983; Burg et al., 1984).

One of the questions about the Himalayan belt is when and how it came to reach its present elevation. The belt consists of tectonic units stacked from the Indian plate and transported towards the south during the collisional stage of orogenesis and subsequent indentation tectonics. All along the orogenic belt, regional scale thrusts or shear zones accommodated crustal shortening related to India-Eurasia convergence since the Middle-Late Eocene. The high peaks of the entire Himalaya occur in, or near, the lithotectonic unit formerly called the High Himalayan Crystallines and known at present as the GHS. The GHS and its exhumation are thus the key to understand topographic relief formation. Various models have been proposed for the exhumation of the GHS whereby the central discriminant between models is the estimated timing of the bounding fault systems. These tectonic models can be divided in two groups: (a) models that require contemporaneity of motion along both the STDS and the MCT; (b) models that do not require contemporaneous motion. The geochronological database for motion on the MCT and STDS is very diverse in quality, in location, and in chronometer choice. Attempts to estimate the timing of MCT movement (sometimes lacking an in-depth microstructural description) are inconclusive, as dozens of age data from various parts of the belt differ by over 20 Myr, between 22 Ma (Daniel et al., 2003) and c. 3 Ma (Catlos et al., 2001). The age estimates for the STDS were reviewed by Godin et al. (2006), who report ages of c. 18 Ma and c. 21 Ma for different branches of the STDS. However, as pointed out by Leloup et al. (2010), the ages associated with these structures are not critically discussed, and their detailed significance is underconstrained.

In the framework of GHS exhumation, one of the main unsolved problems in the Himalayan belt is the nature of the MCT, the most prominent tectonic discontinuity that runs the length of the belt. The MCTz (Heim & Gansser, 1939; Searle et al., 2008) is a km-thick top-to-the-S/SW zone of intensively sheared rocks, dipping to the north, which separates the GHS from the underlying LHS, the latter consisting of low- to medium-grade metamorphic rocks (Arita, 1983). The exact localization of the MCTz boundaries together with its temporal and structural evolution are still a matter of debate (Searle et al., 2008; Martin, 2017; Carosi et al., 2018 for updated reviews). As discussed by Searle et al. (2008), Martin (2017) and Mukhopadhyay et al. (2017), the definition of the MCT has changed since the work of Heim & Gansser (1939). The current debate is especially related to the criteria to define (and thus to localize) the MCT. Several definitions of the MCT have been proposed (see Searle et al. 2008; Martin 2017; Carosi et al., 2018 for an updated review), including a structural–metamorphic definition (Heim & Gansser 1939), a metamorphic–rheological (Searle et al. 2008) and a purely rheological (e.g. Gibson et al., 2016; Parsons et al., 2016) definition, a chronological definition (e.g. Webb et al., 2013) and a compositional definition, assuming that the MCT is a high-strain reverse kinematic shear zone that separates distinguishable protoliths (e.g. Martin et al., 2005; Martin, 2017). The MCT records a protracted deformation, from ductile to brittle (Carosi et al., 2007 and references cited therein; Iaccarino et al., 2017a), and affects several different lithologies along-strike. This further complicates the debate. This controversy led to the definition of two distinct thrusts in NW India (Valdiya, 1980; Saklani et al., 1991; Ahmad et al., 2000) and in Nepal (Hashimoto et al., 1973; Arita, 1983; DeCelles et al., 2000; Robinson et al., 2001; Robinson, 2008). In different areas of the belt, these two bounding thrusts have been named in different ways, although they seem to refer to the same structural setting. In the Garhwal Himalaya (NW India), the MCT Zone (MTCz) is well exposed: Valdiya (1980) and Ahmad et al. (2000) defined the Munsiari Thrust at the bottom and the Vaikrita Thrust at the top of the MCTz, whereas Saklani et al. (1991) defined the lower thrust as MCT2 in the Yamuna valley. The activity time span of the MCT in different areas of the belt was estimated using mutually contrasting methods or criteria. The activity time span ranges from 23–20 to 15 Ma in different areas of the belt (see Godin et al., 2006; Montomoli et al., 2015 for an updated review) down to a reported c. 3 Ma in central Nepal (Catlos et al., 2001). Such a long-lasting activity resulted in a complex structural and kinematic evolution, with the superposition of several deformation stages whose related structures are unevenly preserved along the thrust zone.

In the Garhwal Himalaya (NW India), the MCTz is bounded by two discrete fault zones, the Munsiari Thrust at the bottom and the Vaikrita Thrust at the top (Valdiya, 1980; Jain et al., 2014), constituting the MCT *sensu stricto* in this area.

In this region, several researchers proposed preferred ages for the MCT activity based on different chronometers (K–Ar, Th–Pb and $^{40}Ar/^{39}Ar$) and on different non-isotopic sample characterizations. Metcalfe (1993) obtained K–Ar ages on biotite and muscovite from the Bhagirathi valley. Based on these data, Metcalfe (1993) proposed that the MCT was active between 14 and 5.7 Ma. Catlos et al. (2002) extended their previous work in Nepal to western Garhwal beneath the Vaikrita Thrust and asserted that the Th–Pb ages of monazite constrain the age of the entire activity of the MCT in the central and western Himalaya to c. 6 Ma. Célérier et al. (2009b) reported c. 9 Ma obtained using $^{40}Ar/^{39}Ar$ on muscovite from samples in the middle portion of the MCTz near the village of Helang. Sen et al. (2015) obtained $^{40}Ar/^{39}Ar$ biotite ages of c. 10 Ma and interpreted them as ‘cooling ages’ correlated to the exhumation of the GHS caused by MCT thrusting at that time. In addition, muscovite ages of c. 6 Ma were related to a late-stage deformation post-dating biotite cooling (Sen et al., 2015). However, questions concerning the microstructural and chemical features in context with the protracted deformation have not been addressed by any of these conflicting studies. As our observations of the deformation style of the MCTz in Garhwal strongly suggest a more complex history than that described in previous studies, we apply an integrated structural–microchemical–geochronological approach (Vance et al., 2003) to provide a time frame for the different styles of activity of the shear zone.

The baseline for any interpretation is a detailed microstructural study (e.g. Rolland et al., 2009; Montomoli et al., 2013, 2015; Iaccarino et al., 2015), which is required to clarify the aforementioned contrasting estimates.

Besides the ages of bounding shear zones of GHS, the knowledge of the kinematic and non coaxiality of the flow, i.e the percentage of pure and simple shear components acting together during the activity of shear zones, is a discriminating parameter among the different proposed exhumation models (e.g. Godin et al., 2006; Montomoli et al., 2013; Carosi et al., 2018 and references therein). This component can be derived from kinematic vorticity studies, which are generally performed on thin sections. As the kinematic vorticity estimates using the stable porphyroclasts method suffers severe limitations in 2D, we decided to try a new innovative three-dimensional approach using the X-ray micro computed tomography (microCT). A close examination of literature data shows that our study approach in the study of kinematic vorticity using the microCT has never been applied before.

A microstructural study can distinguish between pre-, syn- and post-kinematic minerals and wherever possible should be linked to dated minerals applying analytical techniques that allow the recognition of heterochemical phases and simultaneously provide their age (e.g. analyses of monazite by electron microprobe, Williams & Jercinovic, 2002; Williams et al., 1999, 2007, 2017; and of mica, amphibole and feldspar by ^{40}Ar/^{39}Ar mass spectrometry; Di Vincenzo et al., 2004; Villa & Williams, 2013; Villa & Hanchar, 2017). A recognition of heterochemical mineral replacements, and of mineral disequilibria in general, is necessary to take into account the metamorphic reactions and fluid circulation that led to the partial resetting and/or growth of new mineral chronometers (Challandes et al., 2003; Sanchez et al., 2011). An ignorance of the occurrence of several mineral generations will lead to inaccurate age estimates.

A feature of ^{40}Ar/^{39}Ar dating, the most useful for the present study, is its ability to characterize the analysed phases by their Cl/K and Ca/K ratios (Müller et al., 2002) and thus to diagnose the presence of heterochemical retrogression phases. This is especially valuable when attempting to date fault movements, because sheared minerals are almost always affected by recrystallization, dissolution/reprecipitation and alteration, and by a resulting grain size of only a few micrometers (Berger et al., 2017). This extreme comminution strongly limits the utility of mineral separations, as it, perforce, does not allow us to produce a monomineralic separate and moreover strongly limits the use of *in situ* analyses, the spatial resolution of which is often insufficient to obtain results for a single-generation mineral (Müller et al., 2002). The impossibility of obtaining monomineralic separates for such metamorphic rocks can be circumvented by a judicious use of correlation diagrams (Villa & Hanchar, 2017) coupled with a new methodological approach first developed in detail during this Ph.D. thesis.

The procedure allows quantifying the bias given by fine-grained phyllosilicates and, through the Ar Differential Release Plots (DRP) to identify the structure collapse of micas *sensu stricto* from that of impurities (clays, feldspars and potentially also relict phyllosilicates). The Ar DRP shows the release of ^{39}Ar as a function of the heating temperature. Combining the Ar DRP with correlation diagrams (from which we derive the chemical signature of micas) allows identifying the step ages pertaining to the minerals that date the deformation: only the isochemical steps that correspond to the degassing of "real" micas have been considered for the calculation of the ages.

This Ph.D. thesis deals with the role and age of the MCTz in the exhumation of GHS and aims to improve the above-mentioned methodological approaches and to derive, through their application, sound geochronological and kinematic data on MCTz mylonitic rocks.

The results of my Ph.D. work have been published in *Geological Society London, Special Publication*, 2019, **481**, 127-146; *Italian Journal of Geosciences*, 2018, **137**, 175-187; and have been accepted for publication in *Terra Nova* ("Three-dimensional vorticity and time-constrained evolution of the Main Central Thrust zone, Garhwal Himalaya (NW India)", 2020). Some chapters of this thesis are extracted from these papers. Other results related to this Ph.D. work have been published in *Tectonics*, 2017, **36**, 2281-2304.

2. GEOLOGICAL SETTING

2.1 The Himalaya

The Himalayan Orogen (Fig. 2.1) formed by the closure of the Tethyan Ocean and the subsequent collision between the Indian and Asian plates. Although the timing of terminal collision is debatable (Najman et al., 2017 and references cited therein), the age of collision has recently been constrained by Najman et al. (2017) at 54 Ma, at least in the NW portion of the belt. The Himalayan mountain belt is composed of several tectonometamorphic units bounded by regional-scale reverse and normal shear zones (Fig. 1): the Main Frontal Thrust, the Main Boundary Thrust, the MCT and the South Tibetan Detachment System (STDS) (Le Fort, 1975; Hodges, 2000). From south to north, the tectonic units of the belt (Fig. 2.1) are as follows:

(1) The Sub-Himalaya is composed of low- to medium Miocene to Pleistocene sediments, derived from the erosion of the belt (Hodges, 2000), and delimited at the bottom by the Main Frontal Thrust, a tectonic lineament that divides this unit from the underlying undeformed sediments of the Ganga plain. At the top of the Sub-Himalaya, the Main Boundary Thrust divides this unit from the LHS above.

(2) The LHS (Fig. 2.1) consists of low- to medium grade marble, orthogneiss, quartzite and schist and is Early Proterozoic to Early Paleozoic in age (Hodges, 2000). The MCT, a wide, ductile to brittle, top-to-the-south shear zone, divides the LHS from the overlying GHS.

(3) The GHS (Fig. 2.1), representing the metamorphic core of the belt, consists of a sequence of medium- to high-grade Late Proterozoic to Cambrian metamorphic rocks, such as gneisses, schists, migmatites and calc-silicate rocks, which are intruded by Oligocene– Miocene leucogranites referred to as the Higher Himalayan Leucogranites (Visonà et al., 2012). The thickness of the GHS is variable (from 2–3 up to 30 km; Carosi et al., 2002, 2010, 2014; Montomoli et al., 2013). At least two main metamorphic events have been recognized in the GHS: an Eocene–Oligocene event in the kyanite stability field, characterized by high-pressure conditions, and a Miocene event of medium- to low-pressure conditions (Pognante & Benna, 1993; Iaccarino et al., 2015 and references cited therein) in the sillimanite to cordierite stability field. The STDS, a system of normal, ductile to brittle top-to-the-north shear zones and faults, divides the GHS from the upper Tethyan Himalayan Sequence (THS; Caby et al., 1983; Burchfiel et al., 1992; Carosi et al., 1998).

(4) The THS (Fig. 2.1) consists of Paleozoic to late Mesozoic low-grade metamorphic and undeformed rocks (Le Fort, 1975). The metamorphic grade increases considerably towards the structurally lower portion of the THS, close to the STDS, locally up to lower amphibolite facies conditions (Hodges, 2000; b et al., 2011; Montomoli et al., 2017b).

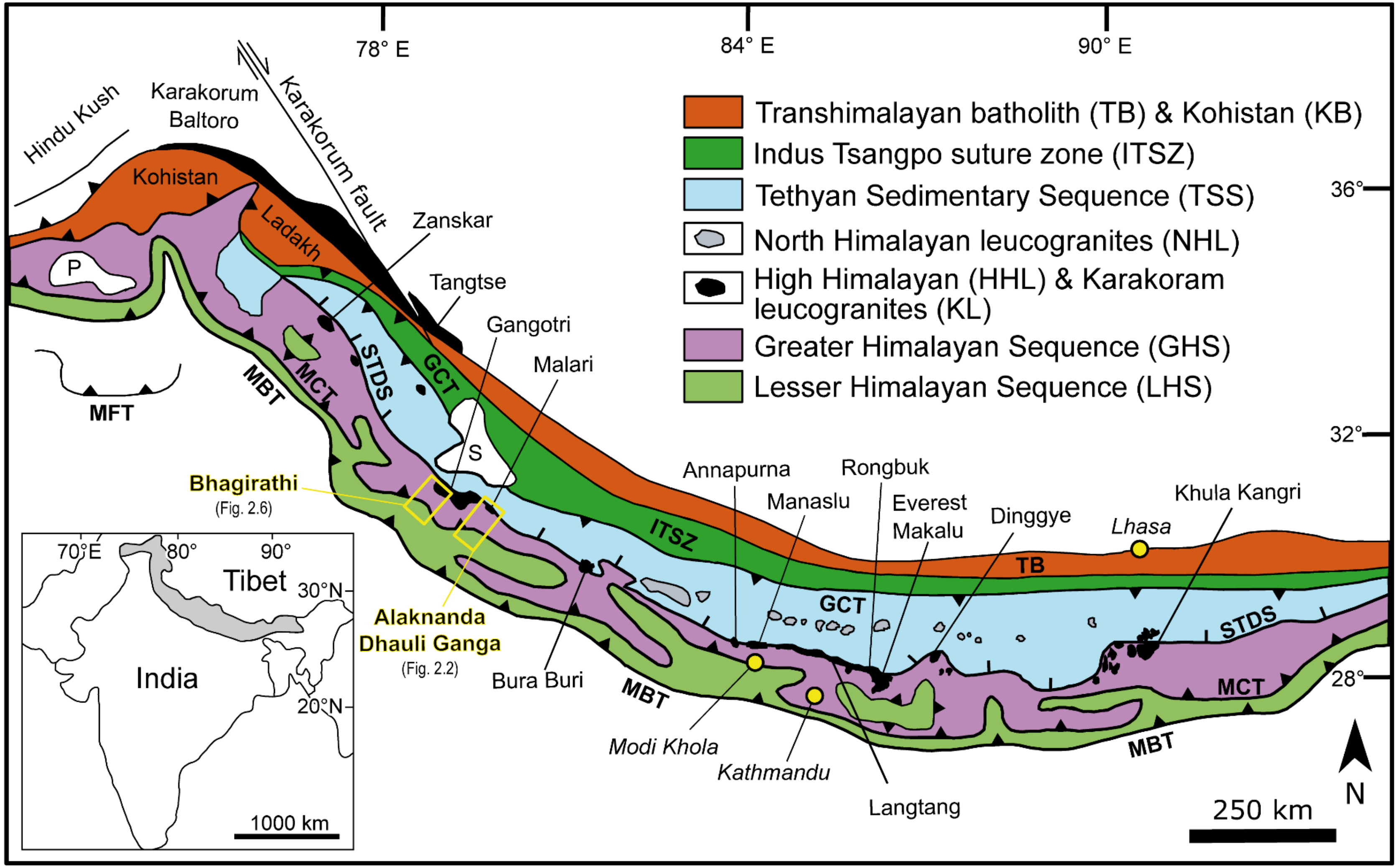

Figure 2.1. Simplified geological map of the Himalaya (modified after Weinberg, 2016). The location of the study areas in the Garhwal region is shown.

2.2 The role of the shear zones in the exhumation models of the Greater Himalayan Sequence

The models of exhumation of the GHS (Montomoli et al., 2013) can be divided in two groups based on the timing of the shearing of the two bounding shear zones of the GHS itself, namely the STDS and the MCT (Fig. 2.2): models that require the contemporaneity between the STDS and MCT (Fig. 2.2a,b,c), and models that do not necessarily require the contemporaneity (Fig. 2.2d,e) to explain the GHS exhumation.

The first group includes the channel flow model (Fig. 2.2a; Beaumont et al., 2001, 2004), the channel flow followed by extrusion model (Fig. 2.2a; Godin et al., 2006) the wedge extrusion model (Fig. 2.2b; Hodges et al., 1992; Grujic et al., 1996; Vannay & Grasemann, 2001) and the wedge insertion model (Fig. 2.2c; Webb et al., 2007).

The channel flow model needs the contemporaneity of the STDS and MCT, which are modelled as parallel and sub-horizontal. In this model the GHS is a hot-channel constituted of partially molten middle to lower crust, exhumed due to a different pressure gradient between the Tibetan plateau and its borders. In the modification of this model proposed by Godin et al. (2006) the erosion focused on the topographic surface enhanced the extrusion of the molten crust channel. In the wedge extrusion model the GHS is extruded southward by combining the antithetic movement of the STDS and the MCT; the extrusion mechanism depends on whether the extruding wedge is dominated by simple shear flow (Grujic et al., 1996), pure shear flow (Vannay & Grasemann, 2001) or acts as a non - deformed rigid body (Hodges et al., 1992). In the wedge insertion model (Webb et al., 2007) the GHS has a southward-tapering geometry and the STDS is portrayed as a back-thrust.

The second group of models includes the critical taper model (Fig. 2.2d; Platt, 1993; Kohn, 2008) and the in-sequence shearing model (Fig. 2.2e; Carosi et al., 2010; Montomoli et al., 2013, 2015). In the critical taper model, the exhumation of the GHS is driven by the alternation of shearing activity between the STDS (when the orogen is overthickened) and the MCT (when the orogen is thinned). The in-sequence shearing model is based on the in-sequence activation, in time and space, of structures toward the south, from the oldest in the hinterland to the youngest in the foreland of the belt.

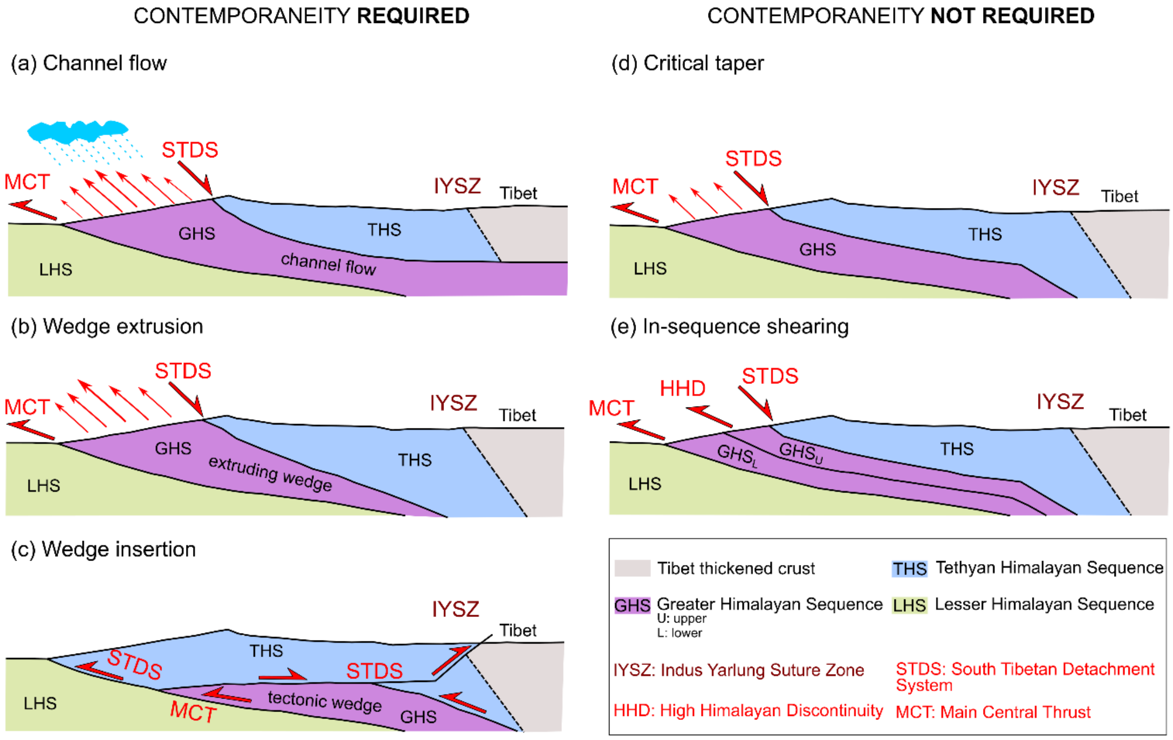

Figure 2.2. Schematic sketches of the current tectonic models for the exhumation of the GHS, divided based on contemporaneity required (a,b,c) or not (d,e) between the MCT and the STDS. (a) Channel flow model; (b) wegde extrusion model: the type of exhumation (i.e. simple shear or pure shear dominated) depends on the mechanism dominating in the extruding wedge; (c) wedge insertion model; (d) critical taper model and, (e) in-sequence shearing model (modified after Montomoli et al., 2013).

2.3 Study areas and field relations

The investigated areas, where a complete structural transect of the Himalaya is well exposed, are located in the NW Indian Himalaya, in the Uttarakhand district of the Garhwal region: the Alaknanda – Dhauli Ganga Valleys (Fig. 2.3) and the Bhagirathi – Gangotri valley (Fig. 2.7).

The geology of the Garhwal Himalaya has been studied for a long time (Heim & Gansser, 1939; Valdiya, 1980; Hodges & Silverberg, 1988; Srivastava & Mitra, 1994; Célérier et al., 2009a, 2009b) and in this area Heim & Gansser (1939) proposed the classical Himalayan division in litho-tectonic units separated by north dipping shear zones and faults.

2.3.1 The Dhauli Ganga – Alaknanda valleys

The study area is located between the villages of Gundala and Malari (Fig. 2.3).

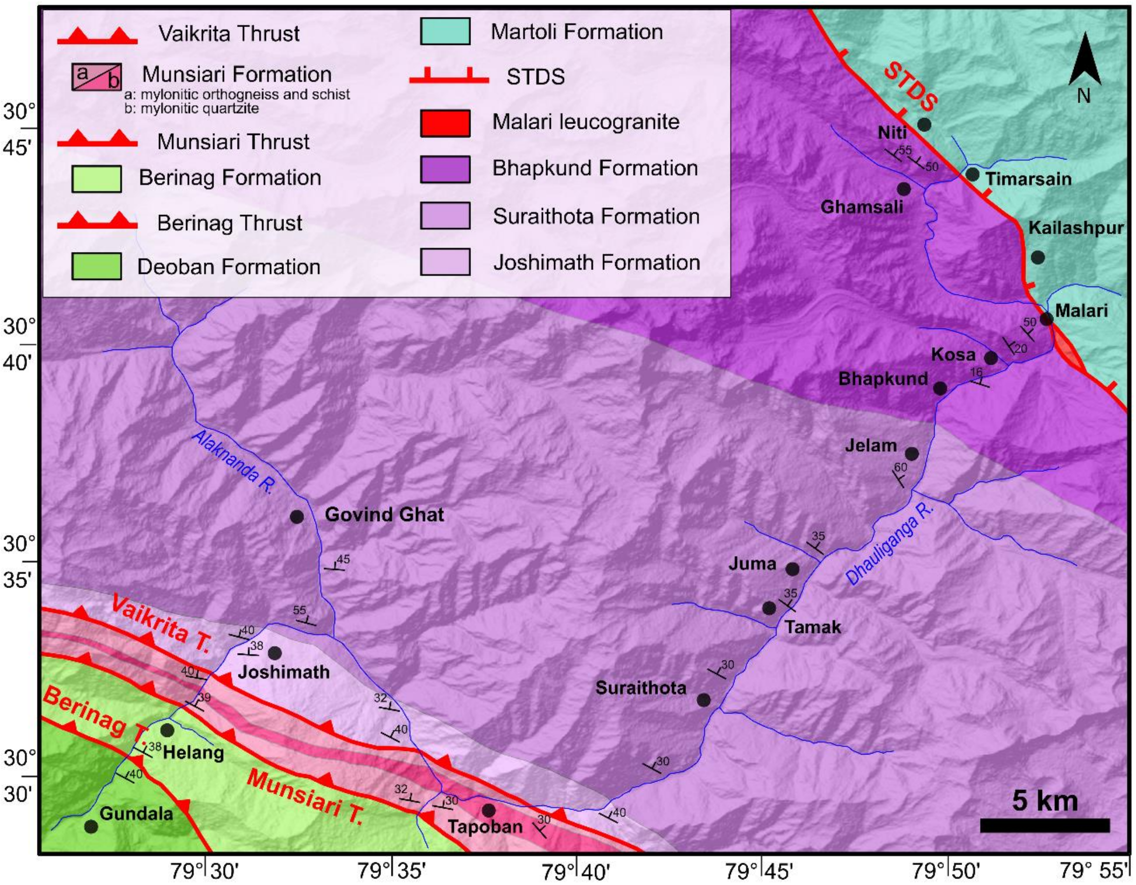

Figure 2.3. The study area in the Alaknanda – Dhauli Ganga valleys (modified after Jain et al., 2014 and Hunter et al., 2018). Main foliation measurements collected in the field are shown.

Outcrop photographs illustrating deformation fabrics on the Munsiari and Vaikrita Thrusts, limiting the MCTz, are shown in Figure 2.4a-c. A third structure, the Berinag Thrust (Fig. 2.4d), has been intensively described by Célérier et al. (2009a), as a thrust separating the lower dolomites, schists and metapelites of the Deoban Formation (LHS) from quartzite of the overlying Berinag Formation (LHS), belonging to the upper and lower Inner LHS, respectively (Célérier et al., 2009a). The Berinag Thrust has a top-to-the-SW shear sense (Fig. 2.4d) and dips c. 35° to the NE. The Berinag Formation crops out near Helang, in the southernmost part of the transect, and belongs to the LHS (Fig. 2.3). This formation consists of schists, quartzites and carbonate rocks affected by a greenschist facies metamorphism. The main foliation strikes NW–SE and dips 30–35° to the NE (Jain et al., 2014). Stereoplots showing the main foliation of the LHS, MCTz and GHS are reported in Figure 2.5.

The Munsiari Formation crops out within the MCTz (Fig. 2.3) and consists of mylonitic quartzite (Fig. 2.4a), Precambrian mylonitic orthogneiss (Fig. 2.4b), garnet-bearing mica schist and calc-silicate rocks (Fig. 2.3, Jain et al., 2014). The main foliation strikes from west–east to NW–SE and dips 45° from the north to NE, whereas the main stretching lineation is oriented N 20°, 45° NE. The main kinematic indicators at the mesoscale (Jain et al., 2014) are S–C and S–C–C′

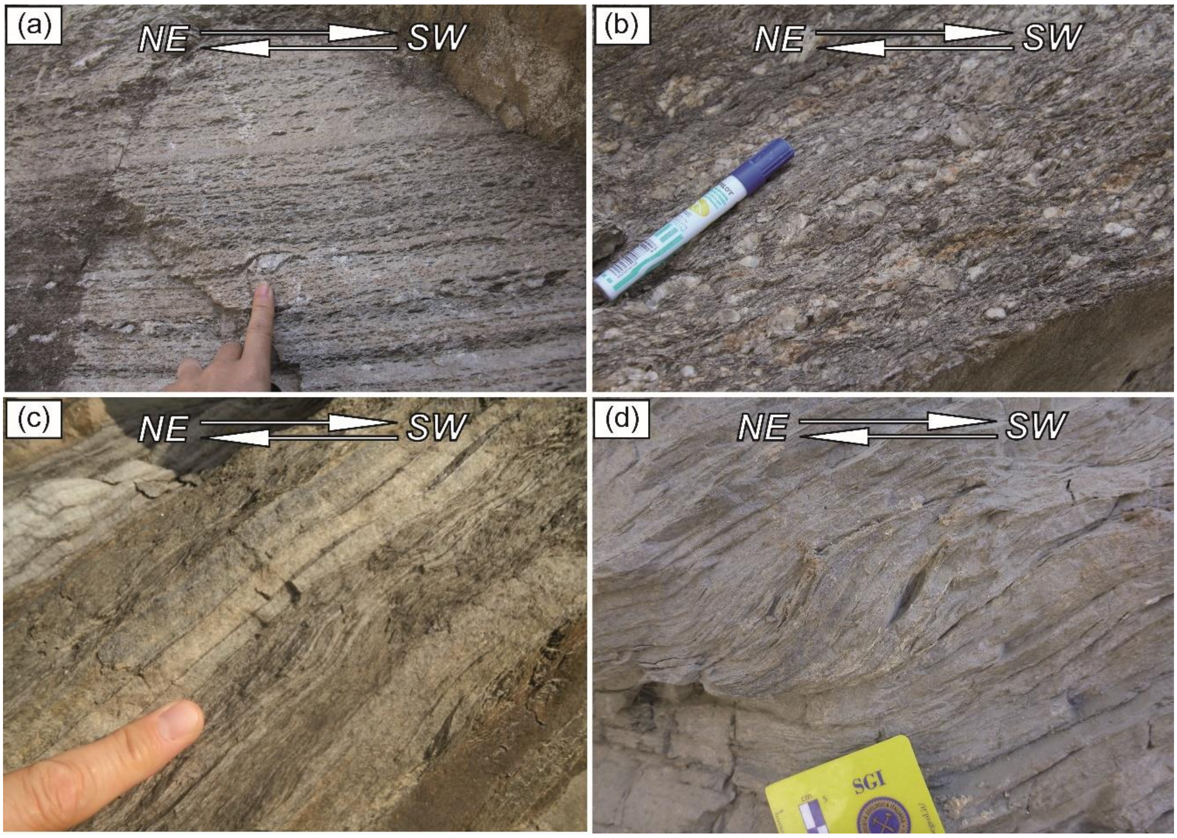

Figure 2.4. (a), (b) outcrops of the pervasively sheared rocks of the MCTz near the Munsiari Thrust, in which the kinematic indicators point a top-to-the-SW sense of shear (a) mylonitic impure marble with millimetric mica fish and asymmetrically deformed quartz porphyroclasts; (b) mylonitic orthogneiss with asymmetric tails around feldspar porphyroclasts; (c) outcrop of the Vaikrita Thrust with mylonitic micaschist interbedded with quartzitic levels showing top-to-the-SW sense of shear; (d) Berinag Thrust separating the Deoban metapelite from the overlying Berinag quartzite.

fabrics and asymmetrical boudins pointing to a top-to-the-south/SW sense of shear (Jain et al., 2014).

At the microscale, the main kinematic indicators – such as the S–C fabric, σ and δ porphyroclasts and mica fish – confirm a top-to-the-SW sense of shear. At the microscale, the samples of the Vaikrita Thrust exhibit a main foliation (S_m) overprinting an older one (S_{m-1}), only locally preserved. Garnet is enveloped by the main foliation, whereas staurolite porphyroblasts are syn-kinematic and contain an internal foliation (S_i) concordant with the external foliation. Grain boundary migration (GBM; Passchier & Trouw, 2005) and minor static recrystallization represent the main deformation mechanisms in quartz. Kinematic indicators, such as the S–C–C′ fabric, mica fish and σ/δ porphyroclasts indicate a top-to-SW sense of shear (Jain et al., 2014).

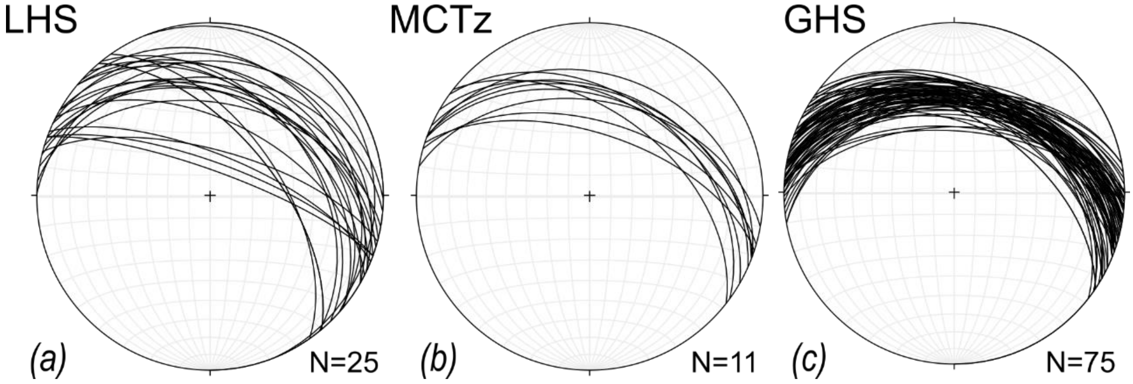

Figure 2.5. Stereoplots of the main foliation measured in the field in the Alaknanda valley of (a) LHS, (b) MCTz and (c) GHS. Wulff net, lower hemisphere projection.

According to Spencer et al. (2012) and Thakur et al. (2015), pressure-temperature (P-T) estimates for the MCTz are in the range of 500–600°C and 0.5–1.2 GPa, with a general structurally upward increase of P-T conditions. Montemagni et al. (2016) reported evidence of aqueous fluid circulation during the first stages of the MT activity. Above the VT (Fig. 2.3), the GHS (the Vaikrita group; Jain et al., 2014) has been subdivided into three main formations: the structurally lower Joshimath Formation consists of kyanite + garnet + biotite + white mica ± staurolite gneiss. In the middle of the GHS, kyanite + garnet ± K-feldspar ± white mica gneiss, migmatitic gneiss, and minor amphibolite form the Suraithota Formation. The Bhapkund Formation, at the top of the GHS, is composed of garnet + K-feldspar + sillimanite migmatite (stromatite and minor diatexite) and small tourmaline-bearing leucogranite lenses. Five different types of leucosomes/melt patches have been described by Jain et al. (2013) from the migmatite, reflecting different stages of structurally controlled melting and melt migration in the Bhapkund Formation. P-T data by Spencer et al. (2012) suggest an increase of P-T conditions from the Joshimath (~700–800°C, 1.0–1.4 GPa) to the Suraithota (~800–860°C, ~1.40 GPa) Formations, whereas similar T for the Suraithota Formation, but lower equilibration P (~0.85–1.00 GPa) were reported for the Bhapkund Formation (Spencer et al., 2012). The P-T estimates by the latter authors are significantly higher than those reported by Hodges & Silverberg (1988) for the GHS rocks along the Alaknanda - Dhauli Ganga valleys (530–680°C, 0.30–1.00 GPa). At the top of the Bhapkund Formation, Jain et al. (2014) reported evidence of top-to-the-NE extensional shearing related to ductile deformation along the STDS. Structurally above the Bhapkund Formation (Fig. 2.3), the THS occurs, composed of the Neoproterozoic-Cambrian low-grade Martoli Formation and very low-grade to unmetamorphosed Post- Martoli Formation (Jain et al., 2014, and references therein). Based on white mica geochronology, the metamorphism of the THS in the study area is as old as ~40 Ma (Crouzet et al., 2007, and references therein).

Near the Malari village (Fig. 2.3, 2.6) the Malari leucogranite, a very small pluton, occurs (Sachan et al., 2010; Spencer et al., 2012; Jain et al., 2014; Thakur et al., 2015). This granite is composed of quartz (30%–35%), K-feldspar (35%–40%), plagioclase (15%–25%), muscovite (~5%), and tourmaline (~5%) (Sachan et al., 2010). It intrudes the upper portion of the GHS, within the extensional deformation zone related to the STDS (Jain et al., 2014; Shreshtha et al., 2015; Iaccarino et al., 2017b). Its relationship with the STDS is debated in the literature. Sachan et al. (2010) stated that the Malari is an undeformed pluton that experienced only minor brittle deformation or alteration and intruded both the STDS and the overlying THS. These authors obtained a U-Pb zircon age of 19.0 ± 0.5 Ma and suggested that the Malari leucogranite post-dates the ductile fabrics related to the STDS. Several other authors (Spencer et al., 2012; Jain et al., 2014; Thakur et al., 2015; Sen et al., 2015; Iaccarino et al., 2017b) regarded the Malari main body and associated leucogranite dykes as affected by both ductile and brittle deformation, related to motion on the STDS. Furthermore, no evidence was found by any of these groups that the leucogranite crosses the THS. The exact trace of the STDS is buried in scree and vegetation in the only visible leucogranite outcrop (Fig. 2.6), and no intrusive rocks are found in the THS over an area c. 100 times wider than the radius of the outcropping pluton.

Sen et al. (2015) proposed that the Malari leucogranite experienced ductile deformation until c. 15 Ma, based on ^{40}Ar/^{39}Ar dating of muscovite and evidence for dynamic recrystallization in quartz and feldspar. Iaccarino et al. (2017b) proposed an age of c. 19-20 Ma for the ductile shearing along the STDS based on in situ U-(Th)-Pb analyses of monazite preserved in high-temperature mylonites located structurally below the Malari granite. The structural position of the Malari granite and associated dykes can provide useful constraints on timing of deformation along the STDS. In fact, according to their kinematic relationship with respect to the ductile fabrics of the STDS, leucogranites have often been used to date shearing along the STDS (Searle et al., 2003, 2010; Carosi et al., 2013; Cottle et al., 2015; Montomoli et al., 2017a). The area around Malari has been subdivided by Iaccarino et al. (2017b) into three main structural domains with different deformation features, mostly related to normal sense top-to-the N/NE STDS-related shearing. With increasing structural height they are: (a) the upper GHS where high temperature (HT)-mylonite are reported at the top; (b) the medium temperature (MT)-mylonite zone, including the sheared Malari granite and dykes and, (c) the Martoli Formation, the basal portion of the THS, where N/NE verging folds were reported (Spencer et al., 2012). The lowermost domain is characterized by the occurrence of HT deformation microstructures, formed during normal sense shearing on the STDS. T ≥ 650 °C have been suggested by GBMII-recrystallization regime microstructures (Law, 2014) and the syn-kinematic growth of sillimanite and biotite (Iaccarino et al., 2017b).

Figure 2.6. (a) outcrop of the main body of the Malari granite. Two clearly visible leucogranitic dykes intruding the main granite body are highlighted with white arrows; (b) leucogranitic dyke intruding the Malari main body; (c) leucogranite intruding the HT-mylonite; (d) close-up on sillimanite shear bands with late muscovite in the migmatite.

The middle domain, with MT-mylonite, is characterized by microstructures suggesting a deformation regime of 400-500 °C (Iaccarino et al., 2017b) based on the occurrence of subgrain rotation recrystallization (SGR) in quartz and brittle-ductile transition in feldspar. Finally, in the uppermost domain temperatures of deformation do not exceed 400 °C, as suggested by mineral assemblages (Sachan et al., 2010) and by bulging recrystallization in quartz (Iaccarino et al., 2017b). Within the previous two domains (MT-mylonites/ HT-mylonites), extensive intrusions of granitic dykes, both deformed and undeformed, have been documented (Jain et al., 2014; Iaccarino et al., 2017b). Moreover, a later extensive brittle faulting, overprinting ductile features, has been recognized in the area (Spencer et al., 2012; Jain et al., 2014; Iaccarino et al., 2017b).

2.3.2 The Bhagirathi – Gangotri valley

The study area is located (Fig. 2.7) from the village of Sainj in the southernmost portion of the transect to the village of Bhaironghati in the Gangotri glacier valley.

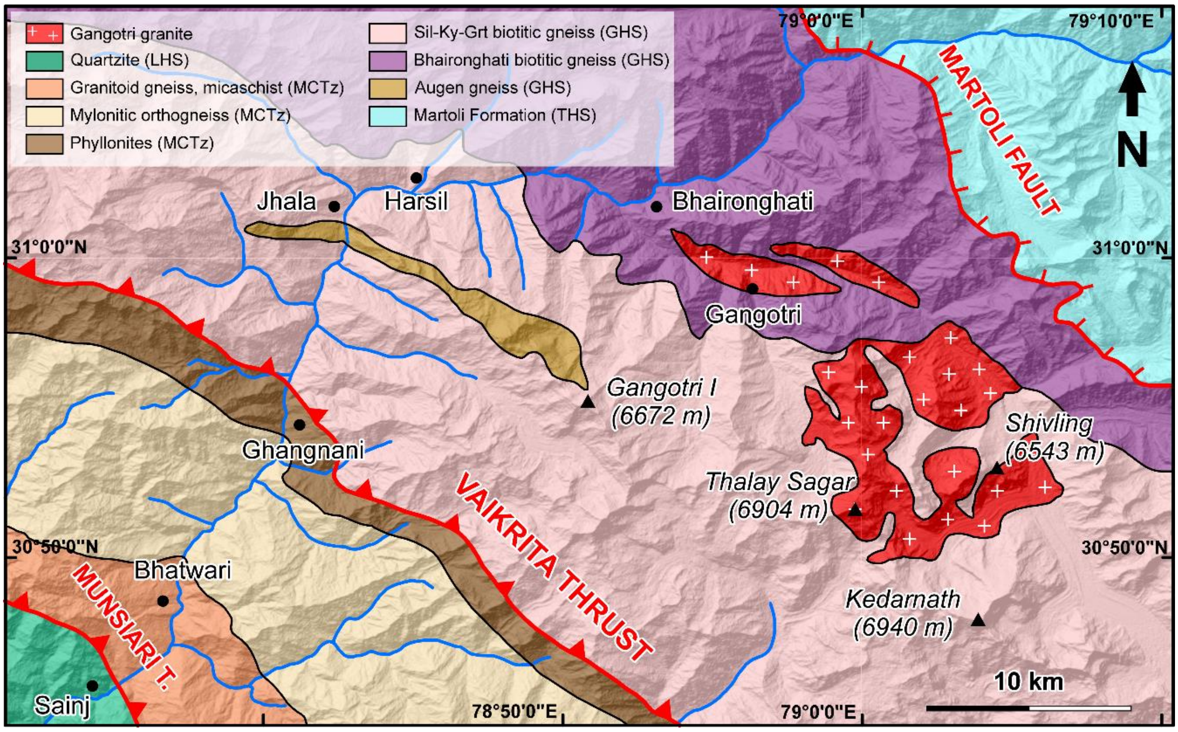

Figure 2.7. Geological map of the Bhagirathi – Gangotri valleys (modified after Searle et al., 1993; Singh, 2019).

In the southernmost portion of the study area low to medium grade quartzite, metapelite, carbonates and volcanics of the LHS crop out (Searle et al., 1993). Structurally above, the MCTz, a 10 km-thick package of intensively sheared rocks (gneiss, granodiorite, metapelite, and amphibolite: Searle et al., 1993), divides the LHS from the overlying GHS. The boundaries of the MCTz are the Munsiari Thrust at the base and the Vaikrita Thrust at the top, the latter considered the MCT sensu stricto as well as further east in the Alaknanda and Dhauli Ganga valleys (Célérier et al., 2009a; Spencer et al., 2012; Jain et al., 2014; Sen et al., 2015; Thakur et al., 2015). According to Metcalfe (1993), the deformation towards the structurally upper part of the MCTz (i.e. the Vaikrita Thrust) is completely ductile, whereas near the Munsiari Thrust fabrics related to ductile-brittle transition occur. Within the MCTz the metamorphic grade increases structurally upward from the Munsiari Thrust to the Vaikrita Thrust (Metcalfe, 1993; Searle et al., 1993), increasing in temperature from 500 to 770 °C and in pressure from 6 to 12 kbar (Metcalfe, 1993). The main shear fabric in the MCTz is related to D2 (Metcalfe, 1993) and a variety of top-to-the-south kinematic indicators show a simple shear dominated deformation during this event. Above the Vaikrita Thrust the GHS consists of high-grade metamorphic rocks increasing in grade northwards up to the top of the unit, where migmatitic orthogneiss occur (Scaillet et al., 1995) and granitic dykes commonly intrude sillimanite plus K-feldspar bearing gneiss (Metcalfe, 1993). The deformation fabrics in the GHS have been extensively described by Metcalfe (1993) and Searle et al. (1993) who recognized an earlier coaxial D1 fabric followed by a penetrative non-coaxial event subdivided in two events: the D2a, synchronous with the MCT south vergent ductile fabric, and the D2b showing a top-to-the-north sense of shear in the upper portion of the GHS. Lastly, D3 related fabrics are characterized by brittle deformation as a consequence of the propagation of thrusting in the LHS and extension upwards (Metcalfe, 1993).

A late brittle structure, the Jhala Normal Fault (Metcalfe, 1993; Searle et al., 1999), separates the lower sillimanite-bearing gneiss from the upper metasediment of the Harsil Formation, the latter interpreted by Searle et al. (1999) to be a slice of medium-grade metamorphic rocks bounded by a normal fault at the top of the GHS.

Along the top of the GHS in the Gangotri glacier valley, the Bhagirathi-Gangotri Miocene granites (Stern et al., 1989; Scaillet et al., 1990; Searle et al., 1993; Searle et al., 1999; Singh et al., 2003; Singh, 2019) are large bodies occurring at the boundary between the GHS and the overlying THS, marked by the ductile STDS, locally named the Martoli Fault (Singh, 2019). Above, the Martoli Formation is the lower structural portion of the little-deformed and unmetamorphosed sediments of the THS. The Bhairongathi granite, which intrudes the Harsil formation at the top of the GHS, has been interpreted to be a Cambrian pre-collisional intrusion linked to Cambro-Ordovician magmatism occurring all along the Himalaya (Scaillet et al., 1990; Searle et al., 1999). According to Stern et al. (1989) and Searle et al. (1999), this large intrusion is quite undeformed except for the base that shows a gneissic texture. The Gangotri and Shivling-Bhagirathi leucogranites intrude the older Bharoingathi body: they are tourmaline-bearing leucogranite and two-mica leucogranite, respectively (Searle et al., 1999; Singh, 2019). Their ages obtained by different geochronometers (i.e. K/Ar, Rb/Sr, ^{40}Ar/^{39}Ar, U-Th-Pb) have been constrained between 18 and 23 Ma (Seitz et al., 1976; Stern et al., 1989; Sorkhabi et al., 1996; Harrison et al., 1997; Searle et al., 1999) and petrochemical and magnetic studies fully describe their features (Scaillet et al., 1990; 1995).

3. METHODS

3.1 Electron Micro Probe Analysis

BSE images, element maps and quantitative chemical analyses of micas were obtained on carbon coated thin sections using a JEOL 8200 Super Probe electron microprobe hosted in the Dipartimento di Scienze della Terra "A. Desio", Università degli Studi di Milano. The system was operated using an accelerating voltage of 15 kV, a beam current of 50 nA for the element maps. Quantitative point analyses used an accelerating voltage of 15 kV, a beam current of 5 nA and a spot size of 3 μm. Counting times for each spot analysis were 30 s on the peaks and 10 s on the right and left backgrounds. Standards used were omphacite (Na), grossular (Ca, Al and Si), fayalite (Fe), olivine (Mg), orthoclase (K), rhodonite (Mn), ilmenite (Ti), niccolite (Ni), pure Cr (Cr) and zircon (Zr, Hf). The raw data were corrected for matrix effects using the ρ-ϕ method from the JEOL series of programs.

3.2 ^{40}Ar/^{39}Ar step-heating geochronology

In many metamorphic rocks, there are several generations of minerals formed at different times that may, or may not, have different chemical composition. A straightforward advantage of the step-heating technique is that the effects of increasing oven temperature results in selective breakdown of crystal structures, whose isotope signatures are thus made accessible to analysis (Villa & Williams, 2013).

Therefore ^{40}Ar/^{39}Ar step-heating approach is a key procedure to unravel petrological and chemical complexities because of the recognition of different ages due to the different steps of Ar release (Rolland et al., 2009; Villa, 2015) characterized by different Cl/K and Ca/K ratios (Villa et al., 2014). As micas are ubiquitous in strongly deformed shear zones (Sanchez et al., 2011), ^{40}Ar/^{39}Ar method on biotite and muscovite has commonly been employed to constrain the ages of mylonitization (West & Lux, 1993).

Samples were sieved and micas, in the fractions 125-250 μm or 150-350 μm depending on the grain size of analyzed sample, were separated by magnetic and gravimetric techniques and subsequently cleaned by prolonged handpicking, a time-consuming but necessary procedure. Biotite and muscovite crystals selected by handpicking are required to be as much as possible homogeneous single-crystal sheets without any inclusion.

Biotite and muscovite samples of 10 to 20 mg were wrapped in Al foil, creating a flat disk 10 mm in diameter and c. 1 mm in thickness. Samples were irradiated in the McMaster University reactor (Ontario, Canada) for 30 MWh, carefully avoiding Cd shielding. In order to control the vertical flux gradient, monitors of Fish Canyon sanidine (FCs) and McClure Mountain hornblende (MMhb) were interlayered with the sample disk wraps. The FCs age was assumed to be 28.172 ± 0.028 Ma (Rivera et al., 2011) and MMhb age 523.98 ± 0.12Ma (Schoene & Bowring, 2006).

Before each sample was analyzed, a blank measurement was followed by two successive measurements of atmospheric Ar delivered by a pipette system. Samples, which were usually heated in 12–15 steps, were step-heated in a low-blank double-vacuum furnace.
Before each analysis, the gas is cleaned in two SAES™ C-50 getters. All five Ar isotopes, as well as hydrocarbons (mass 41) and elemental ^{35}Cl, were measured in a NuInstruments™ Noblesse® noble gas mass spectrometer, equipped with one Faraday (F) collector with a 10^{11} Ω resistor and two MasCom™ ion counters (IC0 and IC1). The simultaneous measurement of the Ar isotopes spaced by two mass units and the direct calibration of the F/IC0 and IC0/IC1 gains in each individual run is guaranteed by this configuration. The F/IC0 and IC0/IC1 gains are similar, but not necessarily equal, to those determined from the atmospheric pipettes, which moreover independently quantify the mass fractionation originating in the source.

The measurement sequence consists of four cycles: ^{40}Ar(F), ^{38}Ar (IC0), ^{36}Ar(IC1); ^{38}Ar(F), ^{36}Ar(IC0), mass 34(IC1); ^{39}Ar(F), ^{37}Ar(IC0), ^{35}Cl(IC1); mass 41(F), ^{39}Ar(IC0), ^{37}Ar(IC1). The fourth cycle is only active when the ^{39}Ar ion count rate is less than 1 MHz. In order to avoid spurious results due to the time-dependent ion counter non-linearities (Barberini & Villa, 2015) the four cycles were repeated 25 times.

The raw data, corrected for mass spectrometer background, ion counter gains, blank measurements, source fractionation, and decay of ^{37}Ar since irradiation, were processed in the CalcolAr Excel spreadsheet, in which also all the associated uncertainties are propagated. To control stoichiometry and obtain Ca/K and Cl/K ratios, the absolute concentrations of K, Cl and Ca have been converted from the total concentration of ^{39}Ar, ^{38}Ar and ^{37}Ar, respectively.
Since the stoichiometry of biotite and muscovite should be Ca-free, we consider only "isochemical steps" with a low Ca/K ratio and constant Cl/K for calculating the final age, as used in Villa et al. (2006).
The irradiation intensity factor, J, was interpolated for each sample from the equation defined by the J values of the monitors. The ^{40}K decay constant used for the age calculation was 5.543 x 10^{-4} Ma^{-1} (Steiger & Jäger, 1977).
The isochron calculations and weighted averages were calculated with software ISOPLOT (Ludwig, 2003).

In some samples, phyllosilicates are found in fine-grained and intimately intergrown mixtures that makes it impossible to obtain monomineralic separates. The interpretation of spectra from such samples is quite complex and could generate misunderstandings. The best approach we developed is the simultaneous use of correlation diagrams (age vs Ca/K and Cl/K; Ca/K vs Cl/K) and the Ar Differential Release Plot (DRP). The Ar release in each step is normalized to the temperature in that step: Merrihue & Turner (1966) reported release vs. T, Villa et al. (2000) reported release vs. T*$t^{1/2}$ (assuming mainly Fickian) however if breakdown is rapid, the $t^{1/2}$ is useless.

DRP procedure applied to separates with different degrees of purity allows to quantify the bias given by fine-grained intergrowths and, combining Ca-Cl-K signatures of the isochemical steps with Ar DRP discriminate the structure collapse of micas *sensu stricto* from that of impurities. The Ar DRP diagram shows the release of ^{39}Ar vs the furnace heating temperature steps coming from the spectrometer. As an example, Figure 3.1 compares the ^{39}Ar release due to pure muscovite, muscovite plus chlorite and pure chlorite separates. This diagram allows us to clearly identify the influence of the compresence of phyllosilicates on the trend of Ar release during the heating steps, allowing to select the proper steps corresponding to the degassing of micas *sensu stricto*, which leads to more reliable age determinations.

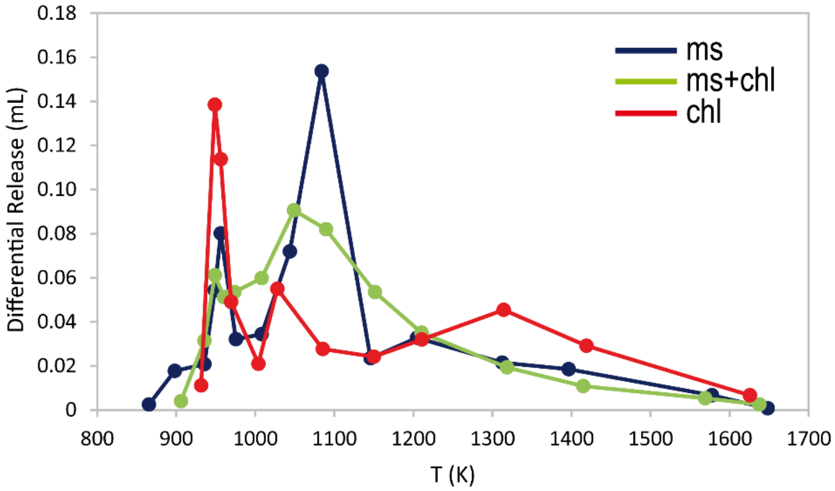

Figure 3.1. Ar release of pure muscovite (blue), muscovite + chlorite (green) and pure chlorite (red). Mineral abbreviation as Whitney & Evans (2010).

In the Ar DRP diagram the abscissa is the degassing temperature and the ordinate the percent release of the respective isotope. It must be stressed that the differential release of ^{39}Ar, ^{37}Ar, etc., do not *per se* identify the mineral phase being degassed; only a mineralogical and microchemical investigation can provide a firm identification. It is advantageous, for a reliable comparison between the Ar release patterns of different samples using this plot, that the heating schedules be identical, both in terms of temperature and of heating time. A general comparison requires normalizing the Ar release of each step by the temperature increase, ΔT, and by the time spent at temperature, Δt.

This diagram was used by Villa et al. (2000) to chart the release characteristics of different members of the amphibole family, as it allows us to choose the optimum degassing schedule, Villa et al. (2000) used it to disentangle the Ar release of finely intergrown coexisting amphibole generations of different petrological significance in a multiply retrogressed rock.

A further development is investigating the Ar budget of retrogressed mica. Unlike amphibole, whose K concentration is not fixed by stoichiometry, micas have a fixed theoretical K concentration, which translates to a well-defined theoretical ^{39}Ar concentration. From the total ^{39}Ar released from a biotite or muscovite separate it is always possible to calculate if the K concentration respects stoichiometry (in which case the mineral is both pure and unaltered) or has lost K, meaning that it has been partly retrogressed to chlorite, smectite, or other K-free phases. In this case, it is frequently observed that secondary clay minerals (with weak interlayer bonds) degas at lower temperature than the mica having a pristine crystal structure. In cases where the phase inventory of a sample is restricted to two, e.g. mica and K-poor alteration intergrowths, it is possible to exploit the entire information provided by all five Ar isotopes. The Ca/K and Cl/K ratios (calculated from the $^{37}Ar/^{39}Ar$ and $^{38}Ar/^{39}Ar$ ratio, respectively) are elevated in chlorite (Lo & Onstott, 1989; Di Vincenzo et al., 2003) and pyrophyllite (Villa et al., 2018) relative to biotite and muscovite. This ensures that the Ar release deriving from pristine mica is easily identified by the lower Ca/Cl/K signature, which predictably coincides with the degassing peak identified in the differential release plot. Since the true age of the mica is given precisely by the steps pertaining to the Ca/Cl/K signature of mica, the degassing of the alteration phases manifests itself as a secondary peak in the differential release plot - by selecting mineral separates with different intensity of handpicking, it can be observed that the differential release peak of pristine mica is unchanged, whereas that related to the alteration phase increases markedly in the less purified aliquot. As most alteration events are resolvably diachronous with respect to the age of the pristine mica, it is expected that the apparent age of the steps lying off the degassing peak should be unreliable.

3.3 Three-dimensional X-ray micro computed tomography for vorticity estimates

X-ray micro computed tomography (microCT) is a non-destructive technique used since the 1990s in different fields of geological sciences (Denison et al. 1997, Denison & Carlson, 1997; Ketcham & Carlson, 2001, Cnudde et al., 2006 and references therein), such as paleontology, soil and petroleum, fractures and rock porosity investigation and 3D visualization of petrography. X-ray microCT produces stacks of 2D grey-scale value images (referred to as “slices”) that allow observing the internal structure of a scanned object. As exhaustively reported in Denison et al. (1997), the contrast in an X-ray CT image is mainly caused by differences in X-ray absorption within the object due to variation in density and chemical composition.

MicroCT analyses were performed with a BIR Actis 130/150 Desktop Micro-focus CT/DR system hosted at Dipartimento di Scienze dell’Ambiente e della Terra, Università degli Studi di Milano – Bicocca following the procedure reported in Zanchetta et al. (2011). The samples were attached to a plastic sample holder with their maximum axis in a vertical position. The dimensions of the voxel (3D pixel, i.e. the resolution of the images) of the obtained images are: x, y, z = 19 μm. The obtained 3D microCT image stacks were processed with the software Avizo^{TM}.

3.4 Universal stage quartz *c*-axis deformation temperature and Crystallographic Preferred Orientation

The quartz *c*-axis fabric opening-angles has been widely used (Law, 1990; Law et al., 2004; Law et al., 2013 and references therein) to derive deformation temperatures and Crystallographic Preferred Orientation (CPO) of quartz rich rocks. This method has been firstly proposed by Kruhl (1996) as a geothermometer: the greater the opening angle of quartz *c*-axis fabric the higher the deformation temperature. The opening angle increase is directly correlated with temperature, as it depends on prism [c] slip that is more and more enhanced with increasing deformation temperatures. As stated by Kruhl (1996) the uncertainties in the calculation of deformation temperatures are ±50 °C. As discussed in Law et al. (2013), this method is useful to determine the temperature of ceasing of plastic deformation, due to mechanisms such as dislocation creep and dynamic recrystallization.

It is widely accepted that quartz CPO depends on temperature, strain rate, water content and differential stress (Lister, 1977; Stipp et al., 2002; Menegon et al., 2008; Pennacchioni et al., 2010; Peternell et al., 2010). The temperature of deformation controls the intra crystalline slip systems, with activation of basal <a>, rhomb <a>, prism <a> and prism <c> slip systems with increasing temperature (Lister & Paterson, 1979; Pennacchioni et al., 2010).

Quartz *c*-axis fabrics have been optically measured with a microscope equipped with a universal stage (U-stage; Fig. 3.2) at Department of Geosciences, Virginia Tech University. The U-stage has been widely used on metamorphic quartz-rich rocks in thin section to assess their fabric as well as their deformation-recrystallization history, determining the orientation of the *c*-axis of each quartz grain (Kile, 2009 and references therein). A disadvantage of the method is that the procedure is time-consuming and therefore Electron Back Scatter Diffraction (EBSD) or Fabric Analyzer (FA) techniques, which are extremely effective, are replacing the U-stage (Kile, 2009; Peternell et al., 2010), notwithstanding operator eye cannot be replaced by these instrumentations.

Crystal fabric data were measured on thin sections cut perpendicular to foliation and parallel to lineation. Starting from the U-stage measurements, stereoplots were obtained through the "C-Axis: Universal Stage Data Conversion" Excel spreadsheet by Sean R. Mulcahy.

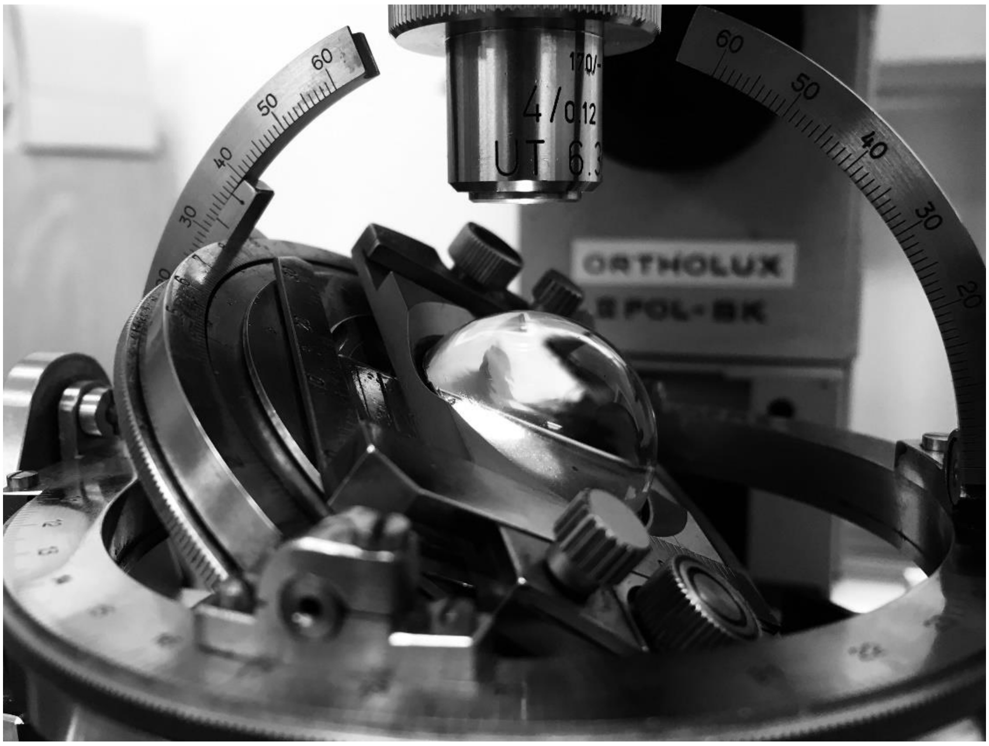

Figure 3.2. Universal stage used for quartz *c*-axis measurements.

4. PETROGRAPHY, MICROSTRUCTURES AND MINERAL CHEMISTRY OF SELECTED SAMPLES

In this chapter the petrography, microstructural features and mineral chemistry of the samples selected for further investigation will be described. The samples have been selected for their structural position and clarity of fabric in order to subsequently be dated through the ^{40}Ar/^{39}Ar stepheating technique or be studied for deformation temperature and/or kinematic vorticity estimates.

4.1 Alaknanda – Dhauli Ganga valleys

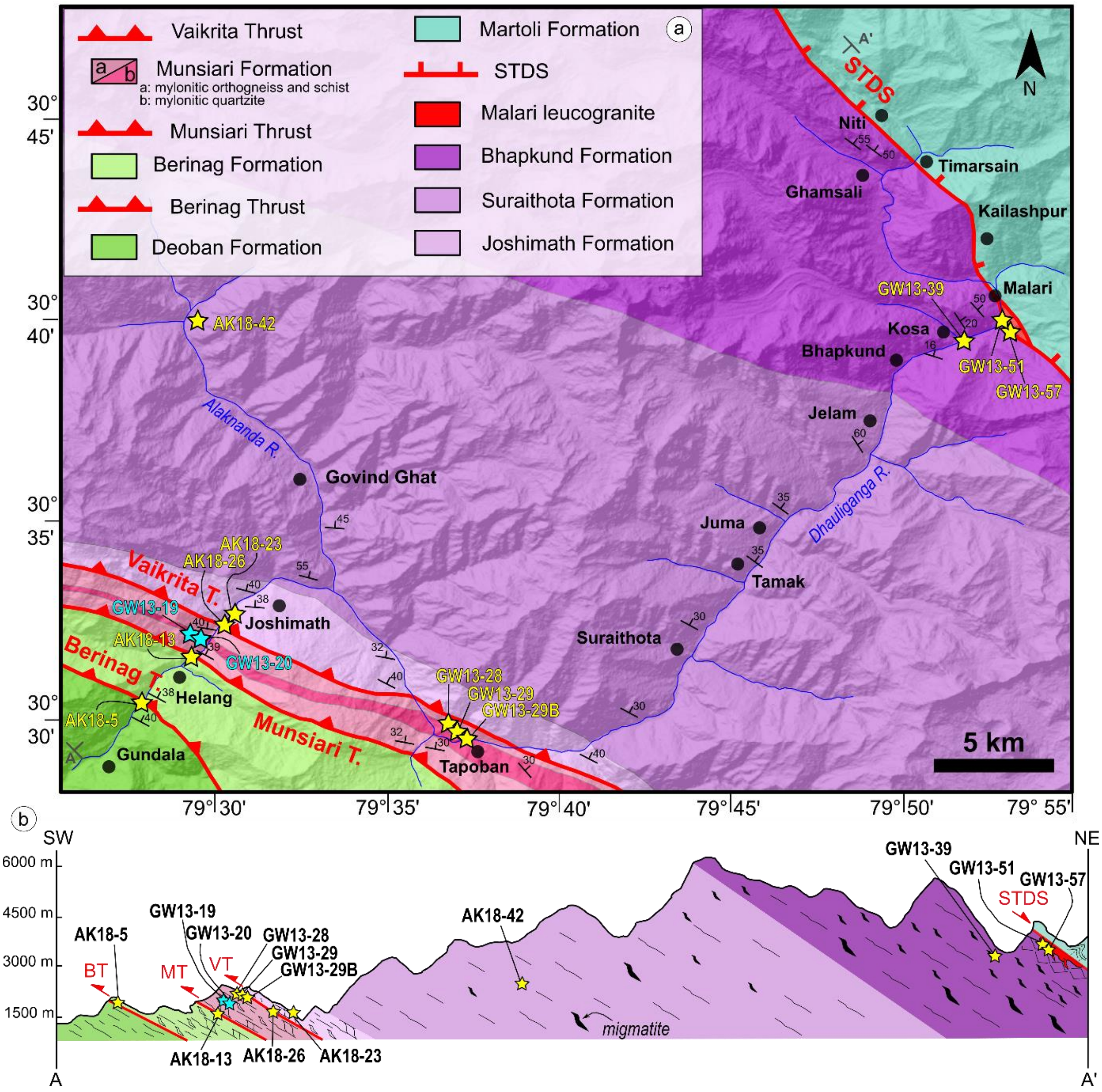

Figure 4.1. Study area (after Jain et al., 2014 and Hunter et al., 2018). Positions of samples are shown with yellow stars (^{40}Ar/^{39}Ar dating, Chapter 5) and light blue stars (CPO and deformation temperature, Chapter 6).

Figure 4.1 shows the position in geological map and cross-section of both samples analyzed by ^{40}Ar/^{39}Ar stepheating dating (yellow stars) and by universal stage (light blue stars) for Crystallographic Preferred Orientation (CPO) and deformation temperature described in Chapter 5 and Chapter 6, respectively.

4.1.1 Main Central Thrust zone

Three samples of mylonitic mica schist (GW13-28, GW13-29 and GW13-29B) were selected from the Vaikrita Thrust close to the village of Tapoban (Fig. 4.1). Sample GW13-29 was collected <30 m downhill from sample GW13-28, following the road between Joshimath and Suraithota. Sample GW13-29B was taken from the same outcrop, <1 m away from GW13-29.

All samples display a main schistosity S2, referred to as S_m, accompanied by variably identifiable rare pre-S_m relicts (S1) and/or post-S_m static mineral growth. Sample GW13-28 is a garnet–staurolite–two mica-bearing impure quartzite that also contains tourmaline, ilmenite, monazite and abundant late chlorite, partially replacing biotite and garnet (Fig. 4.2b). The main foliation is defined by the shape-preferred orientation (SPO, Passchier & Trouw, 2005) of muscovite (muscovite-2), biotite (biotite-2) and ilmenite. This foliation can be classified as disjunctive schistosity characterized by a discrete transition to domains of quartz-rich microlithons. Static recrystallization of biotite and muscovite can be also found sporadically. In the phyllosilicate-rich layers, garnet porphyroclasts are enveloped by the main foliation (Fig. 4.2a), whereas in the quartz-rich granoblastic domains garnet shows a skeletal aspect. Staurolite appears along the main foliation, suggesting syn-kinematic growth (Fig. 4.2a). The main recrystallization mechanism in quartz is GBM supported by sutured and amoeboid grain boundaries (Fig. 4.2c). However, static annealing of quartz is sometimes discernible by straight grain boundaries and triple points. Kinematic indicators at the microscale are represented by asymmetrical recrystallization tails of micas and asymmetrical strain shadows around garnet porphyroclasts (Fig. 4.2a) and foliation fish (Fig. 4.2d; Passchier & Trouw, 2005), which show a top-to-the-south/SW sense of shear.

Sample GW13-29 is a mylonitic mica schist (Fig. 4.2e, f) with the mineral assemblage quartz, biotite, muscovite, garnet, plagioclase and ilmenite. The S_m is an anastomosing disjunctive schistosity (Passchier & Trouw, 2005) defined by the shape-preferred orientation of biotite (biotite-2) and muscovite (muscovite-2). Locally, within the microlithons, micas-1 oriented at a high angle with respect to S_m marks an older foliation (S1, Fig. 4.2f). Garnet is enveloped by the main foliation and often contains aligned inclusions of quartz, plagioclase, micas and allanitic epidote, defining an internal foliation (S_i) that is non continuous with the external foliation (S_e, Fig. 4.2e). Thus garnet can be regarded as forming intertectonic porphyroblasts. However, in some circumstances inclusions in garnet are not aligned. The mica-2 generation is followed structurally by a static growth of larger mica (mica-3) around garnet grains (Fig. 4.2e). Additional sporadic mica-3 grains are found in the matrix: they are oriented in the same direction as mica-2, but are not comminuted and suggest later, static growth by a process resembling Ostwald ripening and pseudomorphism. Relict biotite-1 and muscovite-1 may be present, but are difficult to identify because ductile deformation was intense, reducing the grain size of micas and giving them a shredded appearance. The latest generation consists of large micas (muscovite-3 and minor biotite-3) forming coronitic structures around garnet. These micas are characterized by a lack of internal deformation (undulose extinction or kinking), in contrast with mica oriented along S_m. Static recrystallization of biotite and muscovite is evident as mica flakes cross-cut S_m. The main deformation mechanisms were GBM followed by the minor static recrystallization of quartz. Asymmetrical recrystallization tails of garnet porphyroclasts indicate a top-to-the-south/SW sense of shear.

Sample GW13-29B is a garnet–biotite-bearing mylonitic mica schist (Fig. 4.2g, h), also containing quartz, muscovite, plagioclase and minor chlorite. The S_m, defined by the shape-preferred orientation of biotite (biotite-2) and muscovite (muscovite-2), can be classified as a disjunctive schistosity. The microstructure is characterized by the alternation of granoblastic quartzo-feldspathic layers and lepidoblastic layers. The main foliation envelops intertectonic garnet that contains aligned quartz inclusions defining an internal foliation (S_i) discordant to the external one (Fig. 4.2g, h). Muscovite and biotite crystals (micas-3) show a coronitic texture around garnet porphyroclasts (Fig. 4.2h). These micas lack undulose extinction, kinking and internal deformation (Fig. 4.2h). These features are, instead, observed in mica-2 (Fig. 4.2g, h). Kinematic indicators, such as σ-porphyroclasts and prevalent group 1 mica fishes (Passchier & Trouw, 2005), show a top-to-SW shear sense.

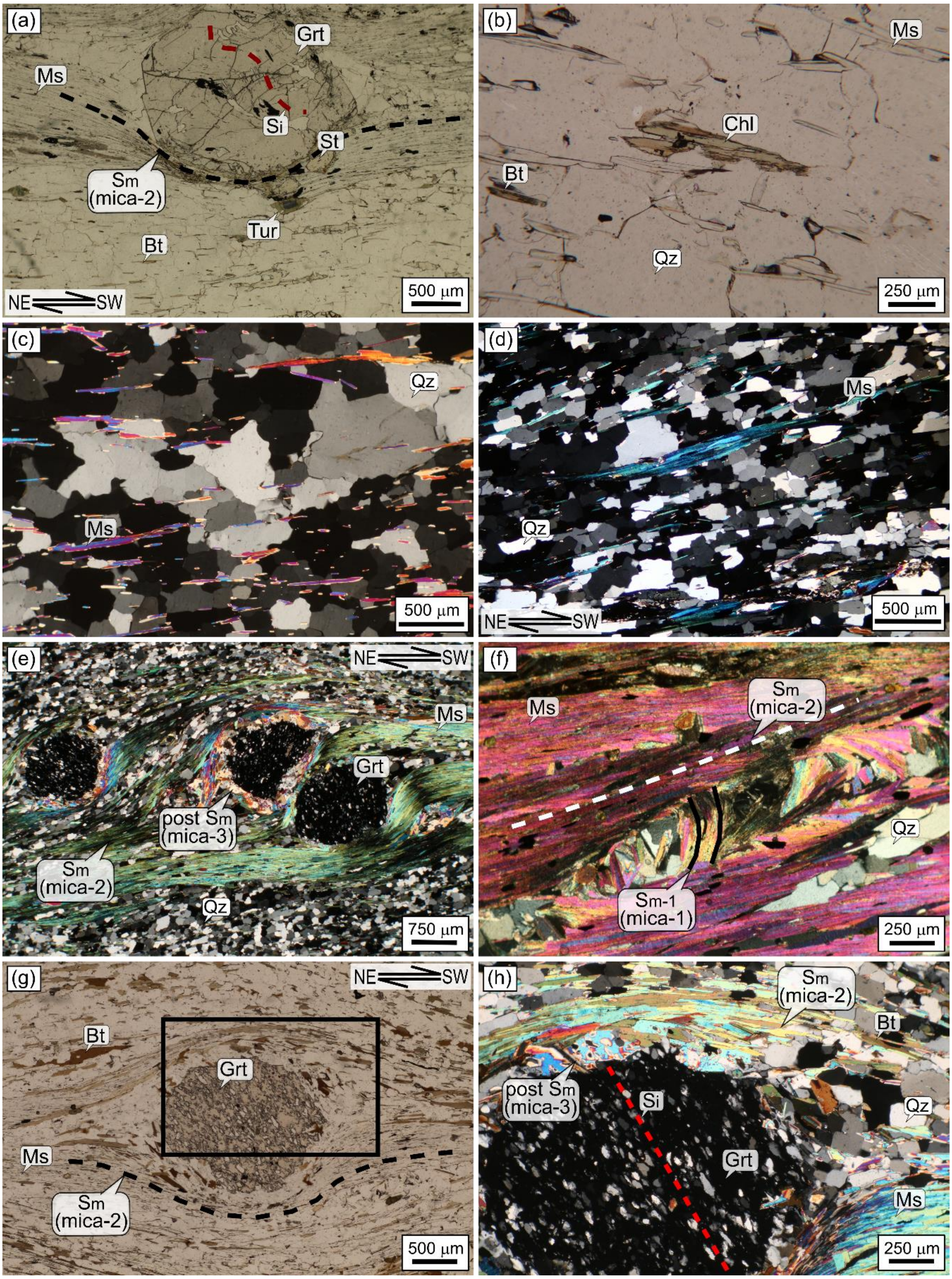
(a)
Grt
Ms
Si
St
Sm (mica-2)
Tur
Bt
NE SW
500 µm
(b)
Ms
Chl
Bt
Qz
250 µm
(c)
Qz
Ms
500 µm
(d)
Ms
Qz
NE SW
500 µm
(e)
NE SW
Ms
Grt
post Sm (mica-3)
Sm (mica-2)
Qz
750 µm
(f)
Ms
Sm (mica-2)
Qz
Sm-1 (mica-1)
250 µm
(g)
NE SW
Bt
Grt
Ms
Sm (mica-2)
500 µm
(h)
Sm (mica-2)
Bt
post Sm (mica-3)
Si
Qz
Grt
Ms
250 µm

Figure 4.2. Microstructures of the Vaikrita Thrust. (a) Garnet porphyroclast wrapped by the main foliation (Sm), showing a top-to-the-SW sense of shear (sample GW13-28). (b) Chloritization of biotite (sample GW13-28). (c) Ameboid grain boundaries in quartz, testifying grain boundary migration recrystallization (sample GW13-28). (d) Foliation fish pointing a top-to-the-SW sense of shear (GW13-28). (e) σ-Type garnet orphyroclasts in sample GW13-29 showing a top-to-the-SW shear sense. Note the coronitic mica-3 around garnet. (f) Sm and relict Sm−1 in ylonitic mica schist (sample GW13-29). (g) σ-Type garnet porphyroclast displaying a top-to-the-SW sense of shear (sample GW13-29B). (h) Detail of the inset in part (g). Note non-deformed coronitic micas and deformed micas on the Sm foliation; intertectonic garnet shows an Si discordant with respect to Sm (sample GW13-29B). Mineral abbreviations following Whitney & Evans (2010).

4.1.1.1 Mica compositions

The representative EMP analyses of micas are reported in Table 4.1, the full set of EMPA from the studied samples are given in Supplementary Material Appendix 1. Muscovite and biotite analyses were recalculated as atoms per formula unit (apfu) on the basis of 11 oxygens. Their compositional variabilities are shown in Figures 4.3 and 4.4. Figure 4.3 shows representative back-scattered electron images in which the variation in XMg (i.e. Mg/(Mg + Fe)) and Ti concentration between micas along the main foliation and coronitic micas is highlighted.

In all three samples, white mica shows limited compositional variation around the muscovite–celadonite join, with Si ranging between 3.05 and 3.17 apfu (Fig. 4.4a). Muscovite in sample GW13-28 is characterized by Al/Si ratios higher than in the other samples (Fig. 4.4a). The Ti concentration (Fig. 4.4b) in the muscovite of sample GW13-28 is lower (0.007–0.023 apfu) and less scattered than in samples GW13-29 and GW13-29B. In GW13-29, muscovite-2 contains more Ti (0.030–0.043 apfu) than muscovite-3 (0.013–0.030 apfu, Figs. 4.3 and 4.4b). The same trend was observed in sample GW13-29B (Fig. 4.4b), where the Ti contents in muscovite-2 (0.023–0.036 apfu) are higher than in mica-3 (0.017–0.035 apfu). The Na/(Na + K) ratio (Guidotti & Sassi, 2002; Fig. 4.4c) of muscovite in sample GW13-28 is higher (c. 0.12–0.14) than in samples GW13-29 and GW13-29B (0.06–0.09) that display similar trends. Muscovite-2 and muscovite-3 from sample GW13-29 have Na/(Na + K) ratios between 0.06–0.09 and 0.06–0.08, respectively. Muscovite-2 and muscovite-3 from sample GW13-29B display similar Na/(Na + K) ratios to those of sample GW13-29 (0.06–0.08, muscovite-2; 0.07–0.08, muscovite-3). The X_{Mg} ratio is lower in muscovite-3 than in muscovite-2. In sample GW13-28, XMg ranges between 0.46 and 0.64. Muscovite-2 in sample GW13-29 shows XMg values between 0.44 and 0.50, whereas XMg of muscovite-3 is between 0.39 and 0.47. XMg in muscovite-2 and muscovite-3 of sample GW13-29B ranges between 0.44 and 0.52 and between 0.40 and 0.51, respectively.

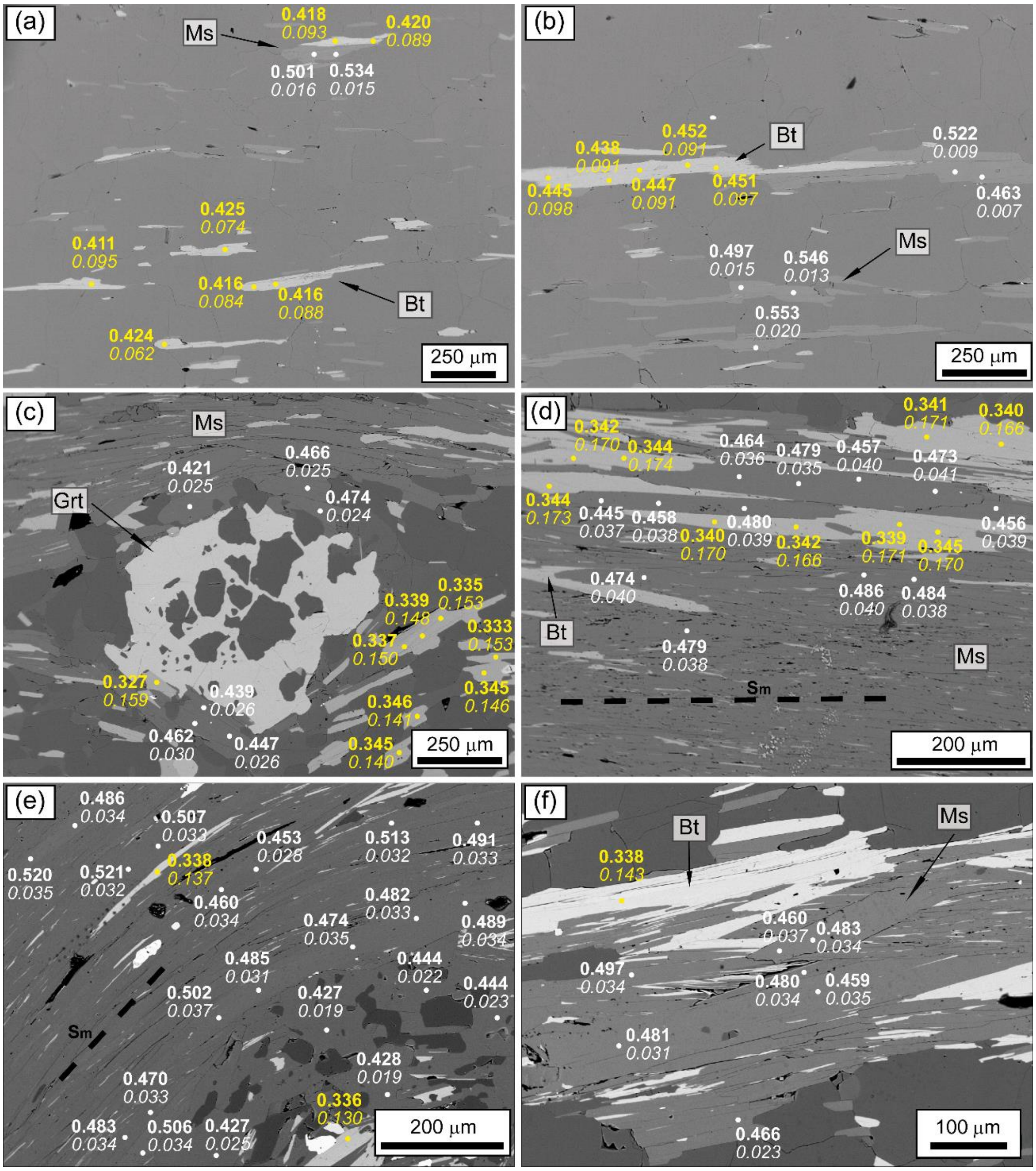

Figure 4.3. Representative back-scattered electron images with X_{Mg} value (bold) and Ti concentration (apfu) (italic) in white for muscovite and yellow for biotite. (a, b) Sample GW13-28; (c, d) sample GW13-29; (e, f) sample GW13-29B. In parts (c) and (e), both biotite and muscovite are observed along the Sm and in static coronites. Mineral abbreviations as in Whitney & Evans (2010).

Table 4.1

	Sample											
	GW13-28				**GW13-29**				**GW13-29B**			
	Muscovite		Biotite		Muscovite		Biotite		Muscovite		Biotite	
	S2	S2	S2	S2	cor.	S2	cor.	S2	cor.	S2	cor.	S2
SiO_2	46.14	46.00	34.36	34.98	46.09	45.79	34.27	34.60	46.17	45.63	34.00	35.00
TiO_2	0.44	0.39	1.52	1.27	0.29	0.77	2.98	3.07	0.47	0.49	2.20	2.52
Al_2O_3	33.79	33.85	18.82	18.93	33.93	32.42	17.18	17.24	34.27	34.65	17.43	17.91
FeO	1.41	1.12	21.69	20.86	1.91	2.26	23.21	23.23	1.99	1.90	24.60	22.19
MnO	0.00	0.00	0.05	0.04	0.01	0.00	0.18	0.18	0.00	0.04	0.11	0.00
MgO	1.06	1.00	8.82	8.64	0.89	1.18	6.68	6.87	0.91	0.80	7.06	8.04
CaO	0.00	0.01	0.00	0.03	0.01	0.00	0.00	0.00	0.00	0.02	0.01	0.00
BaO	0.19	0.19	0.11	0.05	0.27	0.31	0.24	0.15	0.24	0.22	0.12	0.20
Na_2O	0.90	0.91	0.07	0.28	0.65	0.54	0.14	0.16	0.62	0.65	0.08	0.08
K_2O	10.21	10.01	8.96	9.38	10.66	10.97	9.25	9.27	10.88	11.06	9.66	9.74
F	0.00	0.09	0.29	0.38	0.00	0.17	0.16	0.13	0.00	0.12	0.07	0.24
Cl	0.00	0.00	0.04	0.12	0.00	0.00	0.03	0.02	0.00	0.03	0.04	0.03
tot	94.15	93.58	94.73	94.94	94.70	94.42	94.34	94.92	95.53	95.59	95.25	95.96
Si	3.12	3.12	2.66	2.70	3.11	3.12	2.71	2.71	3.09	3.06	2.68	2.70
Ti	0.02	0.02	0.09	0.07	0.01	0.04	0.18	0.18	0.02	0.02	0.13	0.15
Al	2.69	2.70	1.72	1.72	2.70	2.60	1.60	1.59	2.70	2.74	1.62	1.63
Fe	0.08	0.06	1.41	1.35	0.11	0.13	1.53	1.52	0.11	0.11	1.61	1.43
Mn	0.00	0.00	0.00	0.00	0.00	0.00	0.01	0.01	0.00	0.00	0.01	0.00
Mg	0.11	0.10	1.02	0.99	0.09	0.12	0.79	0.80	0.09	0.08	0.83	0.92
Ca	0.00	0.00	0.00	0.00	0.00	0.00	0.00	0.00	0.00	0.00	0.00	0.00
Ba	0.00	0.01	0.00	0.00	0.01	0.01	0.01	0.00	0.01	0.01	0.00	0.01
Na	0.12	0.12	0.01	0.04	0.08	0.07	0.02	0.02	0.08	0.08	0.01	0.01
K	0.88	0.87	0.89	0.92	0.92	0.95	0.93	0.93	0.93	0.95	0.97	0.96
F	0.00	0.02	0.07	0.09	0.00	0.04	0.04	0.03	0.00	0.03	0.02	0.06
Cl	0.00	0.00	0.00	0.02	0.00	0.00	0.00	0.00	0.00	0.00	0.00	0.00
tot	7.02	7.01	7.88	7.91	7.03	7.07	7.82	7.81	7.04	7.08	7.89	7.86

Table 4.1. Representative electron microprobe analyses of muscovite and biotite (wt% oxides). Atomic proportion (apfu) were recalculated based on O = 11.

The mass fractions of the three biotite generations are even more variable than those of muscovite: biotite-1 and -3 are extremely rare. In sample GW13-28, only biotite-2 was analysed. It shows a remarkable chemical variation (Fig. 4.4d–f); in particular, its X_{Mg} is higher and its Ti is mostly lower than that of GW13-29 and GW13-29B. Biotite-2 is fairly homogeneous in GW13-29, whereas it shows two distinct compositional clusters in GW13-29B (Fig. 4.4d–f, green triangles). The ^{IV}Al contents of biotite in sample GW13-28 (Fig. 4.4d) are more variable (1.29–1.42 apfu, Fig. 4.4d) than in biotite-2 and -3 of sample GW13-29 (1.27–1.32 apfu). Biotite from sample GW13-29B forms two compositional clusters discernible in X_{Mg} (0.38–0.40, biotite-2; 0.32–0.34, biotite-3) and ^{IV}Al (1.28–1.30 apfu, biotite-2; 1.30–1.34 apfu, biotite-3) plots (Fig. 4.4d). The Ti concentrations in biotite from sample GW13-28 range between 0.06 and 0.10 apfu, whereas biotite-2 and -3 from sample GW13-29 have higher Ti contents (0.17–0.18 apfu, except for a few analyses, and 0.11–0.16 apfu, respectively, Fig. 4.4e). The Ti concentration of biotite-2 in GW13-29 is detectably higher than that of GW13-29B (Figs. 4.3 and 4.4e). Biotite from sample GW13-29B forms two compositional clusters of biotite-2 discernible in X_{Mg} (0.33–0.34; 0.38–0.40) with the same Ti concentration (c. 0.13–0.15 apfu, Fig. 4.4e). The six spot analyses with a high X_{Mg} all correspond to corroded grains, which might be interpreted as early schistosity-parallel biotite, whereas the other spot analyses with low X_{Mg} correspond to grains with straight grain boundaries. Biotite in sample GW13-29B shows three compositional clusters (Fig. 4.4e). One corresponds to biotite-3, characterized by Ti contents between 0.09 and 0.15 and X_{Mg} 0.33–0.35, identical to that of GW13-29. Two correspond to biotite-2, which shows a bimodal chemical composition: one with Ti concentrations between 0.13 and 0.15 apfu and X_{Mg} values of 0.37–0.40 (Fig. 4.4e) and the other with the same values of the Ti concentration, but XMg values of 0.33–0.34 (Fig. 4.4e). The K concentrations v. X_{Mg} are shown in Figure 4.4f. In sample GW13-28, almost half of the spot analyses yielded low, sub-stoichiometric K (and correspondingly high ^{IV}Al) in biotite. These systematic deviations from the other biotite analyses clearly pertain to (partially) altered grains, as supported by the matching element sums below 96% for these analyses. Both indicators point to a partial replacement by chlorite or smectite and confirm that this sample contains more alteration phases than the others. Both biotite-2 and -3 from sample GW13-29 are characterized by X_{Mg} between 0.32 and 0.35 and K concentrations of 0.91– 0.96 apfu.

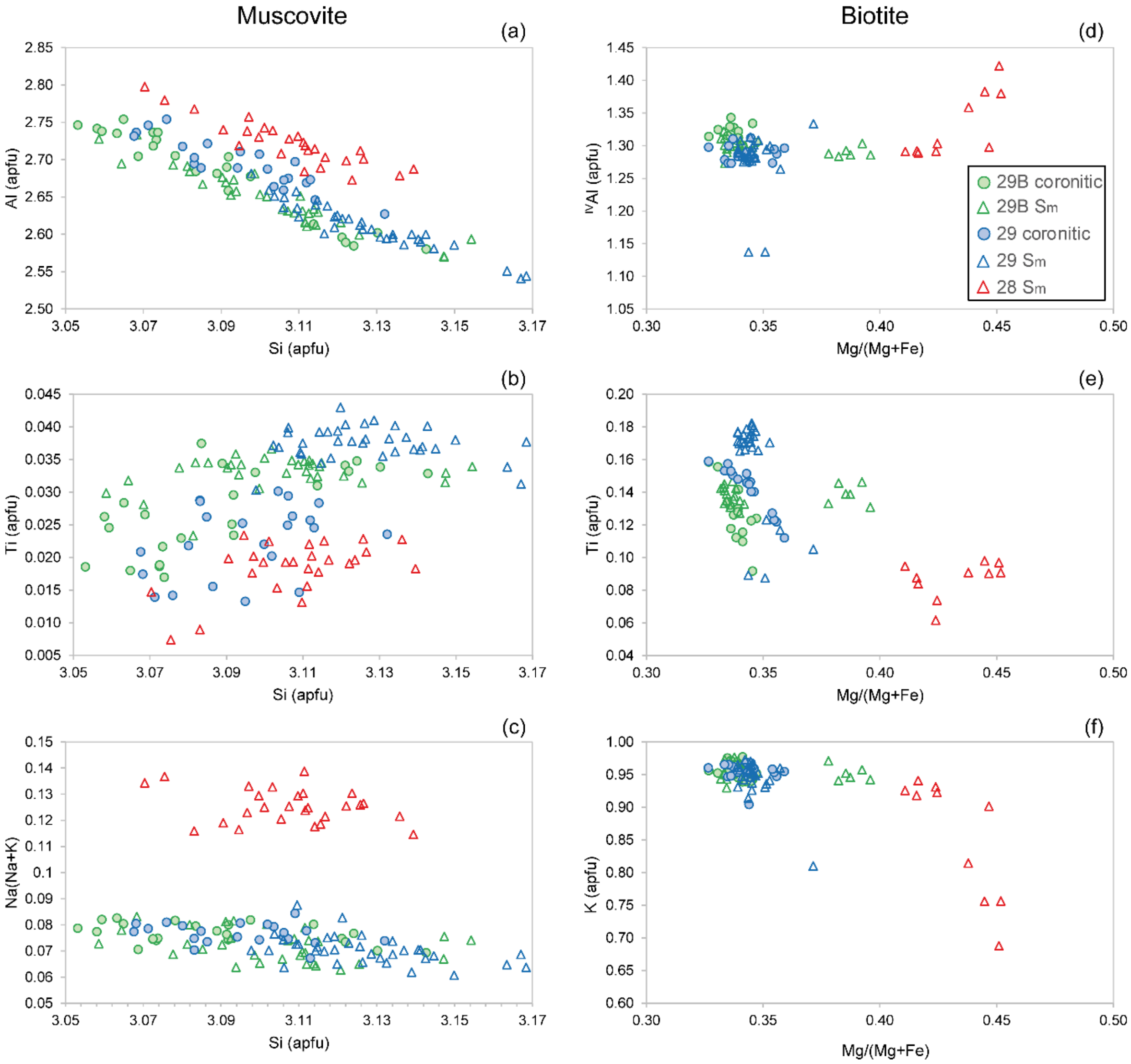

Figure 4.4. Compositional variations in (a–c) muscovite and (d–f) biotite. Symbols in parts (b–f) are the same as in part (a).

4.1.1.2 Ti-in-biotite and Ti-in-muscovite geothermometry

Thermal conditions of mica (re)crystallization, with respect to the different textural positions described in the previous section, were constrained through empirical geothermometers based on the Ti concentration in micas increasing with increasing temperature (Henry et al., 2005 and references cited therein; Chambers & Kohn, 2012; Wu & Chen, 2015). Henry & Guidotti (2002) and Henry et al. (2005), based on an extensive natural biotite dataset from graphite and rutile/ilmenite-bearing samples, reconstructed a Ti saturation surface for biotite in the P–T range 0.4–0.6 GPa and 480–800°C. Based on this saturation surface, they proposed a relationship between T and XMg and the Ti concentration of biotite, with an associated systematic uncertainty of ±24°C in the lower temperature range, approaching ±12°C in the higher temperature calibration range. We applied the Ti-in-biotite thermometer proposed by Henry et al. (2005). The pressure at which the Ti-in-biotite thermometer was originally calibrated (0.4–0.6 GPa, Henry & Guidotti 2002; Henry et al. 2005) is lower than that estimated for rocks that are structurally close to our samples (0.82–0.88 GPa, Spencer et al. 2012; c. 0.73–0.86 GPa, Thakur et al. 2015). Therefore, a conservative systematic uncertainty of 50°C on the calculated absolute temperature should be taken into account (e.g. Mottram et al. 2014). The pressure-dependent Ti-in-muscovite thermometer was proposed by Wu & Chen (2015), who empirically calibrated this thermometer for the P–T range 0.1–1.4 GPa and 450–800°C for ilmenite and aluminosilicate-saturated metapelite. The quoted error of the Ti-in-muscovite thermometer, as suggested by Wu & Chen (2015), is ±65°C. We applied the Ti-in-muscovite thermometer, following the assumption of a corresponding equilibrium pressure of 0.8 GPa, in agreement with the pressure estimates reported previously. Calculation at a lower pressure (0.6 GPa) shows only a minor (c. 5°C) decrease in the temperature estimates. An additional source of bias is the fact that the present rocks do not match the paragenesis used to calibrate the thermometer. Therefore absolute temperature estimates may be inaccurate, but temperature differences between different mica generations of the same rock are probably accurate (Bucher & Grapes 2011). The Ti-in biotite and Ti-in-muscovite geothermometers, as in any geothermobarometric method (Spear 1993), are not without pitfalls (e.g. Chambers & Kohn 2012), such as kinetic problems related to the distance of micas from a Ti source (Waters & Charnley 2002). Aluminosilicate, required for the Ti-in-muscovite thermometer, is lacking in our samples, even if other Al-rich phases such as garnet and staurolite are present as buffers, so the Ti-in-muscovite temperature should be regarded as semi-quantitative.

For muscovite-2, the temperatures obtained with the Ti-in-muscovite thermometer range between 394 and 561, 550 and 626, and 591 and 655°C for samples GW13-28, GW13-29B and GW13-29, respectively (Fig. 4.5). These estimates are similar to, but higher than, those by Spencer et al. (2012) and Thakur et al. (2015). For samples GW13-28, GW13-29B and GW13-29, the average temperatures are 522 ± 41, 609 ± 15 and 632 ± 13°C, respectively. The average temperatures obtained from muscovite-3 are 538 ± 42°C for sample GW13-29 and 571 ± 43°C for sample GW13-29B and are thus systematically lower than the temperatures derived from muscovite-2. The Ti-in-biotite geothermometer applied to biotite-2 gave average temperatures of 522 ± 45°C for sample GW13-28, 647 ± 41°C for sample GW13-29 and 627 ± 8°C for sample GW13-29B. The calculated temperature for biotite-3 is 631 ± 18 and 607 ± 27°C for samples GW13-29 and GW13-29B, respectively, lower than for biotite-2. The obtained temperatures for both muscovite-2 and biotite-2 from sample GW13-28 are c. 90–100°C lower than for the other samples. This low temperature estimate parallels the compositional evidence for retrograde reactions and suggests that chloritization occurred during exhumation at lower temperatures (Massonne et al., 2018). The calculated temperatures span a large range in all samples, which is compatible with a prolonged shearing and recrystallization history. Even taking into account the cautionary notes mentioned earlier, two factors strengthen our temperature estimates, which are sufficient for the interpretation of the $^{40}Ar/^{39}Ar$ data: (1) the temperatures calculated using two different thermometers match within the corresponding uncertainties; and (2) they are similar to the previously reported temperatures of 550–590°C (Spencer et al., 2012; Thakur et al., 2015), which are based on the application of several geothermometric methods (e.g. garnet–biotite thermometer, Ti-in-biotite thermometer and multi-equilibrium thermobarometry) for samples in close proximity to the present samples. These temperature estimates are similar to those recorded by fluid inclusions in quartz near the Munsiari Thrust, 1 km down-section (Montemagni et al., 2016), namely 500–520°C.

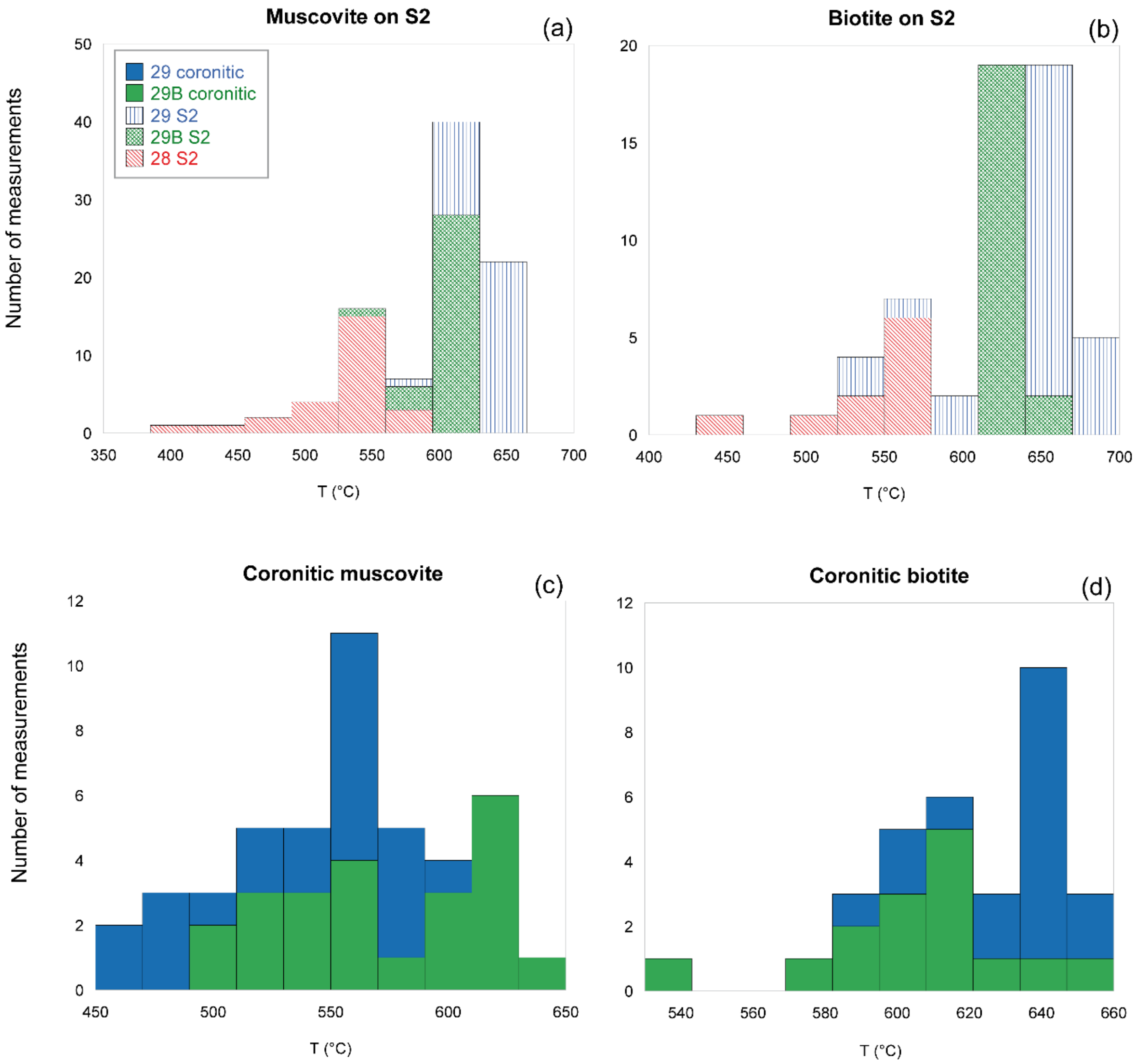

Figure 4.5. Histograms reporting thermometric data obtained with Ti-in-biotite and Ti-in-muscovite geothermometers. (a) and (c): data on muscovite along the S2 (muscovite-2) and coronitic around garnet (muscovite-3), respectively; (b) and (d) data on biotite along the S2 (biotite-2) and coronitic around garnet (biotite-3), respectively. The legend in (b-d) is the same as in (a).

4.1.2 South Tibetan Detachment System

The location of analyzed samples (GW13-39, GW13-51, GW13-57) is reported in Figure 4.1.

Sample GW13-51 is a leucogranitic pegmatite (Fig. 4.6), cropping out near Malari village (Fig. 4.6) intruding the coarser grained granitic body. It consists of quartz (43%), K-feldspar (25%), plagioclase (20%), white mica (4%) and minor zoned tourmaline (8%). Deformation in this sample is heterogeneous (Fig. 4.6a,b) with low- and high-strain domains. Within the low-strain domains, a fine-grained magmatic fabric with euhedral grain shapes and few deformation features can be recognized (Fig. 4.6a). The high-strain domains are widely distributed with subsolidus deformation features affecting the magmatic minerals (Fig. 4.6b,c,d). Quartz grains show undulose extinction (Fig. 4.6b), deformation lamellae and and microstructures related to BLG recrystallization mechanism (Fig. 4.6c, BLG; Passchier & Trouw, 2005) typical of low-T deformation (Stipp et al., 2002a,b) corresponding to regime I dynamic recrystallization conditions of Hirth & Tullis (1992). Plagioclase grains exhibit mechanical twinning (Fig. 4.6c,d) and grain scale fractures (Fig. 4.6d). Following Vernon (2004) these twins are lenticular deformation twins with heterogeneous concentration (Fig. 4.6d) due to local strain variation within the grain. Sometimes twins terminate against fractures (Fig. 4.6d). White mica grains contain kink bands (Fig. 4.6a,e) orthogonal to basal planes (Fig. 4.6e). Tourmaline grains commonly show fractures and pullapart microboudinage. Tourmaline grains are zoned (Fig. 4.6f). In a few cases (Fig. 4.6f), small fibres (Tur2) growing orthogonal to the fracture walls have been found within microboudinaged and coarse grained tourmaline (Tur1). According to microstructural observations, we interpret this sample as being deformed in the solid-state.

Sample GW13-57 is a leucogranitic pegmatite (Fig. 4.7), intruding the HT-mylonites, and is composed of quartz (52%), microcline (32%), plagioclase (6%), white mica (6%) and late retrograde chlorite (2%) and sericite (2%). Perthitic exsolution (Fig. 4.7b) in K-feldspar and tartan twinning in microcline (Fig. 4c) are evident. As discussed by Vernon (2004) this could be transformation twinning, coarsened by strain, due to feldspar phase changes in a lower symmetry during slow cooling, or due to lattice strain adjacent to thick exsolved lamellae (Fig. 4.7c). Plagioclase occasionally shows slightly deformed growth twins (Fig. 4.7d) and commonly underwent late alteration to sericite. Quartz exhibits undulose extinction (Fig. 4.7c,e) and intra and inter- grains fractures (Fig. 4.7c,e). White mica grains are mostly undeformed (Fig. 4.7a,e), but in some circumstances kink bands occur (Fig. 4.7f). Late fractures were also observed in this sample. According to microstructures, this sample is weakly deformed.

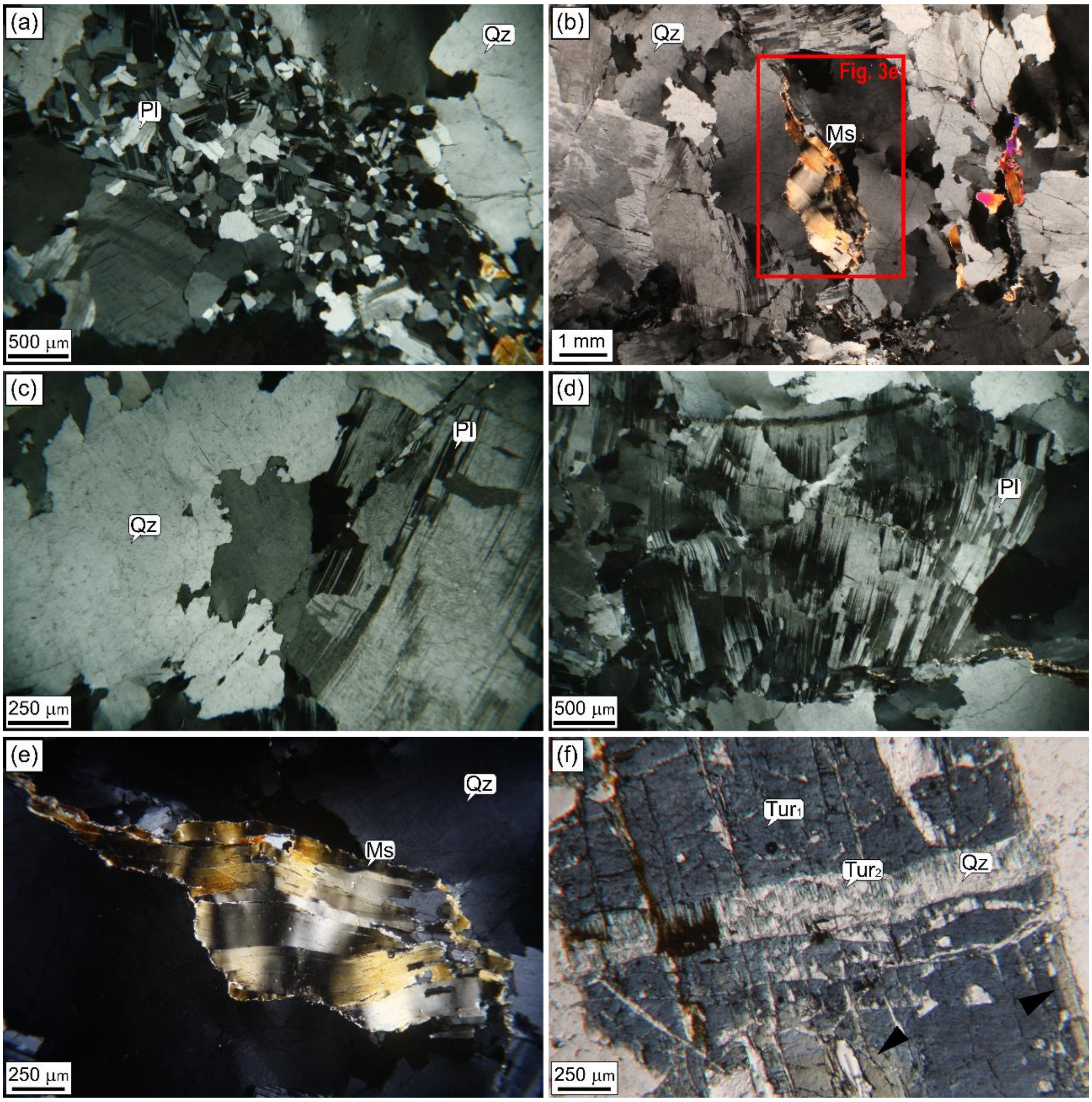

Figure 4.6. Microstructures of sample GW13-51. (a) fine-grained magmatic texture within coarse-grained one; (b) kinked muscovite, undulose extinction in quartz and mechanical twinning in plagioclase; (c) bulging recrystallization microstructures in quartz (a light grey quartz grain bulges into the next dark grey quartz grain) and mechanical twinning in plagioclase; (d) mechanical twinning and grain scale fractures in plagioclase; (e) kink bands in muscovite orthogonal to basal planes; (f) small fibres of Tur2 growing orthogonal to the fracture walls of zoned (black arrows) coarse-grained Tur1. Mineral abbreviations as in Whitney & Evans (2010).

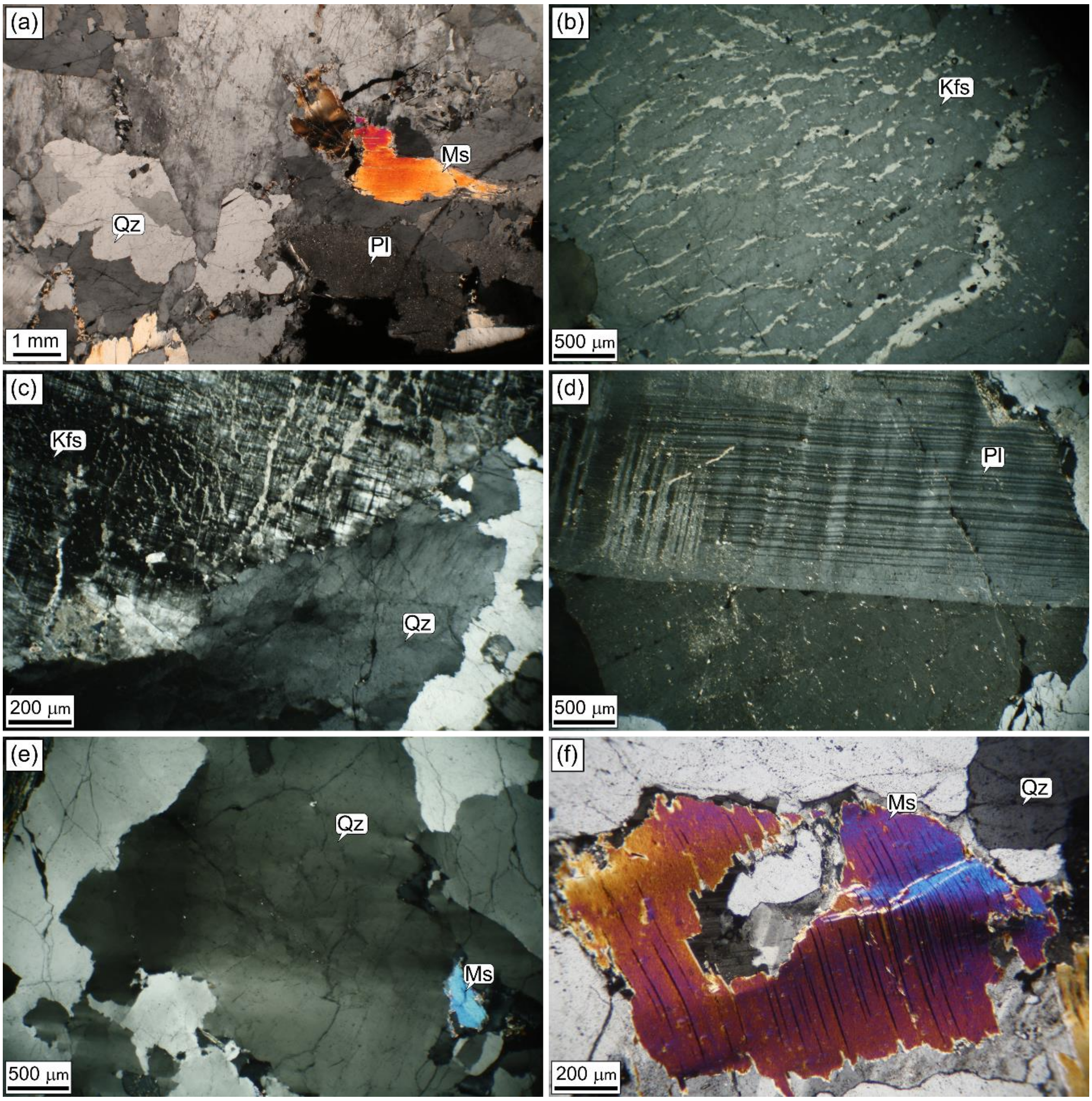

Figure 4.7. (a) microstructures of sample GW13-57. Note one muscovite grain lacking kink bands and one showing kink bands. Perthitic exsolution in K-feldspar (b) and tartan twinning in microcline (c) are evident. In (c) note intra grain fractures in quartz. (d) Slightly deformed growth twins in plagioclase characterized by late alteration to sericite; (e) undulose extinction in quartz and muscovite lacking kink bands; (f): kink band in muscovite orthogonal to (001) planes. Trails of fluid inclusion in quartz are also evident. Mineral abbreviations as in Whitney & Evans (2010).

Sample GW13-39 is a migmatite composed of quartz, K-feldspar, white mica, biotite, sillimanite and minor alteration to chlorite and sericite (Fig. 4.8). Locally, undeformed plagioclase grains having growth twins characterized by abrupt terminations (Vernon, 2004) occur. Quartz shows chessboard extinction (Fig. 4.8b) and Grain Boundary Migration (GBMII, Passchier & Trouw, 2005) recrystallization, which suggests a deformation T higher than 650 °C (Kruhl, 1996). Lobate grain boundaries (Fig. 4.8b) and pinning microstructures (Fig. 4.8c, Passchier & Trouw, 2005) are evident; fluid inclusion planes (Boullier, 1999) affecting quartz grains commonly occur (Fig. 4.8b,c). Static, post kinematic (non-deformed) white mica grew at expense of sillimanite (Fig. 4.8d). The above described deformation features point out the occurrence of ductile shearing on the STDS. Microstructural observations reveal that ductile shearing, gradually fades moving from the structurally uppermost sample to the structurally lowest one.

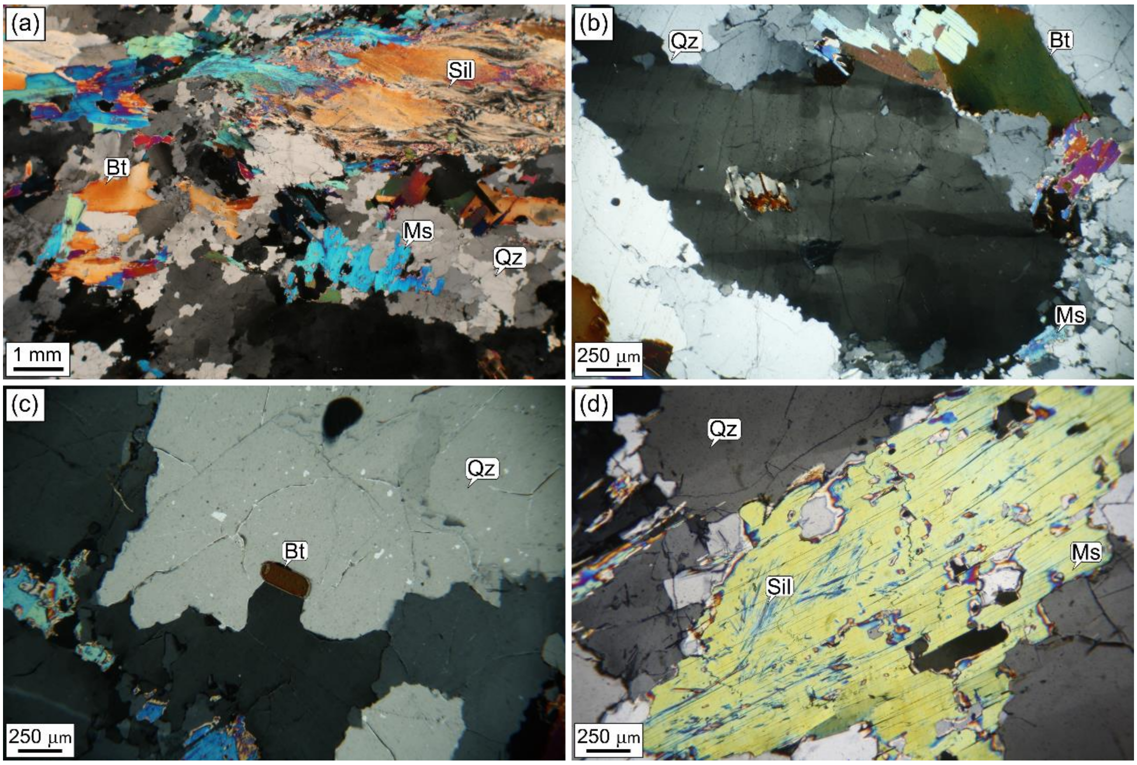

Figure 4.8. (a) microstructures of sample GW13-39. Note static, undeformed muscovite. (b) Chessboard extinction in quartz showing sutured and lobate grain boundaries. Note trails of fluid inclusion planes in quartz. (c) pinning microstructures; (d) static, post kinematic (nondeformed) muscovite growing at expense of sillimanite. Mineral abbreviations as in Whitney & Evans (2010).

Sample GW13-51 experienced deformation at low T, characterized by BLG recrystallization in quartz, bent twins in plagioclase and kink bands in micas. Deformation decreases in sample GW13-57, in which quartz grains show only undulose extinction and kink bands rarely affect white mica grains. In sample GW13-39 high temperature deformation microstructures (chessboard extinction and GBM recrystallization in quartz) are not retrogressed and very well recognizable, but still there is strong evidence of a chemically open system, as late, undeformed mica grains grew during sillimanite breakdown.

4.1.2.1 Mica compositions

The representative EMPA are reported in Table 4.2. The full set of EMP analyses of micas from the studied samples are given in Supplementary Material Appendix 1, and summarized in Figure 4.12. Element maps (Figs. 4.9, 4.10, 4.11) show that mica grains from samples GW13-39 and GW13-57 are homogeneous, whereas mica grains in GW13-51 are less so. White mica analyses were recalculated as atoms per formula unit (apfu) based on 11 oxygens.

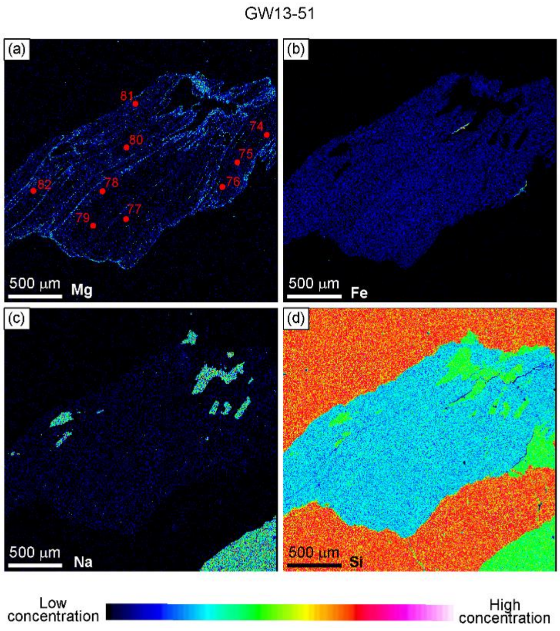

Figure 4.9. X-ray element maps for (a) Mg, (b) Fe, (c) Na and (d) Si of selected muscovite from sample GW13-51. EPMA spot analysis numbers referring to Table S1 are shown in (a).

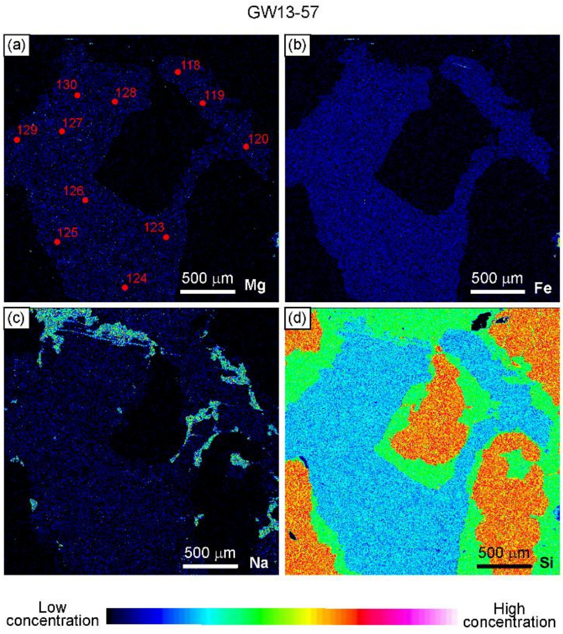

Figure 4.10. X-ray element maps for (a) Mg, (b) Fe, (c) Na and (d) Si of selected muscovite from sample GW13-57. EPMA spot analysis numbers referring to Table S1 are shown in (a).

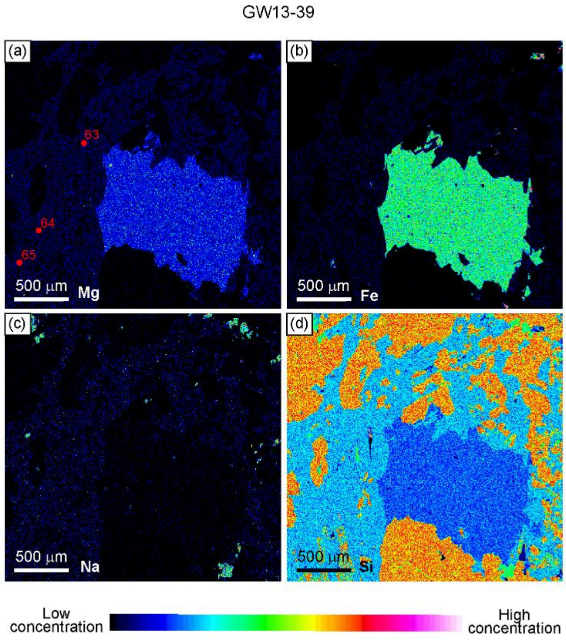

Figure 4.11. X-ray element maps for (a) Mg, (b) Fe, (c) Na and (d) Si of selected muscovite from sample GW13-39. EPMA spot analysis numbers referring to Table S1 are shown in (a).

Table 4.2

					Sample				
	GW13-39			GW13-51			GW13-57		
SiO_2	47.41	46.87	46.06	49.14	46.70	45.97	47.60	47.02	46.28
TiO_2	0.45	0.00	0.18	0.00	0.03	0.05	0.11	0.07	0.16
Al_2O_3	36.42	36.87	36.61	31.41	35.15	34.61	36.80	36.54	35.70
FeO	1.26	1.06	0.97	2.71	3.00	3.45	1.65	1.56	1.75
MnO	0.02	0.00	0.02	0.04	0.06	0.11	0.00	0.00	0.00
MgO	0.57	0.41	0.38	2.33	0.13	0.21	0.47	0.47	0.47
CaO	0.02	0.04	0.02	0.02	0.01	0.01	0.02	0.03	0.02
BaO	0.13	0.07	0.14	0.02	0.00	0.00	0.00	0.00	0.00
Na_2O	0.66	0.52	0.65	0.16	0.55	0.38	0.80	0.76	0.82
K_2O	10.46	10.76	10.62	11.06	10.43	10.26	10.58	10.57	10.35
F	0.00	0.00	0.00	0.92	0.38	0.03	0.00	0.00	0.00
Cl	0.03	0.03	0.04	0.00	0.01	0.01	0.00	0.02	0.03
tot	97.44	96.63	95.69	97.80	96.46	94.99	98.03	97.04	95.57
Si	3.08	3.07	3.05	3.27	3.11	3.10	3.08	3.07	3.08
Ti	0.02	0.00	0.01	0.00	0.00	0.00	0.01	0.00	0.01
Al	2.79	2.85	2.86	2.46	2.76	2.74	2.81	2.82	2.80
Fe	0.07	0.06	0.05	0.15	0.17	0.19	0.09	0.09	0.10
Mn	0.00	0.00	0.00	0.00	0.00	0.01	0.00	0.00	0.00
Mg	0.06	0.04	0.04	0.23	0.01	0.02	0.05	0.05	0.05
Ca	0.00	0.00	0.00	0.00	0.00	0.00	0.00	0.00	0.00
Ba	0.00	0.00	0.00	0.00	0.00	0.00	0.00	0.00	0.00
Na	0.08	0.07	0.08	0.02	0.07	0.05	0.10	0.10	0.11
K	0.87	0.90	0.90	0.94	0.89	0.88	0.87	0.88	0.88
F	0.00	0.00	0.00	0.19	0.08	0.01	0.00	0.00	0.00
Cl	0.00	0.00	0.00	0.00	0.00	0.00	0.00	0.00	0.00
tot	6.98	6.99	7.01	7.27	7.10	7.01	7.00	7.01	7.01

Table 4.2. Representative electron microprobe analyses of muscovite (wt% oxides). Atomic proportion (apfu) were recalculated based on O = 11.

In all analysed samples, white mica grains have only a limited compositional variation in Si and Al content ranging from 3.04 - 3.16 apfu and 2.61 - 2.91 apfu, respectively (Fig. 4.12a). Amongst the three analysed mica samples, GW13- 51 has the largest spread and accounts for almost all of the collective compositional dispersion (Si = 3.07-3.16 apfu) whereas GW13-57 is the most homogeneous one (Si = 3.06-3.09 apfu) and GW13-39 is heterogeneous but shifted towards lower Si and higher Al contents (Fig. 4.12a, Table S1). The Ti content (Fig. 4.12b) is very close to the detection limit in all samples; it is slightly higher in sample GW13-39 (0.00-0.06 apfu) than in samples GW13-57 and GW13-51, but in the expected range for metamorphic muscovite (usually less than 0.10 apfu; Guidotti & Sassi, 1998). The highest Ti concentrations in muscovite from sample GW13-39, albeit poorly resolved from background, appear to reflect the structural position of muscovite grains in the immediate proximity to biotite grains.

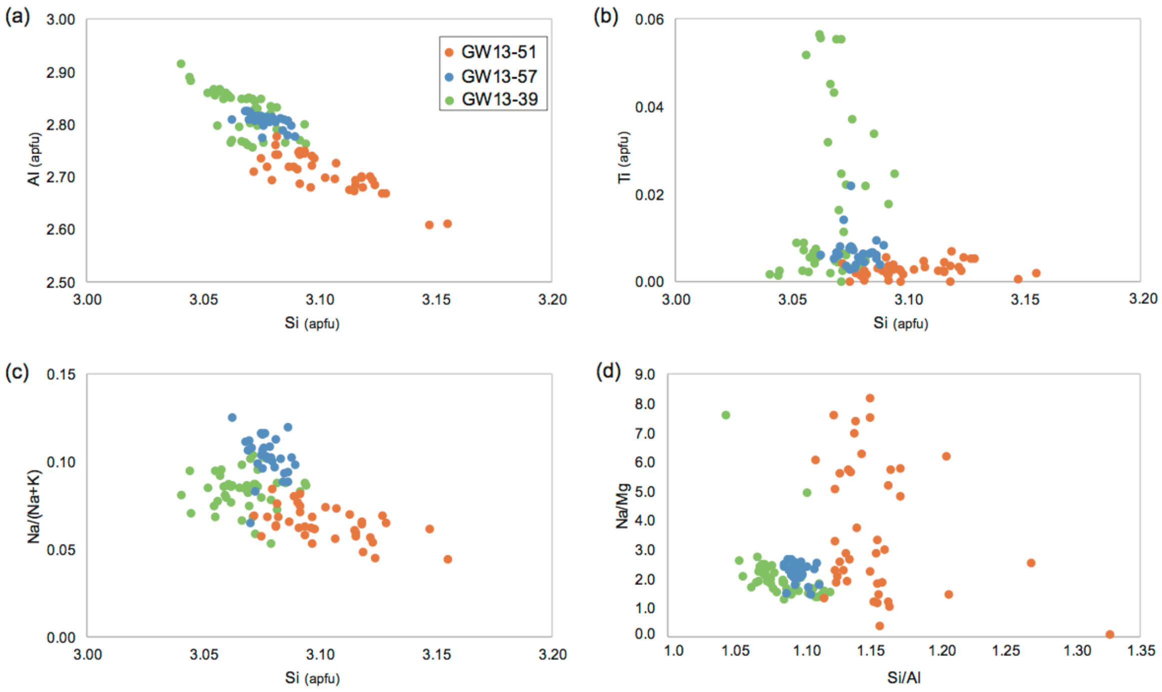

Figure 4.12. Chemical variation (a-d) in muscovite from the selected samples.

The Na/(Na+K) ratio (Fig. 4.12c) of muscovite in sample GW13-57 is higher (0.07-0.13) than in samples GW13-39 and GW13-51, in which it lies between 0.05 and 0.10. In order to explore heterogeneities, we plot our data in a Na/Mg vs Si/Al diagram (Fig. 4.12d) which shows that sample GW13-51 has the most heterogeneous Si/Al and Na/Mg ratios (1.11-1.32 and 0.09-8.17, respectively). This is expected for muscovite recrystallization close to the fault, because faults are chemically open systems. Sample GW13-39 has a more constant Si/Al ratio (1.04-1.11) as befits a statically grown muscovite (M3 of Iaccarino et al., 2017b). Another conclusion from Figure 4.12 is that micas from samples GW13-51 and GW13-57 define distinct fields in all compositional plots. The major element differences require that the two dykes are not comagmatic, despite having been collected only 100 m apart. Ba concentrations are near the detection limit in all samples (Tables S1). Halogens (F, Cl) have been measured but, as expected (Guidotti, 1984; Guidotti & Sassi, 1998), were mostly too close to the detection limit. Moreover, we stress that our chemical data for late muscovite in sample GW13-39 are equivalent to those of Iaccarino et al. (2017b) for late, post-tectonic muscovite in HT-mylonites, from the same study area.

4.2 Bhagirathi – Gangotri valleys

Figure 4.12 shows the position on a geologic map and cross section of the Bhagirathi area of both samples analyzed by ^{40}Ar/^{39}Ar stepheating dating and by X-ray microCT for vorticity estimates described in Chapter 5 and Chapter 6, respectively.

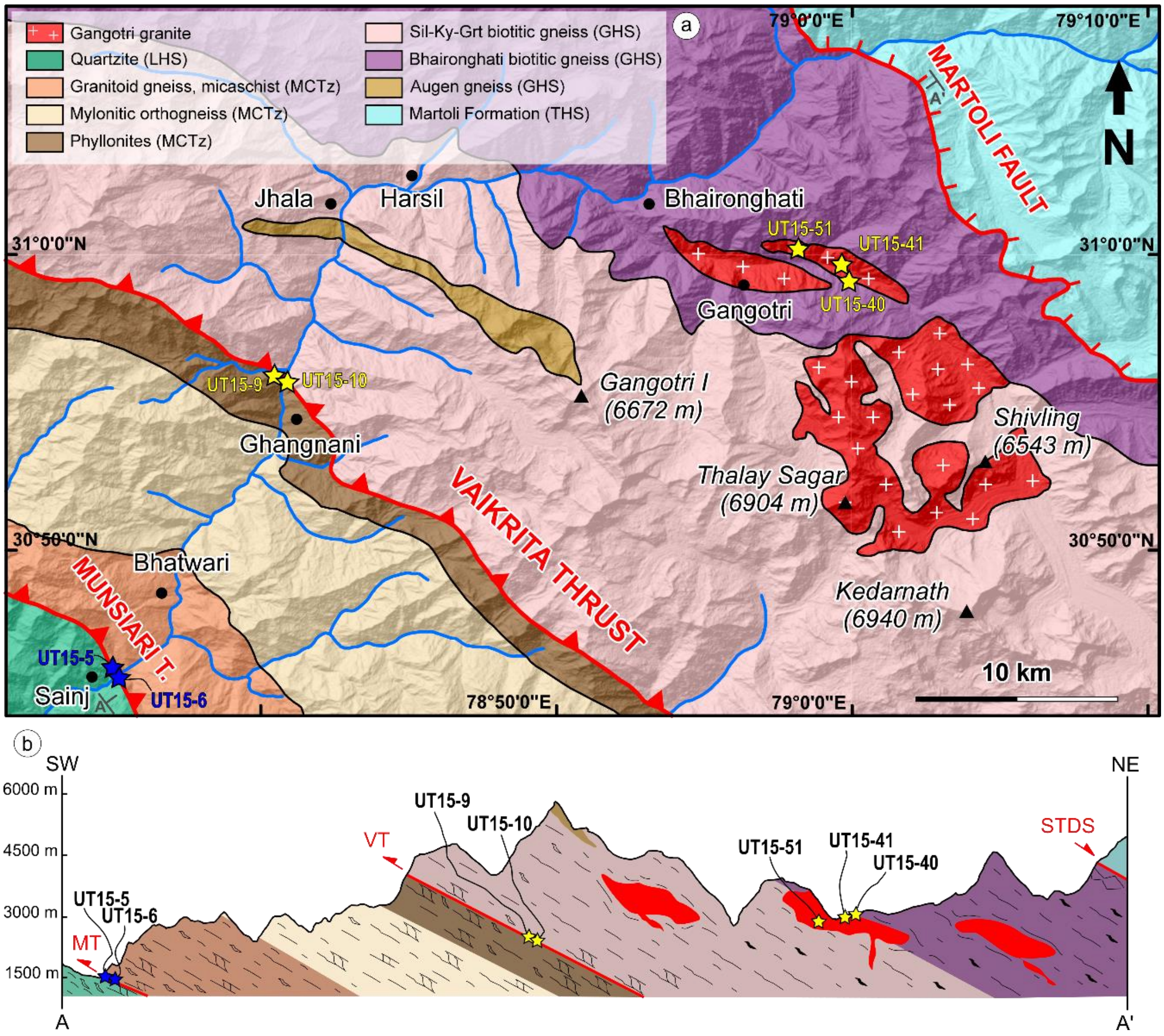

Figure 4.13. The Bhagirathi area (after Searle et al., 1993 and Singh, 2019). Position of analyzed samples is shown with yellow stars (^{40}Ar/^{39}Ar dating, Chapter 5) and blue stars (^{40}Ar/^{39}Ar dating and X-ray microCT, Chapter 5 and 6).

4.2.1 Main Central Thrust zone

Four samples (UT15-5, UT15-6, UT15-9, UT15-10) have been selected from the MCTz in the Bhagirathi valley. Their structural position is reported in Figure 4.13.

Sample UT15-5 (Fig. 4.14a-d) contains quartz, K-feldspar, biotite, rare muscovite, monazite, allanite and zircon. The main foliation (S_m=S2) is defined by shape preferred orientation of biotite and rarely muscovite, and can be defined as a disjunctive schistosity due to the alternation of granoblastic quartzo-feldspathic layers and lepidoblastic ones (Fig. 4.14a). Monazites with a symplectitic halo of allanite and apatite occur enveloped by the S2 (Fig. 4.14b). Pre-kinematic K-feldspar porphyroclasts are sericitized, being fractured or replaced by quartz, which also recrystallized in the strain shadows. In one case, a porphyroclast is bounded by a symplectitic structure at the contact with biotite. Quartz recrystallization mechanisms are represented by GBM recrystallization in sigmoid aggregates and ribbons in which quartz is coarse-grained and pinning structure and over-pinning of micas occur (Fig. 4.14c). Quartz is also characterized by straight grain boundaries in fine-grained domains. Kinematic indicators such SCC’ fabric, group 1 (and minor group 5) biotite fish, asymmetrical strain shadows around K-feldspar porphyroclasts, σ-porphyroclasts and quarter mats (Fig. 4.14d; Passchier & Trouw, 2005) show a top-to-the-S/SW sense of shear.

UT15-6 (Fig. 4.14e-f) contains quartz, K-feldspar, biotite, rare muscovite, titanite and zircon. As in the companion sample UT15-5, the SCC’ fabric is ubiquitous and S2 is defined by shape preferred orientation of biotite. Some sporadic static biotite overgrows the foliation. In this sample, biotite contains numerous titanite needles, suggesting unmixing of these two phases. Feldspar porphyroclasts still preserve their habits and twinning, but are sericitizated and fractured (Fig. 4.14e). SCC’ fabric, δ-type porphyroclasts, quarter mats, asymmetrical strain shadows around K-feldspar porphyroclasts and group 4 biotite fish (Fig. 4.14f) all point to a top-to-the-S/SW shear sense.

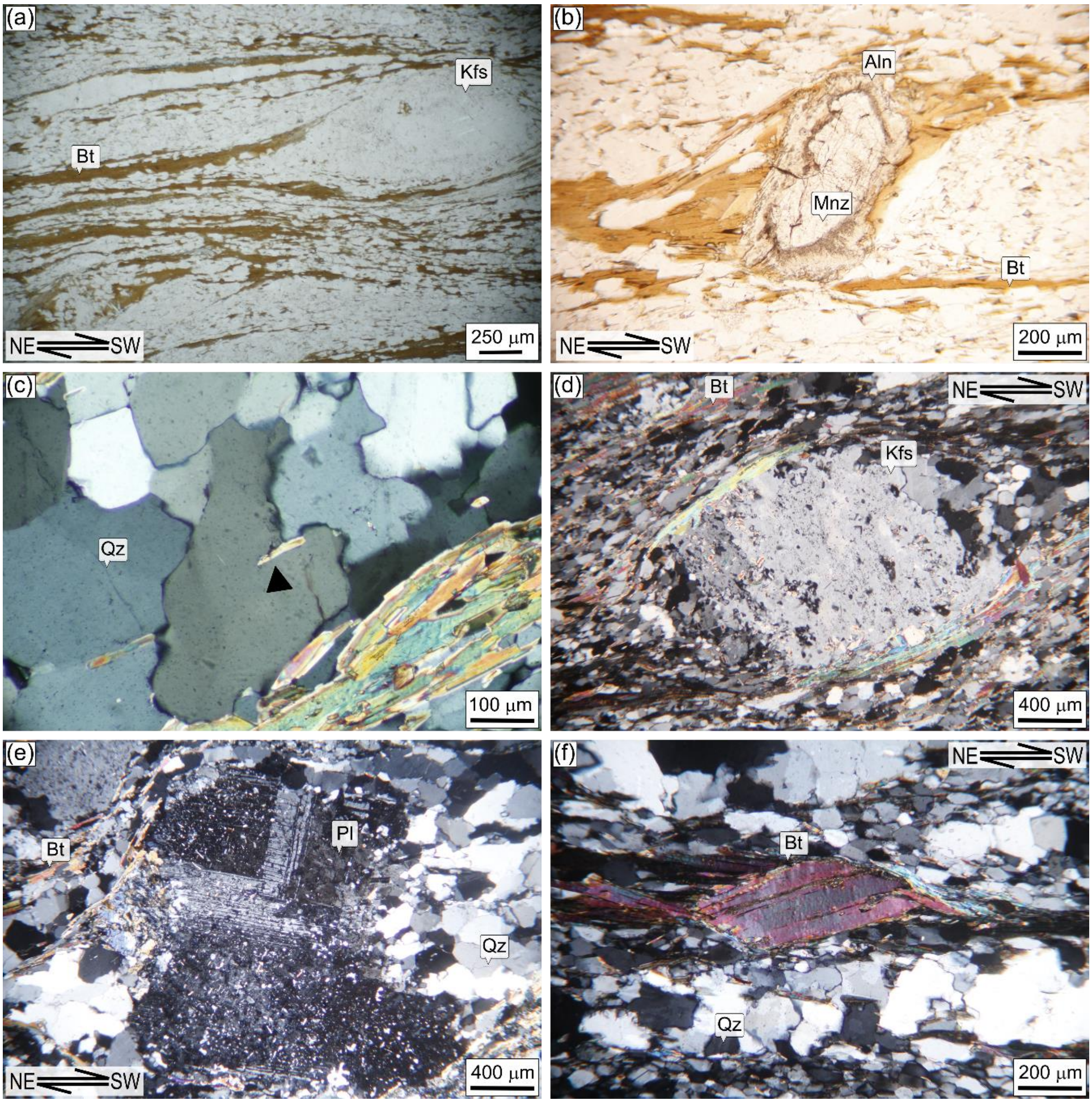

Figure 4.14. Microstructures of the Munsiari Thrust. (a) K-feldspar porphyroclasts embedded by S2 biotite shows a top-to-the-SW shear sense (UT15-5); (b) Monazites with a symplectitic halo of allanite and apatite enveloped by the S2 (UT15-5); (c) Pinning structure and over-pinning of micas in coarse-grained quartz (UT15-5); (d) quarter mats around K-feldspar porphyroclasts are consistent with a top-to-the-SW shear sense (UT15-5); (e) twinned feldspar porphyroclast wrapped by the S2 foliation, with asymmetric tails, show a top-to-the-SW shear sense (UT15-6); (f) group 4 biotite fish shows a top-to-the-SW shear sense (UT15-6). Mineral abbreviation as in Whitney & Evans (2010).

Garnet bearing mylonitic micaschist UT15-9 (Fig. 4.15a-d) contains quartz, muscovite, garnet, Kfeldspar, rare ilmenite and abundant late chlorite replacing biotite and forming coronitic structures around garnet. The S2, defined by the shape-preferred orientation of muscovite and chlorite can be classified as disjunctive foliation (Fig. 4.15a). A late crenulation cleavage (S3) with crystallization of static muscovite (post-S2) and chlorite is pervasive in the lepidoblastic domains (Fig. 4.15b). Incipient polygonal arcs occur as mimetic growth of partly recrystallized relicts of microfolds (Passchier & Trouw, 2005). An older foliation (S1) is rarely preserved. It is defined by micas in microlithons and is oriented at a high angle with respect to S2. The S2 envelops intertectonic garnet porphyroclasts characterized by helicitic-pattern-inclusion cores and inclusion-free (Passchier & Trouw, 2005) rims (Fig. 4.15c). Garnet porphyroclasts have chlorite coronitic structures (Fig. 4.15c). Quartz recrystallization mechanisms are expressed by static annealing in fine-grained quartz characterized by straight grain boundaries and triple points. In some domains, quartz is coarse-grained and characterized by GBM with amoeboid grain boundaries and Fluid Inclusion Planes (Boullier, 1999) occasionally cutting quartz grain boundaries (Fig. 4.15d). Pinning and window structures (Jessel, 1987; Passchier & Trouw, 2005) also occur in quartz (Fig. 4.15d). Kinematic (group 4 biotite fish, Passchier & Trouw (2005) and asymmetrical garnet porphyroclasts) point to a top-to-the-S sense of shear.

Garnet bearing mylonitic micaschist UT15-10 (Fig. 4.15e-h) contains muscovite, quartz, Kfeldspar, garnet and abundant late chlorite replacing biotite. Ilmenite also grew along the main foliation. The S2 is a smooth and mainly anastomosing crenulation cleavage, in which both the cleavage and microlithon domains are mica rich layers (Fig. 4.15e). S1 domains are ubiquitous but in some domains have been almost totally overprinted by polygonal arcs (Fig. 4.15e,h; Passchier & Trouw, 2005) which therefore predominate over the S1 relict foliation. Large crystals of static muscovite also occur (Fig. 4.15f). Two generations of garnet occur in the sample: a first generation of syn-kinematic garnet porphyroclasts enveloped by the S2, with high angle inclusion trails with respect to the S2, and a second generation of post-kinematic, helicitic porphyroblasts cutting the pre-existing foliations (Fig. 4.15g,h) and growing on them. Sometimes micas are deformed around the second generation of garnet porphyroclasts probably due to the fact that deformation has continued and micas deformed since they are weaker than garnet. As shown by Figures 4.14 and 4.15, the different mica generations in samples UT15-9 and UT15-10 are intergrown at a scale < 10 µm.

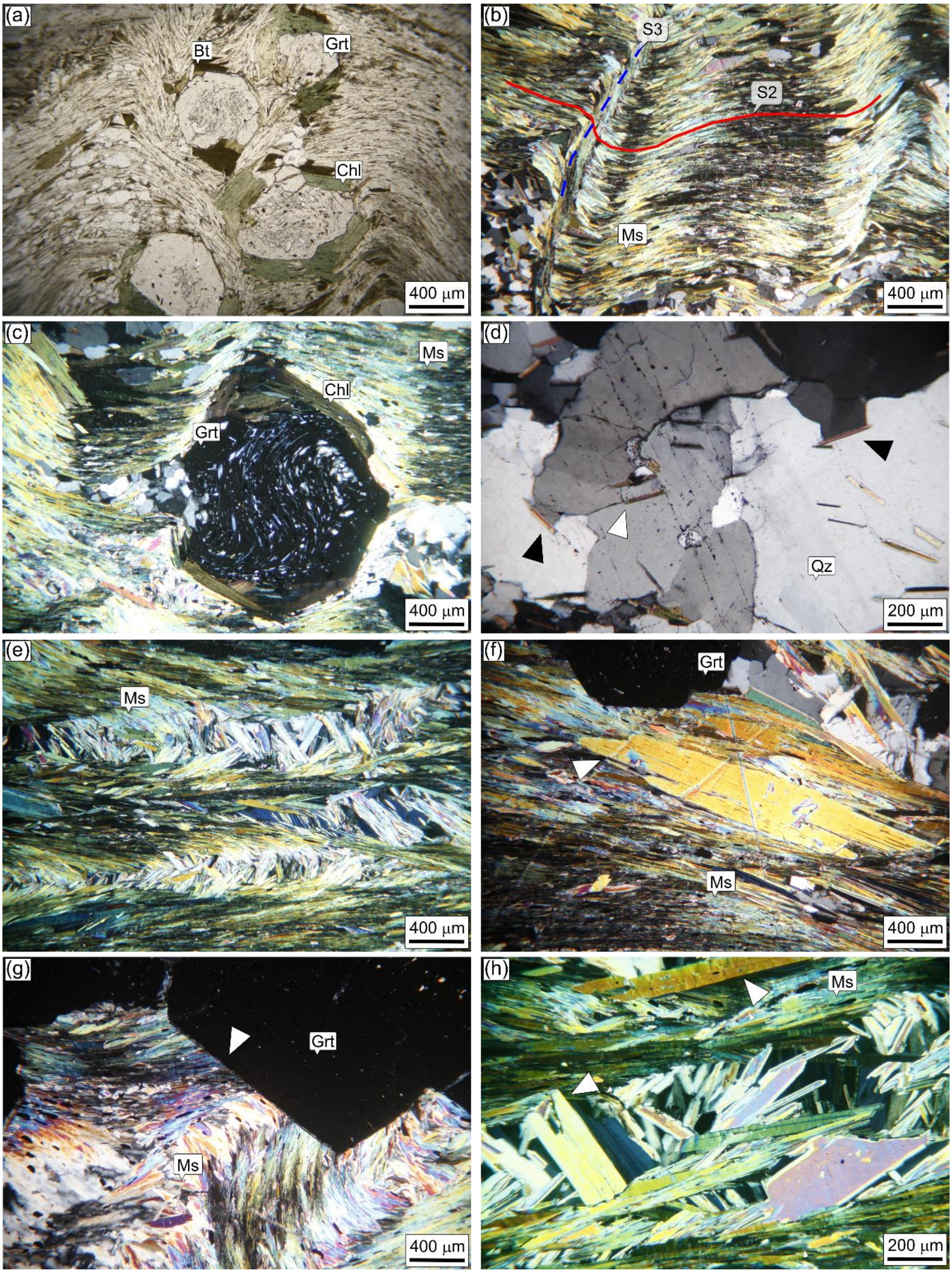

Figure 4.15. Microstructures of the Vaikrita Thrust. (a) – (d) sample UT15-9, (e) – (f) sample UT15-10. (a) garnet bearing micaschist, with chlorite forming coronitic structures around garnet porphyroclasts; (b) the main foliation (S2) crenulated by the successive S3 foliation; helicytic inclusion pattern in garnet; (d) fluid inclusion planes cut quartz grain boundaries. Note pinning structures (black arrows) and window structure (white arrow) in quartz; (e) mica rich microlithon and cleavage domains in garnet bearing micaschist UT15-10; (f) large crystal of static muscovite; (g) garnet porphyroclast with inclusion-free rim. Note that garnet rim truncates the mylonitic S2 foliation (white arrow); (h) late static muscovite crystals (white arrows). Mineral abbreviation as in Whitney & Evans (2010).

4.2.1.1 Mica compositions

The representative EMP analyses of micas are reported in Table 4.3. The full dataset of the studied samples are given in Supplementary Material Appendix 1 and are summarized in Figures 4.16 and 4.17.

EMPA of the four biotite samples are represented in Figure 4.16. Biotite of the Munsiari Thrust shows higher X_{Mg} (i.e. Mg/(Mg + Fe)) with respect to those of the Vaikrita Thrust (Fig. 6a), both showing variable Ti concentration. Sample UT15-5 has the highest X_{Mg} values (0.522-0.576) slightly different from sample UT15-6 (0.448-0.494), both showing the same variation. Biotite of the Vaikrita Thrust has lower X_{Mg} varying from 0.429-0.473 for sample UT15-9 to 0.381-0.406 for sample UT15-10. These values testify to a strong chloritization of biotite from the Vaikrita Thrust as confirmed by the K concentrations v. X_{Mg} diagram shown in Figure 6b: in sample UT15-9 the spot analyses yielded low, sub-stoichiometric K which correspond to high Al^{IV} (Fig. 6c). Because of the strong chloritization of biotite from samples UT15-9 and UT15-10, biotite of the Vaikrita Thrust has not been considered for the successive $^{40}Ar/^{39}Ar$ dating.

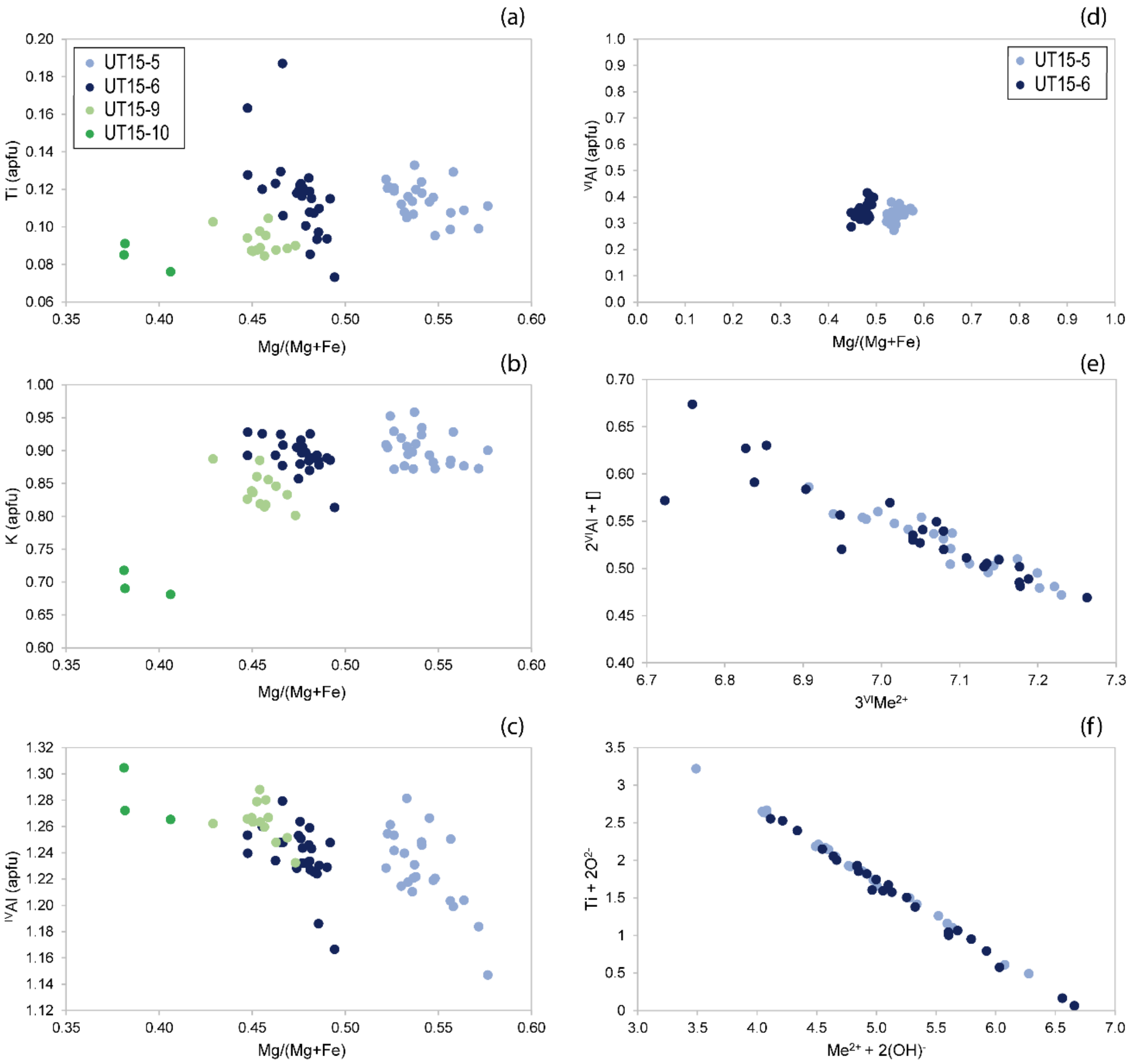

Figure 4.16. Chemical variation (a-f) in biotite from analyzed samples.

Focusing on biotite of the Munsiari Thrust (UT15-5, UT15-6) although similar, biotites from the two samples have different X_{Mg} (Fig. 6d). The chemical variability of biotite trioctahedral sheet (Fig. 6e,f) is maily driven by the "dioctahedral" substitution $3Me^{2+} <> 2^{VI}Al + \square$, with minor insertion of Tschermakitic substitution $Me^{2+} + Si^{4+} <> {}^{IV}Al + {}^{VI}Al$ and Ti by the exchange vector: $Ti^{4+} + 2O^{2-} <> {}^{VI}Me^{2+} + 2OH^{-}$.

Muscovite analyses for the Vaikrita Thrust (UT15-9, UT15-10) samples are summarized in Figure 4.17. White mica is characterized by limited compositional variation around the muscovite-celadonite join, with Si varying between 3.05 and 3.18 apfu (Fig. 4.17a). The Na/(Na + K) ratio (Guidotti & Sassi 2002; Fig. 4.17b) of muscovite in sample UT15-10 is overall slightly higher (0.186-0.264) than UT15-9 (0.126-0.238). The Ti concentration (Fig. 4.17c) is low in muscovite of both samples although in the muscovite of sample UT15-10 (0.007-0.032 apfu) is generally lower than UT15-9 (0.012-0.033 apfu). Muscovite is characterized by variable degrees of phengitic substitution (Fig. 4.17d) expressed as ${}^{IV}Al^{3+} + {}^{VI}Al^{3+} <> {}^{VI}Me^{2+} + {}^{IV}Si^{4+}$, with no differences between the several generations but with more restricted variation in sample UT15-9 with respect to UT15-10 (Fig. 4.17d).

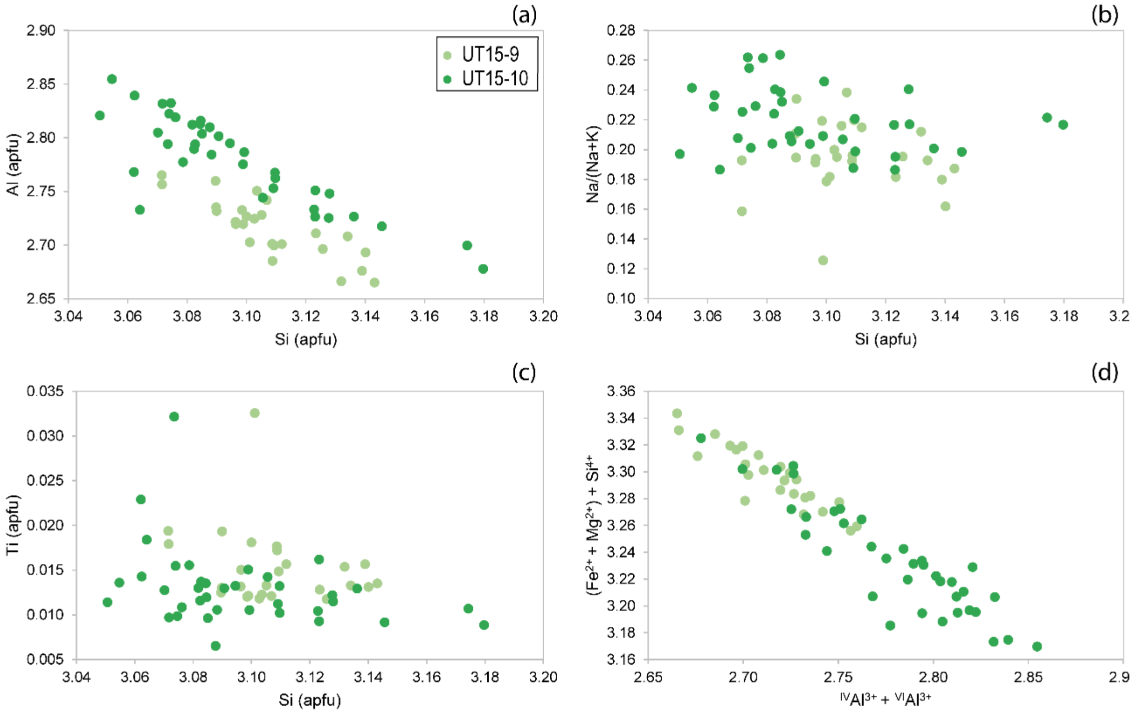

Figure 4.17. Chemical variation (a-d) in muscovite from Vaikrita Thrust samples.

Chlorite analyses of samples UT15-9 and UT15-10 are reported in Supplementary Material Appendix 1. Chlorite in sample UT15-9 has higher X_{Mg} (0.40-0.49) than sample UT15-10 (0.36-0.42) and shows Si concentrations of 2.57-3.46 (apfu) and 2.53-2.97 (apfu), corresponding to Al concentration of 1.94-2.91 (apfu) and 2.54-3.00 (apfu), respectively, suggesting that Al replaces Si more efficiently in chlorite of sample UT15-10. The different Mg/Fe ratio of biotite from UT15-9 and UT15-10 is preserved in the respective chlorite, confirming that chlorite directly derives from alteration of biotite.

Table 4.3

	Sample											
	UT15-5			**UT15-6**			**UT15-9**			**UT15-10**		
	Biotite			Biotite			Muscovite			Muscovite		
SiO_2	37.42	37.17	39.12	37.09	36.43	36.47	46.90	46.46	46.47	48.23	46.83	47.35
TiO_2	2.15	2.05	1.83	2.12	3.33	2.04	0.65	0.26	0.25	0.24	0.20	0.13
Al_2O_3	18.01	18.82	18.16	17.79	18.12	17.41	34.68	34.65	35.22	35.95	36.63	36.56
FeO	18.18	17.22	16.76	19.71	19.06	19.51	2.13	2.16	1.88	1.26	1.05	1.17
MnO	0.20	0.17	0.13	0.16	0.17	0.19	0.00	0.03	0.00	0.00	0.00	0.00
MgO	11.33	11.58	12.55	10.24	9.34	9.97	0.80	0.77	0.66	0.77	0.45	0.69
CaO	0.16	0.10	0.06	0.09	0.78	0.12	0.09	0.09	0.05	0.04	0.05	0.04
BaO	0.09	0.14	0.00	0.09	0.13	0.08	0.28	0.26	0.17	0.03	0.17	0.19
Na_2O	0.31	0.31	0.14	0.27	0.19	0.23	1.32	1.43	1.56	1.56	1.68	1.51
K_2O	9.27	9.52	9.50	9.31	9.21	9.26	9.06	9.19	8.88	8.56	8.78	8.68
F	0.37	0.31	0.38	0.28	0.26	0.32	0.00	0.00	0.00	0.00	0.00	0.00
Cl	0.05	0.07	0.02	0.02	0.03	0.02	0.03	0.06	0.02	0.01	0.11	0.05
tot	97.55	97.45	98.64	97.16	97.05	95.63	95.94	95.37	95.16	96.65	95.95	96.36
Si	2.78	2.75	2.84	2.78	2.74	2.79	3.10	3.10	3.09	3.13	3.08	3.09
Ti	0.12	0.11	0.10	0.12	0.19	0.12	0.03	0.01	0.01	0.01	0.01	0.01
Al	1.58	1.64	1.55	1.57	1.60	1.57	2.70	2.72	2.76	2.75	2.83	2.81
Fe	1.13	1.07	1.02	1.24	1.20	1.25	0.12	0.12	0.10	0.07	0.06	0.06
Mn	0.01	0.01	0.01	0.01	0.01	0.01	0.00	0.00	0.00	0.00	0.00	0.00
Mg	1.26	1.28	1.36	1.15	1.05	1.14	0.08	0.08	0.07	0.07	0.04	0.07
Ca	0.01	0.01	0.00	0.01	0.06	0.01	0.01	0.01	0.00	0.00	0.00	0.00
Ba	0.00	0.00	0.00	0.00	0.00	0.00	0.01	0.01	0.00	0.00	0.00	0.00
Na	0.04	0.04	0.02	0.04	0.03	0.03	0.17	0.18	0.20	0.20	0.21	0.19
K	0.88	0.90	0.88	0.89	0.88	0.90	0.76	0.78	0.75	0.71	0.74	0.72
F	0.09	0.07	0.09	0.07	0.06	0.08	0.00	0.00	0.00	0.00	0.00	0.00
Cl	0.01	0.01	0.00	0.00	0.00	0.00	0.00	0.01	0.00	0.00	0.01	0.01
tot	7.91	7.90	7.87	7.88	7.83	7.90	6.99	7.02	7.00	6.94	6.99	6.96

Table 4.3. Representative electron microprobe analyses of biotite and muscovite (wt% oxides). Atomic proportion (apfu) were recalculated based on O = 11.

Element maps (Figs. 4.18, 4.19, 4.20, 4.21 and 4.22) clearly show that micas from the Munsiari and Vaikrita Thrust samples are intimately intergrown at a scale between 5-50 μm, therefore preventing a complete 100% purity separation and *in situ* geochronological analyses as will be discussed in detail in Chapter 5 and 7.

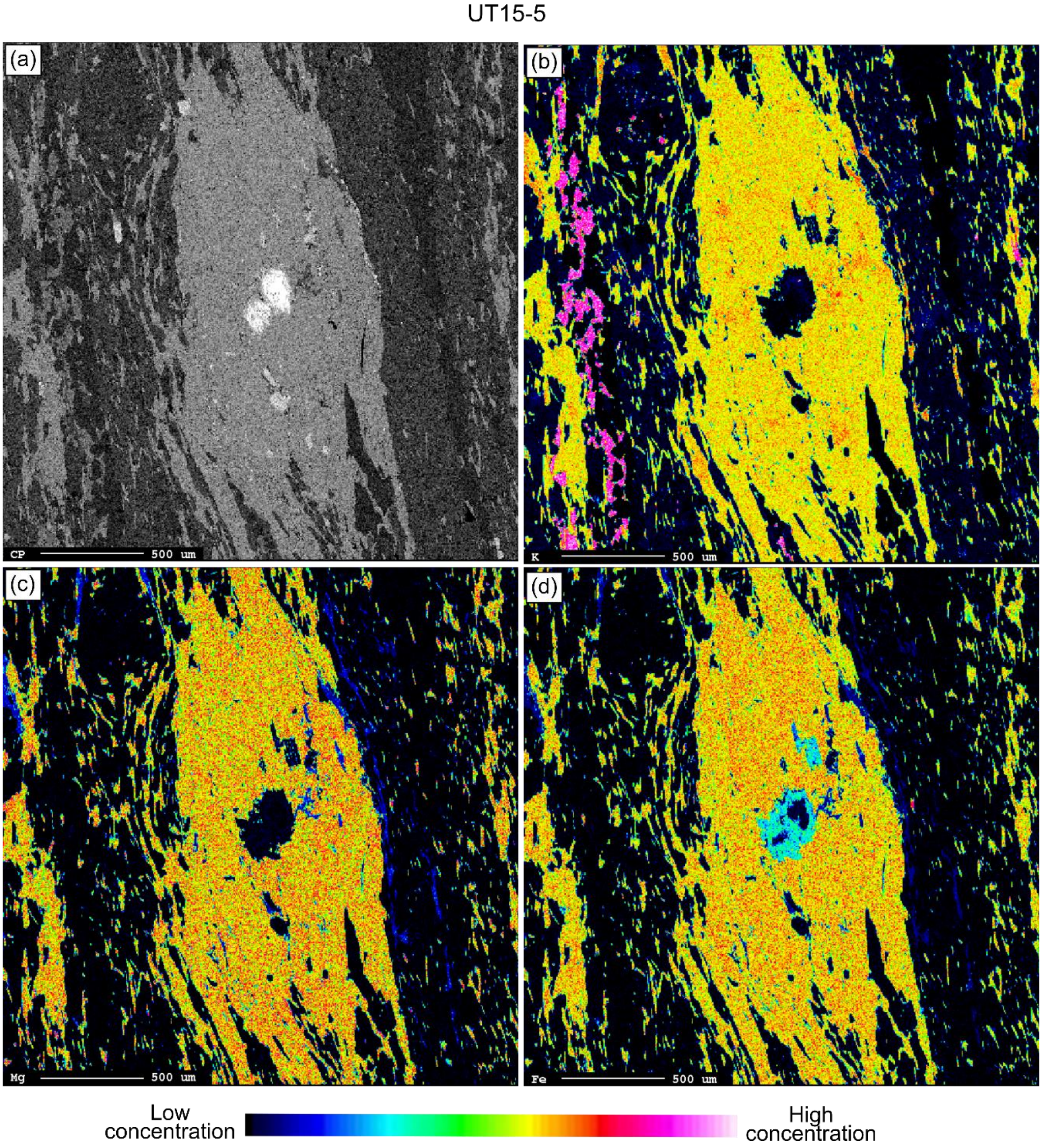

Figure 4.18. BSE (a) and X-ray element maps for (b) K, (c) Mg and (d) Fe of selected micas rich area from mylonitic orthogneiss UT15-5 from the Munsiari Thrust.

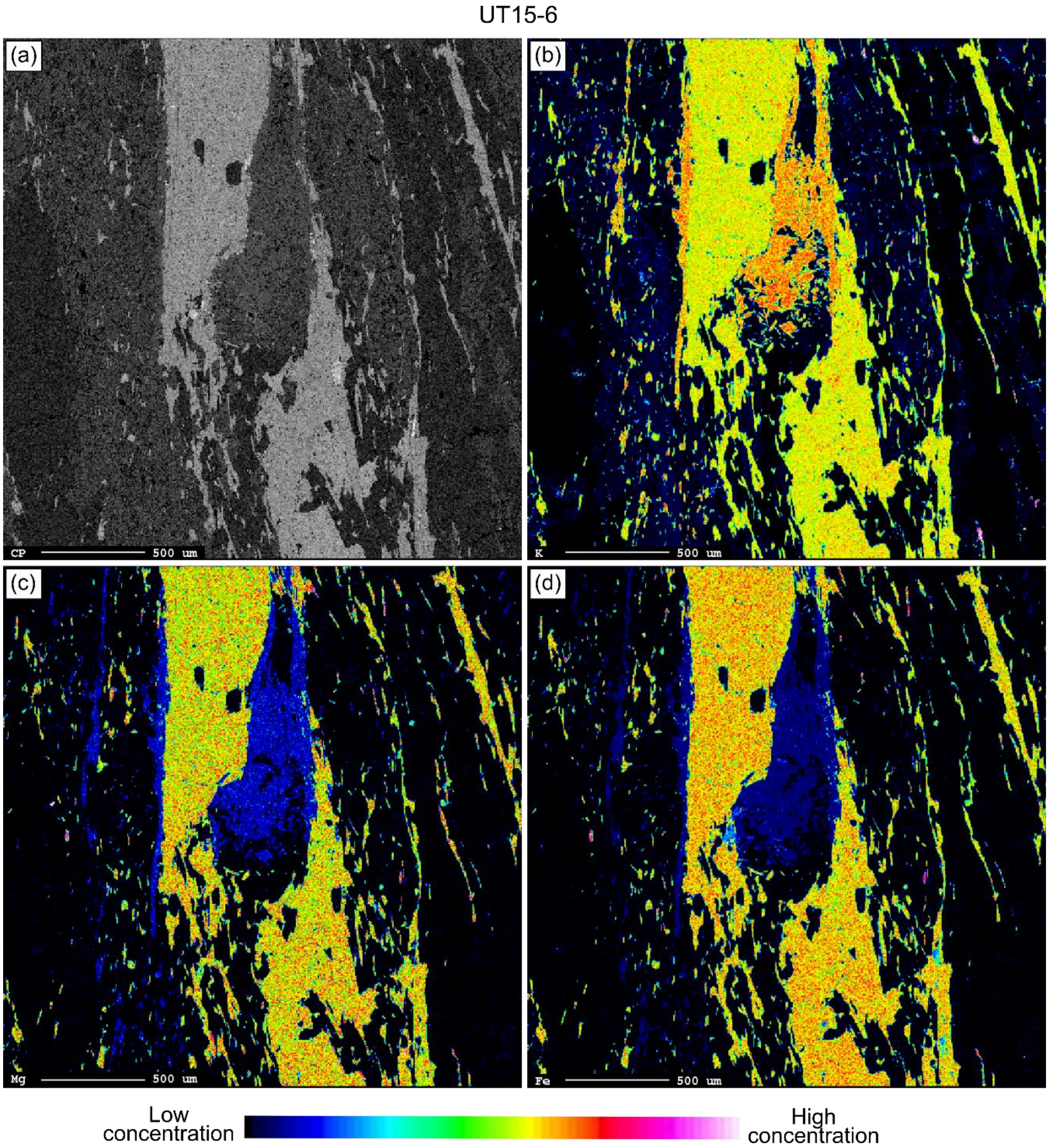

Figure 4.19. BSE (a) and X-ray element maps for (b) K, (c) Mg and (d) Fe of selected micas rich area from mylonitic orthogneiss UT15-6 from the Munsiari Thrust.

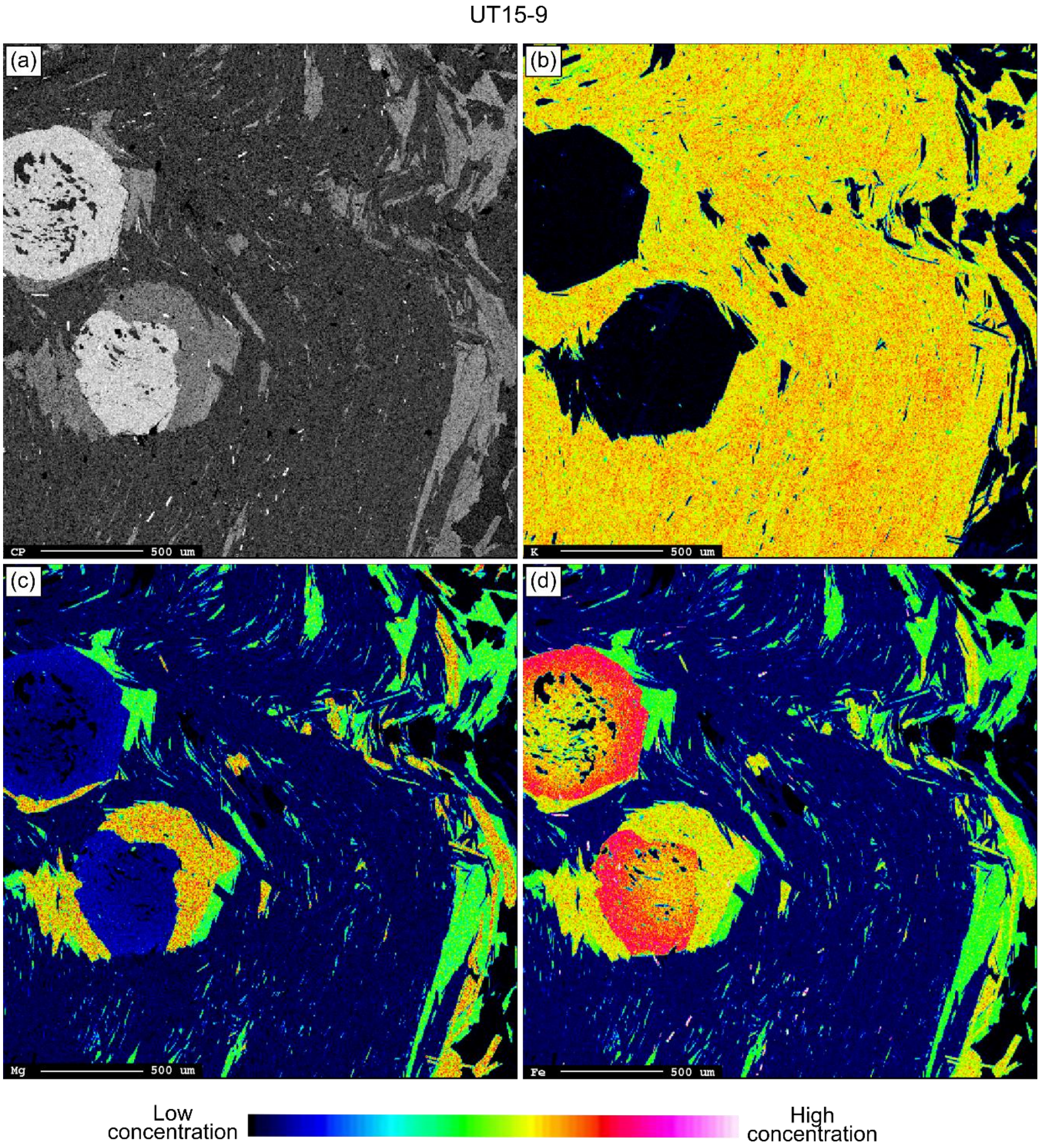

Figure 4.20. BSE (a) and X-ray element maps for (b) K, (c) Mg and (d) Fe of selected area from garnet-bearing micaschist UT15-9 from the Vaikrita Thrust.

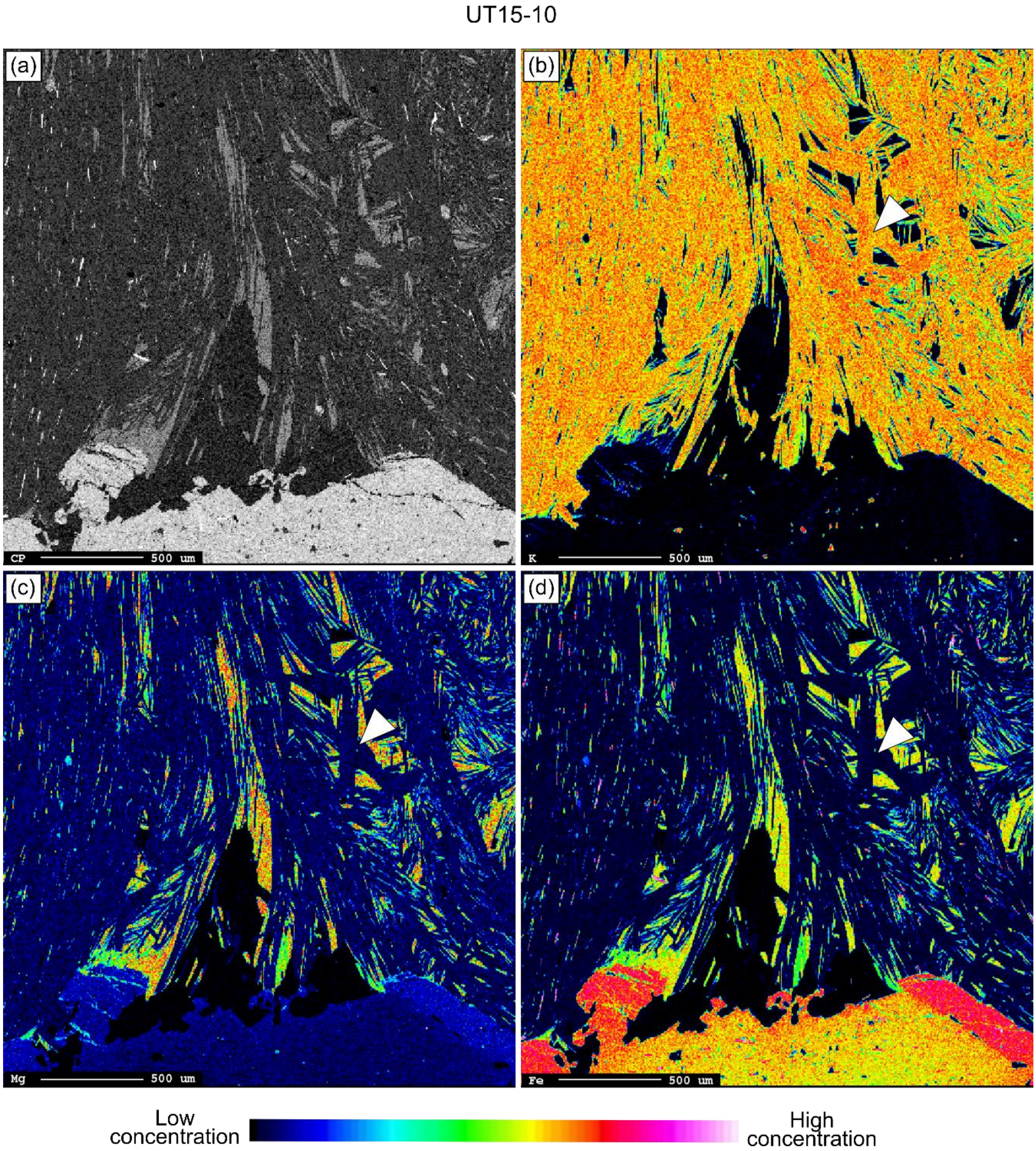

Figure 4.21. BSE (a) and X-ray element maps for (b) K, (c) Mg and (d) Fe of selected area from garnet-bearing micaschist UT15-10 from the Vaikrita Thrust. Note the static muscovite (white arrows) growth on the previous structures.

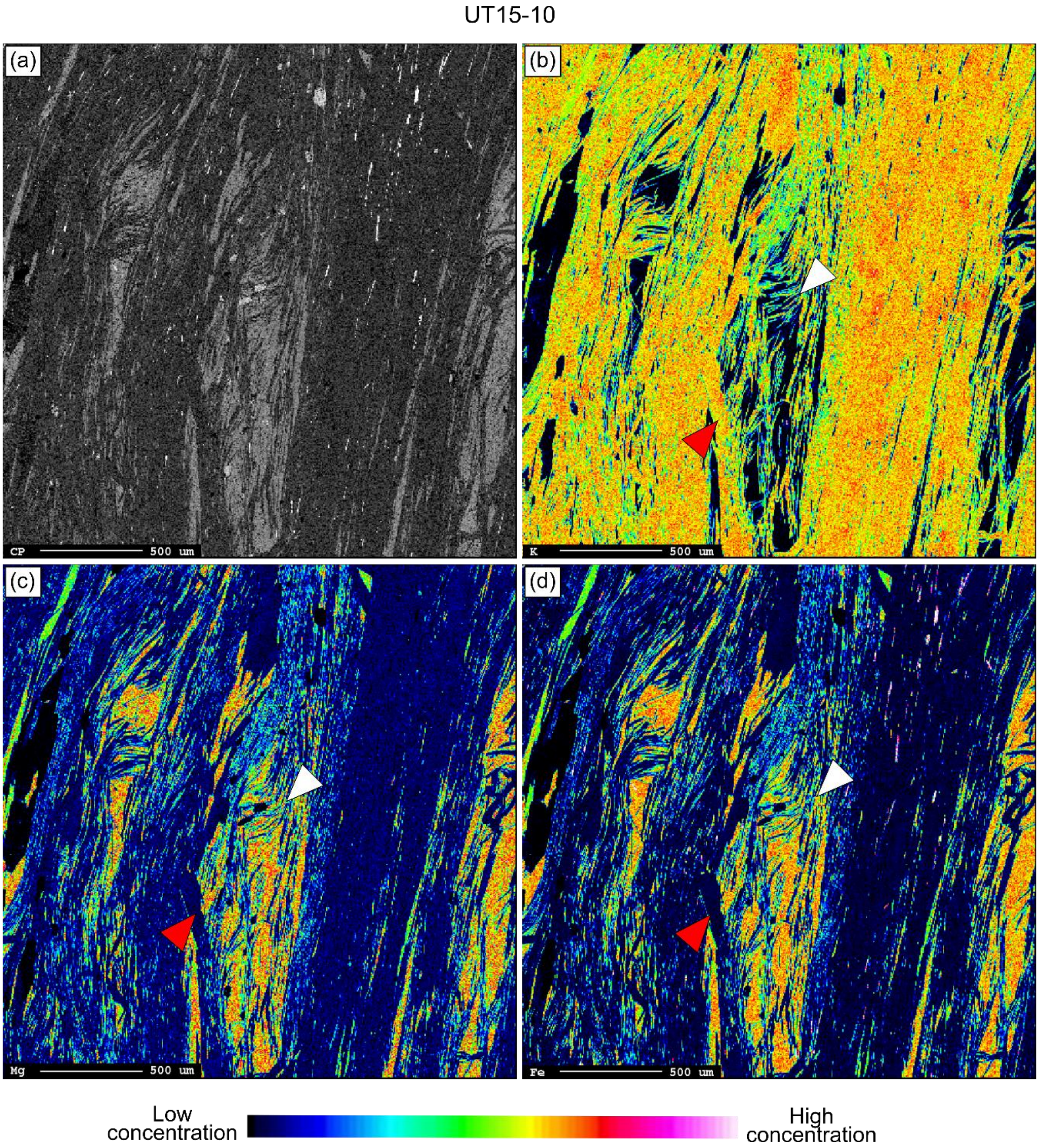

Figure 4.22. BSE (a) and X-ray element maps for (b) K, (c) Mg and (d) Fe of selected micas rich area from garnet-bearing micaschist UT15-10 from the Vaikrita Thrust. Note the static muscovite (red arrows) growth on the previous structures characterized by high K (b) and low Mg (c) and Fe (d). White arrows point to the micron scale intergrowths of micas.

4.2.2 Bhagirathi Granite

Three Bhagirathi granite samples (UT15-41, UT15-51) with the host rock (UT15-40) have been selected for EPMA and ^{40}Ar/^{39}Ar step-heating dating. Their locations are shown in Figure 4.13.

UT15-41 is a tourmaline-bearing leucogranitic dike (Fig. 4.23a) intruding the main Bhagirathi body with a mineral assemblage consisting in quartz, plagioclase, Kfeldspar, tourmaline and muscovite (Fig. 4.23b). Small incipient perthitic exsolutions and tartan twinning occur in Kfeldspar, suggesting a slow cooling lower symmetry change (Vernon, 2004). Plagioclase occasionally displays flame twinnings; quartz grains exhibit undulose extinction and only occasionally microstructural evidences of BLG recrystallization. Myrmekite also sporadically occurs. Tourmaline crystals have re-absorbed rims (Fig. 4.23a).

The relationship between leucogranitic dyke and the host rock has been observed in sample UT15-40 (Fig. 4.23c). The host rock is a biotite-bearing quartzite with a main foliation formed by crystallization of biotite and minor muscovite, with the latter more abundant near the contact.

UT15-51 is a two mica-tourmaline-bearing leucogranite (Fig. 4.23d-f) representing the Bhagirathi granite main body containing quartz, plagioclase, Kfeldspar, biotite, tourmaline and muscovite. Kfeldspar shows tartan twinning and abundant sericitization in some crystals (Fig. 4.23d); flame twinnings occur in plagioclase. Quartz shows a bimodal grain distribution testifying a Subgrain Rotation (SGR, Passchier & Trouw, 2005) recrystallization mechanism. In coarse-grained quartz BLG and undulose extinction are clearly evident. Myrmechites also sporadically occur (Fig. 4.23e). Millimeter size aggregates of undeformed biotite are present in the sample (Fig. 4.23f).

4.2.2.1 Mica compositions

The full set of EMP analyses of micas from the studied samples are given in Supplementary Material Appendix 1 and summarized in Figure 4.24. Representative EMPA are reported in Table 4.4. Micas analyses were recalculated as atoms per formula unit (apfu) based on 11 oxygens. Element maps show that mica grains are almost uniform in the analysed elements; nevertheless, muscovites of the granitic portion of samples UT15-40 are Ti-zoned showing a Ti-rich core with respect to the rim. White mica from UT15-40 and UT15-41 show similar chemical composition, lying along the muscovite-celadonite join (3.09-3.18 apfu) with Si concentration less scattered in sample UT15-41 (Fig. 4.24a). The Mg and Ti concentrations are overlying, ranging between 0.03-0.05 and 0.01-0.05 respectively, with Ti concentration in muscovite UT15-40 more scattered than in muscovite UT15-41 (Fig. 4.24b-c).

The host rock (sample UT15-40) differs from granites showing less scattered Si concentration (3.12-3.17 apfu) and lower Al corresponding to higher Mg concentration (Fig. 4.24c).

Biotite from sample UT15-51 (Fig. 4.24d-f) shows X_{Mg} (i.e. Mg/(Mg+Fe)) ranging between 0.15 and 0.17. The ^{IV}Al (Fig. 4.24d) and Ti (Fig. 4.24e) contents are restricted (1.12-1.18 and 0.11-0.14 respectively), K concentration (Fig. 4.24f) is stoichiometric (0.89-0.93 apfu) confirming that biotites have not been altered.

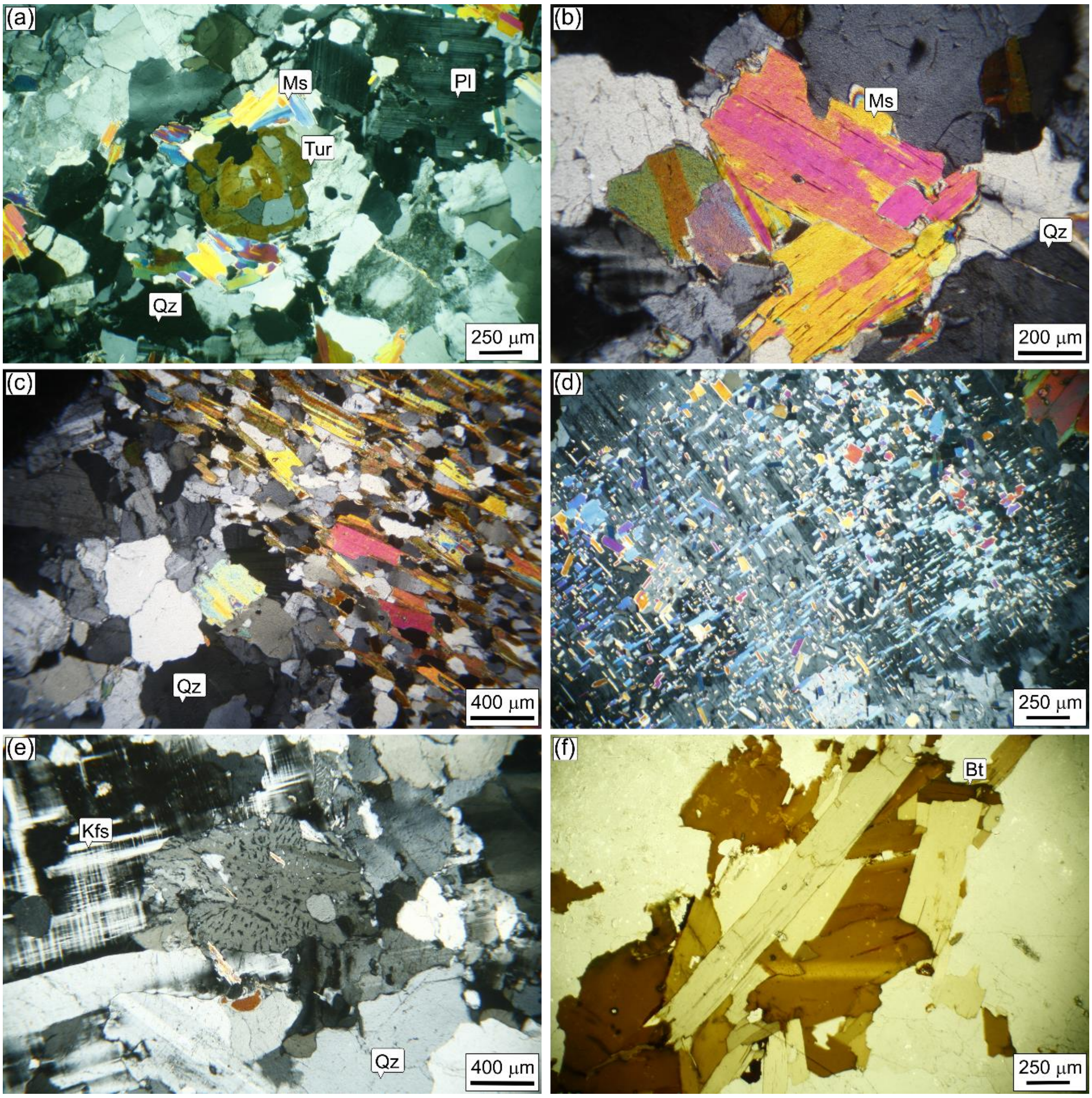

Figure 4.23. The Bhagirathi granite samples. (a) Tourmaline crystal with re-absorbed rims in leucogranitic dike (UT15-41); undeformed muscovite crystals aggregate (UT15-41); contact between granite and the host rock (UT15-40); sericitized coarse grained Kfeldspar crystal in the Bhagirathi granite main body (UT15-51); (e) myrmekites and tartan twinning in Kfeldspar (UT15-51); (f) millimeter size aggregates of undeformed biotite (UT15-51).

Table 4.4

	Sample								
	UT15-40			**UT15-41**			**UT15-51**		
	Muscovite			Muscovite			Biotite		
SiO_2	47.02	46.58	47.16	47.58	47.40	47.22	35.70	36.23	36.19
TiO_2	0.33	0.94	0.77	0.42	0.29	0.42	2.34	2.28	2.05
Al_2O_3	34.98	34.16	33.51	34.14	34.31	33.90	19.03	19.23	19.87
FeO	2.00	2.03	1.80	2.09	1.96	2.07	25.45	26.06	25.50
MnO	0.02	0.01	0.00	0.00	0.02	0.05	0.05	0.05	0.05
MgO	0.43	0.46	1.40	0.48	0.43	0.45	2.73	2.74	2.83
CaO	0.07	0.07	0.08	0.02	0.00	0.01	0.01	0.00	0.00
BaO	0.05	0.00	0.42	0.03	0.00	0.02	0.01	0.01	0.00
Na_2O	0.60	0.72	0.61	0.48	0.50	0.54	0.00	0.01	0.01
K_2O	10.23	10.08	10.22	10.48	10.49	10.41	8.88	9.11	8.97
F	0.06	0.03	0.22	0.04	0.00	0.06	1.14	1.32	1.06
Cl	0.01	0.01	0.09	0.00	0.00	0.00	0.00	0.00	0.00
tot	95.79	95.09	96.28	95.76	95.40	95.14	96.02	97.61	97.17
Si	3.12	3.11	3.14	3.16	3.15	3.16	2.85	2.86	2.84
Ti	0.02	0.05	0.04	0.02	0.01	0.02	0.14	0.14	0.12
Al	2.73	2.69	2.63	2.67	2.69	2.67	1.79	1.79	1.84
Fe	0.11	0.11	0.10	0.12	0.11	0.12	1.70	1.72	1.67
Mn	0.00	0.00	0.00	0.00	0.00	0.00	0.00	0.00	0.00
Mg	0.04	0.05	0.14	0.05	0.04	0.04	0.32	0.32	0.33
Ca	0.00	0.01	0.01	0.00	0.00	0.00	0.00	0.00	0.00
Ba	0.00	0.00	0.01	0.00	0.00	0.00	0.00	0.00	0.00
Na	0.08	0.09	0.08	0.06	0.06	0.07	0.00	0.00	0.00
K	0.87	0.86	0.87	0.89	0.89	0.89	0.90	0.92	0.90
F	0.01	0.01	0.05	0.01	0.00	0.01	0.29	0.33	0.26
Cl	0.00	0.00	0.01	0.00	0.00	0.00	0.00	0.00	0.00
tot	6.99	6.98	7.06	6.97	6.97	6.98	8.00	8.07	7.97

Table 4.4. Representative electron microprobe analyses of muscovite (wt% oxides). Atomic proportion (apfu) were recalculated based on O = 11.

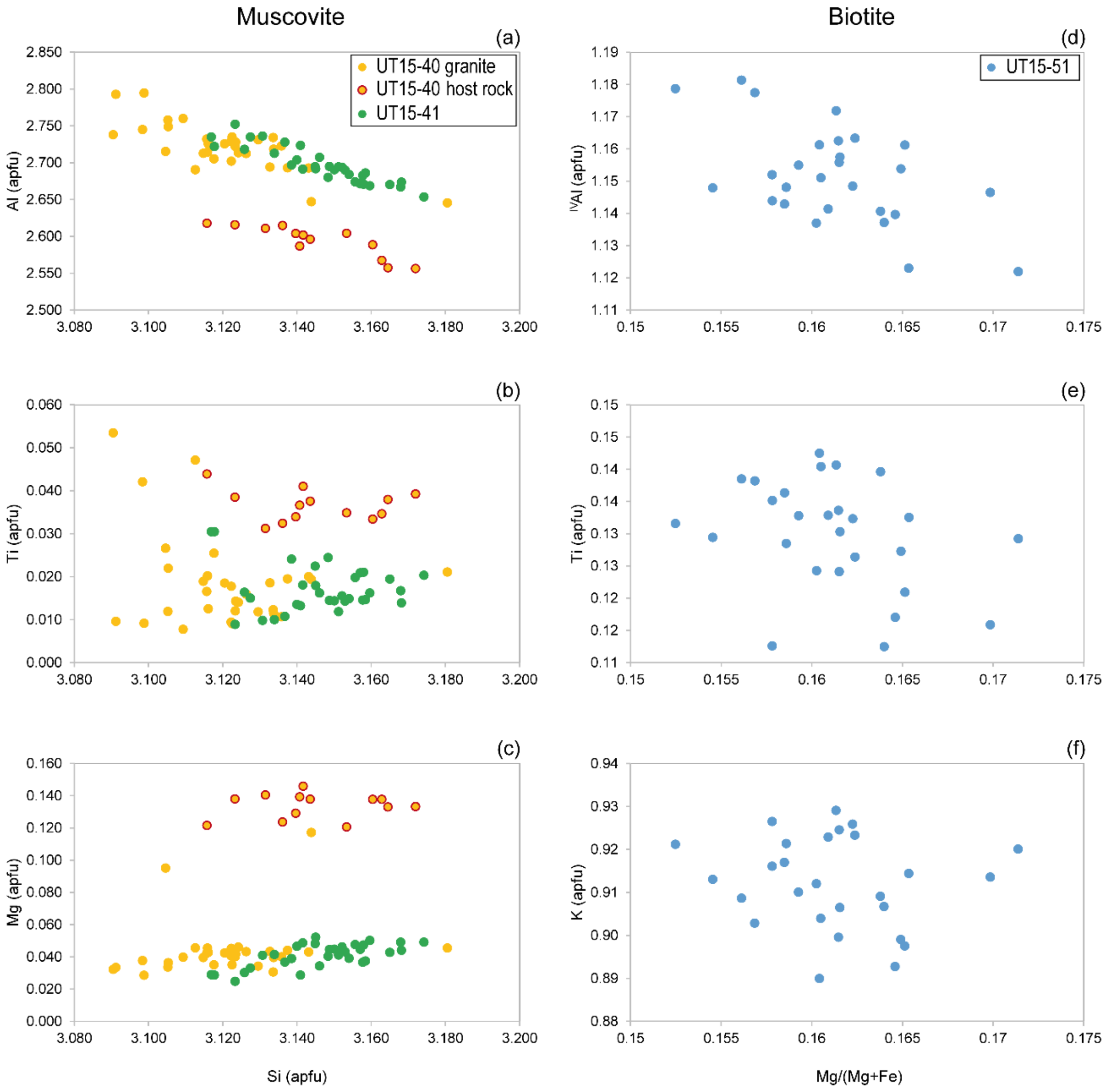

Figure 4.24. Chemical variation in muscovite (a-c) and biotite (d-f) from Bhagirathi samples.

4.3 Lower Alaknanda valley

The locations of samples selected from this valley are reported in Figure 4.1.

Samples GW13-19 and GW13-20 (light blue stars Fig. 4.1) have been studied in order to assess the deformation temperatures from quartz *c*-axis fabric opening angle thermometry. These rocks are quartzites (Fig. 4.25) with mineral assemblage consisting in quartz, muscovite, rare biotite, zircon and apatite. The main foliation is defined by the SPO of micas, more spaced in coarse-grained quartz domains. The operative quartz recrystallization mechanism, GBM, is indicated by over pinning of micas and window structures (Fig. 4.25c,d), testifying to the operation of high grain boundary mobility recrystallization mechanisms.

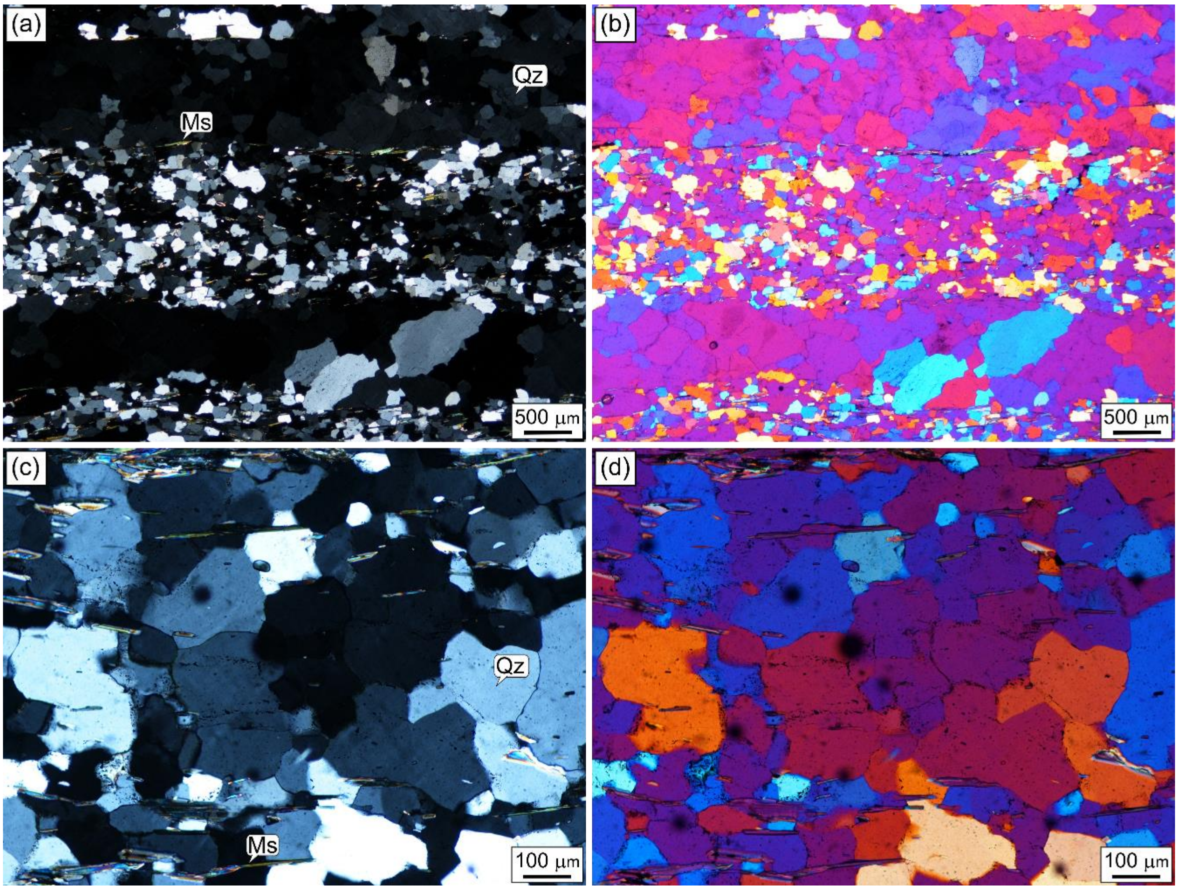

Figure 4.25. Quartzites from the lower MCTz. (a) microstructures of GW13-19. Note the coarse grained quartz domains alternating with fine grained quartz domains; (c) overpinning microstructure of micas in quartz in GW13-20. (b) and (d) the same areas as in (a) and (c) with gypsum accessory plate inserted.

Moreover, five samples (Fig. 4.1) have been selected for further dating: AK18-5, AK18-13, AK18-23, AK18-26 and AK18-42.

AK18-5 is a biotite-tourmaline bearing mylonitic quartzite (Fig. 4.26a) coming from the Berinag Thrust. The mineral assemblage consists in quartz, muscovite, tourmaline and minor chlorite. Tourmaline occurs both along the main foliation and in quartz-rich domains. The main disjunctive foliation is defined by the alternation between quartzitic and muscovite-rich domains, and it is crenulated in some portions (Fig. 4.26a). Chlorite around larger quartz crystals, characterized by weak undulose extinction (Fig. 4.26b), also sporadically occurs. Kinematic indicators such as asymmetric micas around opaques, tourmalines or larger quartz crystals, point to a top-to-the-SW sense of shear (Fig. 4.26b).

Sample AK18-13 is a mylonitic calcschist (Fig. 4.26c-d) from the Munsiari Thrust, containing quartz, calcite, muscovite, biotite and minor late chlorite. The main mylonitic foliation is a disjunctive S2, locally crenulated by a successive deformation. Sporadic S1 relict domains and late static micas occur (Fig. 4.26c). Quartz is characterized by BLG recrystallization mechanism in the coarse-grained aggregates (Fig. 4.26c), whereas it shows straight grain boundaries in the fine-grained domains. Type-I and -II twinnings (Ferrill et al., 2004) occur in calcite (Fig. 4.26d). Sigmoidal aggregates of quartz indicate a top-to-the-SW shear sense (Fig. 4.26c).

AK18-23 is a mylonitic micaschist (Fig. 4.26e) cropping out in the hanging wall of the Vaikrita Thrust containing biotite, quartz, muscovite and minor late chlorite, coming from the hanging wall of the Vaikrita Thrust. The main mylonitic foliation is disjunctive and anastomosing, formed by the alternation of micas and quartz domains. Sporadically static micas also occur. Coarse-grained ribbons and aggregates of quartz characterized by undulose extinction alternate with fine grained portions. A well-defined thin section-scale SC-fabric shows a top-to-the-SW sense of shear (Fig. 4.26e).

Sample AK18-26, coming from the Vaikrita Thrust, is an amphibolite (Fig. 4.26f) containing tremolite, biotite and minor muscovite and quartz. The main foliation is given by the SPO of biotite and tremolite (Fig. 4.26f).

AK18-42 is a biotite-bearing mylonitic quartzite (Fig. 4.26g-h) coming from the GHS, consisting in quartz, biotite and muscovite. The main foliation is due to the SPO of micas (Fig. 4.26g). Quartz is fine-grained but larger crystals with undulose extinction also occur (Fig. 4.26g). Some foliation fish of biotite (Fig. 4.26h) point toward a top-to-the-SW sense of shear.

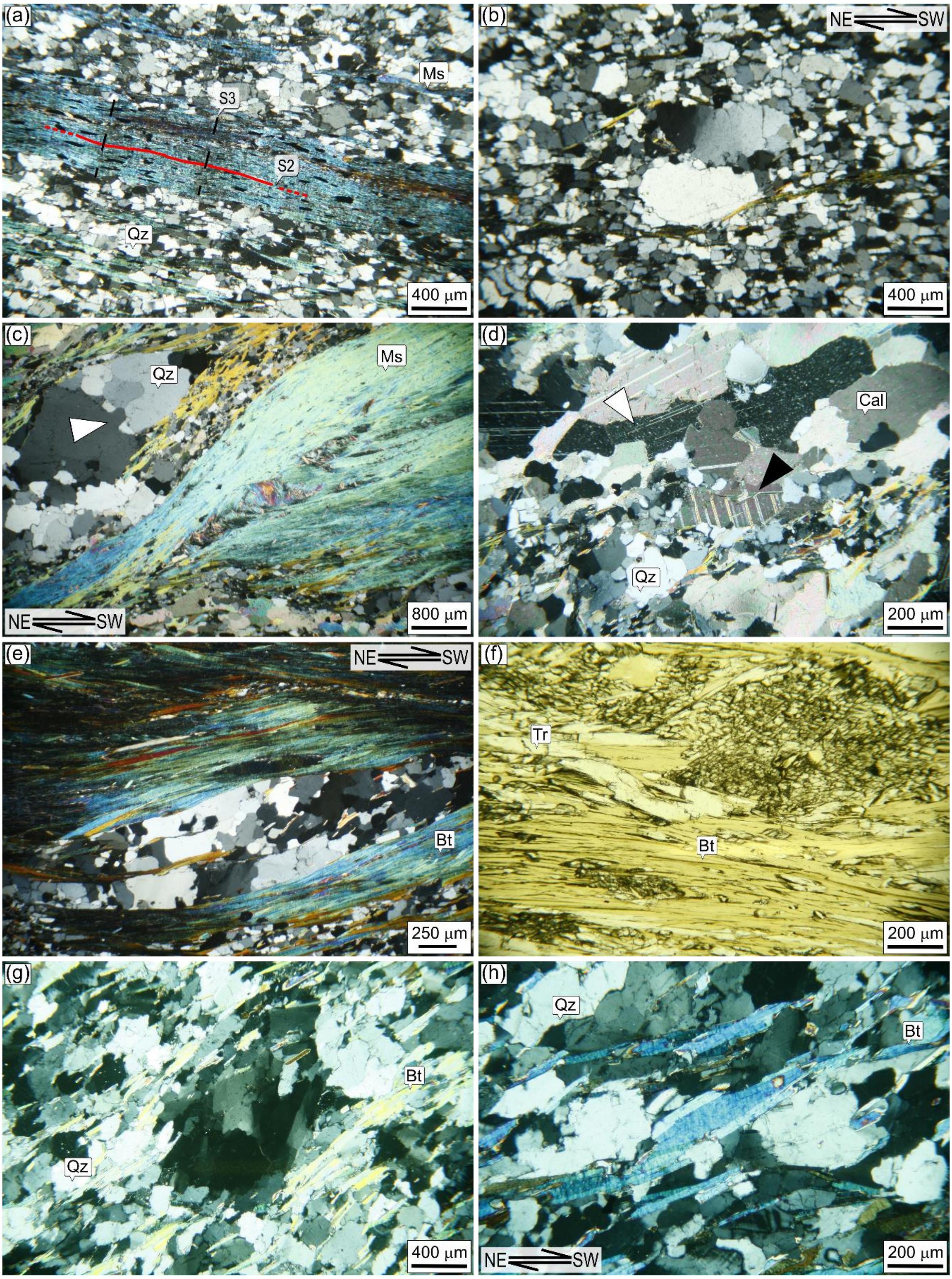
(a)
Ms
S3
S2
Qz
400 μm
(b)
NE SW
400 μm
(c)
Qz
Ms
NE SW
800 μm
(d)
Cal
Qz
200 μm
(e)
NE SW
Bt
250 μm
(f)
Tr
Bt
200 μm
(g)
Bt
Qz
400 μm
(h)
Qz
Bt
NE SW
200 μm

Figure 4.26. Microstructures of the samples from the lower Alaknanda valley. (a) S2 crenulated foliation in quartzite of Berinag Thrust (AK18-5); (b) micas around quartz crystals, characterized by weak undulose extinction, points to a top-to-the-SW shear sense (AK18-5); (c) muscovite forming the S2 schistosity in the calcschist of Munsiari Thrust; note bulging recrystallization in quartz (white arrow). Sigmoid aggregates show a top-to-SW shear sense (AK18-13); (d) type-I (white arrow) and II (black arrow) twinning in calcite (AK18-13); (e) sigmoidal quartz aggregate and SC fabric indicate a top-to-the-SW shear sense (AK18-23); (f) main foliation defined by biotite and tremolite in Vaikrita Thrust sample (AK18-26); (g) quartz crystals with undulose extinction in biotite-bearing quartzite from the GHS (AK18-42); (h) biotite fish points to a top-to-the-SW shear sense (AK18-42). Mineral abbreviation as in Whitney & Evans (2010).

4.3.1. Mica compositions

Representative EMPA are reported in Table 4.6, all the EMPA datasets are reported in Supplementary Material Appendix 1 and summarized in Figure 4.28. Micas analyses were recalculated as atoms per formula unit (apfu) based on 11 oxygens. EPM analyses of the four biotite samples are represented in Figure 4.28a-d. Samples AK18-13, AK18-23 and AK18-26 has a X_{Mg} between 0.63 and 0.77, whereas sample AK18-42 have a X_{Mg} between 0.19-0.23. Al^{IV} concentration mainly ranges between 0.24 and 0.41, being higher in AK18-23 (0.37-0.41). Ti concentration (Fig. 4.28b) is close to the detection limit in sample AK18-23 that shows the lowest Ti values, samples AK18-13 and AK18-26 show values 0.06-0.07 and 0.04-0.06 respectively; whereas sample AK18-42 exhibits the highest Ti values (0.18-0.26). K concentration is stoichiometric (0.9 apfu < K < 1 apfu) in all samples (Fig. 4.28c), more homogeneous in AK18-42 and less homogeneous in sample AK18-26. The insertion of Ti is driven by the exchange vector: $Ti^{4+} + 2O^{2-} <> {}^{VI}Me^{2+} + 2OH^{-}$ (Fig. 4.28d).

EMP analyses of muscovite samples AK18-5 and AK18-13 are represented in Figure 4.28e-h. White mica is characterized by limited compositional variation around the muscovite-celadonite join, with Si varying between 3.10-3.16 and 3.21-3.31 apfu for AK18-5 and AK18-13 respectively (Fig. 4.28d). The Al concentration is higher and more homogeneous in AK18-5 (2.66-2.73 apfu) with respect to AK18-13 (2.31-2.54 apfu). The Ti concentration (Fig. 4.28e) is low in muscovite of both samples although in the muscovite of sample AK18-5 is generally higher than AK18-13 whose values are close to the detection limit. The Na/(Na + K) ratio of muscovite is significantly different in the two samples, with AK18-5 showing a higher paragonite content (0.03-0.05) than AK18-13 (0-0.01). K concentration is stoichiometric in both samples (Fig. 4.28f). Muscovite is characterized by variable degrees of phengitic substitution expressed as ${}^{IV}Al^{3+} + {}^{VI}Al^{3+} <> {}^{VI}Me^{2+} + {}^{IV}Si^{4+}$, with no differences between the several generations but with more restricted variation in sample AK18-5 with respect to AK18-13 (Fig. 4.28h).

Table 4.6

	Sample											
	AK18-5		**AK18-13**				**AK18-23**		**AK18-26**		**AK18-42**	
	Muscovite		Muscovite		Biotite		Biotite		Biotite		Biotite	
SiO_2	47.08	46.55	48.71	48.18	39.49	39.73	39.34	39.88	39.67	40.02	34.81	34.41
TiO_2	0.25	0.19	0.07	0.06	1.27	1.04	0.07	0.08	0.80	0.79	3.19	4.22
Al_2O_3	33.79	34.42	31.02	31.00	16.36	16.45	17.73	17.26	16.86	15.73	17.72	17.57
FeO	2.59	2.63	2.90	2.69	10.49	10.21	11.91	11.52	11.21	10.86	28.80	28.06
MnO	0.00	0.00	0.00	0.00	0.00	0.01	0.01	0.01	0.09	0.11	0.02	0.02
MgO	0.58	0.47	1.98	1.97	17.41	17.77	16.28	16.93	17.32	17.29	4.31	4.12
CaO	0.01	0.00	0.00	0.00	0.00	0.00	0.00	0.01	0.03	0.03	0.00	0.01
BaO	0.09	0.07	0.02	0.01	0.00	0.01	0.01	0.01	0.02	0.02	0.00	0.01
Na_2O	0.31	0.29	0.04	0.05	0.01	0.01	0.02	0.01	0.08	0.09	0.01	0.01
K_2O	10.86	10.80	10.70	10.62	10.28	10.18	10.03	9.98	9.82	9.99	9.46	9.38
F	0.00	0.00	0.00	0.00	0.06	0.05	0.03	0.04	0.24	0.26	0.01	0.01
Cl	0.00	0.00	0.00	0.00	0.00	0.00	0.00	0.00	0.00	0.02	0.00	0.00
tot	95.56	95.42	96.63	95.69	96.04	96.14	96.74	97.20	96.14	95.21	98.70	98.31
Si	3.15	3.12	3.25	3.25	2.88	2.88	2.87	2.89	2.88	2.93	2.69	2.67
Ti	0.01	0.01	0.00	0.00	0.07	0.06	0.00	0.00	0.04	0.04	0.19	0.25
Al	2.66	2.72	2.44	2.46	1.40	1.41	1.52	1.48	1.44	1.36	1.61	1.61
Fe	0.14	0.15	0.16	0.15	0.64	0.62	0.73	0.70	0.68	0.67	1.86	1.82
Mn	0.00	0.00	0.00	0.00	0.00	0.00	0.00	0.00	0.01	0.01	0.00	0.00
Mg	0.06	0.05	0.20	0.20	1.89	1.92	1.77	1.83	1.87	1.89	0.50	0.48
Ca	0.00	0.00	0.00	0.00	0.00	0.00	0.00	0.00	0.00	0.00	0.00	0.00
Ba	0.00	0.00	0.00	0.00	0.00	0.00	0.00	0.00	0.00	0.00	0.00	0.00
Na	0.04	0.04	0.01	0.01	0.00	0.00	0.00	0.00	0.01	0.01	0.00	0.00
K	0.93	0.92	0.91	0.91	0.96	0.94	0.93	0.92	0.91	0.93	0.93	0.93
F	0.00	0.00	0.00	0.00	0.01	0.01	0.01	0.01	0.05	0.06	0.00	0.00
Cl	0.00	0.00	0.00	0.00	0.00	0.00	0.00	0.00	0.00	0.00	0.00	0.00
tot	6.99	7.00	6.98	6.98	7.85	7.85	7.84	7.84	7.90	7.91	7.79	7.75

Table 4.6. Representative electron microprobe analyses (wt% oxides). Atomic proportion (apfu) were recalculated based on O = 11.

Element maps for sample AK18-13 (Fig. 4.27) clearly show that micas from the Munsiari Thrust are intimately intergrown at a scale between 5-50 μm.

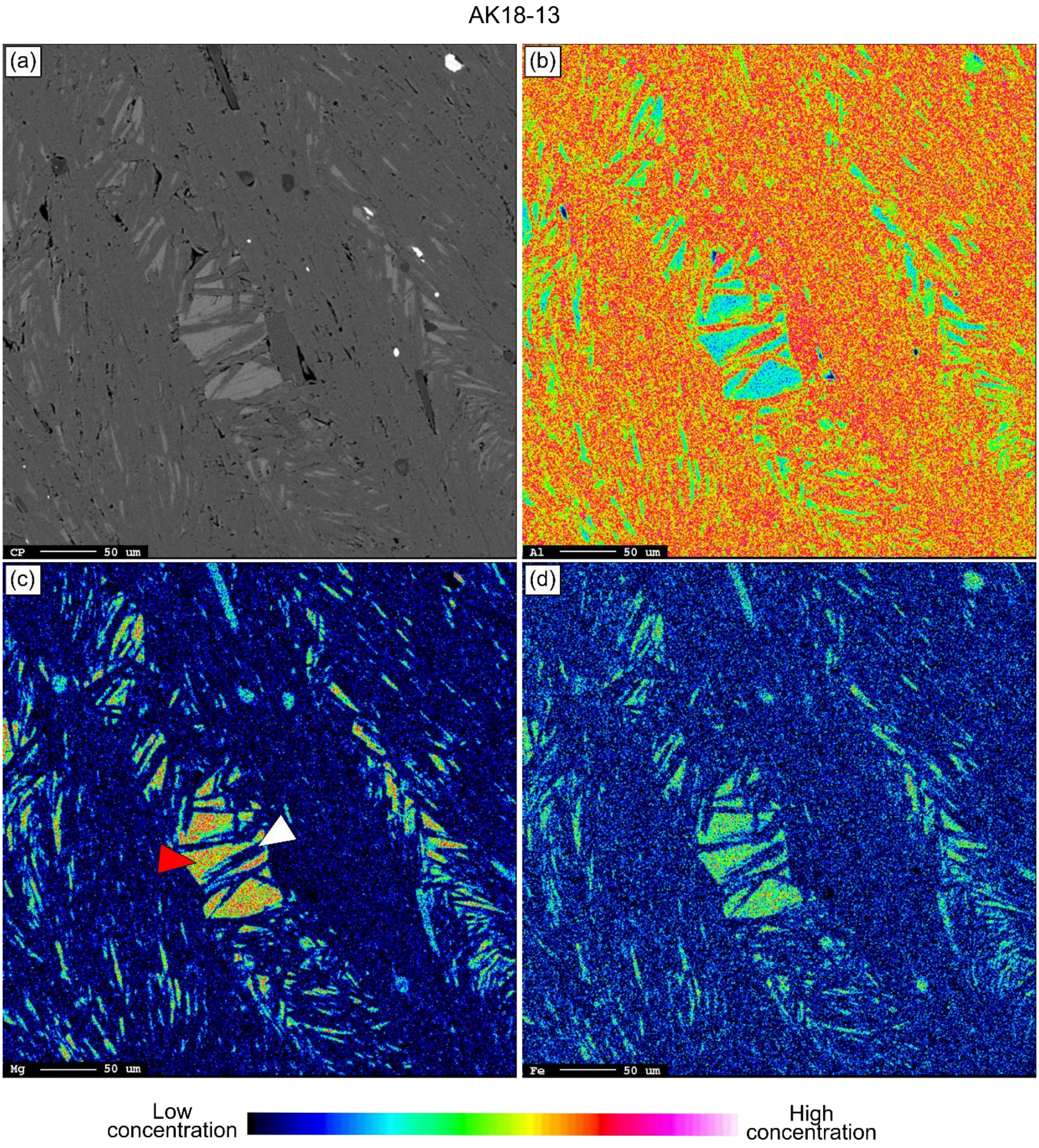

Figure 4.27. BSE (a) and X-ray element maps for (b) Al, (c) Mg and (d) Fe of selected micas rich area from calcschist AK18-13 from the Munsiari Thrust. Note the biotite (red arrow) and muscovite (white arrow) fine-grained intergrown.

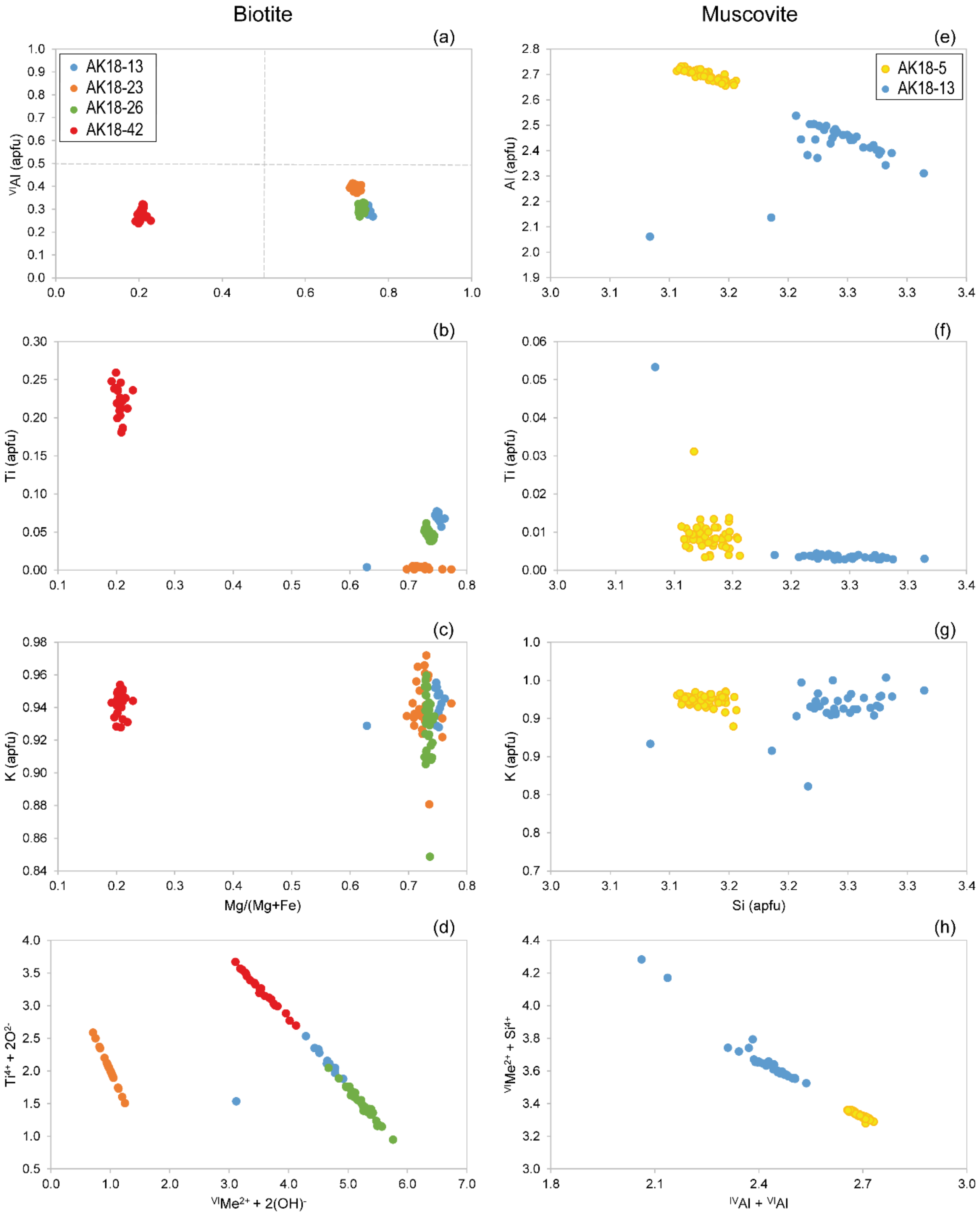

Figure 4.28. Chemical variation in biotite (a-d) and muscovite (e-h) from lower Alaknanda samples, subsequently dated by $^{40}Ar/^{39}Ar$ method.

5. ^{40}Ar/^{39}Ar GEOCHRONOLOGY

In this Chapter the results of ^{40}Ar/^{39}Ar stepheating technique on the previously described samples are reported and discussed. The full ^{40}Ar/^{39}Ar dataset is reported in Supplementary Material Appendix 2.

5.1 Alaknanda – Dhauli Ganga valleys

5.1.1 Main Central Thrust zone (*GW13-28, GW13-29, GW13-29B*)

The first and foremost observation is that all six age spectra (Figs 5.1a and 5.2a) are internally discordant. Even disregarding the steps that clearly do not pertain to mica *sensu stricto* (a first cut off is the Ca/K ratio, which should be <0.03 in mica), the step-ages range between 8.6 and 16 Ma for biotite and 3.6 and 7.8 Ma for muscovite. These results are apparently similar to those reported by Sen et al. (2015) for nearby samples collected in the Suraithota Formation (Fig. 2.2). The age pattern featuring older biotite ages and younger muscovite ages is also found in other MCTz localities (Jain, unpublished results; Mottram et al., 2015). The latter authors disregarded the biotite ages as due to excess Ar. By contrast, our interpretation of the results exploits the context between microstructural, microchemical and geochronological data.

5.1.1.1 Data discussion and interpretation

It is important to note that the biotite separates analysed here belong to an older mica generation than the muscovite separates. We further propose that discordant steps with low Ca/K and high step-ages should be seen as inherited Ar of the sparse relicts of the biotite-1 generation. Therefore there is no need to invoke excess Ar to explain why biotite-2 is older than muscovite-3. As inherited and excess Ar pertain to two completely different geochemical scenarios (Villa et al., 2014, p. 817), namely Ar loss and Ar gain, respectively, neglecting this difference would distort the entire interpretive framework. The biotite age spectra are not only internally discordant (Fig. 5.1a), but also suggest different Ar retention over an extremely small distance. This indicates that 'cooling' (Sen et al., 2015) is unlikely to be the only factor controlling the biotite ages. Because age spectra only provide incomplete information (Chafe et al., 2014), it is necessary to also take into account the information provided by the (often neglected) isotopes ^{38}Ar and ^{37}Ar, which are produced from Cl and Ca, respectively, in the reactor (Merrihue, 1965). From the measured ^{38}Ar/^{39}Ar and ^{37}Ar/^{39}Ar ratios and the known production factors, it is possible to calculate the Cl/K and Ca/K ratios (which can, but need not, be validated by electron microprobe analyses; Villa et al., 2000). Figure 5.1b shows the Cl/K–Ca/K common denominator correlation diagram (e.g. Villa & Williams, 2013 and references cited therein). Data points for all three samples define a peculiar V-shaped trajectory. The first heating steps of all samples have high Ca/K and high Cl/K ratios, which monitor the degassing of Ca-rich alteration phases. At higher oven temperatures, typical of biotite *sensu stricto* degassing (c. 900°C), the Cl/K and Ca/K ratios reach a minimum and the high-temperature steps show an increase in the Ca/K ratio at constant Cl/K. This pattern applies to biotite from all three samples, but to different degrees.

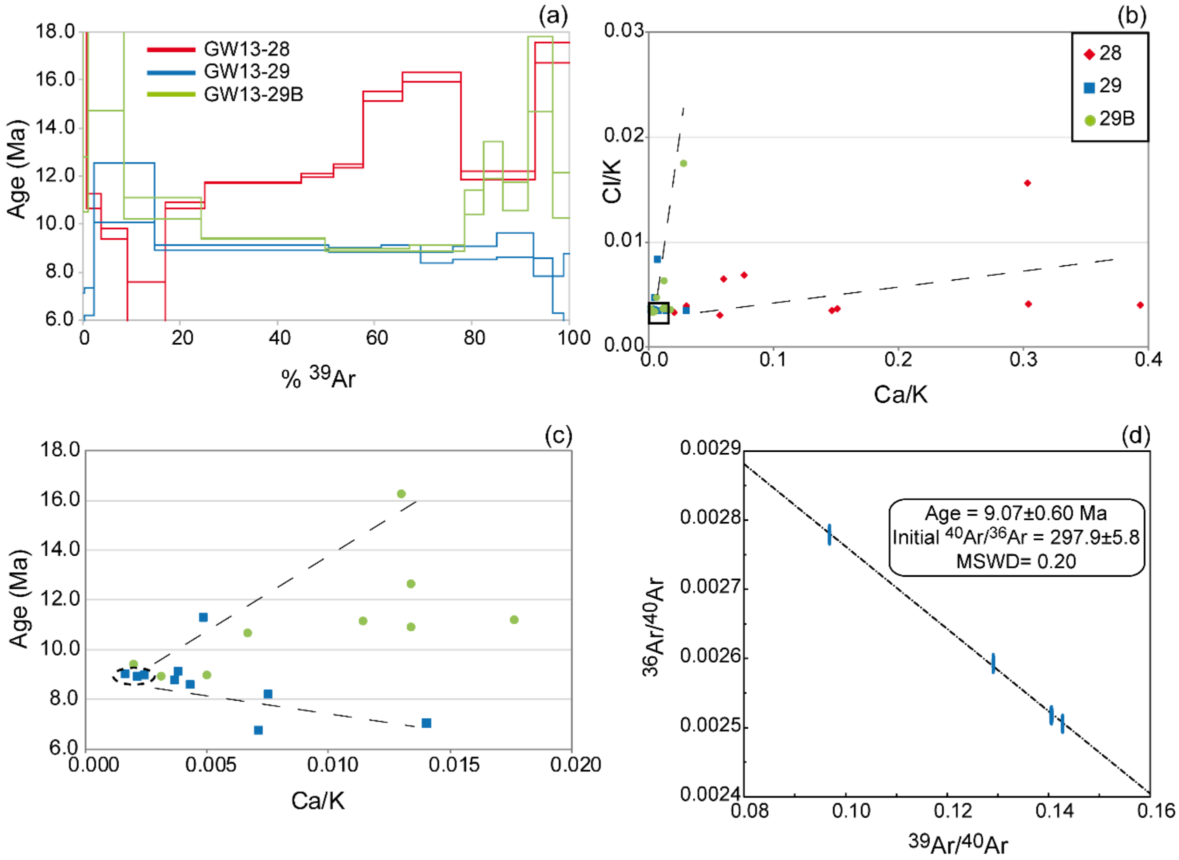

Figure 5.1. (a) ^{40}Ar/^{39}Ar age spectra of biotite comparing the three samples of the Vaikrita Thrust; (b) Cl/K vs Ca/K diagram showing a V-shaped trajectory of the data points. The reliable low Ca – low Cl analyses are highlighted in the inset, the dashed lines represent two trends: low Cl – variable Ca of the alteration phases of sample GW13-28 and variable Cl – low Ca trend; (c) age vs Cl/K correlation diagram of sample GW13-29 and GW13-29B. The dotted ellipse identifies the isochemical steps; (d) isochron obtained with the four isochemical steps of sample GW13-29.

The only way to account for these observations is to hypothesize a three-phase mixture, whereby each sample consists of a different mass fraction of the three end-member phases. Considering the steps most closely matching the Ca-free stoichiometry of biotite, i.e. those with Ca/K < 0.001, it becomes evident that there is none in sample GW13-28, one in sample GW13-29B and four in GW13-29. As the micas are fine grained and intergrown with their retrogression products at a scale <10 μm, even hand-picking cannot achieve a monomineralic separate. In terms of chronological information from biotite, this unexpected observation can be used advantageously, as follows from Figure 5.1c. The three biotite separates show a similar V-shaped trajectory as in Figure 5.1b. The interpretation in terms of a mixture of at least three phases is upheld: the alteration phase(s) having step-ages up to 16 Ma and high Ca/K and Cl/K are most abundant in sample GW13-28. The mica-1 age–Ca/K trend gives an apparent age >16 Ma. This apparent age is likely to be geologically meaningless due to several possible artefacts pertaining to the presence of an alteration phase, such as the decoupling of ^{40}Ar and recoiled ^{39}Ar during the degassing of fine biotite–chlorite intergrowths (Di Vincenzo et al., 2003). Clear evidence for the massive chloritization of biotite GW13-28 is provided by its bulk K concentration of 4.61%, as calculated from the total ^{39}Ar concentration. This low value attests to a clear chloritization of biotite in this separate. Even if the chronological information provided by GW13-28 is meaningless per se, it can provide two kinds of constraint. First, the trend defined by the chloritized biotite shows a shallow slope in the Cl/K v. Ca/K diagram. The observation of a different trend in biotite GW13-29B (higher Cl/K and low, biotite-like Ca/K) suggests the presence of a different biotite generation with a different composition. The second type of constraint provided by chloritized biotite GW13-28 is that it can act as a useful end-member on the effect of alteration for the other two biotite separates, which are much less altered, but not negligibly so. Indeed, in Figure 5.1c the biotite separates GW13-29 and 29B follow the same pattern as in Figure 5.1b, with one branch of the V-shaped trajectory pointing towards GW13-28. The four steps from GW13-29 (Fig. 5.1d) corresponding to the lowest Ca/K ratios, i.e. most closely approximating the biotite stoichiometry, gave an isochron age of 9.07 ± 0.60 Ma (2σ uncertainty) with an atmospheric intercept. The atmospheric intercept allows us to consider the average age of these four steps as a legitimate isochemical age (Müller et al., 2002) of 9.00 ± 0.10 Ma. Strictly speaking, this is a cooling age, as the retention of Ar by biotite is complete only below c. 530°C (Villa, 2015). What is most important here is that biotite-2 formed several million years earlier than muscovite-3.

In contrast with the biotite concentrates, all muscovite separates gave significantly younger ages between c. 6 and 7 Ma. The age spectra are discordant (Fig. 5.2a) but less so than the biotite age spectra. Muscovite from GW13-28 (the sample with the most altered biotite) shows the most disturbed spectrum with some step-ages <5 Ma, the high Cl/K of which clearly identifies them as the degassing of alteration phases (Fig. 5.2a). GW13-29B, with the best-preserved biotite, also shows the least discordant muscovite spectrum. Common regression of the data for muscovite from GW13-29 and -29B in a single Cl/K age diagram, justified by their spatial proximity (<1 m) and compositional similarity, reveals a negative correlation (Fig. 5.2b): a relatively Cl-rich mica with an age ≤5.88 ± 0.03 Ma and a Cl-poor mica >7 Ma old.

An age difference between older biotite and younger muscovite in similar rocks was also observed by Mottram et al. (2015) in samples from the MCTz from Sikkim. Mottram et al. (2015) seem to accept that the retention of Ar in muscovite is fairly high, even if an ambient temperature of 600°C was maintained over several million years, as already documented by Di Vincenzo et al. (2004), Allaz et al. (2011) and Villa et al. (2014, p. 817). However, the discussion in Mottram et al. (2015), based purely on the assumption of thermally activated Fick's law diffusion, is internally contradictory because it does not explain why biotite is reproducibly older than muscovite, in contrast with micas from terrains affected by a static monometamorphic event (e.g. Allaz et al., 2011 and references therein). The exclusive focus on Ar diffusion under the assumption of a static system also forfeits the opportunity to examine the microstructures and microchemistry, and to correlate both with mica ages. Regarding Ar retention in micas, Villa et al. (2014) observed complete, or nearly complete, Ar retention in 100 μm sized phengite in metamorphic terranes at >500°C.

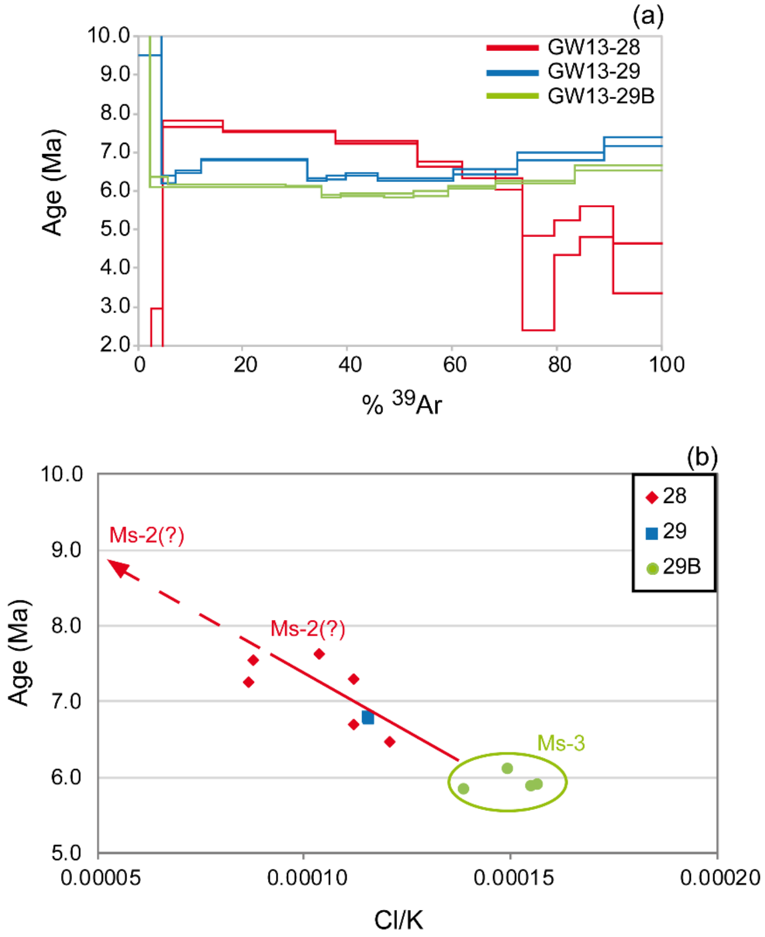

Figure 5.2. (a) ^{40}Ar/^{39}Ar age spectra of muscovite comparing the three samples of the Vaikrita Thrust. (b) Age vs Cl/K correlation diagram reveals a negative correlation between a Cl-rich mica, representing the coronitic muscovite, and a Cl-poor one, possibly representing muscovite along the S_m. Ms-2 – muscovite along the S_m; Ms-3 – coronitic muscovite after garnet.

Villa (2015) went on to interpolate the retention of Ar in static, monometamorphic biotite and derived a revised Ar ‘closure temperature’ estimate of c. 530°C, in good agreement with the scarce reliable experimental data (see Villa 2010, 2015). This Ar retentivity is at the lower end of the estimated temperature interval for our Garhwal samples. The implication is that biotite records ages that are not much younger than the metamorphic event at temperatures recorded by Ti-in-biotite and Ti-in-muscovite thermometers. The 9.00 ± 0.10 Ma isochemical age is therefore a cooling age close to the growth of biotite-2 in sample GW13-29. A fortiori, the 6 Ma age, inferred from the muscovite correlation diagrams, reflects the static growth (especially considering the updated diffusivity data for muscovite; Villa et al. 2014) of muscovite-3 during the subsequent exhumation. Selective sampling bias due to hand-picking could account for the observation of Figure 5.2b, in which an anticorrelation between two clusters is seen in the Cl/K v. age diagram: muscovite from sample GW13-28 is older and has lower Cl/K (red dots), whereas younger muscovite from samples GW13-29 and GW13-29B has higher Cl/K (blue and green dots). Mixing relatively Cl-rich static muscovite-3 with Cl-poor muscovite-2 yields a good anticorrelation of age and Cl/K ratio; the age of the foliation-parallel muscovite-2 is higher or equal to the oldest step, in the present case 7.6 Ma. By extrapolating the correlation trend towards lower Cl/K values, it is possible to infer a muscovite- 2 age matching the biotite-2 age of 9 Ma by assuming Cl/K = 5×10^{-5} for muscovite-2. The age of static mica growth is under-constrained and we can only argue that it was less or equal to the lowest step-age of 5.88 ± 0.03 Ma showing the Ca/Cl/K signature of bona fide muscovite.

5.1.2 South Tibetan Detachment System (*GW13-39, GW13-51, GW13-57*)

5.1.2.1 Data discussion and interpretation

In the Cl/K-Ca/K common-denominator correlation diagram the first heating steps have high Ca/K and high Cl/K ratios, which monitor the degassing of calcium-rich extraneous phases. At higher oven temperatures, Cl/K and Ca/K ratios reach a minimum and remain nearly constant (Fig. 5.3a,b,c; Supplementary Material Appendix 2). As the stoichiometry of mica is Ca-free, we take the low Ca/K ratios as evidence that muscovite sensu stricto was being degassed. The broadly "isochemical" portion of the Ar release includes 7 steps in sample GW13-51, 6 steps in GW13-57, and 6 steps in GW13-39 (which account for 65, 72 and 74 % of the ^{39}Ar release, respectively). In the following we will also consider a narrower definition of "isochemical" (see below). The presence of extraneous phases is diagnosed from the excessively high Ca/K and/or Cl/K signatures. Thus we can observe (Fig. 5.3d,e) that step ages are positively correlated to the Ca/K ratio, and negatively correlated to the Cl/K ratio (Supplementary Material Appendix 2), and attribute the steps with anomalous chemical signatures to the degassing of extraneous (probably alteration) phases. Their step ages will not be considered further. The case of GW13-39 (Fig. 5.3f) is different, in that the statically grown mica is undeformed and probably records rapid formation. The variations of the Ca/K ratio are not mirrored by age variations. It could be speculated that a slightly margaritic white mica grew contemporaneously to a nearly endmember muscovite (neither composition has a sufficiently high Ca concentration to be resolved by electron microprobe, Tables 4.2). The age spectra are shown in Figure 5.3g,h,i. Sample GW13-39 yields the youngest isochemical age of 14.36 ± 0.06 Ma (with MSWD = 0.87), defined by steps 4-8. The isochron through the same five steps gives an age of 14.31 ± 0.09 Ma, an atmospheric intercept of 299.7± 1.8, and MSWD = 0.74. Sample GW13-57 yields an isochron age (on steps 3-9) of 15.7 ± 0.3 Ma with $(^{40}\text{Ar}/^{36}\text{Ar})_i = 302 \pm 3$, MSWD = 1.8. The isochemical age on the three steps with the lowest Ca/K ratio is 16.0 ± 0.5 Ma. The Ca/K ratio is positively correlated with the step ages (Fig. 5.3e). By extrapolating the linear trend to zero Ca (the theoretical stoichiometry of muscovite), the age of c. 16.0 Ma is confirmed. Sample GW13-51 is the most deformed sample and yields an isochemical age (on steps 7-10) of 16.46 ± 0.06 Ma (MSWD = 1.0). The isochron age is 16.8 ± 0.7 Ma, ($^{40}Ar/^{36}Ar$)i = 285 ± 30, MSWD = 2.7.

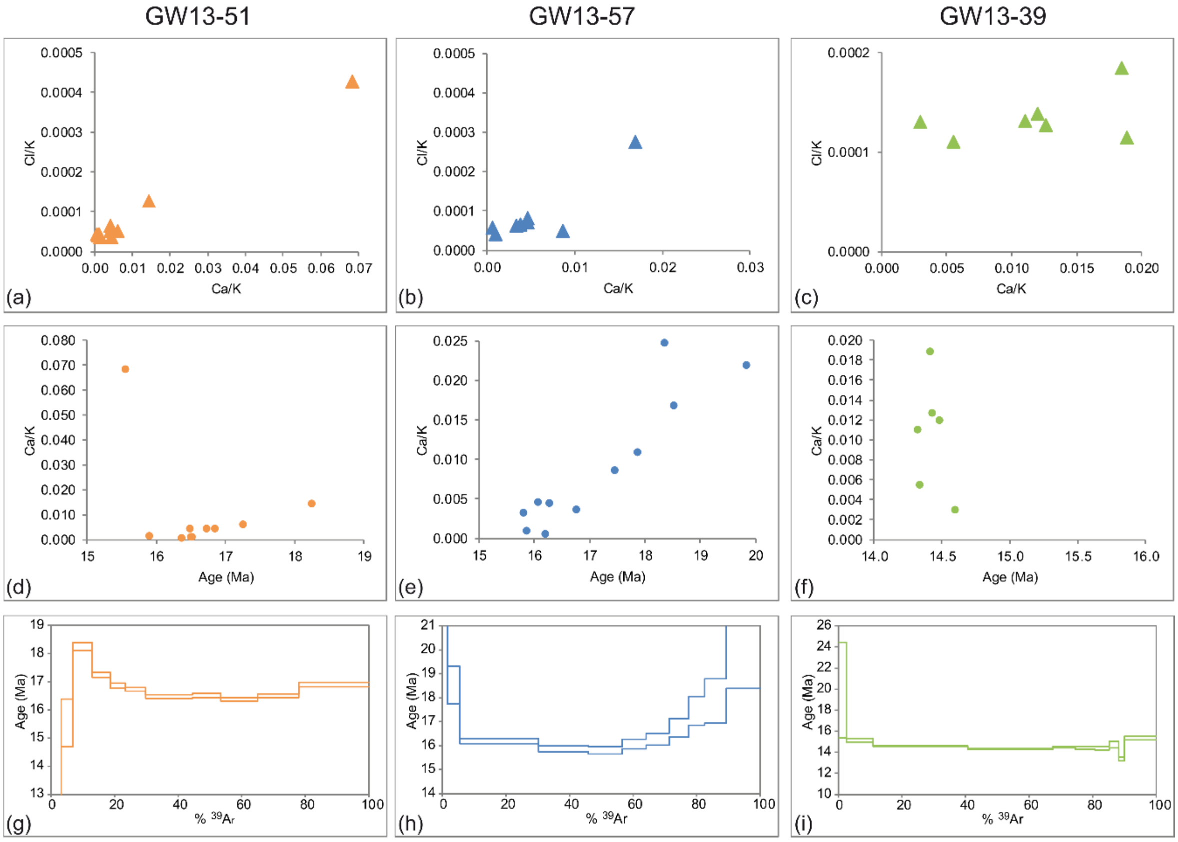

Figure 5.3. Cl/K vs Ca/K diagrams (a,b,c), Ca/K vs age diagrams (d,e,f) and $^{40}Ar/^{39}Ar$ age spectra (g,h,i) of muscovite from sample GW13-51, GW13-57 and GW13-39.

5.2 Bhagirathi – Gangotri valley

5.2.1 Main Central Thrust zone (*UT15-5, UT15-6, UT15-9, UT15-10*)

For both Munsiari and Vaikrita Thrusts we prepared biotite and muscovite separates with different degrees of purity in order to quantify the bias given by fine-grained intergrowths (Figs. 4.20, 4.21, 4.22) of impurity phases, which make 100% mica purity unattainable. Ar Differential Release Plots (DRP) discriminate the in vacuo structure collapse of micas *sensu stricto* from that of impurities (cf. Villa et al., 2000). Combining Ca/Cl/K signatures with DRP robustly identifies the isochemical step ages pertaining to the mica generation that dates deformation.

If only the discordant age spectra are considered, disregarding all of the remaining information provided by ^{39}Ar-^{40}Ar systematics, the microstructurally complex MCTz rocks are apparently puzzling, leading to misunderstanding in the interpretation of Ar/Ar age spectra that are intra and inter-sample discordant. For the first time in the interpretation of such complex data of pervasively sheared rocks from shear zones, we adopted a new innovative approach to unravel the geochronological information of rocks showing multiple generations of fine-grained foliations. The procedure consists of preparing separates with different degrees of purity to quantify the bias given by fine-grained intergrowths and, combining Ca-Cl-K signatures of the isochemical steps with Argon DRP discriminate between the structure collapse of micas *sensu stricto* and that of impurities. Such procedures allow identification of the step ages reliably dating deformation: only the isochemical steps that correspond to the degassing of “real” micas have been considered for the calculation of the ages that pertain to the activity of shear zones.

5.2.1.1 Data discussion and interpretation

All age are given with 2σ uncertainty. As expected when dating mixtures of diachronous minerals (Villa & Williams, 2013; Villa & Hanchar, 2017) the spectra of both Munsiari and Vaikrita Thrust separates (Fig. 5.4 and 5.5) are internally discordant.

For the Munsiari Thrust, in sample UT15-5 the two analyzed separates (bt and bt+ms) are rather pure biotite (as indicated by the correspondence between peaks in DRP) testifying that few muscovite crystals were in the mixture (bt+ms). In sample UT15-6 the observed degassing of the impure mixture clearly distinct from that of the pure biotite, is that the additional phase(s) present in the separate give rise to an additional degassing peak, often (but not necessarily always) at higher T than the biotite peak (c. 700 °C). The degassing peak of muscovite around 850 °C is present but small, supporting that muscovite is not a major contributor of the Ar in the mixture. Combining the chemical signature (Ca/Cl/K ratios closer to the stoichiometry of micas, Fig. 5.4) with the temperature interval of the in vacuo structure collapses most reliably identifies degassing of mica *sensu stricto* structure and deconvolves it from that of contaminant phases. We obtain the isochemical ages of 4.81 ± 0.02 Ma and 4.89 ± 0.04 Ma for bt and bt+ms separates from UT15-5 respectively; and 4.78 ± 0.02 Ma and 5.46 ± 0.26 Ma for bt and bt+ms separates of UT15-6.

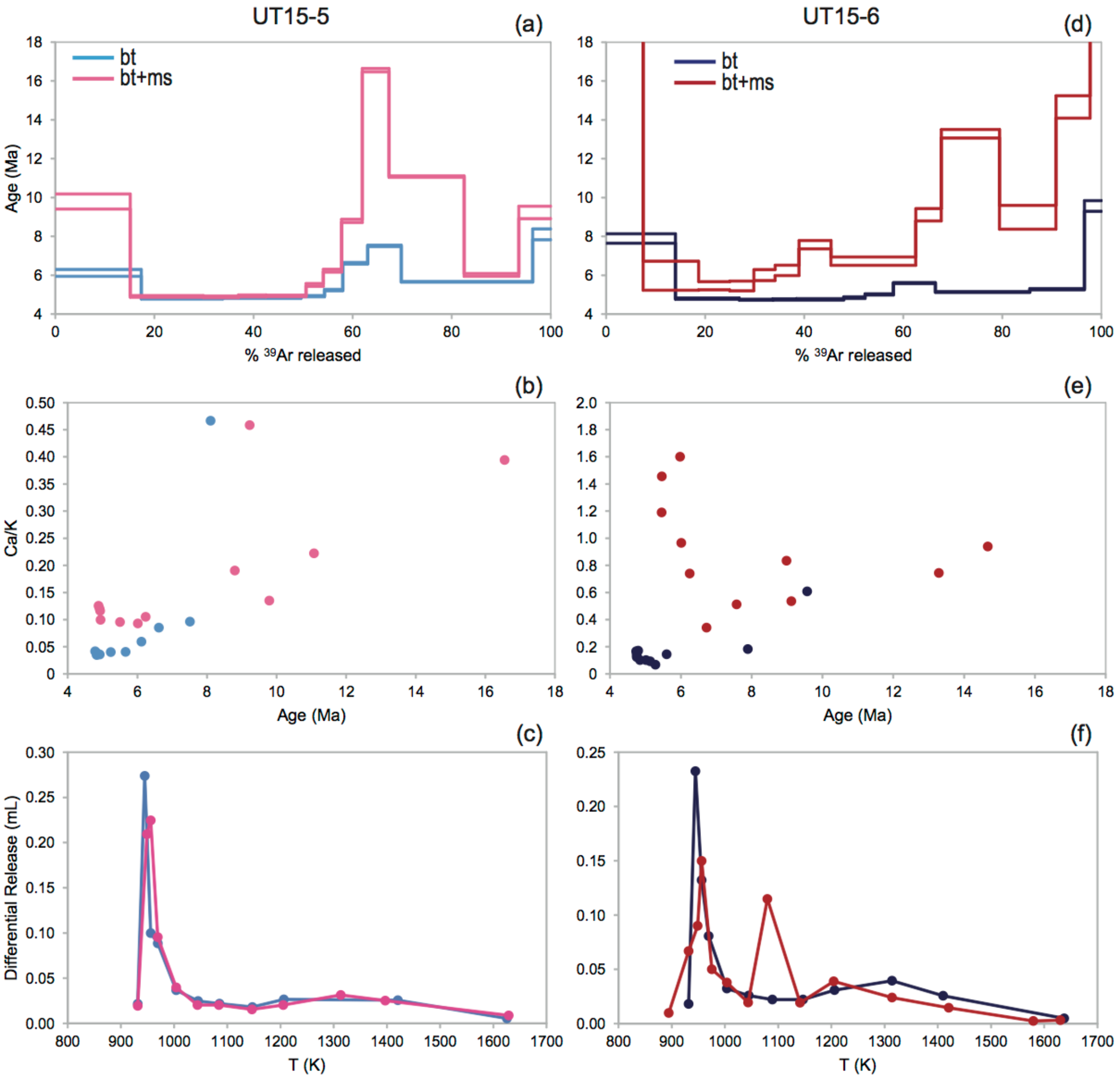

Vaikrita Thrust samples are characterized by a significant chloritization (see EPM analyses), which is well discernible in the DRP from pure muscovite separates (Fig. 5.5c,f). For sample UT15-9 we prepared three separates, i.e. ms, ms+chl, chl; for sample UT15-10 we prepared ms2 and ms3. The chlorite degasses distinctly before pure muscovite in both UT15-9 and UT15-10 (Fig. 5.5c,f).

The steps in UT15-9 and UT15-10 that identify muscovite *sensu stricto* are those with the lowest Ca/K and Cl/K ratios. The isochemical age derived from ms and ms+chl separates of UT15-9 are 4.56 ± 0.04 Ma and 5.52 ± 0.06 Ma, respectively. We use the chl separate to test the method and observe that effectively the chlorite degasses distinctly before muscovite in all separates. This observation allow identifying the reliable steps also in sample UT15-10, in which we micro-drilled S2 and post-S2 domains.

Figure 5.4. ^{40}Ar/^{39}Ar spectra, Ca/K vs age diagrams and DRPs for Munsiari Thrust samples UT15-5 (a,b,c) and UT15-6 (d,e,f).

For ms2 separate of sample UT15-10 we observe two groups of steps with different Ca/K and Cl/K signatures: a relatively Cl-rich cluster (steps 5-7) and a Cl-poor one (steps 8-10). In ms3 separates steps 7-9 show the same chemical signature of steps 5-7 of ms2 separate, which therefore includes an amount of ms3. The age of ms2 is 8.17 ± 0.06 Ma, whereas the age of ms3 is 7.44 ± 0.12 Ma. The dip corresponding to step 6 in Figure 5.5f between the highest degassing peaks 5 and 7 may be due to prolonged heating time of step 6 with respect to the others, as it becomes less prominent when the division by $t^{1/2}$ is omitted.

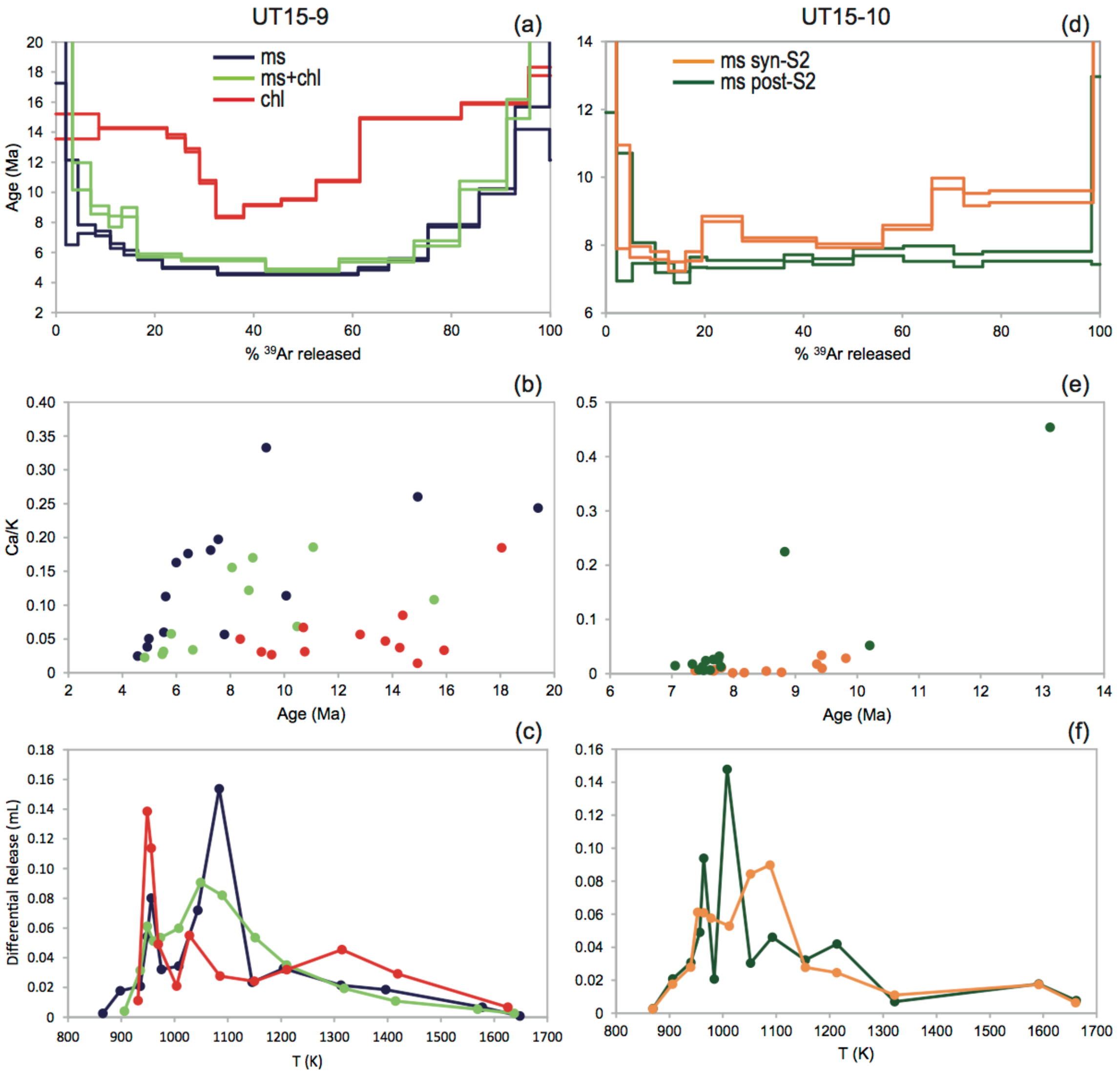

Figure 5.5. ^{40}Ar/^{39}Ar spectra, Ca/K vs age diagrams and DRPs for Vaikrita Thrust samples UT15-9 (a,b,c) and UT15-10 (d,e,f).

5.2.2 Bhagirathi Granite (*UT15-41, UT15-51*)

Muscovite from samples UT15-41 and biotite from UT15-51 have been selected for ^{40}Ar/^{39}Ar stepheating dating. The spectra and correlation diagrams are reported in Figure 5.6, the data in Supplementary Material (Appendix 2).

5.2.2.1 Data discussion and interpretation

The correlation diagrams are useful for detecting the presence of alteration phases, diagnosed by high Ca/K and Cl/K signatures and not considered further. As already pointed out, as the stoichiometry of mica is Ca-free, only steps with low Ca/K ratios have been considered to calculate the isochemical age, in which of mica *sensu stricto* was being degassed.
Muscovite of sample UT15-41 yields an isochemical age of 18.17 ± 0.02 Ma defined by steps 8-9 (those with the lowest Ca/K and Cl/K ratios) giving a plateau with a 44% of ^{39}Ar release.
The same criteria in the selection of steps for the age calculation have been applied to UT15-51 biotite sample, yielding an isochemical age of 18.69 ± 0.02 Ma (steps 8-9, which account for 30% of ^{39}Ar release).

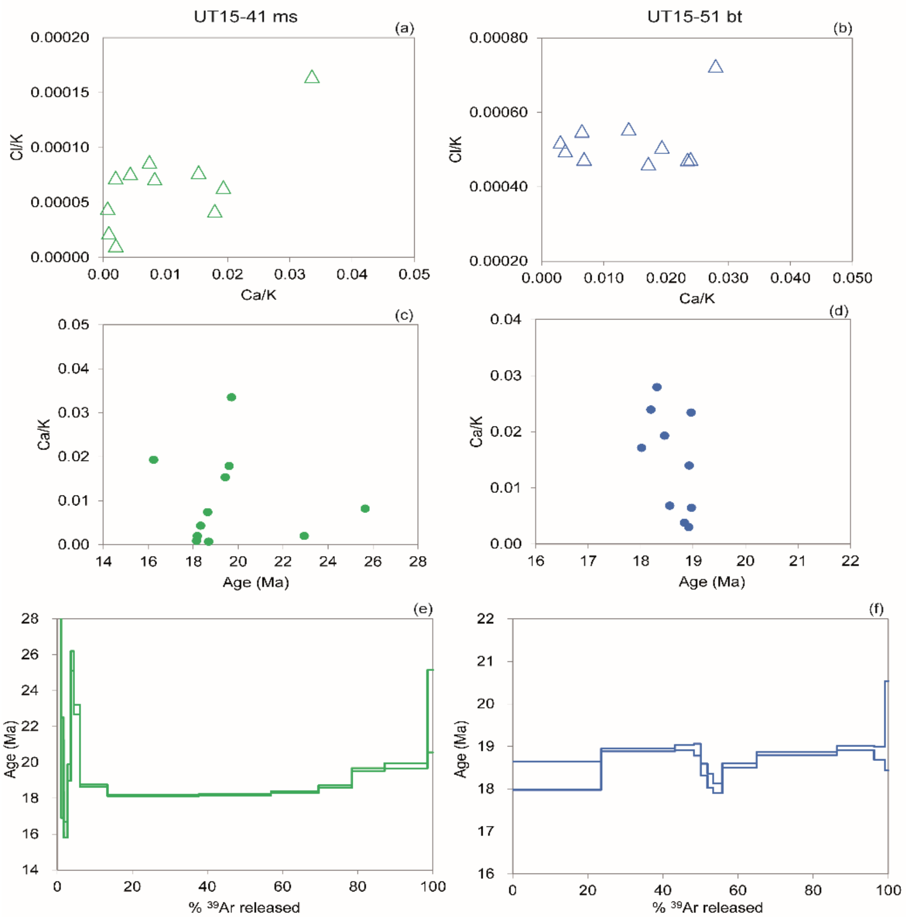

Figure 5.6. Cl/K vs Ca/K diagrams (a,b), Ca/K vs age diagrams (c,d) and ^{40}Ar/^{39}Ar age spectra (e,f) of muscovite from sample UT15-41 and UT15-51.

5.3 Lower Alaknanda valley (*AK18-5, AK18-13, AK18-23, AK18-26, AK18-42*)

The Ar DRP for all samples are reported in Figure 5.7. The first observation is that a good intra-sample correlation is present and confirmed by the overlap of the first degassing peak in each sample. Spectra, correlation diagrams and Ar DRP are reported in Figures 5.8 and 5.9. The full Ar-Ar dataset is reported in the Supplementary Material Appendix 2.

5.3.1 Data discussion and interpretation

AK18-5 muscovite yields an age of 6.22 ± 0.02 Ma, obtained on step 6 showing the lowest Ca/K ratio and DRP peak (Fig. 5.8b-c). The homogeneous chemical signature of the sample is mirrored in the correlation diagram (Fig. 5.8b) but in DRP the first degassing peak (step 2) does not pertain to muscovite as it overlaps with collapses of biotite of other samples, even if this quartzite contains no macroscopic biotite phenocrysts (see Chapter 4).

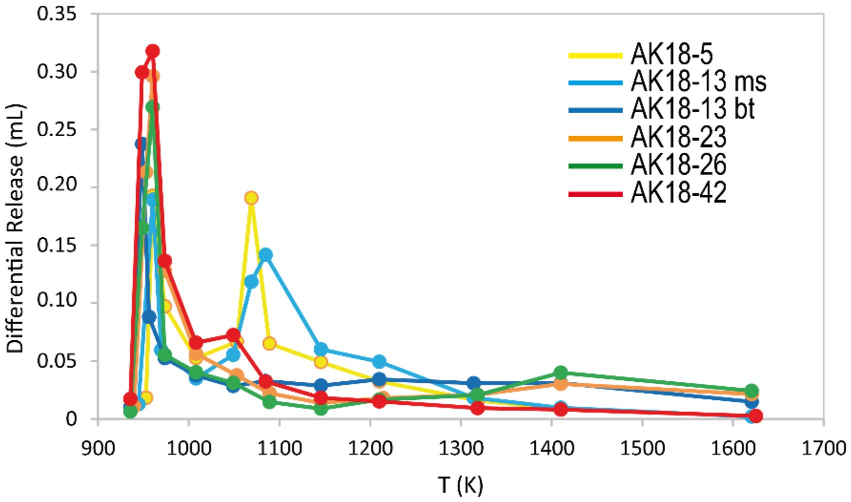

Figure 5.7. Ar DRP for AK samples.

The X-ray element maps of muscovite AK18-13 (Fig. 4.27) demonstrate a very fine-grained intergrowth with Mg-rich biotite. This corresponds to the information provided by the DRP, which exhibits a first degassing peak around 950 K (identical to the coexisting biotite in the same sample) and a second Ar release peak around 1100 K (typical of the other muscovite samples from the AK18 collection; Fig. 5.9). Correspondingly, step 2 (i.e. the step with the highest differential Ar release) has a Cl/K ratio typical of the range of the other AK18 biotite samples, whereas step 7 (corresponding to the second Ar release peak) has the low Cl/K ratio typical of all muscovite samples analyzed here. Step 7 yields an age of 5.31 ± 0.02 Ma (Fig. 5.9). Biotite AK18-13 proves to be more complex. As is evident from the textural relationships (Fig. 4.26c), biotite is a relict phase.

The attempt to match the DRP peak with the Ca/Cl/K signature most closely approaching stoichiometry does not yield an unambiguous age: the DRP peak yields an age of 24 Ma, whereas the lowermost Ca/K ratio corresponds to an age of 14 Ma. This may suggest that the relict biotite is not monogenetic; establishing its detailed prehistory exceeds the purpose of the present study. More complexities of the relict biotite generation(s) are suggested by the high but discrepant ages of biotite samples AK18-23 and -26, c. 30 and 50 Ma, respectively. These samples are not pervasively recrystallized and isotopically reset, and therefore preserve old chemical and chronological signatures. In biotite AK18-42 the DRP and Ca/K signature are matching in identifying step 3 as the closest to biotite *sensu stricto*, assigning it an age of 9.78 ± 0.12 Ma (Fig. 5.8).

A better age resolution of the Mica1-Mica2-Mica3 sequence would require additional sampling, now that the main interpretive difficulties are recognised.

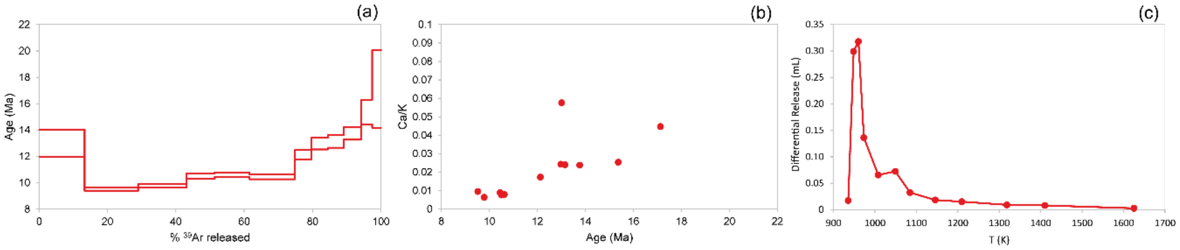

Figure 5.8. $^{40}Ar/^{39}Ar$ spectra, Ca/K vs age diagram and DRP for sample AK18-42.

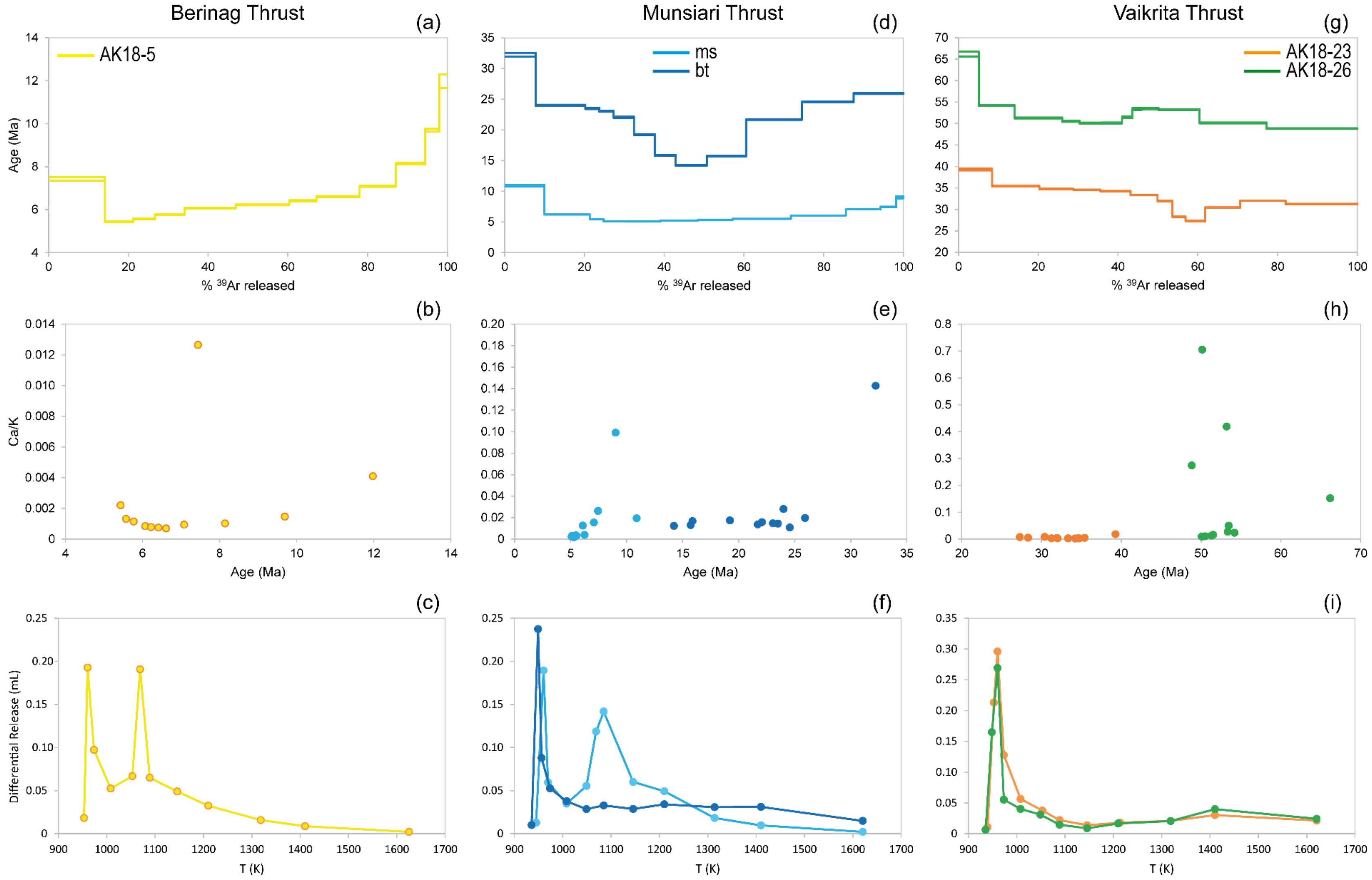

Figure 5.9. ^{40}Ar/^{39}Ar spectra, Ca/K vs age diagrams and DRPs for Berinag Thrust sample AK18-5 (a,b,c), Munsiari Thrust sample AK18-13 (d,e,f) and Vaikrita Thrust sample AK18-23 and AK18-26 (g,h,i).

6. MICROSTRUCTURAL STUDIES ON THE LOWER MAIN CENTRAL THRUST ZONE

6.1 Deformation temperature and Crystallographic Preferred Orientation

In order to assess the deformation temperatures and the Crystallographic Preferred Orientation (CPO) of quartzites from the lower portion of the MCTz, the fabric and the opening angle of quartz *c*-axis fabric has been optically measured for quartzite samples GW13-19 and GW13-20 (Fig. 4.25). Unfortunately, not suitable samples from the upper part of the MCTz and from the GHS have not been found. Locations of samples, coming from the lower Alaknanda Valley, are reported in Figure 4.1. As deformation features in such quartzites are difficult to recognize in the field and also because they show lithological affinity with LHS quartzites (Jain et al., 2014), CPO analysis is necessary to unravel ductile shearing deformation in these rocks.

In Figure 6.1 are reported the fabric diagrams and in Figures 6.2 and 6.3 the graphs of quartz *c*-axis fabric opening angles versus estimated deformation temperatures.

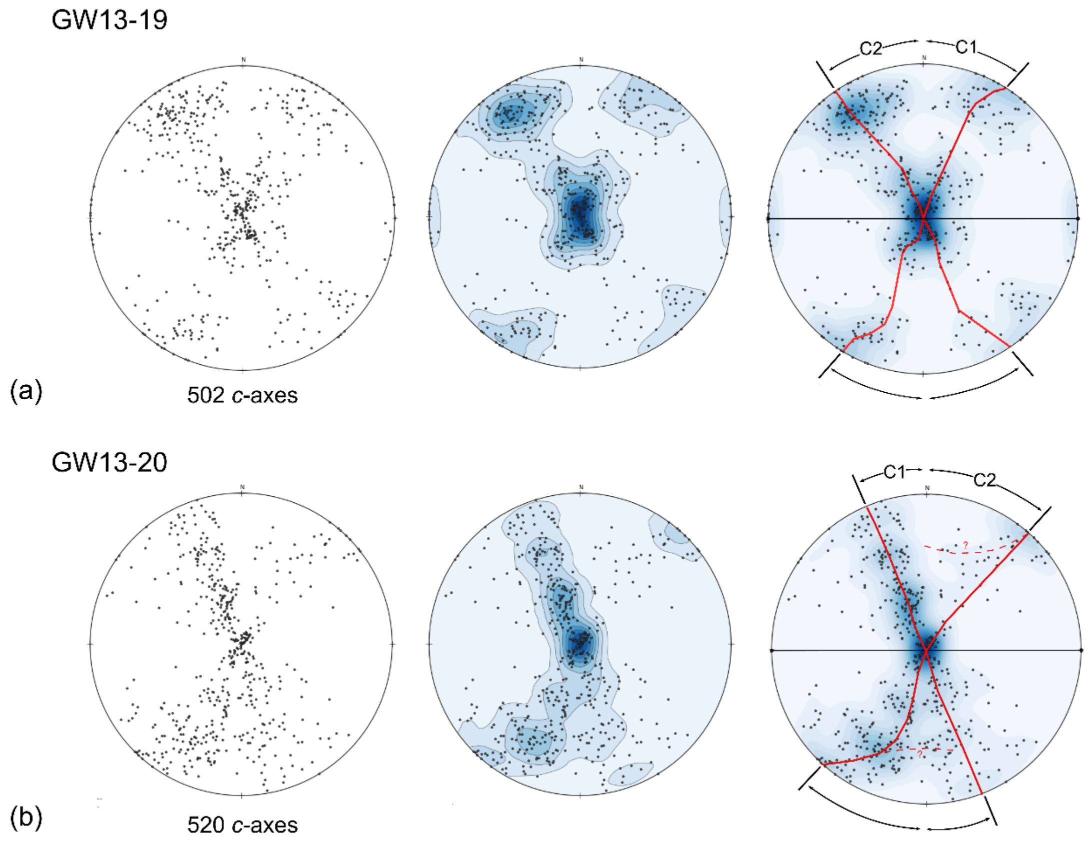

Figure 6.1. Optically measured quartz c-axis fabrics for sample (a) GW13-19 and (b) GW13-20. Mineral lineation is oriented horizontal and foliation left – right and vertical. Sample location is shown in Figure 4.1. Left hand diagrams show point data, central diagrams contoured data, and right hand diagrams fabric skeleton (red lines), which is generally used to help defining fabric opening-angle (measured in plane containing stretching lineation and pole to foliation).

Thin sections were cut perpendicular to foliation and parallel to lineation. The orientation of the lineation is N030, 30NE in both samples.

6.1.1 Data discussion and interpretation

In this section, data will be discussed and deformation temperatures inferred from Kruhl (1998) original thermometer will be compered to those obtained from the Faleiros et al. (2016) two-stage linear thermometer.

In GW13-19 the fabric diagram is a type-I cross girdle of Lister (1977) approximately in plane strain (k=1) with an opening angle of 64°, suggesting a temperature of deformation of 508 °C following the thermometer proposed by Kruhl (1996). Basal <a> and prism <a> represent the more abundant active slips, nevertheless some prism <c> slips occur (Fig. 6.2). The two-stage linear thermometer of Faleiros et al. (2016) indicates deformation temperature of 490 °C for this sample, that is about 20 °C lower inferred temperature than using the original Kruhl (1996) thermometer.

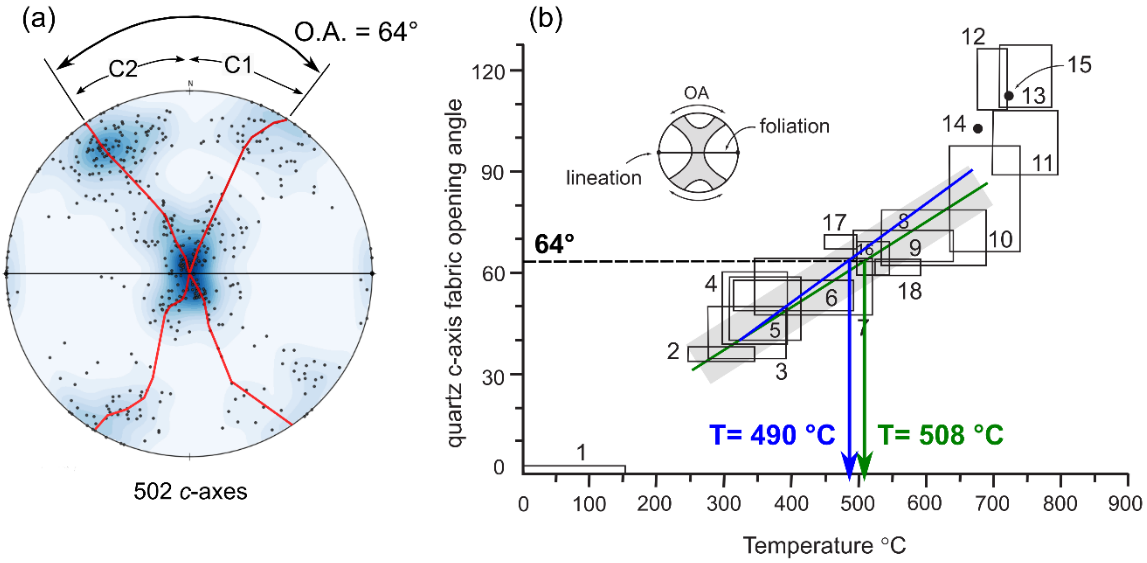

Figure 6.2. (a) GW13-19 optically measured quartz *c*-axis fabric and (b) estimated temperature following Kruhl (green line) and Faleiros et al. (blue line) thermometers (modified after Law et al., 2004).

In GW13-20 the fabric diagram is a type-I cross girdle of Lister (1977) approximately in plane strain (k=1) or slightly into constrictional strain field (k>1). The asymmetry of the fabric allows to infer a top-to-the-SW shear sense. The 63° opening angle suggests a temperature of deformation of nearly 500 °C. As in the companion sample, basal <a> and prism <a> are the more abundant active slip systems (Fig. 6.3). The two-stage linear thermometer of Faleiros et al. (2016) indicates deformation temperature of 483 °C for this sample, that is about 20 °C lower inferred temperature than using the original Kruhl (1996) thermometer, as in the companion sample GW13-19.

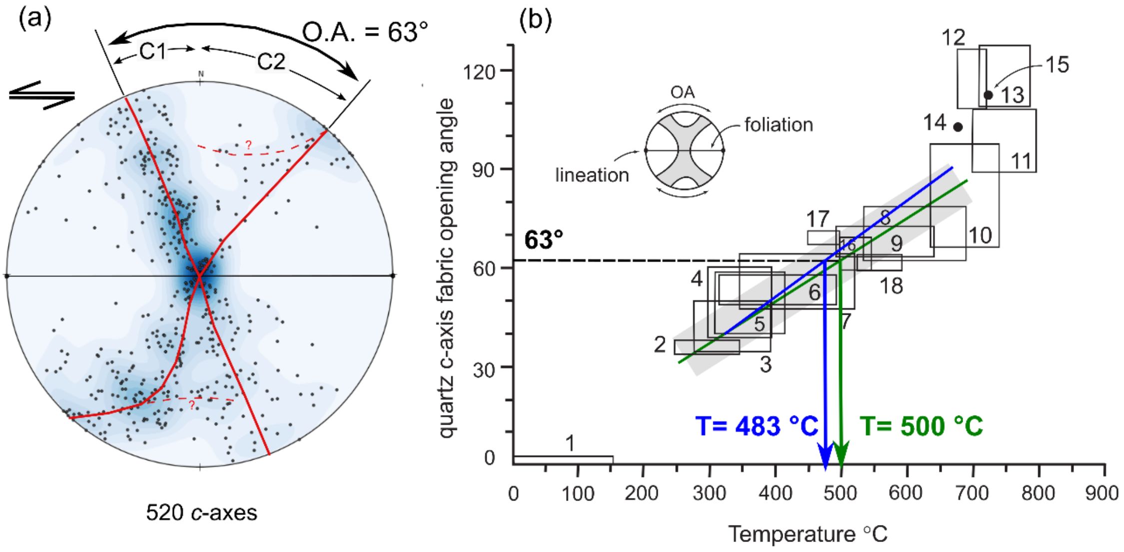

Figure 6.3. (a) GW13-20 optically measured quartz *c*-axis fabric and (b) estimated temperature following Kruhl (green line) and Faleiros et al. (blue line) thermometers (modified after Law et al., 2004). Leading edge is inclined at lower angle (C1) than the trailing edge (C2), giving a defined top to the left (SW) shear sense.

For these opening angles the estimated temperatures from the Kruhl (1996) and Faleiros et al. (2016) thermometers are of course identical within the uncertainty of ± 50 °C. In general, the differences between these deformation temperature estimates get progressively larger with increasing opening angle.

Quartz recrystallization microstructures (Chapter 4, Fig. 4.25) clearly indicate the dominance of GBM recrystallization in quartzite GW13-19 and GW13-20, suggesting a deformation temperature around 500 °C, coherent with temperature estimates inferred from deformation thermometry. The obtained temperatures are also in agreement with pseudosection multi-equilibrium thermobarometry in a close sample (GW13-16) studied by Iaccarino et al. (submitted to JGM) who reported a temperature of 505 ± 15 °C (and a pressure of 0.63 ± 0.7 GPa) close to peak metamorphic conditions. Montemagni et al. (2016) also reported similar *PT* conditions (i.e. 500-520 °C, 0.50-0.53 GPa) based on early fluid inclusions in quartz sigmoids from the Munsiari Thrust (sample GW13-14) in this area.

6.2 Kinematic vorticity estimates

The theory of the stable porphyroclasts method relies on the fact that in a general shear flow porphyroclasts are partitioned into two populations. One rotates continuously and therefore does not develop a preferred orientation, the other aligns along a minimum energy position ("stable sink” position of Jessup et al., 2007). The stable orientation analysis has yielded vorticity estimates (Xypolias, 2010 and references therein) to deduce large-scale tectonics of shear zones (Li & Jiang, 2011 and references therein) from different tectonic settings (Xypolias, 2010; Fossen & Cavalcante, 2017). However, severe limitations arise because a complex three-dimensional problem, the motion of rigid clasts, is reduced to its two-dimensional section or projection in the plane of the thin section (Tikoff & Fossen, 1995; Iacopini et al., 2011; Li & Jiang, 2011; Mancktelow, 2013). We addressed the loss of dimensionality information by employing X-ray micro computed tomography (X-ray microCT), a non-destructive technique used since the 1990s in different fields of geological sciences to image a rock sample in three dimensions (Denison & Carlson, 1997; Denison et al. 1997; Ketcham & Carlson, 2001).

X-ray microCT produces stacks of 2D grey-scale value images (referred to as “slices”) that allows observation of the internal structure of a scanned object. As exhaustively reported in Denison et al. (1997), the contrast in an X-ray CT image is mainly caused by differences in X-ray absorption within the object due to variation in density and chemical composition. K-feldspar porphyroclasts and the matrix dominated by quartz appear generally lighter in color than biotite sheets (Fig. 6.4a, c, e), which define the main foliation. Mineral phases were identified by comparing grey-scale colored slices with grey values of the Back Scattered Electrons (BSE) images on polished thin sections (Fig. 6.4): the comparison between SEM data (compositions and BSE images) and corresponding microCT slices allowed a reliable identification of mineral phases. As quartz and K-feldspar display grey values that are close to each other, it is difficult to apply a segmentation. In order to process the image automatically, we applied a threshold value to the main foliation to highlight wrapped porphyroclasts, making them appear dark on segmented images (Fig. 6.4b, d, f). The stable porphyroclasts method requires processing the slices representative of the XZ plane of the strain ellipsoid. From 3D observation (Fig. 6.5a-b), for each clast we select the 2D slice in which the clast shows the maximum elongation (Fig. 6.5c) measuring the a and b axes together with the angle (θ) between the a axes and the main foliation. The isolation factor (Passchier, 1987; Ildefonse et al., 1992; Iacopini et al., 2011) was also evaluated also on the XY and YZ planes (Figs. 6.4c-f and 6.5) in order to discard porphyroclasts not suitable for vorticity estimates.

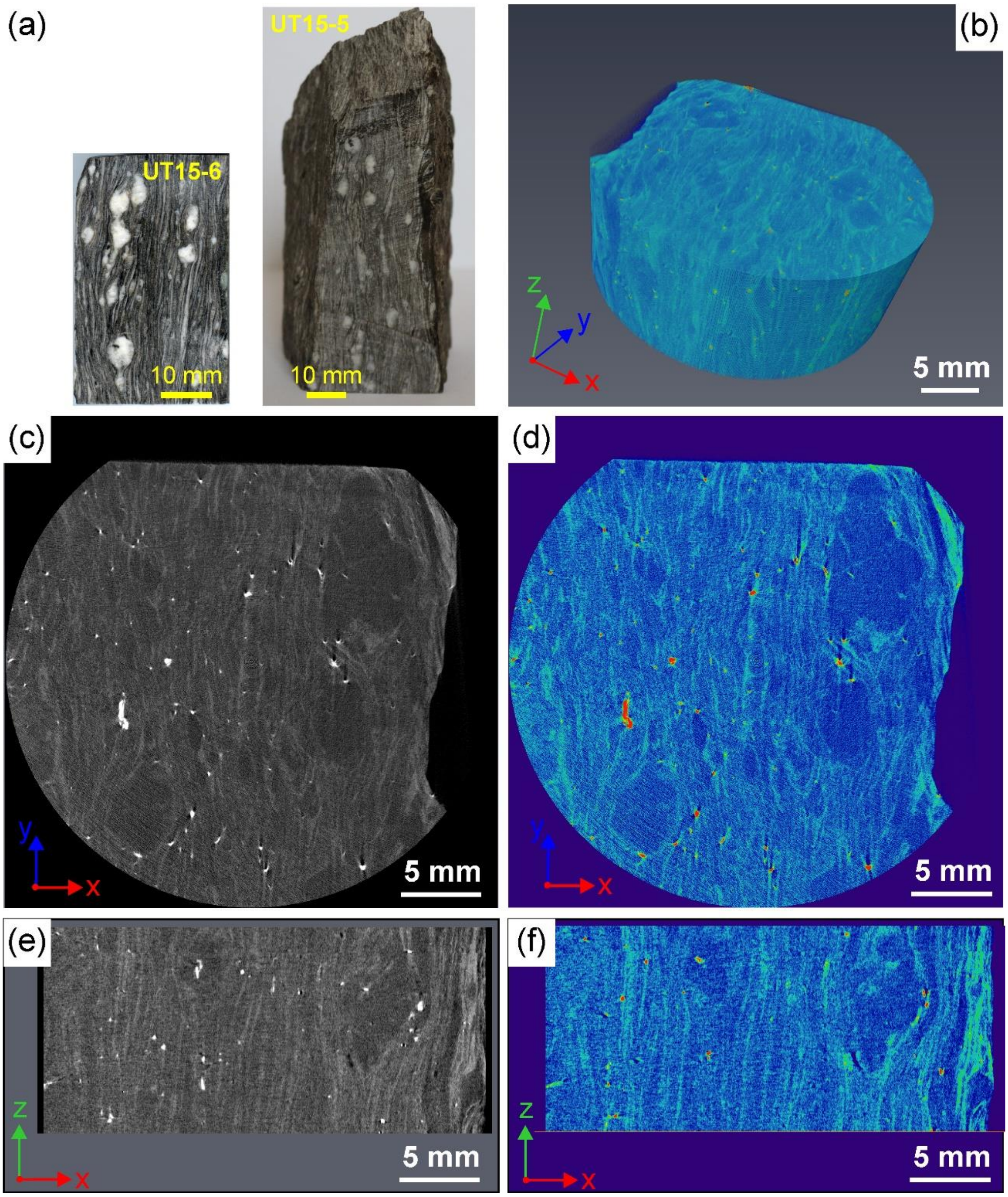

Figure 6.4. MicroCT processed images of sample UT15-5. (a) hand samples, (b), (d) and (f) threshold images, (c) and (e) grey-scale images. (b) 3D visualization of the sample; (c) and (d) visualization on the XY plane of finite strain ellipsoid; (e) and (f) XZ plane of finite strain ellipsoid.

The first and foremost consideration is that the use of microCT certainly increases the number of investigated clasts because hand samples are scanned (Fig. 6.4a): all clasts are evaluated. MicroCT minimizes the problems due to the isolation factor, as it becomes possible to only select the clasts that do not interact with each other.

Moreover, observation in three dimensions allows a more meaningful evaluation of the aspect ratios and radii of clasts, avoiding erroneous measurements that generate systematic errors in the vorticity evaluation (Iacopini et al., 2011).

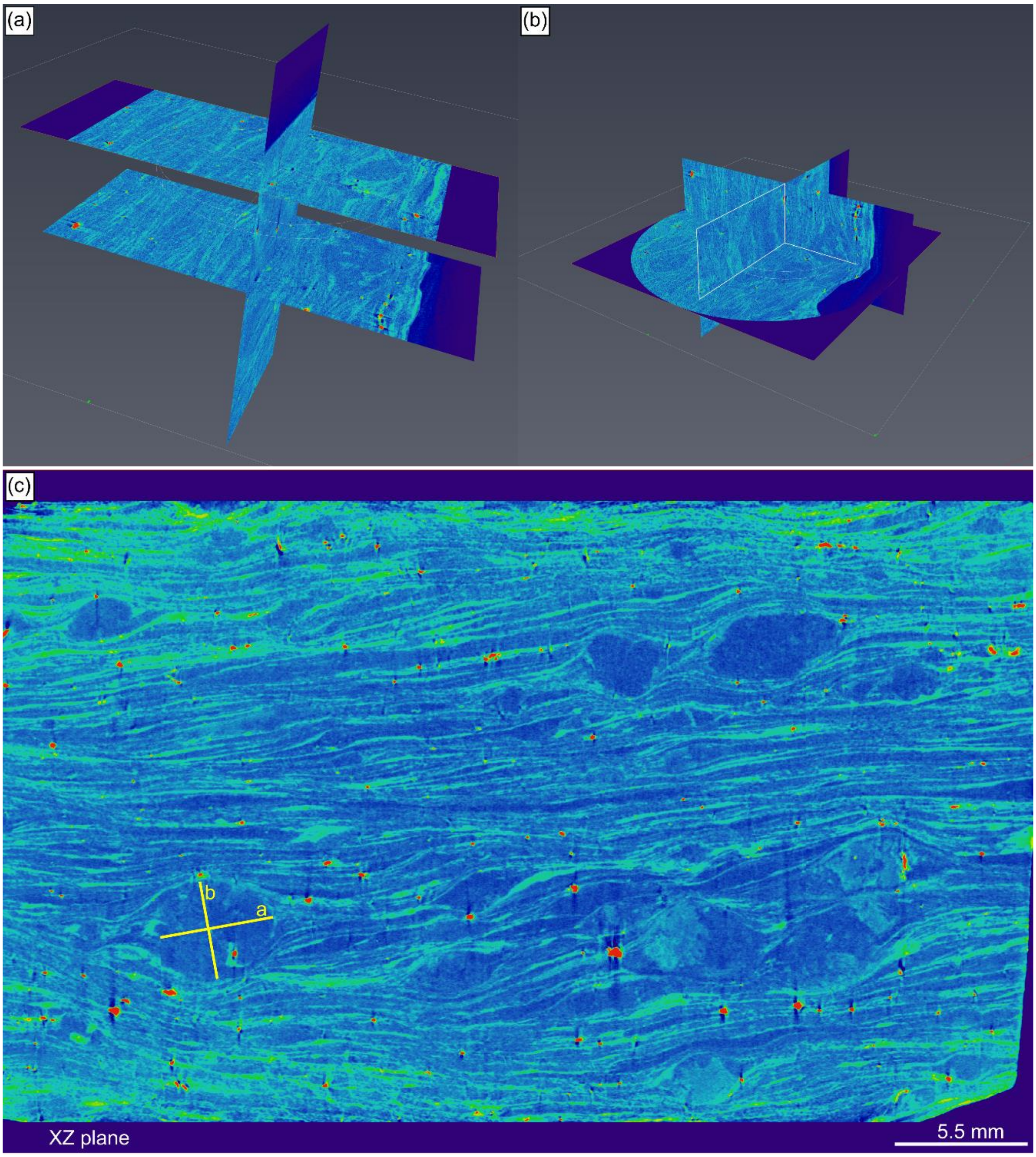

Figure 6.5. MicroCT processed images of sample UT15-5. (a) and (b) show the 3D visualization, (c) shows the 2D slice in which each clast exhibits the maximum elongation.

6.2.1 Data discussion and interpretation

X-ray microCT scanning was performed on the same two mylonitic orthogneisses from the Munsiari Thrust (Figs. 4.13 and 4.14), on which we obtained the ^{40}Ar/^{39}Ar ages of the mylonitic foliation. We analysed 152 and 32 porphyroclasts, ranging in size from 2.5 to 12 mm, from UT15-5 and UT15-6, respectively, to derive vorticity estimates (Fig. 6.6). The analysed sample volume was 130 cm^3 for UT15-5 and 10 cm^3 for UT15-6. We adopt the plot proposed by Wallis et al. (1993) and the Rigid Grain Net (RGN) plot suggested by Jessup et al. (2007), considering all porphyroclasts as tailless. Vorticity numbers range between 0.53-0.58 (Fig. 6.6a) and 0.49-0.57 (Fig. 6.6b-c) for UT15-6 and UT15-5, respectively, suggesting a strong pure shear component between 60-65 %.

For 2D vorticity estimates we selected 30 slices on the XZ plane corresponding to an area of about 30 thin sections. We analyzed 72 porphyroclasts to compare the 2D vs. 3D selection of clasts approach (Fig. 5b). Comparison of porphyroclast population distributions from sample UT15-5 obtained from whole 3D analyses (with microCT) and the one based on 2D sections is shown in Figure 5b. In the 2D approach the clasts distribution is different: i) clasts with the higher B* values and clasts with long axes at higher angles with respect to foliation are missing, ii) vorticity cannot be defined.

We want to stress that using the microCT we are able to evaluate all the clasts in the sample, avoiding those which do not meet the prerequisites of the method, otherwise not possible using classical thin section based analysis.

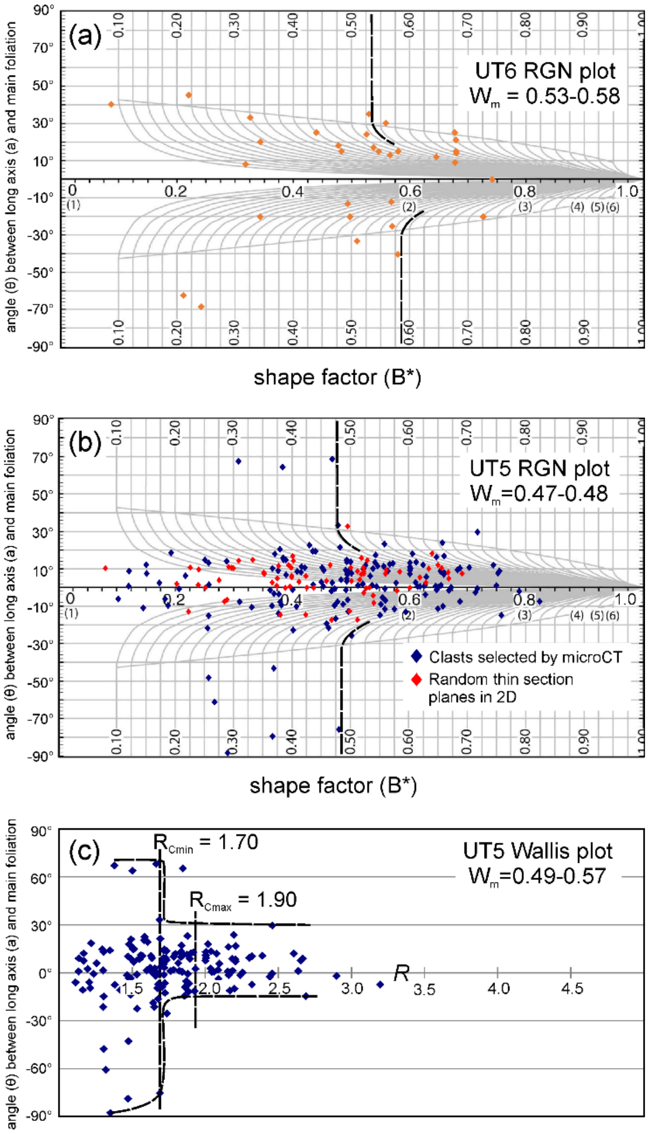

Figure 6.6. Results of the vorticity analyses using (a, b) the RGN plot of Jessup *et al*. (2007) and (c) the Wallis plot (Wallis *et al*., 1993). Note in (b) the comparison between 2D (red dots) and 3D (blue dots) selected clasts. Rc_{min}: minimum value of critical aspect ratio; Rc_{max}: maximum value of critical aspect ratio; a: long axis of the clast; θ: angle between the a axis and the main foliation.

7. DISCUSSION AND CONCLUSIONS

Non-routine technical approaches have been used to study the kinematic and temporal evolution of the MCTz. The first and foremost observation is that the application of $^{40}Ar/^{39}Ar$ ages of micas from mylonites of the MCTz have been analysed through the Differential Release Plot and correlation diagrams (Chapter 5) on both samples from the Bhagirathi – Gangotri valleys (UT series, Fig. 4.13) and samples from the Alaknanda – Dhauli Ganga valleys (AK series, Fig. 4.1). This approach leads straightforwardly to achieve robust age data otherwise almost impossible to obtain through the generally commonly used $^{40}Ar/^{39}Ar$-released *vs.* age spectra only.

The kinematic analysis of flow of most of the studied samples from the MCTz, reported in Chapter 6, have been obtained with a 3D approach, using the X-ray microCT scans. X-ray microCT is a useful technique to improve the estimate of kinematic vorticity using rigid porphyroclasts method, thanks to its spatial resolution and the high number of investigated clasts with respect to 2D thin section method. The possibility to inspect the third dimension avoids potentially misleading 2D measurements that generate systematic errors in the vorticity evaluation.

In the following, a critical discussion is given of our analytical results in the framework of previously puslished research.

The age of shearing along the two bounding faults of the GHS, namely the MCT and the STDS, can help to discriminate among the proposed tectonic models for Himalaya orogen evolution (Montomoli et al., 2013 for a review). Some models require MCT and STDS to be contemporaneously active, e.g. the channel flow model (Beaumont et al., 2001, 2004), the wedge extrusion model (Hodges et al., 1992; Grujic et al., 1996; Vannay & Grasemann, 2001) and the wedge insertion model (Webb et al., 2007). Other models do not necessarily require contemporaneity, e.g. the critical taper model (Platt, 1993; Kohn, 2008) and the in-sequence shearing model (Carosi et al., 2010, 2018; Montomoli et al., 2013, 2015).

The results obtained during this three-year work argue against contemporaneity of the MCT and STDS, at least on the base of what observed in the Garhwal region (NW India).

The analysed pegmatites and the migmatites lie structurally below and close to the STDS in the Dhauli-Ganga valley Garhwal region. One of them (GW13-51) intrudes the main body of the Malari granite, one (GW13-57) intrudes the HT-mylonites, and one (GW13-39) comes from the upper portion of the GHS. We use their deformation features to infer the presence, or absence, of ductile shearing along the STDS. Microstructural observations coupled with $^{40}Ar/^{39}Ar$ dating of the investigated samples demonstrate that deformation linked to ductile shearing on the STDS gradually weakens moving from the structurally upper to the structurally lower sector of the shear zone. In fact, the occurrence of bulging recrystallization in quartz and mechanical twinning in plagioclase, together with the occurrence of kink bands in muscovite (Fig. 4.3) in sample GW13-51, demonstrate that deformation linked to the STDS activity occurred at low T (c. 300-400 °C). The muscovite of this sample yields a $^{40}Ar/^{39}Ar$ age of 16.46 ± 0.06 Ma. Pegmatite GW13-57 is much less deformed with respect to GW13-51. It exhibits undulose extinction in quartz (Fig. 4.4) and sporadic kink bands in mica (Fig. 4.4d). Muscovite yields a younger

^{40}Ar/^{39}Ar age of c. 16.0 Ma. Finally, the structurally lower migmatite GW13-39 contains pristine high-temperature deformation microstructures expressed by chessboard extinction (Fig. 4.5) and GBM recrystallization in quartz, followed by late, static muscovite growth during sillimanite breakdown (Fig. 4.5d). The ^{40}Ar/^{39}Ar age of 14.36 ± 0.06 Ma for the static muscovite provides a minimum age for the cessation of ductile deformation. We maintain that we dated the waning stages of ductile deformation on the STDS: at c. 16.5 Ma ductile deformation was ongoing whereas at, or before, 14.3 Ma at the latest it ceased. Our results are in agreement with those of Sen et al. (2015) who suggest that ductile deformation lasted until c. 15 Ma in the same study area, and with Iaccarino et al. (2017b) who constrained the ductile shearing along the STDS in the Garhwal region to between c. 20 and 15 Ma by U–(Th)–Pb in situ geochronology on monazite occurring in a high-temperature mylonite.

Following the in-depth reviews of shearing activity on the STDS by Leloup et al. (2010), Liu et al. (2017) and Iaccarino et al. (2017b), it appears that the activity on the STDS changed in time along strike of the entire Himalayan belt. From west to east, the age of ductile shearing on the STDS ranges between c. 26 Ma in the Zanskar region (Finch et al., 2014) to c. 15 Ma in the Everest region (Gebelin et al., 2017) and in NW Bhutan (Kellett et al., 2010). In Western Bhutan, Montomoli et al. (2017a) constrained the brittle-ductile transition at 13.9 Ma through U-(Th)-Pb dating on monazite from leucogranitic dykes. The Bura Buri undeformed leucogranite in west Nepal, c. 300 km east of the study area intruded the TSS at 23-25 Ma (Carosi et al., 2013) and thus provides a a mimum age for the termination of the movement along the STDS; the Shivling leucogranite could represent a similar time limit of c. 23 Ma (Searle et al., 1999 and references cited therein). In the Yadong region, multiple leucogranite intrusions, dated at 23–16 Ma by Liu et al. (2017), sealed the STDS at ≥ 20 Ma.

The remarkable microstructural and chemical complexity of mylonites from the MCTz requires a detailed microstructural and petrogenetic study. It must be pointed out that some studies (e.g. Berger et al., 2017 and references cited therein) provide conclusive observational evidence that shear–induced recrystallization is rarely complete and results in extremely small heterochemical relict phases hosted in the recrystallized mineral matrix. In contrast with the interpretation of Sen et al. (2015), we focus on the microstructures and argue that our results reflect a true diachronism across the shear zone.

In tha Alaknanda – Dhauli Ganga valleys, the MCTz rocks in Garhwal record several well-resolvable deformation phases. Microstructural observations show the complex superposition of tectonic foliations, marked by successive mica growth and recrystallization episodes. Microchemical analyses show both pervasive secondary alteration and the primary heterogeneity of biotite. Muscovite is less altered and less clearly heterogeneous. Three different generations of micas were observed: mica-1 in a relict foliation at a high angle with respect to the main mylonitic foliation (S_m); mica-2, oriented along Sm, is characterized by small flakes of both muscovite and biotite; and mica-3, consisting of large crystals of muscovite and rare biotite in coronitic structures around garnet porphyroclasts. Mica-3 lacks undulose extinction; its microstructure and chemical composition suggest formation during retrogression and garnet breakdown. ^{40}Ar/^{39}Ar age spectra are discordant and show both inter- and intra-sample discrepancies, which cannot be interpreted as ‘cooling age’ differences because samples from the same outcrop cooled simultaneously. Instead, Ar systematics reflects sample-specific markers of heterochemical recrystallization. The isochron age of the Ca-poor steps of biotite separate (i.e. the age of biotite-2) of the mylonitic micaschist (GW13-29) sample in the upper portion of the MCTz near Tapoban is 9.07 ± 0.60 Ma, corresponding to a weighted isochemical average age of the steps pertaining to biotite *sensu stricto* of 9.00 ± 0.10 Ma. Muscovite shows a negative correlation between the Cl/K ratio and age as a result of a mixture of a relatively Cl-rich 5.88 ± 0.03 Ma mica (muscovite-3) and a >7 Ma Cl-poor muscovite-2. The extrapolation of the correlation trend to low Cl/K values allows us to suggest, but not to constrain, an end-member (muscovite-2) as old as c. 9 Ma.

Combining microstructural, microchemical and geochronological data from the MCTz, we propose the following evolution:

- stage 1: syntectonic growth of mica-2 occurred along the main foliation at c. 9 Ma;
- stage 2: the formation of coronitic muscovite at 5.88 Ma post-dated the deformation due to shearing along the Vaikrita Thrust; minor to pervasive alteration of muscovite occurred before, during and after coronite growth.

The shearing along the Vaikrita Thrust lasted until at least 9 Ma, i.e. it continued for 6–7 Myr after the cessation of the movement along the STDS in the same study area.

In the lower Alaknanda valley, the age of the Berinag Thrust (AK18-5) of 6.70 ± 0.02 Ma has been interpreted as an out-of-sequence thrust, occurring before the main activity shearing recorded by micas foliation along the Munsiari Thrust at 5.31 ± 0.02 Ma along the same transect. The difference between biotite and muscovite ages obtained in sample AK18-13 is to be referred to the occurrence of three generation of micas: we argue that 14-24 Ma old biotite is the biotite-1 preserved in the sample. Biotite ages from samples AK18-23, AK18-26 and AK18-42 show some geological inconsistency. In our interpretation old relict biotite was not completely recrystallized and isotopically reset, and therefore preserves an old chemical and isotopic signature, reflecting in the age. This preservation could be due to a low strain and/or low permeability domain. In any case, the age of the relict micas is not relevant for the present investigation, which addresses the age of shearing.

In the Gangotri glacier valley, the obtained ages for the intrusion of Bhagirathi granite (UT15-41: 18.17 ± 0.02 Ma; UT15-51: 18.69 ± 0.02 Ma) are in agreement with those previously reported for granitic intrusive bodies in the same study area. An age of 18.4 Ma has been reported (K-Ar on muscovite; Seitz et al., 1976) for the Bhagirathi granite in the Arwa valley, and ages ranging from 18.4 Ma (K-Ar on muscovite; Stern et al., 1989) to 22-23 Ma (K-Ar on muscovite, Th-Pb and U-Pb on monazite; Harrison et al., 1997, Searle et al., 1999) for the Shivling body. The age of Gangotri intrusion has been reported by Stern et al. (1989), Sorkhabi et al. (1996) and Harrison et al. (1997), between 18 and 22.4 Ma.

In the Bhagirathi valley, mylonitic orthogneisses and micaschists from both the Munsiari and Vaikrita Thrust all show a well-resolvable greenschist facies foliation. A top-to-the-SW sense of shear along both these thrusts is confirmed by both meso and microstructural kinematic indicators. For Munsiari Thrust the syntectonic growth of S2 biotite, defining the main mylonitic

foliation at 4.8 Ma, constrains the age of shearing. In the same way, the syntectonic growth of S2 muscovite, defining the main mylonitic foliation at c. 8 Ma, constrains the age of shearing along the Vaikrita Thrust. As demonstrated by the preservation of inherited Ar in S1 micas (GW samples, Fig. 5.1), the S2 micas are (re-)crystallization ages. The formation of large, static S3 muscovite at 7.4 Ma post-dates the deformation due to shearing. For the Vaikrita we also obtained younger ages for muscovite UT15-9 (4.78 ± 0.02 Ma and 5.46 ± 0.26 Ma) but they are probably due to the circulating fluids as testified by the abundance of newly formed chlorite.
In the same study area, Metcalfe (1993) reported 70.2 Ma (K-Ar on biotite), 8.0 Ma (K-Ar on muscovite) and 1491.8 Ma (Ar-Ar on hornblende) for samples in the hanging wall of the Munsiari Thrust. In the footwall of the Vaikrita Thrust they obtained 9.5 Ma (K-Ar on biotite), 5.7-14.9 Ma (K-Ar on muscovite) and 19.8 Ma (Ar-Ar on hornblende), whereas in the hangingwall ages of 74.3 Ma and 14-18 Ma have been reported. His interpretation of K-Ar ages as cooling ages conflicts with the present observations and is internally inconsistent, as the higher-grade rocks are counterintuitively older than lower-grade ones; no re-evaluation of his data can be attempted, as the data-set is incomplete (EPMA-based petrological distinction between the ubiquitous multiple mica generations was not a routine technique in the 1990s; nor were three-element Ca-Cl-K correlation diagrams a routine tool in the 1990s). It can only be noted that several of his samples have pre-Miocene ages, an observation which the present work documents to be due to relict minerals. Catlos et al. (2002) obtained 5.9 Ma for matrix monazite just beneath the MCT; and Catlos et al. (2007) reported c. 4.5 Ma (U-Th-Pb on monazite) for samples in the same structural position, suggesting a Pliocene (re-)activation of this structure. At the bottom of the MCTz the same Authors reported ages of c.1 Ma from hydrothermal monazite, but they assumed (without microstructural support) that this obvious hydrothermal circulation coincides with an out-of-sequence thrusting and reactivation in a critical taper wedge model (Catlos et al., 2007) in which the deformation did not move systematically southward from the MCT toward the foreland. They also reported ages from 38.0 to 19.5 Ma (Th-Pb on monazite ion microprobe) from the internal portion of the GHS, providing support for our conclusion that pre-Miocene relict phases are preserved throughout the GHS, including within the MCTz itself.

In the Sutlej valley (c. 280 km westward of our study area), Jain et al. (2000) obtained apatite fission tracks (AFT) ages from the lower portion of the GHS between 4.2 and 5.1 Ma. The Vaikrita Thrust zone yields 2.7 Ma (zircon fission tracks, ZFT) and 1.3 Ma (AFT). Vannay et al. (2004) reported ^{40}Ar/^{39}Ar ages of c. 17.6-15.4 Ma and 6.6-4.3 Ma in the hangingwall and in the footwall of the MCT (i.e. Vaikrita Thrust), respectively. They also presented apatite and zircon fission track data from the Luhri Syncline (GHS in the frontal part of the range) varying between c. 12 and 10 Ma (ZFT), and c. 4 and 3 Ma (AFT). In the same area, Caddick et al. (2007) obtained 9-10 Ma from matrix and garnet-inclusion monazite from a pelitic schist in the hanging wall of the Munsiari Thrust, suggesting a prograde metamorphism and supporting a foreland-directed shift of metamorphism in the Miocene time.

In the Bhagirathi valley, our results support an in-sequence thrusting from the Vaikrita to the Munsiari Thrusts from c. 8 (the minimum age for the shearing) to c. 5 Ma toward the foreland, in agreement with Metcalfe (1993), Vannay et al. (2004) and Caddick et al. (2007), who furthermore support a propagation of syn-metamorphic deformation toward the foreland.

In the framework of the proposed exhumation models for the GHS, adding as much information as possible to the knowledge on the bounding shear zones of the GHS itself is a crucial task. Quantitative estimates of the flow kinematics have been increasingly used to deduce large scale tectonics from a variety of geodynamic settings (Iacopini et al., 2008; Xypolias, 2010; Xypolias et al., 2010 and references therein). The kinematic vorticity of major Himalayan tectonic discontinuities has been determined both for the STDS, especially in the Eastern Himalaya (Law et al., 2004, 2011; Jessup et al., 2006; Carosi et al., 2006, 2007) and for several sectors of the MCTz: NW India (Grasemann et al., 1999; Law et al., 2013), central Nepal (Larson & Godin, 2009; Larson et al., 2010), eastern Nepal (Jessup et al., 2006) and Bhutan (Long et al., 2011).

Our stable porphyroclasts analysis results (W_m = 0.49-0.58, Fig. 5) on two mylonitic orthogneisses from the Munsiari Thrust reveals a dominance of the pure shear component (65-60 %), which is higher than, but overlaps with, literature reports from the MCTz.

In the Sutlej valley (NW India), Grasemann et al. (1999) support a large pure shear component throughout the entire MCTz from ductile to late stage of ductile-brittle transition. They relate the shift from a simple shear dominated to a pure shear dominated flow to a decelerating strain path, whereby the kinematic vorticity number decreases as deformation proceeds. During the first stages deformation is dominated by simple shear that progressively decreases in favor of pure shear dominated flow during the final stage of deformation (Simpson & De Paor, 1997; Grasemann et al., 1999).

In the same area, Law et al. (2013) combining stable porphyroclasts and quartz c-axis methods, obtained Wm = 0.75-0.82 (Sutlej valley) and 0.90-0.95 (Shimla klippe transect), suggesting a predominantly simple shear flow moving upward from the MCT towards the core of the GHS. In central Nepal, both Larson & Godin (2009) and Larson et al. (2010) obtain a large pure shear component (66-41 %) that decreases with structural distance from the MCTz (Wm = 0.50-0.68 to 0.78-0.87). In eastern Nepal, Jessup et al. (2006) find Wm = 0.63-0.77, i.e. a pure shear component of 44 – 58 %. In Bhutan, Long et al. (2011) find a large component of pure shear.

The progressive rejuvenation of the structures toward the foreland (i.e. from the Vaikrita to the Munsiari thrusts) is supported by the age of shearing constrained along these structures. In the Bhagirathi valley, our results support an in sequence shearing from c. 8.17 to 4.8 Ma from the Vaikrita to the Munsiari thrusts. The same result has been obtained in the Alaknanda valley, where the age of the Vaikrita Thrust, 9 Ma (samples GW13-28, GW13-29, GW13-29B) is older than that of the Munsiari Thrust, 5.4 Ma (AK18-13). The age of both faults is similar but not identical in the two neighboring valleys, suggesting that movement in the MCTz was not rigorously cylindrical.

Our results therefore require the diachroneity of the STDS and MCT in the Garhwal Himalaya (Fig. 7.1), where ductile shearing along the STDS stopped at least 7 Myr earlier than motion on the MCTz in the same transect. This urges for a major revision of tectonic models that require contemporaneity of movement along the STDS and MCTz. Our data instead support models that explain exhumation of the GHS without such contemporaneity (Montomoli et al., 2013, 2015; Carosi et al., 2018).

(a) stage 1: shearing along Vaikrita Thrust

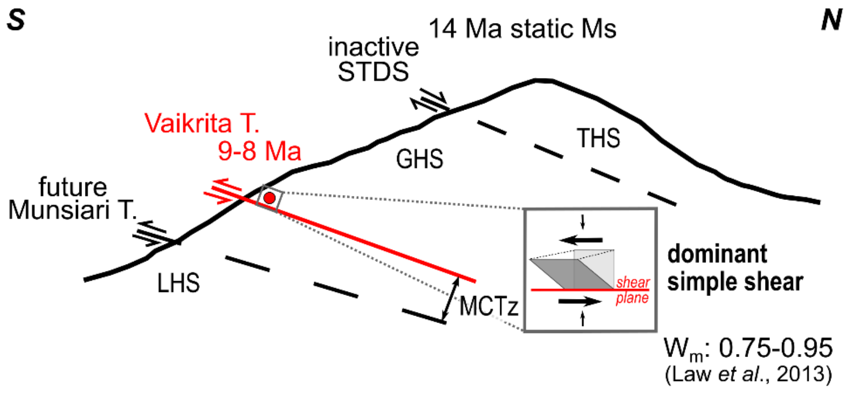

(b) stage 2: shearing along Munsiari Thrust

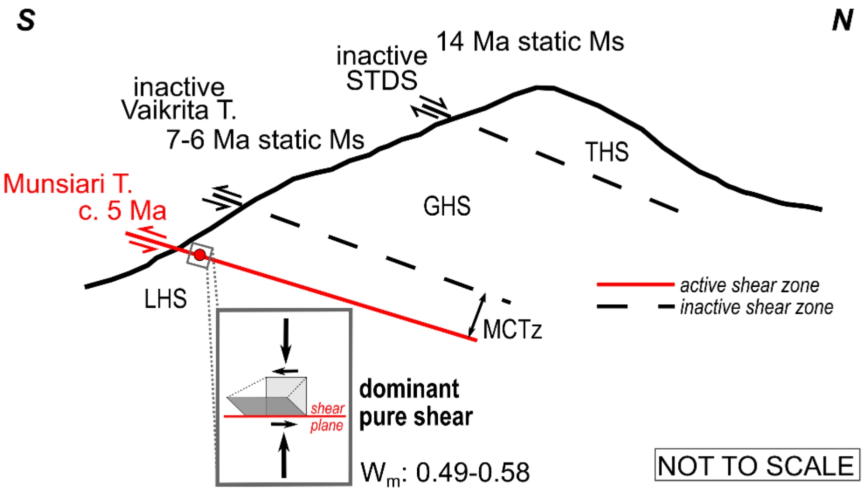

Figure 7.1. Schematic model for the study area. (a) Shearing along the VT at 9-8 Ma. (b) Shearing along the MT at c. 5 Ma. Temporal bracket for the end of STDS shearing in the Alaknanda – Dhauli Ganga valleys is reported. The simple and pure shear components of the general flow are qualitatively represented in the grey boxes. STDS: South Tibetan Detachment System; MCTz: Main Central Thrust zone; W_m: mean kinematic vorticity number. Mineral abbreviation as Whitney & Evans (2010).

The model of the in-sequence shearing was mainly based on the recognition of shear zones in the core of the GHS, which had long been considered as a coherent tectonic unit. The first recognition of a compressive shear zone in the core of the GHS is due to Carosi et al. (2010), who identified in Western Nepal the Toijem shear zone, constraining its activity between 26 and 17 Ma, distinctly before the onset of the MCTz in the same area (22-20 Ma). Several shear zones were subsequently recognized from west to east in the GHS core: Metamorphic Discontinuity (Yakymchuk & Godin, 2012), Mangri Shear Zone (Montomoli et al., 2013), Sinuwa Thrust

(Corrie & Kohn, 2011), Himal Chuli (Larson et al., 2010), Langtang Thrust (Kohn, 2008), Tama Kosi (Larson et al., 2013; Larson & Cottle, 2014), Hidden Discontinuity (Groppo et al., 2009) and High Himal Thrust (Goscombe et al., 2006). Montomoli et al. (2013) correlated the above-mentioned discontinuities along the strike of the belt, as they show the same particular features, defining them as High Himalayan Discontinuity (HHD, Montomoli et al., 2013). In all the studied transects the HHD was active always before the MCTz, and affected the metamorphic evolution of the GHS (Montomoli et al., 2015), resulting in the definition of two GHS units: the lower (GHS_l) and the upper GHS (GHS_u). These units are characterized by different P-T conditions: at similar peak temperatures (675–700°C), the GHS_l recorded higher pressure (c. 0.9 GPa) with respect to the GHS_u (c. 0.7 GPa; Carosi et al., 2019). Moreover, the GHS_u and GHS_l rocks reached peak metamorphic conditions at different times, with the GHS_u reaching peak metamorphism before the GHS_l (Montomoli et al., 2015).

The subduction of India underneath Asia caused a nucleation of shear zones that evolved in time and space towards the foreland of the Himalayan orogeny. Smit et al. (2003) demonstrated, through laboratory experiments, that the in-sequence propagation of thrusts in the thrust wedges is favored by high shortening rate, as in the case of past (c. 60 mm/a at c. 30 Ma) and present-day (c. 50 mm/a) India - Asia convergence rates (Copley et al., 2010 and references therein).

In the MCTz the evolution of deformation appears to follow the structural evolution of the entire belt, suggesting an inter- and intra-shear zone evolution towards the foreland. We can speculate that in the framework of models proposed for shear zones evolution (Hull, 1988; Fossen, 2010), the MCTz could have followed a thickening evolution in space. The correlation between ages and deformation suggests a progressive migration of deformation towards the base of the MCTz, with the upper shear zone (i.e. the Vaikrita Thrust) becoming inactive (as testified by mica-3 microstructures, Chapters 4 and 5) while deformation shifts and concentrates in the basal shear zone (i.e. the Munsiari Thrust). Thus, this mechanism leads to a thickening of the shear zone as a whole (i.e. the MCTz). The migration of deformation could be due to strain hardening with temperature decreasing during exhumation. With respect to the mechanism of evolution of shear zones proposed by Fossen (2010), which is always symmetric, the MCTz evolved asymmetrically, largely following the in-sequence evolution observed at the orogen scale related to the high subduction velocity of India beneath the Eurasia margin. All these considerations lead us to conclude that the MCTz should be considered as a shear zone with deformation progressing in sequence from the upper boundary (i.e. Vaikrita Thrust) to the lower, younger one (i.e. Munsiari Thrust, Fig. 7.1), with mylonites occurring seamlessly between the two structures.

Combining the results of geochronological, microstructural and kinematic studies in the study areas of the Garhwal Himalaya (Fig. 7.1) supports the decelerating strain path model originally proposed by Grasemann et al. (1999). At 9-8 Ma Vaikrita shearing records a higher vorticity, in agreement with Law et al. (2013), who analysed samples in the hangingwall of the MCT. At 5-4 Ma, well after the cessation of Vaikrita thrusting, the Munsiari Thrust becomes active. Our vorticity data, together with literature data, support an increase of the pure shear component toward the base of the MCTz: we argue that the exhumation of the GHS is dominated by simple shear at deeper crustal level and, when deformation shifted toward shallower structural levels, simple shear decreases in favor of an increasing pure shear component. This shift in space of deformation regime is mirrored by a younging of mica ages, further supporting the orogen-scale diachroneity of the STDS and MCTz.

8. ACKNOWLEDGEMENTS

First and foremost, I wish to express my gratitude to my supervisors Professors Igor M. Villa, Chiara Montomoli and Rodolfo Carosi who involved me in an absolutely fascinating research theme in a wonderful Earth place: I will always be grateful for this.

Igor, thanks for your patience in introducing me in the tricky world of Ar-Ar and trying with me to solve such complex and beautiful sheared rocks! Your philosophical criticism helped me to be motivated across these three beautiful years of hard work.

Chiara and Rodolfo, you have always been an example to follow for me for your supportive attitude, tireless dedication and love for this work: thank you. I am greatly in debt to Chiara who provided me with her affectionate support when I needed it more: yes Chiara, we have done it!

I also particularly wish to thank Dr. Salvatore Iaccarino for being a valuable source of support contributing with his illuminating comments and suggestions to this three years' work: thanks because I have learned many things from you.

Once again, thank you all!

I sincerely wish to thank Prof. Stefano Zanchetta for his quiet, but always present, inspiring enthusiasm and concrete help, for his clarifying explanations and for our stimulating and fulfilling discussions. Thank you so much Stefano, you are a touchstone for me.

I wish to thank Prof. Andrea Zanchi for his useful suggestions and shared knowledge from the Orobic Alps to the Himalaya, as well as for his cruel questions that caused me always new magnificent doubts to solve.

I sincerely hope that my work reflects the rigorous approach, geological skills and patience all the above people fed me with.

I particularly wish to thank Prof. Richard D. Law who shared his deep geological knowledge, time and lively enthusiasm, also introducing me to the principles of U-stage studies.

This thesis greatly benefited from valuable and thoughtful reviews by Prof. Richard D. Law and Dr. Lorenzo Gemignani. Thanks for your comments and suggestions that deeply improved this work.

I would also like to acknowledge a number of other geologists with whom I have shared close friendships and academic relationships. Many thanks to Dr. Valentina Barberini for her assistance at the spectrometer and for her patience during my first days in the lab. Dr. Nicoletta Fusi is thanked for the X-ray microCT acquisitions and for her enthusiasm in dealing with my rocks. I wish to thank Dr. Silvia Mittempergher, Prof. Andrea Bistacchi, Dr. Pietro Sternai, Prof. Nadia Malaspina and Prof. Federico Agliardi who have been so hospitable and supportive to me also introducing me in to the beautiful geology of several areas in the Alps. I sincerely wish to thank all the Virginia Tech people for welcoming me sharing your knowledge and ideas.

I feel honored to have shared this road with all of you.

Luca Pellegrino, Giulia Bosio, Mattia Martinelli, Laura Nania, Chiara Crippa, Matteo Simonetti and Sofia Locchi we shared joys and pains of our crazy PhD student life: thank you all!
Luca and Mattia you were the best office mates I could have asked for. Laura and Matteo our time together in Virginia will always be a nice memory for me. Laura, I am happy to have shared our Himalayan adventures with you, notwithstanding the spiders! Chiara and Sofia thanks for all your funny support, I really appreciated it! Giulia thanks for your support in the misadventures during the endless afternoons in the lab.

My dearest friends, Francesca and Iacopo, I always felt you close to me: thanks!

Finally, I express my thankfulness to my mom, my brother and my grandparents who always and unconditionally supported me. Mom, if today I am who I am, I mostly owe it to you.

In the end, thank you Nat, my “ask a mineralogist”, for always having been there, every day. Only you could have brought me out of the water being my wonderwall when my thoughts were dragging me down.

Each of you has enriched me both as a geologist and as a woman: thanks!

9. REFERENCES

Ahmad, T., Harris, N., Bickle, M., Chapman, H., Bunbory, J. & Prince, C., 2000. Isotopic constraints on the structural relationship between the Lesser Himalayan Series and the High Himalayan Crystalline Series, Garhwal Himalaya. *Geological Society of America Bulletin,* **112**, 467-477.

Allaz, J., Engi, M., Berger, A. & Villa, I. M., 2011. The effects of retrograde reactions and of diffusion on ^{40}Ar–^{39}Ar ages of micas. *Journal of Petrology*, **52**, 691-716.

Arita, K., 1983. Origin of the inverted metamorphism of the lower Himalaya, central Nepal. *Tectonophysics*, **95**, 43-60.

Beaumont, C., Jamieson, R. A., Nguyen, M. H. & Lee, B., 2001. Himalayan tectonics explained by extrusion of a low-viscosity crustal channel coupled to focused surface denudation. *Nature*, **414**, 738-742.

Beaumont, C., Jamieson, R. A., Nguyen, M. H. & Medvedev, S., 2004. Crustal channel flows: 1. Numerical models with applications to the tectonics of the Himalayan-Tibetan orogen. Journal of Geophysical Research: Solid Earth, 109(B6).

Beltrando, M., Lister, G. S., Forster, M., Dunlap, W. J., Fraser, G. & Hermann, J., 2009. Dating microstructures by the ^{40}Ar/^{39}Ar step-heating technique: deformation–pressure–temperature–time history of the Penninic units of the Western Alps. *Lithos*, **113**(3), 801-819.

Berger, A., Wehrens, P., Lanari, P., Zwingmann H. & Herwegh, M., 2017. Microstructures, mineral chemistry and geochronology of white micas along a retrograde evolution: An example from the Aar massif (Central Alps, Switzerland). Tectonophysics, 721, 179–195.

Boullier, A. M., 1999. Fluid inclusions: tectonic indicators. *Journal of Structural Geology*, **21**, 1229-1235.

Brown, M., 2002. Retrograde processes in migmatites and granulites revisited. *Journal of Metamorphic Geology*, **20**, 25–40.

Bucher, K. & Grapes, R., 2011. Petrogenesis of metamorphic rocks. *Springer Berlin Heidelberg*.

Burchfiel, B.C., Chen, Z., Hodges, K.V., Liu, Y., Royden, L.H., Deng, C. & Xu, J., 1992. The South Tibetan Detachment System, Himalayan Orogen. *Geological Society of America Special Paper*, **269** (41 pp.).

Burg, J. P., Brunel, M., Gapais, D., Chen, G. M. & Liu, G. H., 1984. Deformation of leucogranites of the crystalline Main Central Sheet in southern Tibet (China). *Journal of Structural Geology*, **6**, 535–542.

Caby, R., Pêcher, A. & Le Fort, P., 1983. Le grand chevauchement central himalayen: Nouvelles données sur le métamorphisme inverse à la base de la Dalle du Tibet. *Revue de Géologie Dynamique et de Géographie Physique*, **24**, 89–100.

Caddick, M. J., Bickle, M. J., Harris, N. B. W., Holland, T. J. B., Horstwood, M. S. A., Parrish, R. R. & Ahmad, T., 2007. Burial and exhumation history of a Lesser Himalayan schist: recording the formation of an inverted metamorphic sequence in NW India. *Earth and Planetary Science Letters*, **264**, 375–390.

Carosi, R., Gemignani, L., Godin, L., Iaccarino, S., Larson, K., Montomoli, C. & Rai, S. M., 2014. A geological journey through the deepest gorge on earth: The Kali Gandaki valley section, west-central Nepal. *Journal of the Virtual Explorer*, **47**, paper 7.

Carosi, R., Lombardo, B., Molli, G., Musumeci, G. & Pertusati, P. C., 1998. The south Tibetan detachment system in the Rongbuk valley, Everest Region. Deformation features and geological implication. *Journal of Asian Earth Sciences,* **16**, 299–311.

Carosi, R., Montomoli, C. & Iaccarino, S., 2018. 20 years of geological mapping of the metamorphic core across Central and Eastern Himalayas. *Earth-Science Reviews*, **177**, 124-138.

Carosi, R., Montomoli, C., Iaccarino, S. & Visonà, D., 2019. Structural evolution, metamorphism and melting in the Greater Himalayan Sequence in central-western Nepal. *Geological Society, London, Special Publications*, **483**, 305-323.

Carosi, R., Montomoli, C. & Visonà, D., 2002. Is there any detachment in the Lower Dolpo (Western Nepal)? *Comptes Rendus Geoscience*, **334**, 933–940.

Carosi, R., Montomoli, C. & Visonà, D., 2007. A structural transect in the Lower Dolpo: insights on the tectonic evolution of Western Nepal. *Journal of Asian Earth Sciences*, **29**, 407-423.

Carosi, R., Montomoli, C., Iaccarino, S., Massonne, H. -J., Rubatto, D., Langone, A., Gemignani, L. & Visonà, D. 2016. Middle to late Eocene exhumation of the Greater Himalayan Sequence in the Central Himalayas: Progressive accretion from the Indian plate. *Geological Society of America Bulletin*, **128(11-12)**, 1571-1592.

Carosi, R., Montomoli, C., Rubatto, D. & Visonà, D., 2006. Normal-sense shear zones in the core of the Higher Himalayan Crystallines (Bhutan Himalayas): evidence for extrusion? In: *Channel flow, ductile extrusion and exhumation in continental collision zones* (Law, R.D., Searle, M.P. and Godin, L., eds). *Geological Society, London, Special Publications,* **268**, 425-444.

Carosi, R., Montomoli, C., Rubatto, D. & Visonà, D., 2010. Late Oligocene high-temperature shear zones in the core of the Higher Himalayan Crystallines (Lower Dolpo, Western Nepal), *Tectonics*, **29**, TC4029, doi: 10.1029/2008TC002400.

Carosi, R., Montomoli, C., Rubatto, D., & Visonà, D., 2013. Leucogranite intruding the South Tibetan Detachment in western Nepal: implications for exhumation models in the Himalayas. *Terra Nova*, **25(6)**, 478-489.

Catlos, E. J., Dubey, C. S., Marston, R. A. & Harrison, T. M., 2007, Geochronologic constraints across the Main Central Thrust shear zone, Bhagirathi River (NW India): Implications for Himalayan tectonics. In: *Convergent Margin Terranes and Associated Regions: A Tribute* *to W.G. Ernst* (Cloos, M., Carlson, W.D., Gilbert, M.C., Liou, J.G. and Sorensen, S.S., eds). *Geological Society of America Special Paper*, **419**,135–151.

Catlos, E. J., Harrison, T. M., Kohn, M. J., Grove, M., Ryerson, F. J., Manning, C. E. & Upreti, B. N., 2001. Geochronologic and thermobarometric constraints on the evolution of the Main Central Thrust, central Nepal Himalaya. *Journal of Geophysical Research*, **106**, 16177–16204.

Catlos, E. J., Harrison, T. M., Manning, C. E., Grove, M., Rai, S. M., Hubbard, M. S. & Upreti, B. N., 2002. Records of the evolution of the Himalayan orogen from in situ Th–Pb microprobe dating of monazite: Eastern Nepal and western Garhwal. *Journal of Asian Earth Sciences*, **20**, 459-479.

Célérier, J., Harrison, T. M., Beyssac, O., Herman, F., Dunlap, W. J. & Webb, A. A. G., 2009b. The Kumaun and Garwhal Lesser Himalaya, India: Part 2. Thermal and deformation histories. *Geological Society of America Bulletin*, **121**, 1281-1297.

Célérier, J., Harrison, T. M., Webb, A. A. G. & Yin, A., 2009a. The Kumaun and Garwhal Lesser Himalaya, India: Part 1. Structure and stratigraphy. *Geological Society of America Bulletin*, **121**, 1262-1280.

Chafe, A. N., Villa, I. M., Hanchar, J. M. & Wirth, R., 2014. A re-examination of petrogenesis and ^{40}Ar/^{39}Ar systematics in the Chain of Ponds K-feldspar: "diffusion domain" archetype versus polyphase hygrochronology. *Contributions to Mineralogy and Petrology*, **167**, 1010, doi: 10.1007/s00410-014-1010-x.

Challandes, N., Marquer, D. & Villa, I. M., 2003. Dating the evolution of C–S microstructures: a combined ^{40}Ar/^{39}Ar step-heating and UV laserprobe analysis of the Alpine Roffna shear zone. *Chemical Geology*, **197**, 3-19.

Chambers, J. A. & Kohn, M. J., 2012. Titanium in muscovite, biotite, and hornblende: Modeling, thermometry, and rutile activities of metapelites and amphibolites. *American Mineralogist*, **97(4)**, 543-555.

Cnudde, V., Masschaele, B., Dierick, M., Vlassenbroeck, J., Van Hoorebeke, L. & Jacobs, P., 2006. Recent progress in X-ray CT as a geosciences tool. *Applied Geochemistry*, **21**(5), 826-832.

Copley, A., Avouac, J. P. & Royer, J. Y., 2010. India-Asia collision and the Cenozoic slowdown of the Indian plate: Implications for the forces driving plate motions. *Journal of Geophysical Research: Solid Earth*, **115**(B3).

Corrie, S. L. & Kohn, M. J., 2011. Metamorphic history of the Central Himalaya, Annapurna region, Nepal, and implication for tectonic models. *Geological Society of America Bulletin*, **123**, 1863–1879.

Cottle, J. M., Searle, M. P., Jessup, M. J., Crowley, J. L. & Law, R. D., 2015. Rongbuk re-visited: Geochronology of leucogranites in the footwall of the South Tibetan Detachment System, Everest Region, Southern Tibet. *Lithos*, **227**, 94-106.

Crouzet, C., Dunkl, I., Paudel, L., Árkai, P., Rainer, T. M., Balogh, K. & Appel, E., 2007. Temperature and age constraints on the metamorphism of the Tethyan Himalaya in Central Nepal: A multidisciplinary approach. *Journal of Asian Earth Sciences*, **30**, 113-130.

Daniel, C. G., Hollister, L., Parrish, R. R. & Grujic, D., 2003. Exhumation of the Main Central thrust from lower crustal depths, Eastern Bhutan Himalaya. *Journal of Metamorphic Geology*, **21**, 317–334.

DeCelles, P. G., Gehrels, G. E., Quade, J., Lareau, B. & Spurlin, M., 2000. Tectonic implications of U–Pb zircon ages of the Himalayan orogenic belt in Nepal. *Science*, **288**, 497-499.

Denison, C. & Carlson, W. D., 1997. Three-dimensional quantitative textural analysis of metamorphic rocks using high-resolution computed X-ray tomography: Part II. Application to natural samples. *Journal of Metamorphic Geology*, **15**, 45-57.

Denison, C., Carlson, W. D. & Ketcham, R. A., 1997. Three-dimensional quantitative textural analysis of metamorphic rocks using high-resolution computed X-ray tomography. Part I: methods and techniques. *Journal of Metamorphic Geology*, **15**, 29–44.

Di Vincenzo, G., Carosi, R. & Palmeri, R., 2004. The relationship between tectono-metamorphic evolution and argon isotope records in white mica: constraints from in situ ^{40}Ar–^{39}Ar laser analysis of the Variscan basement of Sardinia. *Journal of Petrology*, ***45***, 1013-1043.

Di Vincenzo, G., Viti, C. & Rocchi, S., 2003. The effect of chlorite interlayering on ^{40}Ar–^{39}Ar biotite dating: an ^{40}Ar–^{39}Ar laser-probe and TEM investigations of variably chloritised biotites. *Contributions to Mineralogy and Petrology*, **145**(6), 643-658.

Dunkl, I., Antolín, B., Wemmer, K., Rantitsch, G., Kienast, M., Montomoli, C., Ding, L., Carosi, R., Appel, E., El Bay, R., Xu, Q. & von Eynatten, H., 2011. Metamorphic evolution of the Tethyan Himalayan flysch in SE Tibet. In: *Growth and Collapse of the Tibetan Plateau* (Gloaguen, R. and Ratschbacher, L., eds). *Geological Society of London Special Publications*, **353**, 45-69.

Faleiros, F. M., Moraes, R. D., Pavan, M. & Campanha, G. A. D. C., 2016. A new empirical calibration of the quartz c-axis fabric opening-angle deformation thermometer. *Tectonophysics*, **671**, 173-182.

Ferrill, D. A., Morris, A. P., Evans, M. A., Burkhard, M., Groshong Jr, R. H. & Onasch, C. M., 2004. Calcite twin morphology: a low-temperature deformation geothermometer. *Journal of Structural Geology*, **26**, 1521-1529.

Finch, M., Hasalová, P., Weinberg, R. F. & Fanning, C. M., 2014. Switch from thrusting to normal shearing in the Zanskar shear zone, NW Himalaya: Implications for channel flow. *Geological Society of America Bulletin*, **126**, 892–924.

Fossen, H. & Cavalcante, G. C. G., 2017. Shear zones: a review. *Earth-Science Reviews*, **171**, 434–455.

Fossen, H., 2010. *Structural geology*. Cambridge University Press.

Gaetani, M. & Garzanti, E., 1991. Multicyclic history of the northern India continental margin (northwestern Himalaya). *American Association of Petroleum Geologists*, **75**, 1427-1446.

Gebelin, A., Jessup, M., Teyssier, C., Cosca, M., Mulch, A., Law, R. D. & Brunel, M., 2017. Infiltration of meteoric water in the South Tibetan Detachment (Mount Everest, Himalaya): When and why? *Tectonics*, **36**, doi: 10.1002/2016TC004399.

Gibson, R., Godin, L., Kellett, D. A., Cottle, J. M. & Archibald, D., 2016. Diachronous deformation along the base of the Himalayan metamorphic core, west-central Nepal. *Geological Society of America Bulletin*, **128**, 860-878.

Godin, L., Grujic, D., Law, R.D. & Searle, M.P., 2006. Channel flow, ductile extrusion and exhumation in continental collision zones: an introduction. In: *Channel flow, ductile extrusion and exhumation in continental collision zones* (Law, R.D., Searle, M.P. and Godin, L., eds). *Geological Society of London Special Publication*, **268**, 1-23.

Goscombe, B., Gray, D. & Hand, M., 2006. Crustal architecture of the Himalayan metamorphic front in eastern Nepal. *Gondwana Research*, **10**, 232–255.

Grasemann, B., Fritz, H. & Vannay, J.-C., 1999. Quantitative kinematic flow analysis from the main central thrust zone (NW-Himalaya, India): implications for a decelerating strain path and the extrusion of orogenic wedges. *Journal of Structural Geology*, **21**, 837-853.

Groppo, C., Rolfo, F. & Indares, A., 2012. Partial melting in the higher Himalayan Crystallines of Eastern Nepal: the effect of decompression and implications for the ‘Channel Flow’ Model. *Journal of Petrology*, **53**, 1057–1088.

Groppo, C., Rolfo, F. & Lombardo, B., 2009. P–T evolution across the Main Central Thrust Zone (Eastern Nepal): hidden discontinuities revealed by petrology. *Journal of Petrology*, **50**, 1149–1180.

Grujic, D., Casey, M., Davidson, C., Hollister, S.L., Kündig, R., Pavlis, T., & Schmid, S., 1996. Ductile extrusion of the Higher Himalayan Crystalline in Bhutan: evidence from quartz microfabrics. *Tectonophysics*, **260**, 21–43.

Grujic, D., Hollister, L. S. & Parrish, R. R., 2002. Himalayan metamorphic sequence as an orogenic channel: insight from Bhutan. *Earth and Planetary Science Letters*, **198(1)**, 177-191.

Guidotti, C. V. & Sassi F. P., 2002. Constraints on studies of metamorphic K-Na white micas. In: Micas: Crystal Chemistry & Metamorphic Petrology. *Reviews in Mineralogy and Geochemistry,* **46**, 413-448.

Guidotti, C. V. & Sassi, F. P., 1998. Miscellaneous isomorphous substitutions in Na-K white micas: a review, with special emphasis to metamorphic micas. *Rendiconti Lincei Scienze Fisiche e Naturali*, **9**, 57-78.

Guidotti, C. V., 1984. *Micas in metamorphic rocks*. In: S.W. Bailey (ed.), Micas. Rev. Mineral., Min. Soc. Amer., **13**, 357-468.

Guillot, S., Hodges, K., Le Fort, P. & Pêcher, A., 1994. New constraints on the age of the Manaslu leucogranite: Evidence for episodic tectonic denudation in the central Himalayas. *Geology*, **22**, 559-562.

Gururajan, N. S. & Choudhuri, B. K., 1999. Ductile Thrusting, metamorphism and Normal faulting in Dhauliganga Valley, Garhwal Himalaya. *Himalayan Geology*, **20**, 19-29.

Harrison, T. M., Ryerson F. J, LeFort, P., Yin, A., Lovera, O. M. & Catlos, E. J., 1997. A late Miocene-Pliocene origin for the central Himalayan inverted metamorphism. *Earth and Planetary Science Letters*, **146**, E1-E7.

Hashimoto, S., Ohta, Y. & Akiba, C., 1973. Geology of the Nepal Himalayas. Saikon, Tokyo. 286 pp.

Heim, A. A. & Gansser, A., 1939. Central Himalaya: Geological observations of the Swiss Expedition, 1936. *Delhi, India, Hindustan Publishing*, pp. 26.

Henry, D. J. & Guidotti, C. V., 2002. Titanium in biotite from metapelitic rocks: Temperature effects, crystal-chemical controls, and petrologic applications. *American Mineralogist*, **87(4)**, 375-382.

Henry, D. J., Guidotti, C. V. & Thomson, J. A., 2005. The Ti-saturation surface for low-to-medium pressure metapelitic biotites: Implications for geothermometry and Ti-substitution mechanisms. *American Mineralogist*, **90(2-3)**, 316-328.

Hirth, G. & Tullis, J., 1992. Dislocation creep regimes in quartz aggregates. *Journal of Structural Geology*, **14(2)**, 145-159.

Hodges, K. V. & Silverberg, D. S., 1988. Thermal evolution of the Greater Himalaya, Garhwal, India. *Tectonics*, **7**, 583-600.

Hodges, K. V., 2000. Tectonics of the Himalaya and southern Tibet from two perspectives. *Geological Society of America Bulletin*, **112**, 324-350.

Hodges, K. V., Parrish, R. R. & Searle, M. P., 1996. Tectonic evolution of the central Annapurna range, Nepalese Himalayas. *Tectonics*, **15**, 1264-1291.

Hodges, K. V., Parrish, R. R., Housh, T. B., Lux, D. R., Burchfiel, B. C., Royden, L. H. & Chen, Z., 1992. Simultaneous Miocene extension and shortening in the Himalayan Orogen. *Science*, **258**, 1466–1470.

Hull, J., 1988. Thickness-displacement relationships for deformation zones. *Journal of Structural Geology*, **10**(4), 431-435.

Hunter, N. J., Weinberg, R. F., Wilson, C. J. L., Luzin, V. & Misra, S., 2018. Microscopic anatomy of a “hot-on-cold” shear zone: Insights from quartzites of the Main Central Thrust in the Alaknanda region (Garhwal Himalaya). *Geological Society of American Bulletin*, **130**, 1519-1539.

Iaccarino, S., Montomoli, C., Carosi, R., Massonne, H. -J. & Visonà, D., 2017a. Geology and tectono-metamorphic evolution of the Himalayan metamorphic core: insights from the

Mugu Karnali transect, Western Nepal (Central Himalaya). *Journal of Metamorphic Geology*, **35**, 301-325.

Iaccarino, S., Montomoli, C., Carosi, R., Massonne, H. -J., Langone, A. & Visonà, D., 2015. Pressure–temperature–time–deformation path of kyanite-bearing migmatitic paragneiss in the Kali Gandaki valley (Central Nepal): Investigation of Late Eocene–Early Oligocene melting processes. *Lithos*, **231**, 103-121.

Iaccarino, S., Montomoli, C., Carosi, R., Montemagni, C., Massonne, H.-J., Langone, A., Jain, A.K., Visonà, D., 2017b. Pressure-Temperature-Deformation-Time constraints on the South Tibetan Detachment System in Garhwal Himalaya (NW India). *Tectonics*, **36**, 2281-2304.

Iacopini, D., Carosi, R., Montomoli, C. & Passchier, C. W., 2008. Strain analysis of flow in the Northern Sardinian Varisican Belt: recognition of a partitioned oblique deformation event. *Tectonophysics*, **221**, 345-359.

Iacopini, D., Frassi, C., Carosi, R. & Montomoli, C., 2011. Biases in three-dimensional vorticity analysis using porphyroclast system: limits and application to natural examples. *Geological Society of London Special Publication*, **360**, 301-318.

Ildefonse, B., Sokoutis, D. & Mancktelow, N. S., 1992. Mechanical interactions between rigid particles in a deforming ductile matrix. Analogue experiments in simple shear flow. *Journal of Structural Geology*, **14**(10), 1253-1266.

Inger, S. & Harris, N., 1993. Geochemical constraints on leucogranite magmatism in the Langtang Valley, Nepal Himalaya. *Journal of Petrology*, **34**, 345-368.

Jain A. K., Kumar, D., Singh, S., Kumar, A. & Lal, N., 2000. Timing, quantification and tectonic modelling of Pliocene-Quaternary movements in the NW Himalaya: evidence from fission track dating. *Earth and Planetary Science Letters*, 179, 437-451.

Jain, A. K., Shreshtha, M., Seth, P., Kanyal, L., Carosi, R., Montomoli, C., Iaccarino, S. & Mukherjee, P. K., 2014. The higher Himalayan Crystallines, Alaknanda – Dhauli Ganga Valleys, Garhwal Himalaya, India. In: *Geological Field Trips in the Himalaya, Karakoram and Tibet* (Montomoli, C., Carosi, R., Law, R.D., Singh, S. and Rai, S.M., eds). *J. Virtual Explorer Electronic Edition*, **47**, https://doi.org/10.3809/jvirtex.2014.00349.

Jessel, M. W. 1987. Grain boundary migration microstructures in naturally deformed quartzite. *Journal of Structural Geology*, **9**, 1007-1014.

Jessup, M. J., Cottle, J. M., Searle, M. P., Law, R. D., Newell, D. L., Tracy, R. J. & Waters, D. J., 2008. P-T-t-D paths of Everest Series schist, Nepal. *Journal of Metamorphic Geology*, **26**, 717-739.

Jessup, M. J., Law, R. D. & Frassi, C., 2007. The rigid grain net (RGN): an alternative method for estimating mean kinematic vorticity number (W_m). *Journal of Structural Geology*, **29**, 411-421.

Jessup, M. J., Law, R. D., Searle, M. P. & Hubbard, M. S., 2006. Structural evolution and vorticity of flow during extrusion and exhumation of the Greater Himalayan Slab, Mount Everest Massif, Tibet/Nepal: implications for orogen-scale flow partitioning. In: *Channel Flow, Extrusion, and Exhumation in Continental Collision Zones* (Law, R.D., Searle, M.P. and Godin, L., eds). *Geological Society of London Special Publication*, **268**, 379-414.

Kellett, D. A., Grujic, D., Warren, C., Cottle, J., Jamieson, R. & Tenzin, T., 2010. Metamorphic history of a syn-convergent orogen-parallel detachment: The South Tibetan detachment system, Bhutan Himalaya. *Journal of Metamorphic Geology*, **28**, 785–808.

Kellett, D. A., Warren, C., Larson, K. P., Zwingmann, H., van Staal, C. R. & Rogers, N., 2016. Influence of deformation and fluids on Ar retention in white mica: Dating the Dover Fault, Newfoundland Appalachians. *Lithos*, **254**, 1-17.

Ketcham, R. A. & Carlson, W. D., 2001. Acquisition, optimization and interpretation of X-ray computed tomographic imagery: applications to the geosciences. *Computers & Geosciences*, **27**, 381-400.

Kile, D. E., 2009. The universal stage: The past, present, and future of a mineralogical research instrument. *Geochemical News*, **140**(8).

Kohn, M. J., 2008. P-T-t data from Nepal support critical taper and repudiate large channel flow of the Greater Himalayan Sequence. *Geological Society of America Bulletin*, **120**, 259–273.

Kruhl, J. H., 1996. Prism and basal plane parallel subgrain boundaries in quartz: A microstructural geothermobarometer. *Journal of Metamorphic Geology*, **14(5)**, 581-589.

Larson, K. P. & Cottle, J. M., 2014. Midcrustal discontinuities and the assembly of the Himalayan mid-crust. *Tectonics*, **33**, 718–740.

Larson, K. P. & Godin, L., 2009. Kinematics of the Greater Himalayan Sequence, Dhaulagiri Himal: implications for the structural framework of central Nepal. *Journal of Geological Society*, **166**, 25–43.

Larson, K. P., Gervais, F. & Kellett, D. A., 2013. A P–T–t–D discontinuity in east-central Nepal: implications for the evolution of the Himalayan mid-crust. *Lithos*, **179**, 275–292.

Larson, K. P., Godin, L. & Price, R. A., 2010. Relationship between displacement and distortion in orogens: linking the Himalayan foreland and hinterland in Central Nepal. *Geological Society of America Bulletin*, **122**, 1116-1134.

Law, R. D., 1990. Crystallographic fabrics: a selective review of their applications to research in structural geology. *Geological Society, London, Special Publications*, **54**, 335-352.

Law, R. D., 2014. Deformation thermometry based on quartz c-axis fabric and recrystallization microstructures: a review. *Journal of Structural Geology*, **66**, 129-161.

Law, R. D., Jessup, M. J., Searle, M. P., Francis, M., Waters, D. & Cottle, J. M., 2011. Telescoping of isotherms beneath the South Tibetan Detachment System, Mount Everest Massif. *Journal of Structural Geology*, **33**, 1569–1594.

Law, R. D., Searle, M. P. & Simpson, R. L., 2004. Strain, deformation temperatures and vorticity of flow at the top of the Greater Himalayan Slab, Everest Massif, Tibet. *Journal of Geological Society of London*, **161**, 305–320.

Law, R. D., Stahr, D. W., Francsis, M. K., Ashley, K. T., Grasemann, B. & Ahmad, T., 2013. Deformation temperatures and flow vorticities near the base of the Greater Himalayan Series, Sutlej Valley and Shimla Klippe, NW India. *Journal of Structural Geology*, **54**, 21–53.

Le Fort, P., 1975. Himalayas: the collided range. Present knowledge of the continental arc. *American Journal of Science*, **275**, 1-44.

Leloup P. H., Mahéo, G., Arnaud, N., Kali, E., Boutonnet, E., Liu, D., Xiaohan, L. & Haibing, L., 2010. The South Tibet detachment shear zone in the Dinggye area: Time constraints on extrusion models of the Himalayas. *Earth and Planetary Science Letters*, **292**, 1-16.

Li, C. & Jiang, D., 2011. A critique of vorticity analysis using rigid clasts. *Journal of Structural Geology*, **33**, 203-219.

Lister, G. S. & Paterson, M. S., 1979. The simulation of fabric development during plastic deformation and its application to quartzite: Fabric transitions, *Journal of Structural Geology*, **1**, 99-115.

Lister, G. S., 1977. Discussion: crossed-girdle c-axis fabrics in quartzites plastically deformedby plane strain and progressive simple shear. *Tectonophysics*, **39**, 51-54.

Liu, Z. C., Wu, F. Y., Qiu, Z. L., Wang, J. G., Liu, X. C., Ji, W. Q., & Liu, C. Z., 2017. Leucogranite geochronological constraints on the termination of the South Tibetan Detachment in eastern Himalaya. *Tectonophysics*, **721**, 106-122.

Lo, C. H. & Onstott, T. C., 1989. “sup. 39”. Ar recoil artefacts in chloritized biotite. *Geochimica et Cosmochimica Acta*, **53**, 2697-2711.

Long, S., McQuarrie, N., Tobgay, T. & Hawthorne, J., 2011. Quantifying internal strain and deformation temperature in the eastern Himalaya, Bhutan: Implications for the evolution of strain in thrust sheets. *Journal of Structural Geology*, **33**, 579-608.

Ludwig, K. R., 2003. Isoplot/Ex version 3.0. A geochronological toolkit for Microsoft Excel. *Berkeley Geochronology Center, Special Publications*, **4**.

Mancktelow, N. S., 2013. Behaviour of an isolated rimmed elliptical inclusion in 2D slow incompressible viscous flow. *Journal of Structural Geology*, **46**, 235-254.

Martin, A. J., 2017. A review of definitions of the Himalayan Main Central Thrust. International *J. Earth Sci*., **106**, 2131-2145.

Martin, A. J., DeCelles, P. G., Gehrels, G. E., Patchett, P. J. & Isachsen, C., 2005. Isotopic and structural constraints on the location of the Main Central thrust in the Annapurna Range, central Nepal Himalaya. *Geological Society of America Bulletin*, **117**, 926-944.

Massonne, H. -J., 2012. Formation of amphibole and clinozoisite–epidote in eclogite owing to fluid infiltration during exhumation in a subduction channel. *Journal of Petrology,* **53(10)**, 1969-1998.

Massonne, H. -J., Cruciani, G., Franceschelli, M. & Musumeci, G., 2018. Anti-clockwise pressure-temperature paths record Variscan upper-plate exhumation: example from micaschists of the Porto Vecchio region, Corsica. *Journal of Metamorphic Geology,* **36**, 55-77.

Menegon, L., Pennacchioni, G., Heilbronner, R. & Pittarello, L., 2008. Evolution of quartz microstructure and c-axis crystallographic preferred orientation withinductilely deformed granitoids (Arolla unit, Western Alps). *Journal of Structural Geology,* **30**, 1332-1347.

Merrihue, C. & Turner, G., 1966. Potassium-argon dating by activation with fast neutrons. *Journal of Geophysical Research*, **71**, 2852-2857.

Merrihue, C. M., 1965. Trace-element determinations and potassium-argon dating by mass spectroscopy of neutron-irradiated samples. *Transactions of the American Geophysical Union,* **46**, 125.

Metcalfe, R. P., 1993. Pressure, temperature and time constraints on metamorphism across the Main Central Thrust zone and High Himalayan Slab in the Garhwal Himalaya. In: *Himalayan Tectonics* (Treloar, P.J. and Searle, M.P, eds). *Geological Society of London Special Publication*, **74**, 485–509.

Montemagni, C., Fulignati, P., Iaccarino, S., Marianelli, P., Montomoli, C. & Sbrana, A. 2016. Deformation and fluid flow in the Munsiari Thrust (NW India): a preliminary fluid inclusion study. *Atti Società Toscana Scienze Naturali*, **123**, 67-77.

Montomoli, C., Carosi, R. & Iaccarino, S., 2015. Tectonometamorphic discontinuities in the Greater Himalayan Sequence: a local or a regional feature? In: *Tectonics of the Himalaya* (Mukherjee S., van der Beek, P. and Mukherjee, P.K., eds). *Geological Society of London Special Publication,* **412**, 21-41.

Montomoli, C., Carosi, R., Rubatto, D., Visonà, D. & Iaccarino, S., 2017a. Tectonic activity along the inner margin of the South Tibetan Detachment constrained by syntectonic leucogranite emplacement in Western Bhutan. *Italian Journal of Geosciences,* **136**, 5–14.

Montomoli, C., Iaccarino, S., Antolin, B., Apple, E., Carosi, R., Dunkl, I., Ding, L. & Visonà, D., 2017b. Tectono-metamorphic evolution of the Tethyan Sedimentary Sequence (Himalayas, SE Tibet). *Italian Journal of Geosciences*, **136**, 73-88.

Montomoli, C., Iaccarino, S., Carosi, R., Langone, A. & Visonà, D., 2013. Tectonometamorphic discontinuities within the Greater Himalayan Sequence in Western Nepal (Central Himalaya): Insights on the exhumation of crystalline rocks. *Tectonophysics,* **608**, 1349-1370.

Mottram, C. M., Argles, T. W., Harris, N. B. W., Parrish, R. R., Horstwood, M. S. A., Warren, C. J. & Gupta, S., 2014a. Tectonic interleaving along the Main Central Thrust, Sikkim Himalaya. *Journal of the Geological Society,* **171**, 255–268.

Mottram, C. M., Parrish, R. R., Regis, D., Warren, C. J., Argles, T. W., Harris, N. B. & Roberts, N. M., 2015. Using U-Th-Pb petrochronology to determine rates of ductile thrusting: Time windows into the Main Central Thrust, Sikkim Himalaya. *Tectonics*, **34**, 1355-1374.

Mottram, C. M., Warren, C. J., Regis, D., Roberts, N. M., Harris, N. B., Argles, T. W. & Parrish, R. R., 2014b. Developing an inverted Barrovian sequence; insights from monazite petrochronology. *Earth and Planetary Science Letters*, **403**, 418-431.

Mukhopadhyay, D. K., Chakraborty, S., Trepmann, C., Rubatto, D., Anczkiewicz, R., Gaidies, F., Dasgupta, S. & Chowdhury, P., 2017. The nature and evolution of the Main Central Thrust: Structural and geochronological constraints from the Sikkim Himalaya, NE India. *Lithos*, **282**, 447-463.

Müller, W., Kelley, S. P. & Villa, I. M., 2002. Dating fault-generated pseudotachylytes: Comparison of ^{40}Ar/^{39}Ar stepwise-heating, laser-ablation and Rb-Sr microsampling analyses. *Contributions to Mineralogy and Petrology*, **144**, 57-77.

Najman, Y., Jenks, D., Godin, L., Boudagher-Fadel, M., Millar, I., Garzanti, E., Horstwood, M. & Bracciali, L., 2017. The Tethyan Himalayan detrital record shows that India–Asia terminal collision occurred by 54 Ma in the Western Himalaya. *Earth and Planetary Science Letters*, **459**, 301-310.

Najman, Y., Jenks, D., Godin, L., Boudagher-Fadel, M., Millar, I., Garzanti, E., Horstwood, M. & Bracciali, L., 2017. The Tethyan Himalayan detrital record shows that India–Asia terminal collision occurred by 54 Ma in the Western Himalaya. *Earth and Planetary Science Letters*, **459**, 301-310.

Parsons, A. J., Law, R. D., Lloyd, G. E., Phillips, R. J. & Searle, M. P., 2016. Thermo-kinematic evolution of the Annapurna-Dhaulagiri Himalaya, central Nepal: the Composite Orogenic System. *Geochemistry, Geophysics, Geosystems*, **17**, 1511-1539.

Passchier, C. W. & Trouw, R. A. J., 2005. Microtectonics. *Second Edition. Springer, Berlin*.

Passchier, C.W., 1987. Stable position of rigid objects in noncoaxial flow: a study in vorticity analysis. *Journal of Structural Geology*, **9**, 679-690.

Pennacchioni, G., Menegon, L., Leiss, B., Nestola, F. & Bromiley, G., 2010. Development of crystallographic preferred orientation and microstructure during plastic deformation of natural coarse-grained quartz veins. *Journal of Geophysical Research: Solid Earth*, **115**(B12).

Peternell, M., Hasalová, P., Wilson, C. J., Piazolo, S. & Schulmann, K., 2010. Evaluating quartz crystallographic preferred orientations and the role of deformation partitioning using EBSD and fabric analyser techniques. *Journal of Structural Geology*, **32**, 803-817.

Platt, J. P., 1993. Exhumation of high-pressure rocks: a review of concept and processes. *Terra Nova*, **5**, 119–133.

Pognante, U. & Benna, P., 1993. Metamorphic zonation, migmatization and leucogranites along the Everest transect of eastern Nepal and Tibet: record of an exhumation history. *Geological Society, London, Special Publications*, **74**, 323-340.

Rivera, T. A., Storey, M., Zeeden, C., Hilgen, F. J., & Kuiper, K., 2011. A refined astronomically calibrated ^{40}Ar/^{39}Ar age for Fish Canyon sanidine. *Earth and Planetary Science Letters*, **311**, 420-426.

Robert, X., Van Der Beek, P., Braun, J., Perry, C. and Mugnier, J. L., 2011. Control of detachment geometry on lateral variations in exhumation rates in the Himalaya: Insights from low-temperature thermochronology and numerical modeling. *Journal of Geophysical Research, Solid Earth*, **116**(B5).

Robinson, D. M., 2008. Forward modeling the kinematic sequence of the central Himalayan thrust belt, western Nepal. *Geosphere*, **4**, 785-801.

Robinson, D. M., DeCelles, P. G., Garzione, C. N., Pearson, O. N., Harrison, T. M. & Catlos, E. J., 2001. The kinematic evolution of the Nepalese Himalaya interpreted from Nd isotopes. *Earth and Planetary Science Letters*, **192**, 507-521.

Rolland, Y., Cox, S. F. & Corsini, M., 2009. Constraining deformation stages in brittle–ductile shear zones from combined field mapping and ^{40}Ar/^{39}Ar dating: the structural evolution of the Grimsel Pass area (Aar Massif, Swiss Alps). *Journal of Structural Geology*, **31**, 1377-1394.

Sachan, H. K., Kohn, M. J., Saxena, A. & Corrie, S. L., 2010. The Malari leucogranite, Garhwal Himalaya, northern India: chemistry, age, and tectonic implications. *Geological Society of America Bulletin*, **122**, 1865-1876.

Saklani, P. S., Nainwal, D. C. & Singh, V. K., 1991. Geometry of the composite Main Central Thrust (MCT) in the Yamuna Valley, Garhwal Himalaya, India. *Neues Jahrbuch für Geologie und Palaeontologie: Monatshefte*, **6**, 364-380.

Sanchez, G., Rolland, Y., Schneider, J., Corsini, M., Oliot, E., Goncalves, P., Verati, C., Lardeaux, J. -M. & Marquer, D., 2011. Dating low-temperature deformation by ^{40}Ar/^{39}Ar on white mica, insights from the Argentera-Mercantour Massif (SW Alps). *Lithos*, **125**, 521-536.

Scaillet, B., France-Lanord, C. & Le Fort, P. 1990. Badrinath-Gangotri plutons (Garhwal, India): petrological and geochemical evidence for fractionation processes in a high Himalayan leucogranite. *Journal of Volcanology and Geothermal Research*, **44**, 163-188.

Scaillet, B., Pêcher, A., Rochette, P. & Champenois, M., 1995. The Gangotri granite (Garhwal Himalaya): laccolithic emplacement in an extending collisional belt. *Journal of Geophysical Research: Solid Earth*, **100**(B1), 585-607.

Schoene, B. & Bowring, S. A., 2006. U–Pb systematics of the McClure Mountain syenite: thermochronological constraints on the age of the ^{40}Ar/^{39}Ar standard MMhb. *Contributions to Mineralogy and Petrology*, **151**, 615.

Searle, M. P. & Godin, L., 2003. The south Tibetan detachment and the Manaslu Leucogranite: A structural reinterpretation and restoration of the Annapurna-Manaslu Himalaya, Nepal. *Journal of Geology*, **111**, 505-523.

Searle, M. P., 2013. Crustal melting, ductile flow, and deformation in mountain belts: Cause and effect relationships. *Lithospere*, **5(6)**, 547-554.

Searle, M. P., Cottle, J. M., Streule, M. J. & Waters, D. J., 2010. Crustal melt granites and migmatites along the Himalaya: melt source, segregation, transport and granite emplacement mechanisms. *Earth Environmental Science Transactions of the Royal Society of Edinburgh*, **100**, 219-233.

Searle, M. P., Law, R. D., Godin, L., Larson, K. P., Streule, M. J., Cottle, J. M. & Jessup, M. J., 2008. Defining the Himalayan Main Central Thrust in Nepal. *Journal of the Geological Society, London*, **165,** 523-534.

Searle, M. P., Metcalfe, R. P., Rex, A. J. & Norry, M. J., 1993. Field relations, petrogenesis and emplacement of the Bhagirathi leucogranite, Garhwal Himalaya. *Geological Society of London Special Publication*, **74**, 429-444.

Searle, M. P., Noble, S. R., Hurford, A. J. & Rex, D. C., 1999. Age of crustal melting, emplacement and exhumation history of the Shivling leucogranite, Garhwal Himalaya. *Geological Magazine*, **136**, 513-525.

Searle, M. P., Simpson, R. L., Law, R. D., Parrish, R. R. & Waters, D. J., 2003. The structural geometry, metamorphic and magmatic evolution of the Everest massif, High Himalaya of Nepal-South Tibet. *Journal of Geological Society* of *London*, **160**, 345-366.

Seitz, J.F., Tewari, A.P. and Obradovich, J., 1976. A note on the absolute age of the tourmaline-granite, Arwa valley, Garhwal Himalaya. Geol. Soc. India, Misc. Publ., 24(2): 332-337.

Sen, K., Chaudhurya, R. & Pfänder, J., 2015. ^{40}Ar–^{39}Ar age constraint on deformation and brittle–ductile transition of the Main Central Thrust and the South Tibetan Detachment zone from Dhauliganga valley, Garhwal Himalaya, India. *Journal of Geodynamics*, **88**, 1-13.

Shreshtha, M., Jain, A. K. & Singh, S., 2015. Shear sense analysis of the Higher Himalayan Crystalline (HHC) belt, and tectonics of the South Tibetan Detachment System (STDS), Alaknanda–Dhauli Ganga Valley, Uttarakhand Himalaya. *Current Science*, **108(6)**, 1107–1118.

Singh, S., 2019. Protracted zircon growth in migmatites and in situ melt of Higher Himalayan Crystallines: U–Pb ages from Bhagirathi Valley, NW Himalaya, India. *Geoscience Frontiers*, **10**, 793-809.

Singh, S., Mukherjee, P. K., Jain, A. K., Khanna, P. P., Saini, N. K. & Kumar, R., 2003. Source characterization and possible emplacement mechanism of collision-related Gangotri Leucogranite along Bhagirathi Valley, NW-Himalaya. *Journal of the Virtual Explorer*, **11**, 15-26.

Smit, J. H. W., Brun, J. P. & Sokoutis, D., 2003. Deformation of brittle-ductile thrust wedges in experiments and nature. *Journal of Geophysical Research: Solid Earth*, **108**(B10).

Sorkhabi, R. B., Stump, E., Foland, K.A. & Jain, A. K. 1996. Fission-track and ^{40}Ar/^{39}Ar evidence for isotopic denudation of the Gangotri granites in the Garhwal Higher Himalaya, India. *Tectonophysics*, **260**, 187–99.

Spear, F. S., 1993. Metamorphic Phase Equilibria and Pressure- Temperature-Time Paths. Mineralogical Society of America, Washington, DC, 799 pp.

Spencer, C. J., Harris, R. A. & Dorais, M. J., 2012. The metamorphism and exhumation of the Himalayan metamorphic core, eastern Garhwal region, India. *Tectonics*, **31**, 1-18.

Srivastava, P. & Mitra, G., 1994. Thrust geometries and deep structure of the outer and lesser Himalaya, Kumaun and Garhwal (India): Implications for evolution of the Himalayan fold-and-thrust belt. *Tectonics*, **13**, 89–109.

Steiger, R., & Jäger, E., 1977. Subcommission on geochronology: convention on the use of decay constants in geo-and cosmochronology. *Earth and Planetary Science Letters*, **36**, 359-362.

Stern, C. R., Kligfield, R., Schelling, D., Virdi, N. S., Futa, K., Peterman, Z. E. & Amini, H. 1989. The Bhagirathi leucogranite of the high Himalaya (Garhwal, India): age, petrogenesis and tectonic implications. In: *Tectonics of the Western Himalaya* (Malinconico, L.L. and Lillie, R. J., eds). *Geological Society of America Special Paper*, **232**, 33–45.

Stipp, M., Stunitz, H., Heilbronner, R. & Schmid, S. M., 2002a. The eastern Tonale fault zone: A natural laboratory for crystal plastic deformation over a temperature range from 250 to 700 °C. *Journal of Structural Geology*, **24**, 1861‑1884.

Stipp, M., Stunitz, H., Heilbronner, R. & Schmid, S. M., 2002b. Dynamic recrystallization of quartz: Correlation between natural and experimental conditions. In: *Deformation Mechanisms, Rheology and Tectonics: Current Status and Future Perspectives* (De Meer, S. et al., eds). Geological Society: Special Publications, **200**, 171-190.

Thakur, S. S., Patel, S. C. & Singh, A. K., 2015. A P-T pseudosection modelling approach to understand metamorphic evolution of the Main Central Thrust Zone in the Alaknanda valley, NW Himalaya. *Contribution to Mineralogy and Petrology*, **170**, 1-26.

Tikoff, B. & Fossen, H., 1995. The limitations of three-dimensional kinematic vorticity analysis. *Journal of Structural Geology*, **17**(12), 1771-1784.

Valdiya, K. S., 1980. The two intracrustal boundary thrusts of the Himalaya. *Tectonophysics*, **66**, 323-348.

Valdiya, K. S., Paul, S. K., Tarachandra-Bhakuni, S. S. & Upadhyay, R. C., 1999. Tectonic and Iithological characterization of Himadri (Great Himalaya) between Kali and Yamuna rivers, Central Himalaya. *Himalayan Geology*, **10**, 1-17.

Vance, D., Müller, W. & Villa, I. M., 2003. Geochronology: linking the isotopic record with petrology and textures—an introduction. In: *Geochronology: Linking the Isotopic Record* *with Petrology and Textures* (Vance, D., Müller, W. and Villa, I.M., eds). *Geological Society, London, Special Publications*, **220**, 1-24.

Vannay, J. C. & Grasemann, B., 2001. Himalayan inverted metamorphism and synconvergence extension as a consequence of a general shear extrusion. *Geological Magazine*, **138**, 253–276.

Vannay, J. C., Grasemann, B., Rahn, M., Frank, W., Carter, A., Baudraz, V. & Cosca, M., 2004. Miocene to Holocene exhumation of metamorphic crustal wedges in the NW Himalaya: Evidence for tectonic extrusion coupled to fluvial erosion. *Tectonics*, **23**.

Villa, I. M. & Hanchar, J. M., 2017. Age discordance and mineralogy. *American Mineralogist*: *Journal of Earth and Planetary Materials*, **102**, 2422-2439

Villa, I. M. & Williams, M. L., 2013. Geochronology of metasomatic events. In: *Metasomatism and the Chemical Transformation of Rock* (Harlov, D.E. and Austrheim, H., eds). Springer, Heidelberg, pp. 171–202.

Villa, I. M., 2010. Disequilibrium textures versus equilibrium modelling: geochronology at the crossroads. *Geological Society, London, Special Publications*, **332**, 1-15.

Villa, I. M., 2015. ^{39}Ar-^{40}Ar geochronology of mono-and polymetamorphic basement rocks. *Periodico di mineralogia*, **84**, 615-632.

Villa, I. M., Bosio, G. & Barberini, V., 2018. "Excess Ar" by artificial alteration of biotite. In: *EGU General Assembly Conference Abstracts*, **20**, p. 14338.

Villa, I. M., Bucher, S., Bousquet, R., Kleinhanns, I. C. & Schmid, S. M., 2014. Dating polygenetic metamorphic assemblages along a transect across the Western Alps. *Journal of Petrology*, **55**, 803-830.

Villa, I. M., Hermann, J., Müntener, O. & Trommsdorff, V. 2000. ^{39}Ar– ^{40}Ar dating of multiply zoned amphibole generations (Malenco, Italian Alps). *Contributions to Mineralogy and Petrology*, **140(3)**, 363-381.

Villa, I. M., Ruggieri, G., Puxeddu, M. & Bertini, G., 2006. Geochronology and isotope transport systematics in a subsurface granite from the Larderello–Travale geothermal system (Italy). *Journal of Volcanology and Geothermal Research*, **152**, 20–50.

Virdi, N. S., 1986. Lithostratigraphy and structure of Central Crystallines in the Alaknanda and Dhauliganga valleys of Garhwal U.P. Himalayan thrusts and associated rocks. In: *Current Trends in Geology* (Saklani, P.S., eds), **10**, 155–166.

Visonà, D. & Lombardo, B., 2002. Two-mica and tourmaline leucogranites from Everest-Makalu region (Nepal-Tibet). Himalayan leucogranites genesis by isobathic heating? *Lithos*, **62**, 125-150.

Visonà, D., Carosi, R., Montomoli, C., Peruzzo, M. & Tiepolo, L., 2012. Miocene andalusite leucogranite in central-east Himalaya (Everest–Masang Kang area): low-pressure melting during heating. *Lithos*, **144**, 194-208.

Wallis, S. R., Platt, J. P. & Knott, S. D., 1993. Recognition of syn-convergence extension in accretionary wedges with examples from the Calabrian arc and the eastern Alps. *American Journal of Science*, **293**, 463-495.

Waters, D. J. & Charnley, N. R., 2002. Local equilibrium in polymetamorphic gneiss and the titanium substitution in biotite. *American Mineralogist*, **87(4)**, 383-396.

Webb, A. A. G., Yin, A. & Dubey, C. S., 2013. U-Pb zircon geochronology of major lithologic units in the eastern Himalaya: implications for the origin and assembly of Himalayan rocks. *Geological Society of America Bulletin*, **125**, 499-522.

Webb, A. A. G., Yin, A., Harrison, T. M., Célérier, J. & Burgess, W. P., 2007. The leading edge of the Greater Himalayan Crystalline complex revealed in the NW Indian Himalaya: implications for the evolution of the Himalayan orogen. *Geology*, **35**, 955-958.

Weinberg, R. F., 2016. Himalayan leucogranites and migmatites: nature, timing and duration of anatexis, *Journal of Metamorphic Geology*, **34**, 821-843.

West Jr, D. P. & Lux, D. R., 1993. Dating mylonitic deformation by the 40Ar-39Ar method: An example from the Norumbega Fault Zone, Maine. *Earth and Planetary Science Letters*, **120**, 221-237.

Whitney, D. L. & Evans, B. W., 2010. Abbreviations for names of rock-forming minerals. *American Mineralogist*, **95**, 185-187.

Williams, M. L. & Jercinovic, M. J., 2002. Microprobe monazite geochronology: putting absolute time into microstructural analysis. *Journal of Structural Geology*, **24**, 1013–1028.

Williams, M. L., Jercinovic, M. J. & Hetherington, C. J., 2007. Microprobe Monazite Geochronology: Understanding Geologic Processes by Integrating Composition and Chronology. *Annual Review of Earth and Planetary Science*, **35**, 137–175.

Williams, M. L., Jercinovic, M. J. & Mahan, K. H., 2017. Electron Microprobe Petrochronology. *Reviews in Mineralogy & Geochemistry*, **83**, 153–182.

Williams, M. L., Jercinovic, M. J. & Terry, M., 1999. High resolution "age" mapping, chemical analysis, and chemical dating of monazite using the electron microprobe: A new tool for tectonic analysis. *Geology*, **27**, 1023–1026.

Wu, C. M. & Chen, H. X., 2015. Calibration of a Ti-in-muscovite geothermometer for ilmenite- and Al_2SiO_5-bearing metapelites. *Lithos*, **212**, 122-127.

Xypolias, P., 2010. Vorticity analysis in shear zones: a review of methods and applications. *Journal of Structural Geology*, **32**, 2072–2092.

Xypolias, P., Spanos, D., Chatzaras, V., Kokkalas, S. and Koukouvelas, I., 2010. Vorticity of flow in ductile thrust zones: examples from the Attico-Cycladic Massif (Internal Hellenides, Greece). In: *Continental Tectonics and Mountain Building: The Legacy of Peach and Horne* (Law, R.D., Butler, R.W.H., Holdsworth, R.E., Krabbendam, M. and Strachan, R.A., eds). *Geological Society of London Special Publication*, **335**, 687-714.

Yakymchuk, C. J. A. & Godin, L., 2012. Coupled role of deformation and metamorphism in the construction of inverted metamorphic sequences: an example from far northwest Nepal. *Journal of Metamorphic Geology*, **30**, 513–535.

Zanchetta, S., D'Adda, P., Zanchi, A., Barberini, V. & Villa, I. M., 2011. Cretaceous-Eocene compression in the central Southern Alps (N Italy) inferred from ^{40}Ar/^{39}Ar dating of pseudotachylytes along regional thrust faults. *Journal of. Geodynamic*, **51**, 245-263.

10: SUPPLEMENTARY MATERIAL APPENDIX 1: EMPA DATASET

SAMPLE	**GW13-39**																										
	ms	ms	ms	ms	ms	ms	ms	ms	ms	ms	ms	ms	ms	ms	ms	ms	ms	ms	ms	ms	ms	ms	ms	ms	ms	ms	ms
Spot number	1	2	3	4	5	6	7	8	9	10	11	12	13	14	15	33	34	35	36	37	38	39	40	41	42	43	44
OXIDES wt%																											
SiO_2	47.160	46.930	47.090	46.990	47.120	47.250	47.090	47.080	47.150	46.620	46.770	46.980	47.020	46.990	46.870	46.960	46.500	46.910	46.560	46.680	46.630	46.330	46.800	46.520	47.340	47.300	46.750
TiO_2	0.500	0.448	0.232	0.646	0.096	0.336	0.686	0.084	0.062	0.051	1.052	1.123	1.151	1.124	1.130	0.916	0.049	0.180	0.048	0.150	0.114	0.085	0.115	0.028	0.121	0.058	0.081
Al_2O_3	35.720	36.240	36.810	36.350	36.740	36.590	35.810	36.590	36.200	36.330	36.310	35.770	36.040	35.870	35.970	35.970	37.030	37.190	37.400	36.920	36.840	36.500	36.970	37.460	36.990	36.950	37.060
FeO	1.290	1.279	1.184	1.211	1.074	1.286	1.310	1.143	1.159	1.170	1.127	1.350	1.290	1.300	1.282	1.300	0.967	1.056	1.025	1.051	1.105	1.043	0.971	0.925	1.029	1.141	1.020
MnO	0.002	0.015	0.011	0.000	0.000	0.058	0.026	0.000	0.000	0.036	0.030	0.033	0.002	0.000	0.029	0.033	0.000	0.012	0.018	0.029	0.001	0.000	0.000	0.000	0.000	0.000	0.011
MgO	0.561	0.473	0.435	0.544	0.429	0.562	0.548	0.530	0.524	0.565	0.485	0.584	0.585	0.597	0.534	0.600	0.396	0.381	0.340	0.402	0.451	0.362	0.333	0.356	0.468	0.410	0.357
CaO	0.011	0.019	0.023	0.014	0.020	0.036	0.033	0.001	0.029	0.000	0.027	0.015	0.000	0.008	0.000	0.000	0.013	0.046	0.017	0.001	0.032	0.000	0.008	0.048	0.050	0.012	0.019
BaO	0.283	0.230	0.117	0.208	0.181	0.104	0.057	0.137	0.133	0.086	0.115	0.094	0.077	0.062	0.122	0.054	0.214	0.211	0.197	0.158	0.139	0.075	0.103	0.163	0.104	0.216	0.262
Na_2O	0.658	0.736	0.657	0.657	0.540	0.791	0.671	0.598	0.672	0.676	0.577	0.651	0.657	0.617	0.659	0.761	0.572	0.732	0.541	0.655	0.659	0.559	0.604	0.717	0.664	0.401	0.607
K_2O	10.550	10.590	10.420	10.720	10.470	10.640	10.550	10.690	10.630	10.750	10.500	10.430	10.680	10.500	10.580	10.630	10.770	10.600	10.830	10.530	10.640	10.550	11.020	10.450	10.720	10.830	10.680
F	0.000	0.000	0.000	0.000	0.000	0.000	0.000	0.000	0.000	0.000	0.000	0.000	0.000	0.000	0.000	0.000	0.000	0.000	0.000	0.000	0.000	0.000	0.000	0.000	0.000	0.000	0.000
Cl	0.021	0.018	0.006	0.010	0.024	0.012	0.010	0.017	0.007	0.004	0.009	0.021	0.011	0.024	0.000	0.027	0.000	0.000	0.004	0.000	0.012	0.000	0.034	0.018	0.047	0.014	0.000
tot	96.756	96.976	96.985	97.348	96.694	97.665	96.792	96.868	96.565	96.288	97.002	97.052	97.514	97.092	97.177	97.251	96.511	97.317	96.979	96.576	96.621	95.504	96.959	96.687	97.531	97.333	96.848
CATIONS apfu																											
Si	3.095	3.074	3.072	3.066	3.083	3.070	3.085	3.080	3.094	3.072	3.056	3.072	3.062	3.070	3.062	3.067	3.054	3.055	3.045	3.061	3.059	3.070	3.063	3.045	3.075	3.079	3.060
Ti	0.025	0.022	0.011	0.032	0.005	0.016	0.034	0.004	0.003	0.003	0.052	0.055	0.056	0.055	0.056	0.045	0.002	0.009	0.002	0.007	0.006	0.004	0.006	0.001	0.006	0.003	0.004
Al	2.763	2.797	2.830	2.795	2.833	2.802	2.765	2.821	2.799	2.821	2.797	2.757	2.766	2.762	2.770	2.769	2.867	2.855	2.882	2.853	2.849	2.850	2.852	2.890	2.832	2.835	2.859
Fe	0.071	0.070	0.065	0.066	0.059	0.070	0.072	0.063	0.064	0.064	0.062	0.074	0.070	0.071	0.070	0.071	0.053	0.057	0.056	0.058	0.061	0.058	0.053	0.051	0.056	0.062	0.056
Mn	0.000	0.001	0.001	0.000	0.000	0.003	0.001	0.000	0.000	0.002	0.002	0.002	0.000	0.000	0.002	0.002	0.000	0.001	0.001	0.002	0.000	0.000	0.000	0.000	0.000	0.000	0.001
Mg	0.055	0.046	0.042	0.053	0.042	0.054	0.054	0.052	0.051	0.055	0.047	0.057	0.057	0.058	0.052	0.058	0.039	0.037	0.033	0.039	0.044	0.036	0.033	0.035	0.045	0.040	0.035
Ca	0.001	0.001	0.002	0.001	0.001	0.003	0.002	0.000	0.002	0.000	0.002	0.001	0.000	0.001	0.000	0.000	0.001	0.003	0.001	0.000	0.002	0.000	0.001	0.003	0.003	0.001	0.001
Ba	0.007	0.006	0.003	0.005	0.005	0.003	0.001	0.003	0.003	0.002	0.003	0.002	0.002	0.002	0.003	0.001	0.006	0.005	0.005	0.004	0.004	0.002	0.003	0.004	0.003	0.006	0.007
Na	0.084	0.093	0.083	0.083	0.069	0.100	0.085	0.076	0.086	0.086	0.073	0.083	0.083	0.078	0.084	0.096	0.073	0.092	0.069	0.083	0.084	0.072	0.077	0.091	0.084	0.051	0.077
K	0.883	0.885	0.867	0.892	0.874	0.882	0.882	0.892	0.890	0.904	0.875	0.870	0.887	0.875	0.882	0.886	0.902	0.881	0.903	0.881	0.891	0.892	0.920	0.872	0.888	0.899	0.892
F	0.000	0.000	0.000	0.000	0.000	0.000	0.000	0.000	0.000	0.000	0.000	0.000	0.000	0.000	0.000	0.000	0.000	0.000	0.000	0.000	0.000	0.000	0.000	0.000	0.000	0.000	0.000
Cl	0.002	0.002	0.001	0.001	0.003	0.001	0.001	0.002	0.001	0.000	0.001	0.002	0.001	0.003	0.000	0.003	0.000	0.000	0.000	0.000	0.001	0.000	0.004	0.002	0.005	0.002	0.000
tot	6.986	6.998	6.977	6.994	6.971	7.005	6.983	6.992	6.992	7.011	6.969	6.974	6.985	6.974	6.980	6.999	6.997	6.995	6.998	6.988	7.000	6.983	7.010	6.994	6.997	6.977	6.991

SAMPLE	**GW13-39**																	**GW13-51**									
	ms	ms	ms	ms	ms	ms	ms	ms	ms	ms	ms	ms	ms	ms	ms	ms	ms	ms	ms	ms	ms	ms	ms	ms	ms	ms	ms
Spot number	45	46	47	48	49	50	51	52	53	54	58	63	64	65	71	72	73	74	75	76	77	78	79	80	81	82	85
OXIDES wt%																											
SiO_2	46.870	46.600	47.000	47.030	46.790	46.970	47.090	46.060	46.470	46.970	47.080	46.570	47.410	47.210	47.150	46.560	46.110	46.230	46.680	46.780	46.030	46.490	46.740	46.500	46.510	46.200	46.220
TiO_2	0.000	0.096	0.060	0.114	0.126	0.114	0.040	0.175	0.135	0.043	0.033	0.872	0.447	0.359	0.755	0.494	0.144	0.030	0.045	0.064	0.037	0.057	0.063	0.095	0.051	0.000	0.005
Al_2O_3	36.870	36.710	36.950	37.360	36.730	37.170	37.110	36.610	36.770	37.370	38.280	35.600	36.420	35.880	35.970	36.150	36.640	34.860	34.240	34.820	34.490	34.130	34.940	34.220	35.350	34.880	34.880
FeO	1.058	0.821	0.848	0.902	1.026	0.984	0.968	0.974	1.058	1.023	0.777	1.380	1.256	1.390	1.232	0.979	1.015	2.830	3.150	3.140	3.340	3.800	3.270	3.070	2.660	3.450	3.150
MnO	0.000	0.000	0.000	0.000	0.000	0.000	0.025	0.023	0.002	0.064	0.000	0.045	0.023	0.055	0.000	0.000	0.000	0.124	0.124	0.131	0.144	0.217	0.072	0.159	0.072	0.100	0.085
MgO	0.414	0.356	0.362	0.397	0.381	0.351	0.370	0.382	0.380	0.336	0.107	0.613	0.572	0.613	0.571	0.446	0.354	0.318	0.384	0.192	0.232	0.178	0.235	0.436	0.470	0.242	0.207
CaO	0.037	0.013	0.000	0.034	0.000	0.013	0.003	0.021	0.000	0.015	0.030	0.000	0.024	0.002	0.031	0.020	0.020	0.013	0.000	0.021	0.018	0.020	0.008	0.000	0.035	0.016	0.027
BaO	0.074	0.078	0.096	0.082	0.062	0.256	0.223	0.139	0.088	0.132	0.228	0.148	0.129	0.024	0.264	0.053	0.125	0.000	0.079	0.000	0.036	0.035	0.000	0.057	0.044	0.041	0.000
Na_2O	0.520	0.674	0.612	0.735	0.448	0.675	0.519	0.651	0.621	0.707	0.623	0.642	0.663	0.635	0.797	0.802	0.516	0.454	0.432	0.549	0.508	0.453	0.482	0.407	0.473	0.420	0.524
K_2O	10.760	10.800	10.720	10.620	10.850	10.730	11.090	10.620	10.710	10.600	10.770	10.630	10.460	10.700	10.660	10.490	10.720	10.430	10.400	10.550	10.490	10.340	10.410	10.430	10.550	10.500	10.390
F	0.000	0.000	0.000	0.000	0.000	0.000	0.000	0.000	0.000	0.000	0.000	0.000	0.000	0.000	0.000	0.000	0.000	0.199	0.286	0.050	0.591	0.661	0.598	0.364	0.139	0.465	0.099
Cl	0.027	0.000	0.004	0.006	0.014	0.017	0.028	0.035	0.018	0.000	0.029	0.001	0.033	0.020	0.014	0.000	0.027	0.021	0.012	0.017	0.019	0.011	0.015	0.000	0.017	0.011	0.026
tot	96.629	96.148	96.651	97.281	96.426	97.279	97.466	95.692	96.251	97.261	97.957	96.500	97.439	96.887	97.445	95.993	95.670	95.509	95.832	96.313	95.935	96.390	96.833	95.738	96.369	96.326	95.612
CATIONS apfu																											
Si	3.072	3.069	3.075	3.058	3.073	3.061	3.067	3.053	3.060	3.057	3.042	3.068	3.083	3.092	3.076	3.071	3.056	3.104	3.133	3.111	3.114	3.136	3.123	3.129	3.090	3.103	3.098
Ti	0.000	0.005	0.003	0.006	0.006	0.006	0.002	0.009	0.007	0.002	0.002	0.043	0.022	0.018	0.037	0.024	0.007	0.002	0.002	0.003	0.002	0.003	0.003	0.005	0.003	0.000	0.000
Al	2.848	2.849	2.849	2.863	2.843	2.855	2.849	2.860	2.854	2.867	2.915	2.764	2.791	2.770	2.766	2.810	2.862	2.758	2.709	2.729	2.750	2.714	2.751	2.714	2.768	2.761	2.755
Fe	0.058	0.045	0.046	0.049	0.056	0.054	0.053	0.054	0.058	0.056	0.042	0.076	0.068	0.076	0.067	0.054	0.056	0.159	0.177	0.175	0.189	0.214	0.183	0.173	0.148	0.194	0.177
Mn	0.000	0.000	0.000	0.000	0.000	0.000	0.001	0.001	0.000	0.004	0.000	0.002	0.001	0.003	0.000	0.000	0.000	0.007	0.007	0.007	0.008	0.012	0.004	0.009	0.004	0.006	0.005
Mg	0.040	0.035	0.035	0.039	0.037	0.034	0.036	0.038	0.037	0.033	0.010	0.060	0.055	0.060	0.056	0.044	0.035	0.032	0.038	0.019	0.023	0.018	0.023	0.044	0.047	0.024	0.021
Ca	0.003	0.001	0.000	0.002	0.000	0.001	0.000	0.002	0.000	0.001	0.002	0.000	0.002	0.000	0.002	0.001	0.001	0.001	0.000	0.001	0.001	0.001	0.001	0.000	0.002	0.001	0.002
Ba	0.002	0.002	0.002	0.002	0.002	0.007	0.006	0.004	0.002	0.003	0.006	0.004	0.003	0.001	0.007	0.001	0.003	0.000	0.002	0.000	0.001	0.001	0.000	0.002	0.001	0.001	0.000
Na	0.066	0.086	0.078	0.093	0.057	0.085	0.066	0.084	0.079	0.089	0.078	0.082	0.084	0.081	0.101	0.103	0.066	0.059	0.056	0.071	0.067	0.059	0.062	0.053	0.061	0.055	0.068
K	0.900	0.907	0.895	0.881	0.909	0.892	0.922	0.898	0.900	0.880	0.888	0.893	0.868	0.894	0.887	0.883	0.906	0.893	0.890	0.895	0.905	0.890	0.887	0.895	0.894	0.900	0.888
F	0.000	0.000	0.000	0.000	0.000	0.000	0.000	0.000	0.000	0.000	0.000	0.000	0.000	0.000	0.000	0.000	0.000	0.042	0.061	0.010	0.127	0.141	0.126	0.077	0.029	0.099	0.021
Cl	0.003	0.000	0.000	0.001	0.002	0.002	0.003	0.004	0.002	0.000	0.003	0.000	0.004	0.002	0.002	0.000	0.003	0.002	0.001	0.002	0.002	0.001	0.002	0.000	0.002	0.001	0.003
tot	6.991	6.999	6.984	6.993	6.985	6.997	7.004	7.005	6.999	6.992	6.987	6.994	6.981	6.996	7.000	6.992	6.997	7.059	7.077	7.023	7.189	7.192	7.165	7.100	7.048	7.144	7.038

SAMPLE	**GW13-51**																										
	ms	ms	ms	ms	ms	ms	ms	ms	ms	ms	ms	ms	ms	ms	ms	ms	ms	ms	ms	ms	ms	ms	ms	ms	ms	ms	ms
Spot number	86	87	88	89	90	94	95	96	97	98	99	100	101	102	103	104	105	106	107	108	109	110	111	112	113	114	115
OXIDES wt%																											
SiO_2	46.640	46.490	46.000	46.910	46.970	46.700	46.390	47.390	49.140	46.740	46.740	47.140	46.570	46.530	46.620	46.540	46.750	46.690	47.010	46.710	47.000	46.710	45.970	46.950	46.290	47.040	47.140
TiO_2	0.034	0.075	0.080	0.106	0.000	0.031	0.031	0.064	0.000	0.112	0.048	0.055	0.031	0.000	0.071	0.005	0.049	0.051	0.106	0.051	0.110	0.086	0.049	0.071	0.025	0.010	0.039
Al_2O_3	34.940	34.990	34.420	33.950	34.480	35.150	35.460	34.790	31.410	34.820	34.910	34.780	35.160	34.680	34.390	35.150	34.080	33.990	34.020	34.190	34.260	34.140	34.510	34.500	34.350	33.080	33.090
FeO	3.060	2.940	3.620	3.470	3.050	3.000	2.470	2.760	2.710	3.510	3.090	3.120	2.900	3.690	3.950	3.300	3.890	3.930	3.710	3.570	3.180	3.830	3.450	3.700	3.970	4.540	3.780
MnO	0.040	0.109	0.181	0.113	0.102	0.059	0.032	0.069	0.039	0.064	0.069	0.023	0.098	0.122	0.099	0.095	0.069	0.124	0.108	0.096	0.117	0.128	0.111	0.112	0.112	0.128	0.164
MgO	0.307	0.232	0.117	0.134	0.338	0.128	0.129	0.472	2.330	0.100	0.141	0.096	0.132	0.097	0.097	0.080	0.127	0.102	0.107	0.267	0.401	0.180	0.215	0.215	0.129	0.093	0.286
CaO	0.026	0.000	0.044	0.074	0.010	0.015	0.000	0.033	0.020	0.000	0.023	0.008	0.012	0.037	0.000	0.016	0.002	0.000	0.026	0.013	0.031	0.055	0.011	0.007	0.041	0.016	0.000
BaO	0.013	0.043	0.039	0.013	0.000	0.000	0.019	0.000	0.017	0.000	0.007	0.000	0.042	0.000	0.000	0.000	0.000	0.036	0.000	0.026	0.079	0.030	0.000	0.000	0.000	0.000	0.101
Na_2O	0.450	0.458	0.513	0.497	0.479	0.552	0.601	0.427	0.157	0.568	0.609	0.553	0.513	0.519	0.610	0.468	0.508	0.450	0.474	0.385	0.323	0.412	0.379	0.473	0.623	0.443	0.318
K_2O	10.390	10.330	10.490	10.180	10.390	10.430	11.080	10.760	11.060	10.350	10.600	10.530	10.650	10.710	10.420	10.540	10.340	10.510	10.370	10.320	10.440	10.340	10.260	10.410	10.250	10.250	10.470
F	0.196	0.241	0.729	0.466	0.341	0.380	0.073	0.144	0.917	0.552	0.589	0.790	0.520	0.117	0.610	0.482	0.488	0.383	0.310	0.092	0.228	0.231	0.030	0.000	0.769	0.514	0.473
Cl	0.054	0.022	0.004	0.018	0.015	0.011	0.004	0.000	0.000	0.000	0.007	0.021	0.000	0.011	0.006	0.012	0.016	0.015	0.008	0.002	0.018	0.005	0.009	0.008	0.001	0.000	0.000
tot	96.151	95.930	96.237	95.931	96.175	96.455	96.290	96.907	97.800	96.815	96.833	97.115	96.630	96.513	96.874	96.687	96.320	96.280	96.249	95.723	96.186	96.146	94.994	96.447	96.559	96.116	95.859
CATIONS apfu																											
Si	3.111	3.109	3.115	3.156	3.139	3.115	3.086	3.130	3.269	3.123	3.124	3.150	3.113	3.104	3.128	3.110	3.143	3.139	3.148	3.128	3.138	3.130	3.099	3.119	3.125	3.179	3.184
Ti	0.002	0.004	0.004	0.005	0.000	0.002	0.002	0.003	0.000	0.006	0.002	0.003	0.002	0.000	0.004	0.000	0.002	0.003	0.005	0.003	0.006	0.004	0.002	0.004	0.001	0.001	0.002
Al	2.747	2.758	2.747	2.692	2.716	2.763	2.780	2.708	2.463	2.742	2.750	2.739	2.770	2.727	2.719	2.768	2.700	2.693	2.685	2.699	2.696	2.696	2.742	2.701	2.733	2.634	2.634
Fe	0.171	0.164	0.205	0.195	0.170	0.167	0.137	0.152	0.151	0.196	0.173	0.174	0.162	0.206	0.222	0.184	0.219	0.221	0.208	0.200	0.178	0.215	0.194	0.206	0.224	0.257	0.214
Mn	0.002	0.006	0.010	0.006	0.006	0.003	0.002	0.004	0.002	0.004	0.004	0.001	0.006	0.007	0.006	0.005	0.004	0.007	0.006	0.005	0.007	0.007	0.006	0.006	0.006	0.007	0.009
Mg	0.031	0.023	0.012	0.013	0.034	0.013	0.013	0.046	0.231	0.010	0.014	0.010	0.013	0.010	0.010	0.008	0.013	0.010	0.011	0.027	0.040	0.018	0.022	0.021	0.013	0.009	0.029
Ca	0.002	0.000	0.003	0.005	0.001	0.001	0.000	0.002	0.001	0.000	0.002	0.001	0.001	0.003	0.000	0.001	0.000	0.000	0.002	0.001	0.002	0.004	0.001	0.001	0.003	0.001	0.000
Ba	0.000	0.001	0.001	0.000	0.000	0.000	0.001	0.000	0.000	0.000	0.000	0.000	0.001	0.000	0.000	0.000	0.000	0.001	0.000	0.001	0.002	0.001	0.000	0.000	0.000	0.000	0.003
Na	0.058	0.059	0.067	0.065	0.062	0.071	0.077	0.055	0.020	0.074	0.079	0.072	0.067	0.067	0.079	0.061	0.066	0.059	0.062	0.050	0.042	0.054	0.050	0.061	0.082	0.058	0.042
K	0.884	0.881	0.906	0.874	0.886	0.887	0.940	0.907	0.938	0.882	0.904	0.898	0.908	0.911	0.892	0.898	0.887	0.901	0.886	0.882	0.889	0.884	0.882	0.882	0.883	0.884	0.902
F	0.041	0.051	0.156	0.099	0.072	0.080	0.015	0.030	0.193	0.117	0.124	0.167	0.110	0.025	0.129	0.102	0.104	0.081	0.066	0.020	0.048	0.049	0.006	0.000	0.164	0.110	0.101
Cl	0.006	0.003	0.000	0.002	0.002	0.001	0.000	0.000	0.000	0.000	0.001	0.002	0.000	0.001	0.001	0.001	0.002	0.002	0.001	0.000	0.002	0.001	0.001	0.001	0.000	0.000	0.000
tot	7.056	7.059	7.228	7.114	7.087	7.104	7.055	7.038	7.269	7.153	7.177	7.216	7.152	7.061	7.189	7.140	7.139	7.117	7.078	7.015	7.049	7.061	7.005	7.000	7.235	7.139	7.120

SAMPLE	**GW13-51**		**GW13-57**																								
	ms	ms	ms	ms	ms	ms	ms	ms	ms	ms	ms	ms	ms	ms	ms	ms	ms	ms	ms	ms	ms	ms	ms	ms	ms	ms	ms
Spot number	116	117	118	119	120	123	124	125	126	127	128	129	130	131	132	133	134	135	136	137	138	139	140	141	142	143	144
OXIDES wt%																											
SiO_2	46.720	46.600	46.610	46.850	46.840	47.080	46.940	47.210	46.690	46.860	46.990	46.750	46.590	46.870	46.450	46.670	46.280	46.780	46.770	47.270	47.450	47.460	47.600	47.490	47.410	47.380	47.350
TiO_2	0.055	0.136	0.166	0.148	0.153	0.060	0.123	0.135	0.121	0.154	0.148	0.076	0.438	0.163	0.161	0.187	0.155	0.124	0.284	0.081	0.109	0.111	0.114	0.109	0.057	0.109	0.124
Al_2O_3	35.220	33.970	35.540	36.230	36.280	36.520	36.450	36.200	36.340	36.310	36.320	36.250	35.650	36.330	36.180	35.650	35.700	36.480	36.260	36.350	36.600	36.690	36.800	36.810	36.830	37.010	36.520
FeO	3.100	3.410	1.540	1.490	1.560	1.610	1.660	1.470	1.950	1.630	1.700	1.490	1.720	1.550	1.350	1.670	1.750	1.480	1.470	1.560	1.460	1.670	1.650	1.620	1.640	1.600	1.440
MnO	0.138	0.200	0.000	0.000	0.021	0.044	0.036	0.021	0.010	0.000	0.000	0.018	0.000	0.005	0.020	0.005	0.000	0.016	0.000	0.000	0.008	0.051	0.000	0.003	0.013	0.003	0.018
MgO	0.268	0.377	0.555	0.486	0.438	0.403	0.464	0.613	0.548	0.468	0.517	0.446	0.507	0.482	0.412	0.483	0.466	0.433	0.465	0.427	0.446	0.444	0.471	0.444	0.443	0.451	0.410
CaO	0.004	0.041	0.007	0.005	0.039	0.020	0.040	0.030	0.040	0.021	0.011	0.005	0.004	0.020	0.000	0.005	0.021	0.027	0.026	0.019	0.001	0.030	0.017	0.000	0.000	0.004	0.027
BaO	0.000	0.009	0.000	0.001	0.000	0.038	0.000	0.021	0.011	0.094	0.053	0.000	0.000	0.000	0.002	0.051	0.000	0.007	0.000	0.038	0.000	0.002	0.000	0.000	0.009	0.000	0.028
Na_2O	0.425	0.351	0.761	0.757	0.801	0.795	0.873	0.687	0.955	0.884	0.884	0.780	0.904	0.812	0.834	0.931	0.825	0.500	0.635	0.790	0.721	0.837	0.797	0.763	0.902	0.860	0.679
K_2O	10.460	10.470	10.610	10.780	10.540	10.510	10.490	10.790	10.140	10.200	10.220	10.500	10.490	10.330	10.510	10.390	10.350	10.890	10.690	10.530	10.590	10.480	10.580	10.400	10.440	10.410	10.610
F	0.079	0.140	0.000	0.000	0.000	0.000	0.000	0.000	0.000	0.000	0.000	0.000	0.000	0.000	0.000	0.000	0.000	0.000	0.000	0.000	0.000	0.000	0.000	0.000	0.000	0.000	0.000
Cl	0.027	0.035	0.013	0.000	0.001	0.017	0.010	0.000	0.000	0.002	0.006	0.011	0.012	0.008	0.009	0.018	0.025	0.000	0.011	0.025	0.011	0.000	0.000	0.021	0.002	0.022	0.000
tot	96.496	95.738	95.802	96.747	96.674	97.096	97.086	97.176	96.806	96.622	96.849	96.326	96.315	96.571	95.928	96.058	95.572	96.736	96.610	97.089	97.396	97.775	98.028	97.660	97.747	97.849	97.205
CATIONS apfu																											
Si	3.099	3.128	3.090	3.076	3.075	3.077	3.070	3.084	3.062	3.075	3.077	3.078	3.076	3.076	3.071	3.087	3.077	3.070	3.072	3.088	3.087	3.079	3.079	3.080	3.075	3.069	3.087
Ti	0.003	0.007	0.008	0.007	0.008	0.003	0.006	0.007	0.006	0.008	0.007	0.004	0.022	0.008	0.008	0.009	0.008	0.006	0.014	0.004	0.005	0.005	0.006	0.005	0.003	0.005	0.006
Al	2.753	2.688	2.777	2.803	2.807	2.813	2.810	2.787	2.809	2.808	2.803	2.813	2.774	2.810	2.819	2.779	2.797	2.822	2.807	2.799	2.806	2.805	2.806	2.814	2.815	2.825	2.806
Fe	0.172	0.191	0.085	0.082	0.086	0.088	0.091	0.080	0.107	0.089	0.093	0.082	0.095	0.085	0.075	0.092	0.097	0.081	0.081	0.085	0.079	0.091	0.089	0.088	0.089	0.087	0.079
Mn	0.008	0.011	0.000	0.000	0.001	0.002	0.002	0.001	0.001	0.000	0.000	0.001	0.000	0.000	0.001	0.000	0.000	0.001	0.000	0.000	0.000	0.003	0.000	0.000	0.001	0.000	0.001
Mg	0.027	0.038	0.055	0.048	0.043	0.039	0.045	0.060	0.054	0.046	0.050	0.044	0.050	0.047	0.041	0.048	0.046	0.042	0.045	0.042	0.043	0.043	0.045	0.043	0.043	0.044	0.040
Ca	0.000	0.003	0.001	0.000	0.003	0.001	0.003	0.002	0.003	0.001	0.001	0.000	0.000	0.001	0.000	0.000	0.001	0.002	0.002	0.001	0.000	0.002	0.001	0.000	0.000	0.000	0.002
Ba	0.000	0.000	0.000	0.000	0.000	0.001	0.000	0.001	0.000	0.002	0.001	0.000	0.000	0.000	0.000	0.001	0.000	0.000	0.000	0.001	0.000	0.000	0.000	0.000	0.000	0.000	0.001
Na	0.055	0.046	0.098	0.096	0.102	0.101	0.111	0.087	0.122	0.112	0.112	0.100	0.116	0.103	0.107	0.119	0.106	0.064	0.081	0.100	0.091	0.105	0.100	0.096	0.113	0.108	0.086
K	0.885	0.897	0.897	0.903	0.883	0.876	0.875	0.899	0.848	0.854	0.854	0.882	0.883	0.865	0.886	0.877	0.878	0.912	0.896	0.878	0.879	0.867	0.873	0.860	0.864	0.860	0.882
F	0.016	0.030	0.000	0.000	0.000	0.000	0.000	0.000	0.000	0.000	0.000	0.000	0.000	0.000	0.000	0.000	0.000	0.000	0.000	0.000	0.000	0.000	0.000	0.000	0.000	0.000	0.000
Cl	0.003	0.004	0.001	0.000	0.000	0.002	0.001	0.000	0.000	0.000	0.001	0.001	0.001	0.001	0.001	0.002	0.003	0.000	0.001	0.003	0.001	0.000	0.000	0.002	0.000	0.002	0.000
tot	7.021	7.043	7.013	7.015	7.007	7.004	7.014	7.008	7.012	6.997	6.999	7.004	7.017	6.997	7.009	7.015	7.013	7.000	7.000	7.001	6.992	7.000	6.999	6.989	7.003	7.001	6.988

SAMPLE	GW13-57						GW13-29B																				
	ms	ms	ms	ms	ms	ms	ms	ms	ms	ms	ms	ms	ms	ms	ms	ms	ms	ms	ms	ms	ms	ms	ms	ms	ms	ms	ms
Spot number	145	146	147	148	149	150	189	190	191	192	193	194	195	196	197	198	199	200	201	202	203	204	205	206	207	208	209
OXIDES wt%																											
SiO_2	47.120	47.300	47.100	47.200	47.020	47.580	46.187	45.652	45.714	45.832	44.996	45.930	46.472	45.749	45.169	45.244	45.394	44.844	45.109	46.420	46.042	45.505	44.993	45.203	45.577	44.863	44.519
TiO_2	0.127	0.136	0.090	0.128	0.073	0.136	0.671	0.646	0.677	0.607	0.727	0.661	0.646	0.649	0.669	0.674	0.667	0.654	0.671	0.646	0.637	0.554	0.662	0.424	0.452	0.512	0.360
Al_2O_3	36.460	36.940	36.370	36.510	36.540	36.750	32.594	32.126	32.090	32.642	33.235	32.396	32.372	33.554	33.271	32.266	32.523	33.290	33.086	32.160	32.744	34.391	32.969	34.029	33.985	34.127	33.978
FeO	1.450	1.480	1.540	1.440	1.560	1.490	2.614	2.605	2.718	2.265	1.814	2.145	2.093	1.859	1.994	2.070	2.089	1.973	1.979	2.245	2.177	1.708	1.995	1.898	1.993	1.876	2.016
MnO	0.015	0.000	0.046	0.032	0.003	0.000	0.000	0.017	0.000	0.005	0.031	0.000	0.037	0.000	0.000	0.000	0.000	0.000	0.000	0.000	0.000	0.000	0.022	0.008	0.013	0.000	0.000
MgO	0.388	0.445	0.440	0.409	0.472	0.459	1.403	1.365	1.375	1.199	1.026	1.237	1.234	0.925	1.045	1.260	1.111	0.955	1.001	1.371	1.257	0.794	0.952	0.852	0.925	0.784	0.846
CaO	0.000	0.043	0.000	0.000	0.026	0.027	0.000	0.013	0.000	0.000	0.000	0.000	0.013	0.028	0.000	0.000	0.017	0.000	0.014	0.000	0.011	0.029	0.011	0.006	0.000	0.022	0.000
BaO	0.099	0.064	0.000	0.022	0.000	0.000	0.198	0.207	0.284	0.249	0.253	0.203	0.249	0.195	0.249	0.250	0.277	0.220	0.240	0.223	0.234	0.231	0.215	0.229	0.186	0.241	0.261
Na_2O	0.753	0.818	0.873	0.779	0.761	0.711	0.573	0.565	0.574	0.623	0.609	0.539	0.523	0.640	0.588	0.539	0.574	0.532	0.547	0.585	0.484	0.651	0.629	0.581	0.647	0.604	0.625
K_2O	10.640	10.430	10.460	10.430	10.570	10.460	10.769	10.828	10.497	10.862	10.708	10.853	10.661	10.898	10.610	10.991	10.900	10.952	10.934	10.879	10.981	10.904	10.809	11.038	11.054	10.945	11.117
F	0.000	0.000	0.000	0.000	0.000	0.000	0.000	0.000	0.059	0.192	0.054	0.066	0.299	0.037	0.016	0.097	0.064	0.056	0.221	0.029	0.057	0.104	0.084	0.011	0.093	0.077	0.000
Cl	0.018	0.007	0.009	0.000	0.016	0.010	0.000	0.004	0.004	0.008	0.000	0.014	0.004	0.000	0.004	0.006	0.000	0.005	0.000	0.013	0.000	0.011	0.002	0.005	0.001	0.000	0.000
tot	97.069	97.662	96.928	96.950	97.040	97.623	95.009	94.028	93.992	94.484	93.453	94.044	94.603	94.534	93.615	93.397	93.616	93.481	93.802	94.571	94.624	94.882	93.343	94.284	94.926	94.051	93.722
CATIONS apfu																											
Si	3.081	3.069	3.082	3.083	3.074	3.085	3.121	3.122	3.124	3.114	3.083	3.130	3.143	3.098	3.089	3.112	3.113	3.078	3.085	3.147	3.121	3.068	3.091	3.073	3.078	3.058	3.053
Ti	0.006	0.007	0.004	0.006	0.004	0.007	0.034	0.033	0.035	0.031	0.037	0.034	0.033	0.033	0.034	0.035	0.034	0.034	0.035	0.033	0.032	0.028	0.034	0.022	0.023	0.026	0.019
Al	2.810	2.825	2.805	2.811	2.816	2.808	2.596	2.589	2.585	2.614	2.684	2.602	2.580	2.678	2.682	2.615	2.628	2.693	2.667	2.570	2.616	2.733	2.670	2.727	2.705	2.742	2.746
Fe	0.079	0.080	0.084	0.079	0.085	0.081	0.148	0.149	0.155	0.129	0.104	0.122	0.118	0.105	0.114	0.119	0.120	0.113	0.113	0.127	0.123	0.096	0.115	0.108	0.113	0.107	0.116
Mn	0.001	0.000	0.003	0.002	0.000	0.000	0.000	0.001	0.000	0.000	0.002	0.000	0.002	0.000	0.000	0.000	0.000	0.000	0.000	0.000	0.000	0.000	0.001	0.000	0.001	0.000	0.000
Mg	0.038	0.043	0.043	0.040	0.046	0.044	0.141	0.139	0.140	0.121	0.105	0.126	0.124	0.093	0.107	0.129	0.114	0.098	0.102	0.139	0.127	0.080	0.097	0.086	0.093	0.080	0.086
Ca	0.000	0.003	0.000	0.000	0.002	0.002	0.000	0.001	0.000	0.000	0.000	0.000	0.001	0.002	0.000	0.000	0.001	0.000	0.001	0.000	0.001	0.002	0.001	0.000	0.000	0.002	0.000
Ba	0.003	0.002	0.000	0.001	0.000	0.000	0.005	0.006	0.008	0.007	0.007	0.005	0.007	0.005	0.007	0.007	0.007	0.006	0.006	0.006	0.006	0.006	0.006	0.006	0.005	0.006	0.007
Na	0.095	0.103	0.111	0.099	0.096	0.089	0.075	0.075	0.076	0.082	0.081	0.071	0.069	0.084	0.078	0.072	0.076	0.071	0.073	0.077	0.064	0.085	0.084	0.077	0.085	0.080	0.083
K	0.887	0.863	0.873	0.869	0.882	0.865	0.928	0.945	0.915	0.941	0.936	0.944	0.920	0.941	0.926	0.964	0.953	0.959	0.954	0.941	0.949	0.938	0.947	0.957	0.952	0.952	0.973
F	0.000	0.000	0.000	0.000	0.000	0.000	0.000	0.000	0.013	0.041	0.012	0.014	0.064	0.008	0.003	0.021	0.014	0.012	0.048	0.006	0.012	0.022	0.018	0.002	0.020	0.017	0.000
Cl	0.002	0.001	0.001	0.000	0.002	0.001	0.000	0.000	0.000	0.001	0.000	0.002	0.000	0.000	0.000	0.001	0.000	0.001	0.000	0.001	0.000	0.001	0.000	0.001	0.000	0.000	0.000
tot	7.002	6.996	7.005	6.989	7.006	6.983	7.049	7.060	7.051	7.081	7.051	7.050	7.061	7.047	7.040	7.075	7.061	7.063	7.084	7.048	7.052	7.060	7.065	7.060	7.075	7.069	7.083

SAMPLE	GW13-29B																										
	ms	ms	ms	ms	ms	ms	ms	ms	ms	ms	ms	ms	ms	ms	ms	ms	ms	ms	ms	ms	ms	ms	ms	ms	ms	ms	ms
Spot number	210	211	212	213	214	215	216	217	218	219	220	221	222	223	224	225	226	227	228	229	230	231	232	233	234	235	236
OXIDES wt%																											
SiO_2	45.511	45.625	45.896	45.727	44.981	45.734	45.558	44.467	44.970	45.396	46.168	45.772	45.674	45.205	45.036	44.020	45.625	45.406	44.632	46.012	47.000	45.618	46.279	45.370	44.703	44.151	45.000
TiO_2	0.367	0.487	0.651	0.627	0.330	0.357	0.372	0.512	0.572	0.559	0.465	0.494	0.704	0.626	0.654	0.572	0.677	0.677	0.657	0.612	0.672	0.716	0.681	0.607	0.667	0.644	0.652
Al_2O_3	34.393	34.645	32.940	32.547	33.979	34.869	34.201	33.252	32.808	34.393	34.255	33.794	33.241	32.445	33.093	33.307	32.999	33.551	32.530	31.888	32.791	33.076	33.150	32.016	32.120	31.501	32.031
FeO	2.051	1.904	2.209	2.125	1.973	1.860	2.036	2.075	2.043	1.932	1.986	1.990	2.024	2.123	1.980	1.796	2.064	2.235	2.134	2.295	2.024	2.192	2.183	2.372	2.394	2.137	2.204
MnO	0.000	0.035	0.018	0.000	0.014	0.000	0.000	0.000	0.012	0.000	0.004	0.000	0.000	0.000	0.000	0.000	0.025	0.012	0.000	0.000	0.023	0.006	0.026	0.000	0.027	0.000	0.000
MgO	0.859	0.799	1.194	1.254	0.774	0.768	0.877	0.919	1.086	0.744	0.910	0.925	1.142	1.126	0.942	0.806	1.113	0.967	1.091	1.386	1.101	1.050	1.147	1.237	1.142	1.108	1.225
CaO	0.000	0.018	0.015	0.003	0.015	0.000	0.000	0.000	0.000	0.001	0.000	0.000	0.014	0.004	0.020	0.000	0.010	0.004	0.000	0.011	0.000	0.000	0.010	0.000	0.015	0.018	0.000
BaO	0.238	0.220	0.180	0.247	0.237	0.200	0.204	0.210	0.236	0.278	0.239	0.238	0.269	0.195	0.229	0.186	0.262	0.210	0.288	0.181	0.231	0.209	0.230	0.207	0.181	0.204	0.189
Na_2O	0.574	0.651	0.539	0.507	0.581	0.623	0.584	0.550	0.581	0.647	0.623	0.598	0.582	0.500	0.559	0.572	0.510	0.620	0.487	0.514	0.572	0.621	0.576	0.499	0.554	0.611	0.496
K_2O	10.832	11.063	10.946	11.098	10.901	10.827	10.999	11.004	10.989	10.909	10.879	10.991	10.900	10.901	10.875	11.062	10.562	10.826	10.863	10.873	10.854	10.823	10.999	10.913	10.527	10.827	10.957
F	0.000	0.119	0.030	0.236	0.000	0.126	0.183	0.102	0.119	0.098	0.000	0.069	0.158	0.000	0.062	0.092	0.000	0.000	0.000	0.000	0.000	0.000	0.007	0.039	0.000	0.052	0.068
Cl	0.007	0.026	0.000	0.006	0.005	0.004	0.004	0.007	0.000	0.006	0.000	0.000	0.010	0.011	0.000	0.000	0.000	0.005	0.000	0.000	0.003	0.000	0.000	0.012	0.000	0.005	0.016
tot	94.832	95.592	94.618	94.377	93.790	95.368	95.018	93.098	93.416	94.963	95.529	94.871	94.718	93.136	93.450	92.413	93.847	94.513	92.682	93.772	95.271	94.311	95.288	93.272	92.330	91.258	92.838
CATIONS apfu																											
Si	3.072	3.059	3.111	3.112	3.074	3.065	3.073	3.069	3.092	3.063	3.092	3.091	3.092	3.114	3.090	3.059	3.110	3.082	3.094	3.147	3.154	3.102	3.115	3.125	3.107	3.112	3.114
Ti	0.019	0.025	0.033	0.032	0.017	0.018	0.019	0.027	0.030	0.028	0.023	0.025	0.036	0.032	0.034	0.030	0.035	0.035	0.034	0.031	0.034	0.037	0.034	0.031	0.035	0.034	0.034
Al	2.737	2.738	2.631	2.611	2.737	2.754	2.719	2.705	2.658	2.735	2.704	2.690	2.653	2.634	2.676	2.728	2.651	2.684	2.658	2.571	2.594	2.651	2.630	2.599	2.631	2.617	2.613
Fe	0.116	0.107	0.125	0.121	0.113	0.104	0.115	0.120	0.117	0.109	0.111	0.112	0.115	0.122	0.114	0.104	0.118	0.127	0.124	0.131	0.114	0.125	0.123	0.137	0.139	0.126	0.128
Mn	0.000	0.002	0.001	0.000	0.001	0.000	0.000	0.000	0.001	0.000	0.000	0.000	0.000	0.000	0.000	0.000	0.001	0.001	0.000	0.000	0.001	0.000	0.001	0.000	0.002	0.000	0.000
Mg	0.086	0.080	0.121	0.127	0.079	0.077	0.088	0.095	0.111	0.075	0.091	0.093	0.115	0.116	0.096	0.083	0.113	0.098	0.113	0.141	0.110	0.106	0.115	0.127	0.118	0.116	0.126
Ca	0.000	0.001	0.001	0.000	0.001	0.000	0.000	0.000	0.000	0.000	0.000	0.000	0.001	0.000	0.001	0.000	0.001	0.000	0.000	0.001	0.000	0.000	0.001	0.000	0.001	0.001	0.000
Ba	0.006	0.006	0.005	0.007	0.006	0.005	0.005	0.006	0.006	0.007	0.006	0.006	0.007	0.005	0.006	0.005	0.007	0.006	0.008	0.005	0.006	0.006	0.006	0.006	0.005	0.006	0.005
Na	0.075	0.085	0.071	0.067	0.077	0.081	0.076	0.074	0.077	0.085	0.081	0.078	0.076	0.067	0.074	0.077	0.067	0.082	0.065	0.068	0.074	0.082	0.075	0.067	0.075	0.083	0.067
K	0.933	0.946	0.946	0.963	0.950	0.926	0.946	0.969	0.964	0.939	0.929	0.947	0.941	0.958	0.952	0.980	0.919	0.937	0.961	0.949	0.929	0.939	0.944	0.959	0.933	0.973	0.967
F	0.000	0.025	0.006	0.051	0.000	0.027	0.039	0.022	0.026	0.021	0.000	0.015	0.034	0.000	0.013	0.020	0.000	0.000	0.000	0.000	0.000	0.000	0.001	0.008	0.000	0.012	0.015
Cl	0.001	0.003	0.000	0.001	0.001	0.000	0.000	0.001	0.000	0.001	0.000	0.000	0.001	0.001	0.000	0.000	0.000	0.001	0.000	0.000	0.000	0.000	0.000	0.001	0.000	0.001	0.002
tot	7.045	7.077	7.052	7.092	7.055	7.057	7.080	7.085	7.083	7.063	7.038	7.058	7.072	7.050	7.058	7.087	7.022	7.051	7.056	7.044	7.017	7.047	7.046	7.061	7.046	7.081	7.071

SAMPLE	GW13-29B																										
	ms	ms	ms	ms	ms	ms	ms	ms	ms	ms	ms	bt	bt	bt	bt	bt	bt	bt	bt	bt	bt	bt	bt	bt	bt	bt	bt
Spot number	237	238	239	240	241	242	243	244	245	246	247	316	317	318	319	320	321	322	323	324	325	326	327	328	329	330	331
OXIDES wt%																											
SiO_2	44.553	45.400	44.016	45.539	44.264	43.137	45.383	45.126	45.376	45.612	44.991	33.886	34.761	33.989	33.689	34.254	34.365	34.481	33.811	33.835	35.191	33.384	33.995	34.907	34.314	34.594	34.162
TiO_2	0.449	0.627	0.594	0.694	0.612	0.595	0.664	0.682	0.595	0.641	0.634	2.127	2.127	1.556	2.215	2.649	1.910	2.707	2.370	2.245	2.120	1.967	2.195	1.983	1.857	2.192	2.193
Al_2O_3	33.016	33.260	32.944	33.199	32.793	32.184	32.562	32.772	33.316	33.447	32.364	17.617	17.819	18.157	17.473	17.840	18.029	17.770	16.720	17.022	17.948	17.460	17.428	17.780	17.473	17.717	17.126
FeO	2.096	1.966	2.133	2.119	2.139	2.138	2.318	2.190	2.022	2.121	2.147	24.255	24.105	24.390	24.208	24.178	24.273	24.323	24.414	24.572	24.221	24.707	24.497	24.506	24.465	24.565	23.905
MnO	0.000	0.019	0.005	0.000	0.000	0.004	0.000	0.000	0.010	0.000	0.000	0.090	0.075	0.070	0.093	0.048	0.062	0.000	0.050	0.087	0.114	0.058	0.110	0.123	0.006	0.108	0.114
MgO	1.028	1.028	0.962	1.053	0.995	1.003	1.179	1.038	0.894	0.938	1.234	6.929	7.189	7.221	6.863	6.699	6.967	6.621	7.037	6.936	7.155	7.020	7.057	7.121	7.110	7.073	6.929
CaO	0.000	0.000	0.007	0.008	0.000	0.000	0.007	0.000	0.003	0.008	0.014	0.000	0.001	0.000	0.003	0.041	0.003	0.048	0.020	0.000	0.000	0.032	0.010	0.000	0.006	0.000	0.007
BaO	0.248	0.230	0.233	0.230	0.236	0.214	0.223	0.214	0.236	0.267	0.258	0.100	0.117	0.102	0.146	0.153	0.132	0.142	0.147	0.128	0.138	0.160	0.117	0.170	0.128	0.154	0.174
Na_2O	0.555	0.593	0.603	0.553	0.522	0.596	0.574	0.493	0.523	0.629	0.514	0.131	0.116	0.094	0.139	0.112	0.121	0.115	0.127	0.082	0.115	0.108	0.078	0.111	0.092	0.112	0.115
K_2O	10.773	10.876	10.909	10.999	10.858	10.709	10.810	10.709	10.814	10.765	10.894	9.501	9.629	9.414	9.457	9.557	9.537	9.621	9.522	9.634	9.575	9.567	9.655	9.496	9.735	9.538	9.710
F	0.067	0.051	0.102	0.000	0.062	0.000	0.005	0.084	0.000	0.077	0.000	0.277	0.256	0.278	0.216	0.149	0.103	0.114	0.242	0.139	0.229	0.071	0.070	0.180	0.041	0.187	0.122
Cl	0.003	0.005	0.004	0.000	0.000	0.000	0.000	0.010	0.008	0.001	0.002	0.018	0.017	0.028	0.020	0.027	0.034	0.022	0.033	0.026	0.021	0.023	0.037	0.029	0.027	0.031	0.023
tot	92.788	94.055	92.512	94.394	92.481	90.580	93.725	93.318	93.797	94.506	93.052	94.931	96.212	95.299	94.522	95.707	95.536	95.964	94.493	94.706	96.827	94.557	95.249	96.406	95.254	96.271	94.580
CATIONS apfu																											
Si	3.081	3.094	3.061	3.096	3.076	3.064	3.109	3.100	3.099	3.093	3.106	2.672	2.695	2.666	2.671	2.675	2.687	2.686	2.688	2.685	2.708	2.657	2.678	2.704	2.700	2.688	2.705
Ti	0.023	0.032	0.031	0.035	0.032	0.032	0.034	0.035	0.031	0.033	0.033	0.126	0.124	0.092	0.132	0.156	0.112	0.159	0.142	0.134	0.123	0.118	0.130	0.116	0.110	0.128	0.131
Al	2.691	2.671	2.700	2.660	2.685	2.695	2.629	2.653	2.681	2.673	2.633	1.637	1.628	1.679	1.633	1.642	1.662	1.631	1.566	1.592	1.628	1.638	1.618	1.623	1.620	1.623	1.598
Fe	0.121	0.112	0.124	0.120	0.124	0.127	0.133	0.126	0.115	0.120	0.124	1.600	1.563	1.600	1.605	1.579	1.587	1.585	1.623	1.631	1.558	1.645	1.614	1.588	1.610	1.596	1.583
Mn	0.000	0.001	0.000	0.000	0.000	0.000	0.000	0.000	0.001	0.000	0.000	0.006	0.005	0.005	0.006	0.003	0.004	0.000	0.003	0.006	0.007	0.004	0.007	0.008	0.000	0.007	0.008
Mg	0.106	0.104	0.100	0.107	0.103	0.106	0.120	0.106	0.091	0.095	0.127	0.814	0.831	0.844	0.811	0.780	0.812	0.769	0.834	0.820	0.821	0.833	0.829	0.822	0.834	0.819	0.818
Ca	0.000	0.000	0.001	0.001	0.000	0.000	0.001	0.000	0.000	0.001	0.001	0.000	0.000	0.000	0.000	0.003	0.000	0.004	0.002	0.000	0.000	0.003	0.001	0.000	0.001	0.000	0.001
Ba	0.007	0.006	0.006	0.006	0.006	0.006	0.006	0.006	0.006	0.007	0.007	0.003	0.004	0.003	0.005	0.005	0.004	0.004	0.005	0.004	0.004	0.005	0.004	0.005	0.004	0.005	0.005
Na	0.074	0.078	0.081	0.073	0.070	0.082	0.076	0.066	0.069	0.083	0.069	0.020	0.017	0.014	0.021	0.017	0.018	0.017	0.020	0.013	0.017	0.017	0.012	0.017	0.014	0.017	0.018
K	0.950	0.945	0.968	0.954	0.962	0.970	0.945	0.938	0.942	0.931	0.959	0.956	0.952	0.942	0.956	0.952	0.951	0.956	0.966	0.975	0.940	0.971	0.970	0.938	0.977	0.945	0.981
F	0.015	0.011	0.022	0.000	0.014	0.000	0.001	0.018	0.000	0.017	0.000	0.069	0.063	0.069	0.054	0.037	0.025	0.028	0.061	0.035	0.056	0.018	0.017	0.044	0.010	0.046	0.031
Cl	0.000	0.001	0.000	0.000	0.000	0.000	0.000	0.001	0.001	0.000	0.000	0.002	0.002	0.004	0.003	0.004	0.005	0.003	0.004	0.003	0.003	0.003	0.005	0.004	0.004	0.004	0.003
tot	7.070	7.056	7.094	7.052	7.073	7.083	7.054	7.050	7.036	7.053	7.059	7.906	7.884	7.917	7.898	7.853	7.869	7.842	7.913	7.898	7.864	7.911	7.885	7.870	7.883	7.879	7.881

SAMPLE	GW13-29B																							GW13-29			
	bt	bt	bt	bt	bt	bt	bt	bt	bt	bt	bt	bt	bt	bt	bt	bt	bt	bt	bt	bt	bt	bt	bt	bt	bt	bt	bt
Spot number	332	333	334	335	336	337	338	339	340	341	342	343	344	345	346	347	348	349	350	351	352	353	354	1	2	3	4
OXIDES wt%																											
SiO_2	34.134	34.378	34.128	34.372	34.184	34.693	34.691	34.999	34.025	35.215	34.785	35.444	35.001	35.176	35.230	34.727	35.003	33.722	34.917	34.432	34.543	34.798	34.526	34.539	34.278	34.601	34.727
TiO_2	2.128	2.158	2.325	2.275	2.260	2.269	2.235	2.392	2.132	2.394	2.375	2.272	2.524	2.507	2.300	2.445	2.407	2.212	2.534	2.307	2.454	2.497	2.427	2.966	2.877	3.072	3.014
Al_2O_3	17.526	17.504	17.400	17.150	17.130	17.623	17.742	17.598	17.300	17.676	17.492	17.694	17.910	17.524	17.407	17.589	17.014	16.667	17.436	17.421	17.441	17.524	17.250	17.364	16.975	17.239	17.194
FeO	24.188	24.654	24.127	24.142	23.819	24.280	24.305	24.753	23.913	22.470	22.364	22.690	22.192	22.706	23.221	25.019	24.495	24.237	25.021	24.448	25.191	24.994	24.704	23.240	23.392	23.226	23.037
MnO	0.081	0.022	0.068	0.088	0.019	0.000	0.075	0.097	0.018	0.036	0.054	0.066	0.000	0.017	0.056	0.045	0.067	0.028	0.041	0.118	0.053	0.114	0.127	0.125	0.118	0.178	0.120
MgO	6.808	6.961	6.903	6.805	6.884	7.077	6.898	6.977	6.909	7.969	7.868	8.343	8.040	7.884	7.917	6.974	6.876	6.803	7.130	6.980	7.060	7.014	7.087	6.896	7.155	6.869	6.861
CaO	0.007	0.022	0.000	0.004	0.014	0.000	0.003	0.015	0.025	0.008	0.006	0.000	0.000	0.010	0.000	0.000	0.000	0.015	0.000	0.003	0.000	0.028	0.000	0.025	0.025	0.000	0.028
BaO	0.204	0.128	0.181	0.152	0.157	0.180	0.121	0.189	0.094	0.199	0.169	0.200	0.201	0.160	0.166	0.153	0.198	0.186	0.218	0.179	0.166	0.205	0.171	0.178	0.205	0.154	0.194
Na_2O	0.190	0.168	0.074	0.140	0.093	0.105	0.106	0.075	0.133	0.106	0.093	0.128	0.078	0.081	0.070	0.097	0.104	0.092	0.096	0.164	0.148	0.102	0.081	0.152	0.082	0.160	0.152
K_2O	9.610	9.396	9.722	9.243	9.564	9.458	9.767	9.563	9.548	9.619	9.588	9.646	9.741	9.549	9.884	9.549	9.581	9.531	9.676	9.544	9.625	9.639	9.696	9.537	9.363	9.268	9.493
F	0.000	0.263	0.193	0.302	0.145	0.210	0.069	0.097	0.151	0.250	0.312	0.140	0.243	0.198	0.293	0.127	0.244	0.300	0.274	0.192	0.176	0.129	0.000	0.242	0.147	0.129	0.114
Cl	0.023	0.020	0.024	0.025	0.023	0.019	0.027	0.032	0.022	0.021	0.014	0.013	0.027	0.031	0.017	0.025	0.021	0.022	0.040	0.021	0.020	0.033	0.023	0.020	0.023	0.019	0.020
tot	94.899	95.674	95.145	94.698	94.292	95.914	96.039	96.787	94.270	95.963	95.120	96.636	95.957	95.843	96.561	96.750	96.010	93.815	97.383	95.809	96.877	97.077	96.092	95.284	94.640	94.915	94.954
CATIONS apfu																											
Si	2.695	2.689	2.687	2.711	2.710	2.700	2.701	2.705	2.699	2.714	2.707	2.714	2.697	2.716	2.712	2.689	2.727	2.699	2.688	2.691	2.678	2.689	2.696	2.699	2.700	2.710	2.719
Ti	0.126	0.127	0.138	0.135	0.135	0.133	0.131	0.139	0.127	0.139	0.139	0.131	0.146	0.146	0.133	0.142	0.141	0.133	0.147	0.136	0.143	0.145	0.143	0.174	0.170	0.181	0.177
Al	1.631	1.614	1.615	1.594	1.600	1.616	1.628	1.603	1.617	1.606	1.605	1.597	1.626	1.595	1.580	1.605	1.562	1.572	1.582	1.605	1.594	1.596	1.587	1.599	1.576	1.591	1.587
Fe	1.597	1.613	1.589	1.592	1.579	1.580	1.582	1.600	1.586	1.448	1.456	1.453	1.430	1.466	1.495	1.620	1.596	1.622	1.611	1.598	1.633	1.615	1.613	1.519	1.541	1.521	1.509
Mn	0.005	0.001	0.005	0.006	0.001	0.000	0.005	0.006	0.001	0.002	0.004	0.004	0.000	0.001	0.004	0.003	0.004	0.002	0.003	0.008	0.003	0.007	0.008	0.008	0.008	0.012	0.008
Mg	0.801	0.812	0.810	0.800	0.813	0.821	0.800	0.804	0.817	0.915	0.913	0.952	0.923	0.907	0.909	0.805	0.798	0.812	0.818	0.813	0.816	0.808	0.825	0.803	0.840	0.802	0.801
Ca	0.001	0.002	0.000	0.000	0.001	0.000	0.000	0.001	0.002	0.001	0.001	0.000	0.000	0.001	0.000	0.000	0.000	0.001	0.000	0.000	0.000	0.002	0.000	0.002	0.002	0.000	0.002
Ba	0.006	0.004	0.006	0.005	0.005	0.005	0.004	0.006	0.003	0.006	0.005	0.006	0.006	0.005	0.005	0.005	0.006	0.006	0.007	0.005	0.005	0.006	0.005	0.005	0.006	0.005	0.006
Na	0.029	0.025	0.011	0.021	0.014	0.016	0.016	0.011	0.020	0.016	0.014	0.019	0.012	0.012	0.010	0.015	0.016	0.014	0.014	0.025	0.022	0.015	0.012	0.023	0.013	0.024	0.023
K	0.968	0.938	0.976	0.930	0.967	0.939	0.970	0.943	0.966	0.946	0.952	0.942	0.957	0.941	0.971	0.943	0.952	0.973	0.950	0.952	0.952	0.950	0.966	0.951	0.941	0.926	0.948
F	0.000	0.065	0.048	0.075	0.036	0.052	0.017	0.024	0.038	0.061	0.077	0.034	0.059	0.048	0.071	0.031	0.060	0.076	0.067	0.047	0.043	0.032	0.000	0.060	0.037	0.032	0.028
Cl	0.003	0.003	0.003	0.003	0.003	0.003	0.004	0.004	0.003	0.003	0.002	0.002	0.004	0.004	0.002	0.003	0.003	0.003	0.005	0.003	0.003	0.004	0.003	0.003	0.003	0.003	0.003
tot	7.863	7.892	7.887	7.872	7.866	7.864	7.858	7.846	7.879	7.857	7.874	7.855	7.860	7.843	7.892	7.862	7.866	7.915	7.892	7.884	7.892	7.869	7.858	7.846	7.838	7.806	7.811

SAMPLE	**GW13-29**																										
	bt	bt	bt	bt	bt	bt	bt	ms	ms	ms	ms	ms	ms	bt	bt	bt	bt	bt	bt	bt	bt	bt	bt	bt	bt	ms	ms
Spot number	5	6	7	8	9	10	11	12	13	14	15	16	17	18	19	20	21	22	23	24	25	26	27	28	29	30	31
OXIDES wt%																											
SiO_2	34.387	34.286	34.383	34.502	34.254	33.959	34.520	45.374	45.712	45.325	45.212	45.595	45.045	34.085	33.970	34.278	34.162	34.415	34.038	34.502	34.276	34.828	34.755	35.022	34.684	45.436	45.618
TiO_2	3.002	2.984	3.062	3.036	2.966	2.951	2.846	0.492	0.457	0.484	0.497	0.589	0.509	2.667	2.527	2.484	2.577	2.577	2.465	2.369	2.357	2.082	2.102	2.172	1.913	0.279	0.275
Al_2O_3	16.861	17.181	16.618	16.901	17.029	17.024	17.211	33.456	32.534	32.927	32.901	33.205	33.316	16.925	17.337	17.269	17.143	17.020	17.283	16.971	17.145	17.727	17.798	17.526	18.065	34.516	34.607
FeO	22.996	23.207	23.140	23.065	23.361	23.402	23.679	2.035	2.051	2.036	2.016	1.995	2.076	24.187	23.570	23.146	23.801	23.725	23.757	23.781	23.224	23.441	23.609	23.527	23.252	1.883	2.064
MnO	0.106	0.181	0.127	0.120	0.119	0.124	0.168	0.000	0.030	0.000	0.000	0.053	0.017	0.187	0.165	0.159	0.209	0.110	0.145	0.137	0.151	0.123	0.136	0.088	0.187	0.035	0.000
MgO	6.733	6.682	6.841	6.843	6.727	6.899	7.007	0.832	1.040	0.997	0.887	0.962	0.943	6.581	6.722	6.665	6.733	6.659	7.007	7.062	6.859	7.262	7.281	7.231	7.309	0.741	0.754
CaO	0.024	0.000	0.014	0.000	0.000	0.017	0.029	0.000	0.000	0.000	0.001	0.029	0.001	0.036	0.031	0.013	0.007	0.032	0.029	0.000	0.011	0.004	0.000	0.000	0.056	0.013	0.014
BaO	0.220	0.243	0.161	0.245	0.210	0.203	0.188	0.299	0.289	0.343	0.291	0.305	0.261	0.174	0.191	0.153	0.202	0.151	0.144	0.150	0.130	0.146	0.124	0.109	0.092	0.318	0.277
Na_2O	0.166	0.143	0.092	0.148	0.094	0.163	0.102	0.586	0.561	0.577	0.580	0.616	0.603	0.073	0.120	0.125	0.073	0.075	0.094	0.057	0.077	0.062	0.116	0.084	0.077	0.612	0.605
K_2O	9.482	9.245	9.535	9.613	9.561	9.374	9.381	10.921	10.681	10.744	10.457	10.863	10.888	9.496	9.527	9.435	9.574	9.570	9.514	9.541	9.575	9.533	9.598	9.647	9.599	10.552	10.786
F	0.101	0.158	0.125	0.153	0.014	0.233	0.118	0.050	0.100	0.123	0.078	0.000	0.050	0.128	0.218	0.205	0.166	0.105	0.152	0.185	0.253	0.226	0.104	0.113	0.071	0.000	0.072
Cl	0.029	0.026	0.019	0.022	0.017	0.021	0.021	0.000	0.000	0.000	0.000	0.001	0.000	0.024	0.028	0.031	0.026	0.021	0.025	0.023	0.021	0.022	0.014	0.015	0.025	0.002	0.001
tot	94.107	94.336	94.117	94.648	94.352	94.370	95.270	94.045	93.455	93.556	92.920	94.213	93.709	94.563	94.406	93.963	94.673	94.460	94.653	94.778	94.079	95.456	95.637	95.534	95.330	94.387	95.073
CATIONS apfu																											
Si	2.722	2.706	2.724	2.717	2.710	2.687	2.702	3.094	3.132	3.106	3.112	3.104	3.085	2.702	2.690	2.716	2.700	2.721	2.688	2.718	2.716	2.713	2.705	2.727	2.704	3.076	3.071
Ti	0.179	0.177	0.182	0.180	0.176	0.176	0.168	0.025	0.024	0.025	0.026	0.030	0.026	0.159	0.150	0.148	0.153	0.153	0.146	0.140	0.140	0.122	0.123	0.127	0.112	0.014	0.014
Al	1.573	1.598	1.551	1.569	1.588	1.587	1.588	2.689	2.627	2.659	2.669	2.664	2.689	1.581	1.618	1.613	1.597	1.586	1.609	1.576	1.601	1.627	1.633	1.608	1.660	2.754	2.746
Fe	1.522	1.532	1.533	1.519	1.546	1.548	1.550	0.116	0.118	0.117	0.116	0.114	0.119	1.604	1.561	1.534	1.573	1.569	1.569	1.567	1.539	1.527	1.537	1.532	1.516	0.107	0.116
Mn	0.007	0.012	0.009	0.008	0.008	0.008	0.011	0.000	0.002	0.000	0.000	0.003	0.001	0.013	0.011	0.011	0.014	0.007	0.010	0.009	0.010	0.008	0.009	0.006	0.012	0.002	0.000
Mg	0.794	0.786	0.808	0.803	0.793	0.814	0.818	0.085	0.106	0.102	0.091	0.098	0.096	0.778	0.793	0.787	0.793	0.785	0.825	0.829	0.810	0.843	0.845	0.839	0.849	0.075	0.076
Ca	0.002	0.000	0.001	0.000	0.000	0.001	0.002	0.000	0.000	0.000	0.000	0.002	0.000	0.003	0.003	0.001	0.001	0.003	0.002	0.000	0.001	0.000	0.000	0.000	0.005	0.001	0.001
Ba	0.007	0.008	0.005	0.008	0.007	0.006	0.006	0.008	0.008	0.009	0.008	0.008	0.007	0.005	0.006	0.005	0.006	0.005	0.004	0.005	0.004	0.004	0.004	0.003	0.003	0.008	0.007
Na	0.025	0.022	0.014	0.023	0.014	0.025	0.015	0.077	0.075	0.077	0.077	0.081	0.080	0.011	0.018	0.019	0.011	0.011	0.014	0.009	0.012	0.009	0.018	0.013	0.012	0.080	0.079
K	0.957	0.931	0.963	0.966	0.965	0.946	0.937	0.950	0.934	0.939	0.918	0.943	0.951	0.960	0.962	0.954	0.965	0.965	0.959	0.959	0.968	0.947	0.953	0.958	0.955	0.911	0.926
F	0.025	0.039	0.031	0.038	0.004	0.058	0.029	0.011	0.022	0.027	0.017	0.000	0.011	0.032	0.055	0.051	0.041	0.026	0.038	0.046	0.063	0.056	0.026	0.028	0.018	0.000	0.015
Cl	0.004	0.003	0.003	0.003	0.002	0.003	0.003	0.000	0.000	0.000	0.000	0.000	0.000	0.003	0.004	0.004	0.003	0.003	0.003	0.003	0.003	0.003	0.002	0.002	0.003	0.000	0.000
tot	7.819	7.815	7.824	7.833	7.812	7.860	7.829	7.055	7.046	7.061	7.034	7.047	7.065	7.852	7.871	7.843	7.859	7.835	7.868	7.862	7.866	7.859	7.854	7.842	7.848	7.029	7.052

SAMPLE	**GW13-29**																										
	ms	ms	ms	ms	ms	ms	ms	ms	ms	ms	ms	ms	ms	ms	ms	ms	ms	ms	ms	bt	bt	bt	bt	bt	bt	bt	bt
Spot number	32	33	34	35	36	37	38	39	40	41	42	43	44	45	46	47	48	49	50	51	52	53	54	55	56	57	58
OXIDES wt%																											
SiO_2	46.089	45.943	45.811	45.533	45.631	45.933	45.791	45.779	45.428	45.543	45.592	45.635	45.727	45.905	46.003	45.809	45.950	45.571	45.901	34.695	34.795	34.641	34.567	34.517	34.556	34.402	34.485
TiO_2	0.289	0.262	0.307	0.344	0.721	0.739	0.767	0.731	0.697	0.684	0.784	0.787	0.797	0.771	0.781	0.781	0.737	0.764	0.744	2.937	2.977	2.882	2.941	2.876	2.816	2.887	2.891
Al_2O_3	33.927	34.142	34.274	34.457	33.071	32.708	32.423	32.460	32.666	32.702	32.485	32.407	32.328	32.585	32.292	32.241	32.007	32.814	32.474	16.882	16.867	16.680	16.765	16.916	16.708	16.536	16.829
FeO	1.905	2.034	2.101	2.093	2.197	2.154	2.262	2.267	2.069	2.125	2.249	2.218	2.200	2.348	2.112	1.994	2.082	2.083	2.084	23.673	23.673	23.939	23.679	23.743	24.141	24.178	23.863
MnO	0.013	0.000	0.048	0.000	0.000	0.023	0.000	0.000	0.023	0.000	0.017	0.000	0.000	0.028	0.015	0.036	0.000	0.000	0.037	0.101	0.118	0.111	0.151	0.152	0.099	0.054	0.119
MgO	0.889	0.763	0.854	0.786	0.990	1.023	1.176	1.137	1.006	1.096	1.063	1.079	1.109	1.104	1.069	1.060	1.098	1.081	1.076	6.967	6.889	6.982	6.972	6.856	7.048	6.962	7.040
CaO	0.010	0.052	0.035	0.015	0.000	0.000	0.003	0.004	0.006	0.000	0.001	0.001	0.011	0.000	0.000	0.017	0.003	0.000	0.014	0.000	0.006	0.090	0.000	0.000	0.000	0.000	0.000
BaO	0.266	0.296	0.293	0.304	0.344	0.306	0.310	0.338	0.306	0.299	0.309	0.310	0.312	0.373	0.265	0.308	0.300	0.209	0.334	0.145	0.231	0.229	0.228	0.203	0.198	0.176	0.183
Na_2O	0.647	0.624	0.558	0.634	0.589	0.559	0.543	0.542	0.677	0.562	0.620	0.563	0.522	0.588	0.504	0.567	0.460	0.572	0.507	0.080	0.113	0.061	0.069	0.073	0.057	0.084	0.032
K_2O	10.664	10.799	10.676	11.009	10.805	10.776	10.974	10.663	10.715	10.516	10.440	10.393	10.716	10.918	10.645	10.817	10.809	10.835	10.953	9.587	9.428	9.462	9.532	9.593	9.729	9.593	9.685
F	0.000	0.094	0.011	0.033	0.000	0.072	0.172	0.006	0.111	0.000	0.017	0.045	0.000	0.000	0.000	0.078	0.017	0.117	0.106	0.180	0.114	0.184	0.048	0.204	0.212	0.156	0.090
Cl	0.003	0.000	0.001	0.000	0.000	0.003	0.002	0.000	0.005	0.000	0.000	0.000	0.000	0.002	0.002	0.000	0.010	0.000	0.000	0.013	0.019	0.029	0.022	0.023	0.022	0.020	0.033
tot	94.702	95.009	94.969	95.208	94.348	94.296	94.423	93.927	93.709	93.527	93.577	93.438	93.722	94.622	93.688	93.708	93.473	94.046	94.230	95.260	95.230	95.290	94.974	95.156	95.586	95.048	95.250
CATIONS apfu																											
Si	3.109	3.095	3.086	3.068	3.104	3.123	3.116	3.126	3.110	3.117	3.121	3.126	3.129	3.119	3.143	3.134	3.150	3.106	3.126	2.717	2.725	2.717	2.719	2.711	2.708	2.712	2.708
Ti	0.015	0.013	0.016	0.017	0.037	0.038	0.039	0.038	0.036	0.035	0.040	0.041	0.041	0.039	0.040	0.040	0.038	0.039	0.038	0.173	0.175	0.170	0.174	0.170	0.166	0.171	0.171
Al	2.697	2.711	2.722	2.736	2.651	2.621	2.601	2.612	2.635	2.638	2.621	2.616	2.607	2.609	2.600	2.600	2.586	2.636	2.607	1.558	1.557	1.542	1.554	1.566	1.543	1.536	1.558
Fe	0.107	0.115	0.118	0.118	0.125	0.122	0.129	0.129	0.118	0.122	0.129	0.127	0.126	0.133	0.121	0.114	0.119	0.119	0.119	1.550	1.550	1.571	1.558	1.559	1.582	1.594	1.567
Mn	0.001	0.000	0.003	0.000	0.000	0.001	0.000	0.000	0.001	0.000	0.001	0.000	0.000	0.002	0.001	0.002	0.000	0.000	0.002	0.007	0.008	0.007	0.010	0.010	0.007	0.004	0.008
Mg	0.089	0.077	0.086	0.079	0.100	0.104	0.119	0.116	0.103	0.112	0.108	0.110	0.113	0.112	0.109	0.108	0.112	0.110	0.109	0.813	0.804	0.816	0.817	0.802	0.823	0.818	0.824
Ca	0.001	0.004	0.003	0.001	0.000	0.000	0.000	0.000	0.000	0.000	0.000	0.000	0.001	0.000	0.000	0.001	0.000	0.000	0.001	0.000	0.001	0.008	0.000	0.000	0.000	0.000	0.000
Ba	0.007	0.008	0.008	0.008	0.009	0.008	0.008	0.009	0.008	0.008	0.008	0.008	0.008	0.010	0.007	0.008	0.008	0.006	0.009	0.004	0.007	0.007	0.007	0.006	0.006	0.005	0.006
Na	0.085	0.082	0.073	0.083	0.078	0.074	0.072	0.072	0.090	0.075	0.082	0.075	0.069	0.077	0.067	0.075	0.061	0.076	0.067	0.012	0.017	0.009	0.011	0.011	0.009	0.013	0.005
K	0.918	0.928	0.918	0.946	0.938	0.935	0.953	0.929	0.936	0.918	0.912	0.908	0.935	0.946	0.928	0.944	0.945	0.942	0.952	0.958	0.942	0.947	0.956	0.961	0.973	0.965	0.970
F	0.000	0.020	0.002	0.007	0.000	0.015	0.037	0.001	0.024	0.000	0.004	0.010	0.000	0.000	0.000	0.017	0.004	0.025	0.023	0.045	0.028	0.046	0.012	0.051	0.053	0.039	0.022
Cl	0.000	0.000	0.000	0.000	0.000	0.000	0.000	0.000	0.001	0.000	0.000	0.000	0.000	0.000	0.000	0.000	0.001	0.000	0.000	0.002	0.003	0.004	0.003	0.003	0.003	0.003	0.004
tot	7.029	7.051	7.034	7.064	7.041	7.041	7.075	7.032	7.062	7.025	7.027	7.021	7.029	7.049	7.015	7.044	7.025	7.058	7.053	7.839	7.816	7.844	7.821	7.850	7.873	7.859	7.843

SAMPLE	**GW13-29**																										
	bt	bt	bt	bt	bt	bt	bt	ms	ms	ms	ms	ms	ms	ms	ms	ms	ms	ms	ms	ms	ms	ms	ms	ms	ms	ms	ms
Spot number	59	60	61	62	63	64	65	66	67	68	69	70	71	72	73	74	75	76	77	78	79	80	81	82	83	84	85
OXIDES wt%																											
SiO_2	34.686	34.226	34.308	34.629	34.389	34.575	34.710	45.781	46.316	46.570	46.121	45.800	45.488	45.920	45.943	46.206	46.155	45.505	46.767	46.517	45.610	46.067	45.421	45.571	45.905	45.323	45.926
TiO_2	2.899	2.794	2.807	2.974	2.854	2.894	2.797	0.756	0.756	0.716	0.806	0.822	0.592	0.709	0.842	0.697	0.709	0.777	0.614	0.721	0.736	0.747	0.429	0.395	0.517	0.562	0.482
Al_2O_3	16.967	16.910	17.114	16.873	17.003	17.060	16.878	33.743	32.736	32.613	33.932	33.883	33.409	33.299	32.802	32.509	32.428	32.931	31.835	32.693	32.551	32.372	33.660	33.498	33.532	33.611	33.462
FeO	23.678	24.094	23.809	23.889	23.224	23.800	23.998	1.991	2.026	2.220	1.998	2.057	1.982	2.047	2.133	2.350	2.130	2.003	2.222	2.022	2.096	2.147	1.762	2.062	1.940	2.143	1.930
MnO	0.147	0.154	0.151	0.103	0.102	0.137	0.147	0.008	0.000	0.000	0.001	0.000	0.000	0.058	0.014	0.000	0.046	0.000	0.046	0.000	0.026	0.000	0.000	0.000	0.000	0.013	0.000
MgO	6.873	6.967	7.126	7.010	7.039	6.883	6.869	0.846	1.076	1.245	0.803	0.862	0.884	0.945	0.975	1.204	1.195	1.035	1.297	1.187	1.050	1.230	0.748	0.874	0.927	0.914	0.839
CaO	0.007	0.018	0.021	0.034	0.000	0.000	0.010	0.024	0.000	0.000	0.000	0.027	0.011	0.014	0.000	0.024	0.001	0.022	0.046	0.004	0.010	0.003	0.032	0.000	0.007	0.011	0.035
BaO	0.207	0.247	0.171	0.209	0.199	0.185	0.243	0.323	0.241	0.217	0.278	0.262	0.326	0.288	0.385	0.275	0.258	0.306	0.280	0.262	0.286	0.259	0.282	0.295	0.293	0.263	0.285
Na_2O	0.143	0.093	0.070	0.106	0.046	0.092	0.117	0.565	0.512	0.503	0.536	0.570	0.535	0.553	0.497	0.504	0.522	0.479	0.534	0.472	0.539	0.505	0.566	0.621	0.570	0.580	0.518
K_2O	9.481	9.535	9.509	9.415	9.645	9.574	9.582	10.838	10.854	10.659	10.610	10.568	10.765	10.733	10.846	10.604	10.758	10.711	10.997	10.875	10.789	10.966	10.711	10.823	10.735	10.898	10.906
F	0.199	0.189	0.123	0.118	0.114	0.109	0.212	0.056	0.017	0.000	0.050	0.072	0.061	0.000	0.028	0.161	0.134	0.056	0.111	0.078	0.067	0.039	0.045	0.000	0.072	0.000	0.050
Cl	0.022	0.023	0.020	0.021	0.021	0.020	0.021	0.004	0.005	0.003	0.002	0.007	0.000	0.000	0.000	0.008	0.006	0.005	0.000	0.012	0.000	0.000	0.000	0.000	0.000	0.001	0.002
tot	95.309	95.250	95.229	95.381	94.636	95.329	95.584	94.935	94.539	94.746	95.137	94.930	94.053	94.566	94.465	94.542	94.342	93.830	94.749	94.843	93.760	94.335	93.656	94.139	94.498	94.319	94.435
CATIONS apfu																											
Si	2.716	2.693	2.692	2.711	2.710	2.709	2.716	3.090	3.136	3.144	3.098	3.085	3.098	3.109	3.120	3.131	3.134	3.106	3.167	3.139	3.119	3.133	3.100	3.102	3.107	3.083	3.113
Ti	0.171	0.165	0.166	0.175	0.169	0.171	0.165	0.038	0.038	0.036	0.041	0.042	0.030	0.036	0.043	0.036	0.036	0.040	0.031	0.037	0.038	0.038	0.022	0.020	0.026	0.029	0.025
Al	1.566	1.568	1.583	1.557	1.579	1.575	1.556	2.684	2.612	2.595	2.686	2.690	2.681	2.657	2.625	2.596	2.595	2.649	2.541	2.600	2.624	2.594	2.707	2.687	2.675	2.695	2.673
Fe	1.550	1.585	1.562	1.564	1.530	1.559	1.570	0.112	0.115	0.125	0.112	0.116	0.113	0.116	0.121	0.133	0.121	0.114	0.126	0.114	0.120	0.122	0.101	0.117	0.110	0.122	0.109
Mn	0.010	0.010	0.010	0.007	0.007	0.009	0.010	0.000	0.000	0.000	0.000	0.000	0.000	0.003	0.001	0.000	0.003	0.000	0.003	0.000	0.002	0.000	0.000	0.000	0.000	0.001	0.000
Mg	0.802	0.817	0.833	0.818	0.827	0.804	0.801	0.085	0.109	0.125	0.080	0.087	0.090	0.095	0.099	0.122	0.121	0.105	0.131	0.119	0.107	0.125	0.076	0.089	0.094	0.093	0.085
Ca	0.001	0.002	0.002	0.003	0.000	0.000	0.001	0.002	0.000	0.000	0.000	0.002	0.001	0.001	0.000	0.002	0.000	0.002	0.003	0.000	0.001	0.000	0.002	0.000	0.001	0.001	0.003
Ba	0.006	0.008	0.005	0.006	0.006	0.006	0.007	0.009	0.006	0.006	0.007	0.007	0.009	0.008	0.010	0.007	0.007	0.008	0.007	0.007	0.008	0.007	0.008	0.008	0.008	0.007	0.008
Na	0.022	0.014	0.011	0.016	0.007	0.014	0.018	0.074	0.067	0.066	0.070	0.074	0.071	0.073	0.065	0.066	0.069	0.063	0.070	0.062	0.071	0.067	0.075	0.082	0.075	0.076	0.068
K	0.947	0.957	0.952	0.940	0.969	0.957	0.956	0.933	0.937	0.918	0.909	0.908	0.935	0.927	0.940	0.917	0.932	0.933	0.950	0.936	0.941	0.951	0.932	0.940	0.927	0.946	0.943
F	0.049	0.047	0.031	0.029	0.028	0.027	0.052	0.012	0.004	0.000	0.011	0.015	0.013	0.000	0.006	0.035	0.029	0.012	0.024	0.017	0.014	0.008	0.010	0.000	0.015	0.000	0.011
Cl	0.003	0.003	0.003	0.003	0.003	0.003	0.003	0.000	0.001	0.000	0.000	0.001	0.000	0.000	0.000	0.001	0.001	0.001	0.000	0.001	0.000	0.000	0.000	0.000	0.000	0.000	0.000
tot	7.841	7.869	7.849	7.830	7.836	7.833	7.856	7.040	7.024	7.015	7.014	7.027	7.041	7.026	7.030	7.045	7.047	7.034	7.053	7.032	7.045	7.045	7.033	7.045	7.037	7.052	7.037

SAMPLE	**GW13-29**																									**GW13-28**	
	ms	ms	ms	ms	ms	ms	ms	ms	ms	ms	ms	ms	ms	ms	bt	bt	bt	bt	bt	bt	bt	bt	bt	bt	bt	ms	ms
Spot number	86	87	88	89	90	91	92	93	94	95	96	97	98	99	100	101	102	103	104	105	106	107	108	109	110	1	2
OXIDES wt%																											
SiO_2	45.802	45.533	45.011	45.289	45.952	45.924	46.316	46.072	46.581	46.224	46.570	45.299	46.643	45.655	45.898	37.705	31.657	34.781	34.359	39.312	34.594	34.725	34.757	34.321	34.505	46.144	46.331
TiO_2	0.554	0.429	0.407	0.559	0.579	0.769	0.754	0.721	0.737	0.717	0.719	0.722	0.664	0.671	0.736	1.533	1.660	1.975	2.080	1.630	2.567	2.667	2.592	2.457	2.440	0.444	0.447
Al_2O_3	33.020	34.087	34.008	33.685	33.547	33.027	32.398	32.230	31.737	32.190	32.627	32.944	31.914	32.902	32.850	22.388	16.300	17.407	17.286	25.037	17.150	16.944	17.164	16.995	16.771	33.791	33.579
FeO	2.055	2.115	2.160	2.036	1.935	2.038	2.244	2.074	2.183	2.231	2.223	2.078	2.419	2.021	2.074	16.165	22.956	23.127	23.979	14.545	23.818	24.075	23.694	23.842	23.940	1.413	1.081
MnO	0.030	0.017	0.000	0.000	0.030	0.000	0.013	0.005	0.035	0.030	0.030	0.003	0.003	0.000	0.017	0.062	0.105	0.084	0.125	0.176	0.066	0.072	0.118	0.090	0.142	0.000	0.000
MgO	0.945	0.856	0.894	0.847	0.866	1.026	1.172	1.172	1.255	1.161	1.164	0.920	1.302	0.955	1.069	4.901	7.612	7.213	7.289	4.273	6.974	6.801	6.733	6.982	7.042	1.061	1.079
CaO	0.000	0.000	0.000	0.007	0.000	0.001	0.001	0.000	0.000	0.000	0.000	0.000	0.000	0.017	0.027	0.041	0.085	0.000	0.032	0.059	0.010	0.000	0.007	0.032	0.028	0.000	0.006
BaO	0.339	0.275	0.300	0.279	0.304	0.303	0.232	0.279	0.297	0.242	0.243	0.284	0.220	0.312	0.236	0.214	0.064	0.160	0.162	0.222	0.191	0.188	0.208	0.165	0.209	0.185	0.165
Na_2O	0.566	0.611	0.590	0.539	0.592	0.532	0.538	0.539	0.488	0.519	0.535	0.539	0.489	0.541	0.567	0.228	0.070	0.051	0.069	0.332	0.089	0.084	0.073	0.127	0.113	0.904	0.900
K_2O	10.900	10.718	10.685	10.823	10.776	10.740	10.827	10.807	10.891	10.782	10.723	10.842	10.735	10.661	11.005	9.608	7.537	9.566	9.313	9.837	9.678	9.449	9.470	9.462	8.972	10.208	9.882
F	0.117	0.028	0.000	0.067	0.094	0.061	0.133	0.073	0.050	0.100	0.083	0.022	0.067	0.106	0.211	0.121	0.185	0.086	0.080	0.161	0.076	0.090	0.175	0.147	0.217	0.000	0.039
Cl	0.000	0.000	0.003	0.000	0.002	0.001	0.003	0.000	0.000	0.001	0.003	0.000	0.004	0.004	0.000	0.054	0.049	0.032	0.029	0.020	0.020	0.013	0.014	0.024	0.025	0.002	0.000
tot	94.328	94.669	94.058	94.131	94.677	94.422	94.631	93.972	94.254	94.197	94.920	93.653	94.460	93.845	94.690	93.020	88.280	94.482	94.803	95.604	95.233	95.108	95.005	94.644	94.404	94.152	93.509
CATIONS apfu																											
Si	3.114	3.080	3.068	3.083	3.106	3.114	3.137	3.141	3.168	3.145	3.141	3.102	3.163	3.115	3.110	2.863	2.667	2.736	2.706	2.863	2.714	2.727	2.727	2.710	2.725	3.116	3.136
Ti	0.028	0.022	0.021	0.029	0.029	0.039	0.038	0.037	0.038	0.037	0.036	0.037	0.034	0.034	0.038	0.088	0.105	0.117	0.123	0.089	0.151	0.157	0.153	0.146	0.145	0.023	0.023
Al	2.646	2.718	2.732	2.703	2.673	2.640	2.586	2.590	2.544	2.581	2.593	2.659	2.551	2.646	2.623	2.003	1.618	1.614	1.604	2.149	1.586	1.568	1.587	1.582	1.561	2.689	2.679
Fe	0.117	0.120	0.123	0.116	0.109	0.116	0.127	0.118	0.124	0.127	0.125	0.119	0.137	0.115	0.118	1.026	1.617	1.521	1.579	0.886	1.563	1.581	1.555	1.574	1.581	0.080	0.061
Mn	0.002	0.001	0.000	0.000	0.002	0.000	0.001	0.000	0.002	0.002	0.002	0.000	0.000	0.000	0.001	0.004	0.007	0.006	0.008	0.011	0.004	0.005	0.008	0.006	0.009	0.000	0.000
Mg	0.096	0.086	0.091	0.086	0.087	0.104	0.118	0.119	0.127	0.118	0.117	0.094	0.132	0.097	0.108	0.555	0.956	0.846	0.856	0.464	0.815	0.796	0.787	0.822	0.829	0.107	0.109
Ca	0.000	0.000	0.000	0.001	0.000	0.000	0.000	0.000	0.000	0.000	0.000	0.000	0.000	0.001	0.002	0.003	0.008	0.000	0.003	0.005	0.001	0.000	0.001	0.003	0.002	0.000	0.000
Ba	0.009	0.007	0.008	0.007	0.008	0.008	0.006	0.007	0.008	0.006	0.006	0.008	0.006	0.008	0.006	0.006	0.002	0.005	0.005	0.006	0.006	0.006	0.006	0.005	0.006	0.005	0.004
Na	0.075	0.080	0.078	0.071	0.078	0.070	0.071	0.071	0.064	0.068	0.070	0.072	0.064	0.072	0.074	0.034	0.011	0.008	0.011	0.047	0.014	0.013	0.011	0.019	0.017	0.118	0.118
K	0.945	0.925	0.929	0.940	0.929	0.929	0.935	0.940	0.945	0.936	0.922	0.947	0.929	0.928	0.951	0.931	0.810	0.960	0.936	0.914	0.968	0.947	0.948	0.953	0.904	0.879	0.853
F	0.025	0.006	0.000	0.014	0.020	0.013	0.028	0.016	0.011	0.022	0.018	0.005	0.014	0.023	0.045	0.029	0.049	0.021	0.020	0.037	0.019	0.022	0.043	0.037	0.054	0.000	0.008
Cl	0.000	0.000	0.000	0.000	0.000	0.000	0.000	0.000	0.000	0.000	0.000	0.000	0.000	0.000	0.000	0.007	0.007	0.004	0.004	0.002	0.003	0.002	0.002	0.003	0.003	0.000	0.000
tot	7.057	7.045	7.049	7.050	7.042	7.033	7.049	7.040	7.032	7.041	7.031	7.043	7.031	7.039	7.076	7.548	7.858	7.837	7.854	7.473	7.844	7.823	7.828	7.860	7.839	7.016	6.992

SAMPLE	**GW13-28**																										
	ms	ms	ms	ms	ms	ms	ms	ms	ms	ms	ms	ms	ms	ms	ms	ms	ms	ms	ms	ms	ms	bt	bt	bt	bt	bt	bt
Spot number	3	4	5	6	7	8	9	10	11	12	13	14	15	16	17	18	19	20	21	22	23	24	25	26	27	28	29
OXIDES wt%																											
SiO_2	46.271	46.489	45.680	46.523	46.003	45.824	46.076	46.316	46.268	46.080	46.606	46.194	46.191	46.114	46.455	46.170	46.149	46.696	46.296	45.967	45.879	34.819	34.361	34.994	34.977	35.174	34.259
TiO_2	0.450	0.360	0.377	0.389	0.385	0.397	0.434	0.309	0.304	0.444	0.379	0.382	0.382	0.349	0.402	0.464	0.350	0.414	0.362	0.309	0.295	1.591	1.518	1.628	1.273	1.448	1.475
Al_2O_3	34.064	33.764	33.800	33.775	33.853	34.616	34.161	34.397	34.650	34.582	34.178	34.405	34.522	34.597	34.357	34.420	34.132	34.225	33.887	34.420	34.597	18.696	18.817	19.096	18.930	18.839	18.450
FeO	1.009	1.030	1.292	1.268	1.122	0.946	1.038	1.010	1.051	0.991	1.168	0.948	1.091	1.081	1.048	1.274	1.261	1.068	1.254	1.323	1.235	21.206	21.689	20.759	20.864	21.190	20.669
MnO	0.000	0.000	0.005	0.019	0.001	0.001	0.034	0.015	0.010	0.005	0.000	0.000	0.000	0.000	0.000	0.000	0.003	0.000	0.000	0.000	0.000	0.017	0.050	0.006	0.037	0.034	0.025
MgO	0.912	0.985	1.166	1.118	0.998	0.756	0.902	0.933	0.933	0.832	1.066	0.917	0.978	1.001	1.020	1.023	1.023	1.076	1.118	0.746	0.794	8.551	8.824	8.120	8.635	8.481	8.252
CaO	0.000	0.004	0.000	0.003	0.013	0.000	0.000	0.004	0.000	0.053	0.000	0.013	0.000	0.000	0.029	0.071	0.001	0.025	0.035	0.039	0.000	0.056	0.000	0.000	0.027	0.034	0.035
BaO	0.131	0.163	0.171	0.170	0.191	0.156	0.127	0.159	0.170	0.185	0.148	0.172	0.163	0.150	0.159	0.175	0.150	0.142	0.160	0.134	0.153	0.080	0.109	0.052	0.046	0.116	0.038
Na_2O	0.918	0.861	0.895	0.989	0.911	0.999	0.945	0.997	1.004	0.926	0.946	0.945	0.980	0.942	0.948	0.883	0.872	0.934	1.077	0.940	0.829	0.105	0.070	0.089	0.276	0.038	0.085
K_2O	9.678	10.106	9.929	10.028	10.014	9.890	10.158	10.110	9.969	9.847	10.021	10.014	10.017	10.212	10.102	10.182	9.941	9.803	10.159	9.920	9.756	8.848	8.964	9.374	9.379	9.569	9.102
F	0.045	0.000	0.022	0.200	0.089	0.034	0.000	0.078	0.050	0.061	0.039	0.117	0.100	0.000	0.050	0.067	0.000	0.011	0.150	0.084	0.000	0.172	0.294	0.207	0.381	0.167	0.141
Cl	0.007	0.000	0.000	0.009	0.000	0.002	0.000	0.000	0.000	0.009	0.005	0.005	0.002	0.007	0.003	0.042	0.024	0.012	0.063	0.003	0.002	0.031	0.035	0.024	0.115	0.028	0.029
tot	93.485	93.762	93.337	94.491	93.580	93.621	93.875	94.328	94.409	94.015	94.556	94.112	94.426	94.453	94.573	94.771	93.906	94.406	94.561	93.885	93.540	94.172	94.731	94.349	94.940	95.118	92.560
CATIONS apfu																											
Si	3.126	3.139	3.105	3.124	3.117	3.097	3.112	3.111	3.103	3.101	3.122	3.107	3.100	3.097	3.112	3.095	3.114	3.127	3.111	3.103	3.102	2.703	2.663	2.709	2.697	2.711	2.708
Ti	0.023	0.018	0.019	0.020	0.020	0.020	0.022	0.016	0.015	0.022	0.019	0.019	0.019	0.018	0.020	0.023	0.018	0.021	0.018	0.016	0.015	0.093	0.088	0.095	0.074	0.084	0.088
Al	2.712	2.687	2.708	2.673	2.703	2.757	2.719	2.723	2.739	2.743	2.698	2.728	2.730	2.738	2.713	2.719	2.715	2.701	2.684	2.739	2.757	1.710	1.719	1.742	1.720	1.711	1.719
Fe	0.057	0.058	0.073	0.071	0.064	0.053	0.059	0.057	0.059	0.056	0.065	0.053	0.061	0.061	0.059	0.071	0.071	0.060	0.070	0.075	0.070	1.377	1.406	1.344	1.345	1.366	1.366
Mn	0.000	0.000	0.000	0.001	0.000	0.000	0.002	0.001	0.001	0.000	0.000	0.000	0.000	0.000	0.000	0.000	0.000	0.000	0.000	0.000	0.000	0.001	0.003	0.000	0.002	0.002	0.002
Mg	0.092	0.099	0.118	0.112	0.101	0.076	0.091	0.093	0.093	0.083	0.106	0.092	0.098	0.100	0.102	0.102	0.103	0.107	0.112	0.075	0.080	0.989	1.019	0.937	0.992	0.974	0.972
Ca	0.000	0.000	0.000	0.000	0.001	0.000	0.000	0.000	0.000	0.004	0.000	0.001	0.000	0.000	0.002	0.005	0.000	0.002	0.003	0.003	0.000	0.005	0.000	0.000	0.002	0.003	0.003
Ba	0.003	0.004	0.005	0.004	0.005	0.004	0.003	0.004	0.004	0.005	0.004	0.005	0.004	0.004	0.004	0.005	0.004	0.004	0.004	0.004	0.004	0.002	0.003	0.002	0.001	0.004	0.001
Na	0.120	0.113	0.118	0.129	0.120	0.131	0.124	0.130	0.131	0.121	0.123	0.123	0.128	0.123	0.123	0.115	0.114	0.121	0.140	0.123	0.109	0.016	0.011	0.013	0.041	0.006	0.013
K	0.834	0.871	0.861	0.859	0.865	0.853	0.875	0.866	0.853	0.845	0.856	0.859	0.857	0.875	0.863	0.871	0.856	0.837	0.871	0.854	0.842	0.876	0.886	0.926	0.922	0.941	0.918
F	0.010	0.000	0.005	0.042	0.019	0.007	0.000	0.017	0.011	0.013	0.008	0.025	0.021	0.000	0.011	0.014	0.000	0.002	0.032	0.018	0.000	0.042	0.072	0.051	0.093	0.041	0.035
Cl	0.001	0.000	0.000	0.001	0.000	0.000	0.000	0.000	0.000	0.001	0.001	0.001	0.000	0.001	0.000	0.005	0.003	0.001	0.007	0.000	0.000	0.004	0.005	0.003	0.015	0.004	0.004
tot	6.978	6.990	7.013	7.036	7.014	7.000	7.006	7.018	7.009	6.995	7.004	7.013	7.019	7.016	7.010	7.025	6.997	6.983	7.053	7.009	6.979	7.818	7.876	7.822	7.905	7.845	7.830

SAMPLE	**GW13-28**										
	bt	bt	bt	bt	bt	bt	ms	ms	ms	ms	ms
Spot number	30	31	32	33	34	35	36	37	38	39	40
OXIDES wt%											
SiO_2	35.320	33.615	34.081	35.457	33.542	32.774	45.796	45.954	45.832	46.337	45.967
TiO_2	1.068	1.675	1.558	1.576	1.546	1.640	0.177	0.147	0.292	0.260	0.392
Al_2O_3	19.265	19.261	19.006	19.096	19.164	19.040	34.884	35.240	35.436	34.531	34.580
FeO	21.109	21.344	21.498	20.440	21.143	21.893	1.110	1.341	1.162	1.276	1.290
MnO	0.000	0.063	0.009	0.000	0.009	0.054	0.005	0.000	0.000	0.004	0.017
MgO	8.715	9.595	9.396	9.257	9.776	10.089	0.680	0.648	0.645	0.861	0.897
CaO	0.024	0.000	0.001	0.032	0.031	0.000	0.004	0.000	0.017	0.000	0.000
BaO	0.042	0.061	0.076	0.045	0.055	0.040	0.106	0.122	0.163	0.123	0.188
Na_2O	0.049	0.066	0.085	0.092	0.058	0.078	0.884	1.064	1.030	0.983	0.910
K_2O	9.516	7.609	8.235	9.272	7.589	6.854	10.245	10.209	10.085	10.053	10.237
F	0.200	0.186	0.266	0.201	0.182	0.181	0.295	0.161	0.000	0.017	0.022
Cl	0.015	0.044	0.045	0.030	0.038	0.041	0.017	0.001	0.004	0.000	0.000
tot	95.323	93.519	94.256	95.498	93.133	92.684	94.203	94.887	94.666	94.445	94.500
CATIONS apfu											
Si	2.709	2.617	2.642	2.702	2.620	2.578	3.083	3.075	3.070	3.110	3.091
Ti	0.062	0.098	0.091	0.090	0.091	0.097	0.009	0.007	0.015	0.013	0.020
Al	1.741	1.767	1.736	1.715	1.764	1.765	2.768	2.780	2.798	2.731	2.740
Fe	1.354	1.390	1.393	1.303	1.381	1.440	0.062	0.075	0.065	0.072	0.073
Mn	0.000	0.004	0.001	0.000	0.001	0.004	0.000	0.000	0.000	0.000	0.001
Mg	0.996	1.114	1.085	1.052	1.138	1.183	0.068	0.065	0.064	0.086	0.090
Ca	0.002	0.000	0.000	0.003	0.003	0.000	0.000	0.000	0.001	0.000	0.000
Ba	0.001	0.002	0.002	0.001	0.002	0.001	0.003	0.003	0.004	0.003	0.005
Na	0.007	0.010	0.013	0.014	0.009	0.012	0.115	0.138	0.134	0.128	0.119
K	0.931	0.756	0.814	0.901	0.756	0.688	0.880	0.872	0.862	0.861	0.878
F	0.049	0.046	0.065	0.048	0.045	0.045	0.063	0.034	0.000	0.004	0.005
Cl	0.002	0.006	0.006	0.004	0.005	0.005	0.002	0.000	0.000	0.000	0.000
tot	7.853	7.810	7.849	7.833	7.814	7.818	7.054	7.049	7.014	7.008	7.020

SAMPLE	**UT15-05**																										**UT15-06**
	bt	bt	bt	bt	bt	bt	bt	bt	bt	bt	bt	bt	bt	bt	bt	bt	bt	bt	bt	bt	bt	bt	bt	bt	ms	chl	bt
Spot number	1	2	5	6	7	9	10	11	12	13	14	15	20	21	24	25	29	31	32	33	34	35	39	40	30	51	55
OXIDES wt%																											
SiO_2	37.460	36.260	36.420	35.850	36.470	37.420	36.610	37.460	37.390	37.150	37.170	37.910	35.870	37.480	37.470	37.500	38.400	34.940	36.750	36.490	36.150	39.120	37.400	36.050	47.290	35.620	36.500
TiO_2	2.080	2.180	2.140	1.840	2.130	2.150	2.140	2.030	1.910	1.930	2.050	1.730	1.920	1.950	1.940	1.760	1.990	2.230	2.110	2.240	2.060	1.830	2.070	2.160	0.573	1.730	1.910
Al_2O_3	17.730	17.040	17.920	18.180	17.920	18.010	17.980	17.620	17.650	18.500	18.820	18.460	16.510	18.560	17.660	17.480	17.070	16.110	16.980	16.920	17.160	18.160	17.670	17.430	32.610	17.720	18.410
FeO	17.660	17.700	17.510	17.600	17.940	18.180	17.480	17.390	17.690	17.470	17.220	17.230	17.320	16.950	16.400	16.910	15.620	16.420	17.460	15.840	17.260	16.760	17.270	16.990	1.730	14.890	19.380
MnO	0.169	0.192	0.203	0.153	0.177	0.198	0.170	0.173	0.169	0.217	0.169	0.196	0.212	0.164	0.219	0.222	0.172	0.174	0.193	0.192	0.210	0.129	0.151	0.133	0.000	0.164	0.106
MgO	11.340	10.840	10.820	11.270	11.020	11.330	10.890	11.270	11.490	11.130	11.580	11.730	10.960	11.940	11.890	11.900	11.930	10.690	11.400	11.220	11.420	12.550	11.710	11.230	1.604	11.480	10.070
CaO	0.076	0.110	0.052	0.073	0.097	0.165	0.084	0.082	0.129	0.068	0.103	0.076	0.109	0.091	0.053	0.163	0.045	0.044	0.116	0.093	0.092	0.057	0.080	0.092	0.045	0.147	0.178
BaO	0.017	0.126	0.077	0.106	0.000	0.089	0.128	0.209	0.093	0.167	0.139	0.179	0.087	0.219	0.193	0.109	0.242	0.176	0.166	0.088	0.148	0.000	0.170	0.095	0.924	0.207	0.146
Na_2O	0.242	0.232	0.445	0.149	0.219	0.308	0.371	0.204	0.413	0.266	0.307	0.254	0.286	0.258	0.171	0.202	0.076	0.233	0.129	0.183	0.120	0.141	0.226	0.178	0.306	0.231	0.332
K_2O	9.440	9.320	9.930	9.370	9.420	9.270	9.710	9.450	9.200	9.250	9.520	9.330	9.280	9.460	9.210	9.250	9.500	9.480	9.440	9.480	9.620	9.500	9.300	9.490	10.510	8.990	9.080
F	0.352	0.328	0.320	0.349	0.238	0.374	0.343	0.427	0.372	0.261	0.307	0.342	0.291	0.403	0.317	0.353	0.500	0.550	0.438	0.354	0.366	0.381	0.275	0.304	0.000	0.334	0.229
Cl	0.000	0.016	0.287	0.015	0.020	0.052	0.196	0.040	0.046	0.048	0.065	0.036	0.050	0.030	0.041	0.024	0.034	0.019	0.037	0.000	0.033	0.015	0.026	0.050	0.000	0.037	0.036
tot	96.566	94.345	96.124	94.954	95.650	97.546	96.103	96.355	96.551	96.456	97.450	97.472	92.894	97.503	95.563	95.872	95.579	91.066	95.220	93.100	94.639	98.644	96.349	94.202	95.591	91.550	96.377
CATIONS apfu																											
Si	2.803	2.792	2.767	2.740	2.760	2.782	2.773	2.817	2.803	2.777	2.753	2.801	2.805	2.774	2.817	2.819	2.885	2.805	2.806	2.823	2.777	2.839	2.798	2.772	3.165	3.549	2.756
Ti	0.117	0.126	0.122	0.106	0.121	0.120	0.122	0.115	0.108	0.109	0.114	0.096	0.113	0.109	0.110	0.099	0.112	0.135	0.121	0.130	0.119	0.100	0.116	0.125	0.029	0.130	0.108
Al	1.564	1.546	1.605	1.638	1.599	1.578	1.605	1.561	1.559	1.630	1.643	1.607	1.522	1.619	1.565	1.548	1.511	1.524	1.528	1.543	1.554	1.553	1.558	1.580	2.573	2.081	1.638
Fe	1.105	1.140	1.113	1.125	1.136	1.130	1.107	1.093	1.109	1.092	1.067	1.065	1.133	1.049	1.031	1.063	0.981	1.102	1.115	1.025	1.109	1.017	1.081	1.093	0.097	1.241	1.224
Mn	0.011	0.013	0.013	0.010	0.011	0.012	0.011	0.011	0.011	0.014	0.011	0.012	0.014	0.010	0.014	0.014	0.011	0.012	0.012	0.013	0.014	0.008	0.010	0.009	0.000	0.014	0.007
Mg	1.265	1.244	1.225	1.284	1.243	1.256	1.230	1.263	1.284	1.240	1.279	1.292	1.278	1.317	1.332	1.333	1.336	1.279	1.297	1.294	1.308	1.358	1.306	1.287	0.160	1.705	1.133
Ca	0.006	0.009	0.004	0.006	0.008	0.013	0.007	0.007	0.010	0.005	0.008	0.006	0.009	0.007	0.004	0.013	0.004	0.004	0.009	0.008	0.008	0.004	0.006	0.008	0.003	0.016	0.014
Ba	0.001	0.004	0.002	0.003	0.000	0.003	0.004	0.006	0.003	0.005	0.004	0.005	0.003	0.006	0.006	0.003	0.007	0.006	0.005	0.003	0.004	0.000	0.005	0.003	0.024	0.008	0.004
Na	0.035	0.035	0.066	0.022	0.032	0.044	0.054	0.030	0.060	0.039	0.044	0.036	0.043	0.037	0.025	0.029	0.011	0.036	0.019	0.027	0.018	0.020	0.033	0.026	0.040	0.045	0.049
K	0.901	0.915	0.962	0.914	0.910	0.879	0.938	0.906	0.880	0.882	0.900	0.879	0.926	0.893	0.883	0.887	0.910	0.971	0.919	0.936	0.943	0.879	0.888	0.931	0.897	1.143	0.875
F	0.083	0.080	0.077	0.084	0.057	0.088	0.082	0.101	0.088	0.062	0.072	0.080	0.072	0.094	0.075	0.084	0.119	0.140	0.106	0.087	0.089	0.087	0.065	0.074	0.000	0.105	0.055
Cl	0.000	0.002	0.037	0.002	0.003	0.006	0.025	0.005	0.006	0.006	0.008	0.004	0.007	0.004	0.005	0.003	0.004	0.003	0.005	0.000	0.004	0.002	0.003	0.007	0.000	0.006	0.005
tot	7.891	7.906	7.993	7.933	7.879	7.912	7.959	7.916	7.920	7.861	7.903	7.884	7.923	7.920	7.866	7.896	7.892	8.015	7.944	7.887	7.947	7.868	7.869	7.913	6.988	10.042	7.867

SAMPLE	**UT15-06**																										
	bt	bt	bt	bt	bt	bt	bt	bt	bt	bt	bt	bt	bt	bt	bt	bt	bt	bt	bt	bt	bt	bt	bt	bt	bt	ms	ms
Spot number	57	60	61	63	64	68	69	70	71	74	77	79	81	82	83	84	88	89	93	95	99	101	102	106	108	86	87
OXIDES wt%																											
SiO_2	35.780	36.920	36.630	36.220	35.450	36.150	34.450	36.950	36.160	36.460	37.090	36.750	36.790	36.430	34.660	34.510	35.640	36.150	36.360	37.730	36.410	36.310	36.470	35.520	36.180	47.050	47.570
TiO_2	1.465	1.651	1.770	2.050	2.110	2.150	2.120	1.661	1.860	2.220	2.120	2.120	1.690	3.330	2.740	2.010	2.230	2.140	2.020	1.297	1.920	2.120	2.040	1.820	2.010	0.701	0.284
Al_2O_3	17.990	18.160	17.820	17.450	17.420	17.810	16.730	18.100	17.230	17.490	17.790	18.150	17.670	18.120	16.490	16.950	17.660	17.560	18.470	17.680	17.320	17.620	17.410	17.280	17.480	33.630	33.470
FeO	18.220	19.060	19.370	19.210	18.870	19.700	19.010	19.060	19.110	19.570	19.710	19.830	18.240	19.060	19.210	19.270	18.780	19.640	18.400	18.040	19.480	19.480	19.510	19.610	19.400	2.100	1.840
MnO	0.129	0.174	0.181	0.152	0.169	0.212	0.148	0.195	0.172	0.212	0.156	0.145	0.117	0.174	0.182	0.157	0.171	0.185	0.145	0.201	0.163	0.193	0.189	0.161	0.161	0.015	0.000
MgO	9.480	10.060	9.980	9.710	9.620	10.030	8.640	10.280	10.020	10.150	10.240	10.060	9.660	9.340	8.730	9.040	9.170	9.480	9.990	9.890	10.330	9.970	9.970	9.620	10.120	1.434	1.415
CaO	0.151	0.054	0.065	0.115	0.041	0.199	0.209	0.134	0.038	0.080	0.090	0.136	0.093	0.780	0.539	0.170	0.131	0.097	0.059	0.241	0.107	0.066	0.122	0.126	0.097	0.025	0.003
BaO	0.112	0.263	0.222	0.029	0.145	0.061	0.075	0.152	0.103	0.080	0.091	0.165	0.180	0.132	0.160	0.077	0.147	0.200	0.164	0.095	0.121	0.114	0.084	0.041	0.020	0.393	0.641
Na_2O	0.153	0.201	0.209	0.286	0.173	0.219	0.370	0.140	0.124	0.216	0.270	0.265	0.217	0.187	0.240	0.341	0.405	0.268	0.152	1.247	0.217	0.189	0.230	0.268	0.178	0.315	0.249
K_2O	9.360	9.310	9.310	9.270	9.260	9.110	9.080	9.290	9.080	9.180	9.310	8.990	9.060	9.210	8.830	9.140	9.390	9.150	9.170	8.490	9.050	9.350	9.260	9.190	9.140	10.700	10.720
F	0.347	0.301	0.375	0.231	0.335	0.273	0.190	0.358	0.453	0.365	0.275	0.306	0.336	0.264	0.270	0.262	0.240	0.107	0.238	0.343	0.181	0.219	0.320	0.294	0.318	0.000	0.000
Cl	0.026	0.024	0.025	0.018	0.016	0.015	0.012	0.031	0.010	0.015	0.019	0.005	0.020	0.027	0.065	0.032	0.145	0.056	0.010	0.412	0.027	0.030	0.021	0.039	0.020	0.020	0.004
tot	93.213	96.178	95.957	94.741	93.607	95.928	91.035	96.351	94.360	96.037	97.161	96.922	94.072	97.054	92.115	91.960	94.110	95.033	95.178	95.666	95.326	95.661	95.626	93.968	95.124	96.382	96.195
CATIONS apfu																											
Si	2.795	2.795	2.792	2.786	2.770	2.753	2.773	2.794	2.803	2.777	2.783	2.765	2.836	2.737	2.766	2.758	2.772	2.774	2.767	2.868	2.782	2.771	2.788	2.772	2.777	3.121	3.158
Ti	0.086	0.094	0.101	0.119	0.124	0.123	0.128	0.094	0.108	0.127	0.120	0.120	0.098	0.188	0.164	0.121	0.130	0.124	0.116	0.074	0.110	0.122	0.117	0.107	0.116	0.035	0.014
Al	1.656	1.620	1.601	1.582	1.604	1.599	1.587	1.613	1.574	1.570	1.573	1.610	1.605	1.604	1.551	1.596	1.619	1.588	1.657	1.584	1.559	1.585	1.569	1.589	1.581	2.630	2.618
Fe	1.190	1.207	1.235	1.236	1.233	1.255	1.280	1.205	1.239	1.246	1.237	1.248	1.176	1.198	1.282	1.288	1.221	1.260	1.171	1.147	1.245	1.243	1.247	1.280	1.245	0.117	0.102
Mn	0.009	0.011	0.012	0.010	0.011	0.014	0.010	0.012	0.011	0.014	0.010	0.009	0.008	0.011	0.012	0.011	0.011	0.012	0.009	0.013	0.011	0.012	0.012	0.011	0.010	0.001	0.000
Mg	1.104	1.135	1.134	1.113	1.120	1.139	1.037	1.158	1.158	1.152	1.145	1.128	1.110	1.046	1.038	1.077	1.063	1.084	1.133	1.121	1.176	1.134	1.136	1.119	1.158	0.142	0.140
Ca	0.013	0.004	0.005	0.009	0.003	0.016	0.018	0.011	0.003	0.007	0.007	0.011	0.008	0.063	0.046	0.015	0.011	0.008	0.005	0.020	0.009	0.005	0.010	0.011	0.008	0.002	0.000
Ba	0.003	0.008	0.007	0.001	0.004	0.002	0.002	0.005	0.003	0.002	0.003	0.005	0.005	0.004	0.005	0.002	0.004	0.006	0.005	0.003	0.004	0.003	0.003	0.001	0.001	0.010	0.017
Na	0.023	0.029	0.031	0.043	0.026	0.032	0.058	0.020	0.019	0.032	0.039	0.039	0.032	0.027	0.037	0.053	0.061	0.040	0.022	0.184	0.032	0.028	0.034	0.041	0.026	0.040	0.032
K	0.933	0.899	0.905	0.910	0.923	0.885	0.932	0.896	0.898	0.892	0.891	0.863	0.891	0.883	0.899	0.932	0.932	0.896	0.890	0.823	0.882	0.910	0.903	0.915	0.895	0.906	0.908
F	0.086	0.072	0.090	0.056	0.083	0.066	0.048	0.086	0.111	0.088	0.065	0.073	0.082	0.063	0.068	0.066	0.059	0.026	0.057	0.082	0.044	0.053	0.077	0.072	0.077	0.000	0.000
Cl	0.003	0.003	0.003	0.002	0.002	0.002	0.002	0.004	0.001	0.002	0.002	0.001	0.003	0.003	0.009	0.004	0.019	0.007	0.001	0.053	0.004	0.004	0.003	0.005	0.003	0.002	0.000
tot	7.902	7.878	7.915	7.868	7.905	7.885	7.875	7.898	7.928	7.908	7.877	7.871	7.852	7.827	7.878	7.922	7.902	7.826	7.833	7.972	7.856	7.870	7.899	7.921	7.897	7.005	6.989

SAMPLE	**UT15-06**		**UT15-9**	**UT15-9**																							
	ms	ms	bt	bt	bt	bt	bt	bt	bt	bt	bt	bt	bt	bt	bt	ms	ms	ms	ms	ms	ms	ms	ms	ms	ms	ms	ms
Spot number	87	103	116	122	124	129	131	134	135	138	140	146	153	154	159	113	119	123	126	127	128	130	132	133	136	137	139
OXIDES wt%																											
SiO_2	47.570	46.540	36.100	34.870	35.770	35.150	34.690	37.360	36.660	36.840	34.740	35.540	35.340	36.790	36.690	44.920	46.270	48.100	46.900	46.740	44.560	46.460	48.280	48.120	46.810	46.910	46.920
TiO_2	0.284	0.401	1.530	1.740	1.820	1.485	1.488	1.617	1.569	1.720	1.666	1.537	1.502	1.511	1.680	0.301	0.302	0.253	0.655	0.234	0.346	0.263	0.275	0.275	0.311	0.238	0.264
Al_2O_3	33.470	32.180	17.780	17.010	18.040	17.490	17.250	18.640	18.650	19.250	17.660	17.770	17.620	18.800	18.660	33.080	33.420	36.170	34.680	34.210	33.930	34.650	35.990	34.620	33.860	34.950	34.400
FeO	1.840	1.950	20.190	21.120	19.990	20.660	20.470	20.100	19.930	20.820	20.170	20.600	20.680	20.670	21.090	1.890	2.000	2.060	2.130	2.080	2.060	2.160	2.040	2.010	1.940	2.170	2.070
MnO	0.000	0.000	0.122	0.083	0.051	0.103	0.073	0.078	0.093	0.076	0.064	0.060	0.033	0.118	0.063	0.000	0.007	0.042	0.000	0.000	0.028	0.032	0.028	0.036	0.000	0.060	0.000
MgO	1.415	1.539	9.760	8.900	9.500	9.500	9.490	10.130	9.870	9.840	9.410	9.620	9.480	9.740	9.580	0.552	0.851	0.652	0.798	0.747	0.639	0.772	0.828	0.930	0.640	0.774	0.630
CaO	0.003	0.195	0.127	0.087	0.085	0.098	0.141	0.086	0.067	0.054	0.067	0.109	0.091	0.089	0.094	0.071	0.117	0.055	0.090	0.075	0.081	0.088	0.065	0.055	0.125	0.074	0.045
BaO	0.641	0.699	0.062	0.065	0.056	0.107	0.113	0.039	0.084	0.034	0.095	0.122	0.064	0.104	0.060	0.276	0.312	0.201	0.278	0.187	0.310	0.262	0.394	0.227	0.254	0.265	0.210
Na_2O	0.249	0.352	0.486	0.471	0.345	0.265	0.358	0.336	0.276	0.350	0.391	0.377	0.370	0.416	0.420	1.630	1.570	1.420	1.324	1.440	1.143	1.430	1.610	1.400	1.339	1.470	1.350
K_2O	10.720	10.520	8.700	8.860	8.780	8.420	8.600	8.480	8.710	8.680	8.890	8.340	8.500	8.570	8.690	9.050	8.870	8.910	9.060	9.020	9.210	9.190	8.880	9.230	9.280	8.950	8.590
F	0.000	0.000	0.340	0.235	0.494	0.314	0.451	0.322	0.402	0.328	0.296	0.337	0.476	0.399	0.385	0.000	0.000	0.000	0.000	0.000	0.000	0.000	0.000	0.000	0.000	0.000	0.000
Cl	0.004	0.078	0.126	0.091	0.052	0.052	0.066	0.066	0.051	0.107	0.158	0.058	0.031	0.051	0.067	0.084	0.069	0.036	0.029	0.024	0.075	0.064	0.026	0.068	0.080	0.011	0.048
tot	96.195	94.453	95.322	93.531	94.983	93.643	93.190	97.255	96.362	98.099	93.606	94.470	94.187	97.257	97.478	91.852	93.788	97.900	95.944	94.757	92.382	95.370	98.417	96.971	94.638	95.873	94.527
CATIONS apfu																											
Si	3.158	3.161	2.777	2.755	2.765	2.758	2.751	2.789	2.774	2.742	2.735	2.759	2.764	2.766	2.759	3.115	3.134	3.105	3.102	3.127	3.074	3.098	3.106	3.145	3.141	3.103	3.136
Ti	0.014	0.020	0.089	0.103	0.106	0.088	0.089	0.091	0.089	0.096	0.099	0.090	0.088	0.085	0.095	0.016	0.015	0.012	0.033	0.012	0.018	0.013	0.013	0.014	0.016	0.012	0.013
Al	2.618	2.576	1.612	1.584	1.643	1.617	1.612	1.640	1.663	1.689	1.639	1.626	1.624	1.666	1.654	2.703	2.668	2.752	2.703	2.697	2.759	2.723	2.729	2.667	2.678	2.725	2.709
Fe	0.102	0.111	1.299	1.396	1.292	1.355	1.358	1.255	1.261	1.296	1.328	1.337	1.352	1.300	1.326	0.110	0.113	0.111	0.118	0.116	0.119	0.120	0.110	0.110	0.109	0.120	0.116
Mn	0.000	0.000	0.008	0.006	0.003	0.007	0.005	0.005	0.006	0.005	0.004	0.004	0.002	0.008	0.004	0.000	0.000	0.002	0.000	0.000	0.002	0.002	0.002	0.002	0.000	0.003	0.000
Mg	0.140	0.156	1.119	1.048	1.094	1.111	1.122	1.127	1.113	1.092	1.104	1.113	1.105	1.091	1.074	0.057	0.086	0.063	0.079	0.074	0.066	0.077	0.079	0.091	0.064	0.076	0.063
Ca	0.000	0.014	0.010	0.007	0.007	0.008	0.012	0.007	0.005	0.004	0.006	0.009	0.008	0.007	0.008	0.005	0.008	0.004	0.006	0.005	0.006	0.006	0.005	0.004	0.009	0.005	0.003
Ba	0.017	0.019	0.002	0.002	0.002	0.003	0.004	0.001	0.002	0.001	0.003	0.004	0.002	0.003	0.002	0.007	0.008	0.005	0.007	0.005	0.008	0.007	0.010	0.006	0.007	0.007	0.006
Na	0.032	0.046	0.072	0.072	0.052	0.040	0.055	0.049	0.040	0.050	0.060	0.057	0.056	0.061	0.061	0.219	0.206	0.178	0.170	0.187	0.153	0.185	0.201	0.177	0.174	0.189	0.175
K	0.908	0.911	0.854	0.893	0.866	0.843	0.870	0.808	0.841	0.824	0.893	0.826	0.848	0.822	0.834	0.800	0.766	0.734	0.764	0.770	0.811	0.782	0.729	0.770	0.794	0.755	0.732
F	0.000	0.000	0.083	0.059	0.121	0.078	0.113	0.076	0.096	0.077	0.074	0.083	0.118	0.095	0.091	0.000	0.000	0.000	0.000	0.000	0.000	0.000	0.000	0.000	0.000	0.000	0.000
Cl	0.000	0.009	0.016	0.012	0.007	0.007	0.009	0.008	0.007	0.014	0.021	0.008	0.004	0.006	0.009	0.010	0.008	0.004	0.003	0.003	0.009	0.007	0.003	0.008	0.009	0.001	0.005
tot	6.989	7.023	7.940	7.938	7.958	7.915	7.999	7.855	7.900	7.891	7.965	7.915	7.971	7.909	7.916	7.043	7.015	6.969	6.986	6.996	7.024	7.021	6.985	6.992	7.002	6.996	6.958

SAMPLE	**UT15-9**																	**UT15-10**									
	ms	ms	ms	ms	ms	ms	ms	ms	ms	chl	chl	chl	chl	chl	chl	chl	chl	bt	bt	bt	ms	ms	ms	ms	ms	ms	ms
Spot number	141	142	143	144	150	151	152	155	157	112	118	120	121	125	148	156	160	24	27	42	2	4	6	7	8	9	10
OXIDES wt%																											
SiO_2	46.510	46.470	45.210	47.170	46.050	43.110	45.290	47.890	47.890	23.770	25.390	23.930	24.650	23.640	30.550	35.260	25.690	35.640	34.730	36.870	44.210	45.450	46.310	48.630	46.710	47.360	45.530
TiO_2	0.254	0.250	0.233	0.300	0.348	0.225	0.351	0.248	0.266	0.125	0.101	0.068	0.153	0.054	1.680	1.690	0.085	1.583	1.458	1.366	0.244	0.305	0.193	0.218	0.219	0.210	0.207
Al_2O_3	34.250	35.220	33.830	34.750	33.950	32.100	33.800	35.860	34.850	22.810	23.960	22.070	22.410	21.840	14.670	17.980	23.880	19.260	19.340	20.010	34.270	34.790	35.710	35.090	36.320	35.170	34.830
FeO	1.920	1.880	1.990	2.160	2.180	2.050	2.010	1.860	1.900	25.520	27.110	26.000	25.610	25.830	20.700	20.300	26.560	22.440	22.340	22.180	1.114	1.063	1.400	1.138	1.267	1.380	1.420
MnO	0.005	0.000	0.000	0.000	0.030	0.016	0.000	0.000	0.000	0.165	0.216	0.170	0.169	0.210	0.127	0.118	0.181	0.000	0.000	0.000	0.035	0.006	0.000	0.000	0.001	0.054	0.000
MgO	0.700	0.659	0.667	0.923	0.734	0.599	0.671	0.645	0.769	13.060	13.670	13.160	14.020	13.190	7.600	9.300	14.200	7.770	7.720	8.510	0.516	0.460	0.556	0.675	0.518	0.686	0.729
CaO	0.038	0.053	0.037	0.063	0.065	0.084	0.039	0.081	0.073	0.129	0.088	0.062	0.094	0.120	0.149	0.126	0.088	0.079	0.084	0.000	0.055	0.088	0.027	0.086	0.086	0.029	0.078
BaO	0.259	0.169	0.353	0.294	0.497	0.239	0.245	0.149	0.291	0.000	0.011	0.000	0.000	0.000	0.148	0.142	0.000	0.013	0.000	0.085	0.149	0.185	0.049	0.048	0.114	0.167	0.215
Na_2O	1.304	1.560	1.600	1.640	1.400	0.894	1.287	1.800	1.172	0.164	0.048	0.246	0.224	0.076	0.296	0.414	0.074	0.298	0.357	0.286	1.530	2.020	1.680	1.550	1.670	1.600	1.430
K_2O	8.930	8.880	8.660	8.850	8.940	9.450	8.990	8.740	9.220	0.102	0.102	0.167	0.186	0.039	8.470	8.710	0.028	7.070	7.250	7.200	8.870	8.680	8.450	8.280	8.540	8.800	8.400
F	0.000	0.000	0.000	0.000	0.000	0.000	0.000	0.000	0.000	0.000	0.000	0.000	0.000	0.005	0.397	0.401	0.000	0.467	0.395	0.613	0.000	0.000	0.000	0.000	0.000	0.000	0.000
Cl	0.111	0.018	0.014	0.061	0.045	0.023	0.052	0.033	0.033	0.039	0.033	0.100	0.052	0.005	0.064	0.070	0.015	0.038	0.023	0.040	0.042	0.340	0.020	0.053	0.044	0.154	0.049
tot	94.280	95.159	92.594	96.211	94.239	88.789	92.736	97.306	96.464	85.884	90.728	85.972	87.568	85.009	84.851	94.512	90.801	94.658	93.697	97.159	91.036	93.388	94.394	95.767	95.489	95.611	92.889
CATIONS apfu																											
Si	3.127	3.090	3.099	3.111	3.110	3.100	3.102	3.108	3.141	2.573	2.600	2.601	2.614	2.593	3.462	3.495	2.617	2.757	2.720	2.772	3.072	3.090	3.086	3.176	3.078	3.128	3.090
Ti	0.013	0.012	0.012	0.015	0.018	0.012	0.018	0.012	0.013	0.010	0.008	0.006	0.012	0.004	0.143	0.126	0.006	0.092	0.086	0.077	0.013	0.016	0.010	0.011	0.011	0.010	0.011
Al	2.714	2.760	2.733	2.701	2.702	2.720	2.728	2.743	2.694	2.910	2.892	2.827	2.801	2.824	1.959	2.100	2.867	1.756	1.785	1.773	2.806	2.787	2.804	2.701	2.820	2.737	2.786
Fe	0.108	0.105	0.114	0.119	0.123	0.123	0.115	0.101	0.104	2.310	2.322	2.363	2.272	2.370	1.962	1.683	2.263	1.452	1.463	1.395	0.065	0.060	0.078	0.062	0.070	0.076	0.081
Mn	0.000	0.000	0.000	0.000	0.002	0.001	0.000	0.000	0.000	0.015	0.019	0.016	0.015	0.020	0.012	0.010	0.016	0.000	0.000	0.000	0.002	0.000	0.000	0.000	0.000	0.003	0.000
Mg	0.070	0.065	0.068	0.091	0.074	0.064	0.069	0.062	0.075	2.107	2.087	2.132	2.216	2.157	1.284	1.374	2.156	0.896	0.901	0.954	0.053	0.047	0.055	0.066	0.051	0.068	0.074
Ca	0.003	0.004	0.003	0.004	0.005	0.006	0.003	0.006	0.005	0.015	0.010	0.007	0.011	0.014	0.018	0.013	0.010	0.007	0.007	0.000	0.004	0.006	0.002	0.006	0.006	0.002	0.006
Ba	0.007	0.004	0.009	0.008	0.013	0.007	0.007	0.004	0.007	0.000	0.000	0.000	0.000	0.000	0.007	0.006	0.000	0.000	0.000	0.003	0.004	0.005	0.001	0.001	0.003	0.004	0.006
Na	0.170	0.201	0.213	0.210	0.183	0.125	0.171	0.226	0.149	0.034	0.009	0.052	0.046	0.016	0.065	0.080	0.015	0.045	0.054	0.042	0.206	0.266	0.217	0.196	0.213	0.205	0.188
K	0.766	0.753	0.757	0.745	0.770	0.867	0.785	0.724	0.771	0.014	0.013	0.023	0.025	0.005	1.224	1.101	0.004	0.698	0.724	0.691	0.786	0.753	0.718	0.690	0.718	0.741	0.727
F	0.000	0.000	0.000	0.000	0.000	0.000	0.000	0.000	0.000	0.000	0.000	0.000	0.000	0.002	0.142	0.126	0.000	0.114	0.098	0.146	0.000	0.000	0.000	0.000	0.000	0.000	0.000
Cl	0.013	0.002	0.002	0.007	0.005	0.003	0.006	0.004	0.004	0.007	0.006	0.018	0.009	0.001	0.012	0.012	0.003	0.005	0.003	0.005	0.005	0.039	0.002	0.006	0.005	0.017	0.006
tot	6.990	6.997	7.010	7.011	7.005	7.028	7.003	6.989	6.964	9.997	9.966	10.045	10.022	10.005	10.291	10.125	9.956	7.822	7.842	7.856	7.016	7.069	6.974	6.915	6.974	6.992	6.973

SAMPLE	**UT15-10**																										
	ms	ms	ms	ms	ms	ms	ms	ms	ms	ms	ms	ms	ms	ms	ms	ms	ms	ms	ms	ms	ms	ms	ms	ms	ms	ms	ms
Spot number	11	12	13	14	15	17	18	19	20	22	23	25	26	28	30	32	33	36	39	40	45	46	48	49	52	54	55
OXIDES wt%																											
SiO_2	45.240	46.970	44.670	46.830	45.870	46.420	48.150	48.220	47.350	48.450	46.730	46.430	47.720	46.850	47.470	45.880	46.840	47.460	47.270	46.540	46.270	48.600	46.100	46.810	46.510	48.230	48.050
TiO_2	0.450	0.324	0.215	0.197	0.280	0.261	0.323	0.249	0.133	0.251	0.266	0.210	0.664	0.200	0.176	0.229	0.265	0.265	0.183	0.275	0.287	0.266	0.298	0.204	0.184	0.236	0.280
Al_2O_3	34.700	34.790	33.560	36.630	34.390	35.940	37.510	37.350	36.560	35.820	35.810	35.420	36.810	36.620	33.920	35.230	35.370	36.500	34.650	35.790	36.400	35.850	35.030	35.280	34.760	35.950	37.180
FeO	1.520	1.700	1.330	1.053	1.128	1.155	1.198	1.202	1.166	1.243	1.330	1.091	1.063	1.290	1.430	1.590	1.132	1.188	1.470	1.620	1.053	1.370	1.140	1.610	1.370	1.262	1.139
MnO	0.000	0.000	0.008	0.000	0.000	0.030	0.007	0.031	0.000	0.000	0.009	0.000	0.016	0.000	0.034	0.039	0.009	0.013	0.040	0.000	0.031	0.024	0.007	0.000	0.000	0.003	0.000
MgO	0.584	0.875	0.724	0.448	0.708	0.616	0.603	0.646	0.685	0.803	0.633	0.597	0.665	0.626	0.653	0.595	0.724	0.690	0.747	0.620	0.549	0.920	0.722	0.659	0.721	0.767	0.516
CaO	0.044	0.052	0.087	0.049	0.122	0.043	0.035	0.078	0.039	0.058	0.048	0.052	0.131	0.066	0.082	0.036	0.072	0.061	0.082	0.121	0.072	0.099	0.146	0.081	0.082	0.043	0.026
BaO	0.110	0.174	0.093	0.173	0.148	0.191	0.197	0.036	0.185	0.228	0.163	0.085	0.177	0.136	0.070	0.065	0.122	0.163	0.178	0.158	0.136	0.132	0.114	0.036	0.126	0.026	0.115
Na_2O	1.760	1.275	1.296	1.680	1.490	1.450	1.880	1.720	1.510	1.810	1.420	1.800	1.930	1.390	1.500	1.620	1.570	1.510	1.370	1.690	1.710	1.400	1.470	1.400	1.350	1.560	1.990
K_2O	9.020	8.460	8.530	8.780	8.680	8.600	8.360	8.350	8.680	8.690	8.430	8.400	8.270	8.390	8.240	8.530	8.430	8.510	8.410	8.120	8.390	8.470	8.450	8.580	8.460	8.560	8.450
F	0.000	0.000	0.000	0.000	0.000	0.000	0.000	0.000	0.000	0.000	0.000	0.000	0.000	0.000	0.000	0.000	0.000	0.000	0.000	0.000	0.000	0.000	0.000	0.000	0.000	0.000	0.000
Cl	0.383	0.023	0.033	0.107	0.412	0.000	0.030	0.034	0.051	0.129	0.014	0.004	0.030	0.048	0.031	0.020	0.033	0.018	0.002	0.017	0.019	0.030	0.013	0.029	0.000	0.010	0.000
tot	93.810	94.643	90.545	95.947	93.228	94.705	98.293	97.916	96.360	97.481	94.853	94.088	97.477	95.616	93.606	93.834	94.567	96.377	94.401	94.951	94.917	97.162	93.490	94.689	93.563	96.646	97.746
CATIONS apfu																											
Si	3.074	3.124	3.110	3.075	3.119	3.082	3.075	3.086	3.089	3.132	3.095	3.099	3.074	3.076	3.181	3.083	3.111	3.091	3.146	3.083	3.063	3.137	3.099	3.111	3.123	3.128	3.084
Ti	0.023	0.016	0.011	0.010	0.014	0.013	0.015	0.012	0.007	0.012	0.013	0.011	0.032	0.010	0.009	0.012	0.013	0.013	0.009	0.014	0.014	0.013	0.015	0.010	0.009	0.012	0.014
Al	2.779	2.727	2.754	2.835	2.756	2.812	2.823	2.817	2.811	2.729	2.795	2.787	2.795	2.834	2.679	2.790	2.768	2.802	2.718	2.794	2.840	2.727	2.776	2.763	2.751	2.748	2.813
Fe	0.086	0.095	0.077	0.058	0.064	0.064	0.064	0.064	0.064	0.067	0.074	0.061	0.057	0.071	0.080	0.089	0.063	0.065	0.082	0.090	0.058	0.074	0.064	0.089	0.077	0.068	0.061
Mn	0.000	0.000	0.000	0.000	0.000	0.002	0.000	0.002	0.000	0.000	0.000	0.000	0.001	0.000	0.002	0.002	0.001	0.001	0.002	0.000	0.002	0.001	0.000	0.000	0.000	0.000	0.000
Mg	0.059	0.087	0.075	0.044	0.072	0.061	0.057	0.062	0.067	0.077	0.062	0.059	0.064	0.061	0.065	0.060	0.072	0.067	0.074	0.061	0.054	0.089	0.072	0.065	0.072	0.074	0.049
Ca	0.003	0.004	0.006	0.003	0.009	0.003	0.002	0.005	0.003	0.004	0.003	0.004	0.009	0.005	0.006	0.003	0.005	0.004	0.006	0.009	0.005	0.007	0.011	0.006	0.006	0.003	0.002
Ba	0.003	0.005	0.003	0.004	0.004	0.005	0.005	0.001	0.005	0.006	0.004	0.002	0.004	0.004	0.002	0.002	0.003	0.004	0.005	0.004	0.004	0.003	0.003	0.001	0.003	0.001	0.003
Na	0.232	0.164	0.175	0.214	0.196	0.187	0.233	0.213	0.191	0.227	0.182	0.233	0.241	0.177	0.195	0.211	0.202	0.191	0.177	0.217	0.219	0.175	0.192	0.180	0.176	0.196	0.248
K	0.782	0.718	0.758	0.735	0.753	0.728	0.681	0.682	0.722	0.717	0.712	0.715	0.680	0.703	0.704	0.731	0.714	0.707	0.714	0.686	0.708	0.697	0.725	0.727	0.725	0.708	0.692
F	0.000	0.000	0.000	0.000	0.000	0.000	0.000	0.000	0.000	0.000	0.000	0.000	0.000	0.000	0.000	0.000	0.000	0.000	0.000	0.000	0.000	0.000	0.000	0.000	0.000	0.000	0.000
Cl	0.044	0.003	0.004	0.012	0.047	0.000	0.003	0.004	0.006	0.014	0.002	0.000	0.003	0.005	0.004	0.002	0.004	0.002	0.000	0.002	0.002	0.003	0.001	0.003	0.000	0.001	0.000
tot	7.086	6.941	6.974	6.990	7.035	6.957	6.960	6.947	6.964	6.984	6.944	6.971	6.961	6.945	6.926	6.985	6.956	6.947	6.932	6.960	6.970	6.928	6.958	6.956	6.942	6.940	6.966

SAMPLE	**UT15-10**																				**UT15-40**						
	ms	ms	chl	chl	chl	chl	chl	chl	chl	chl	chl	chl	chl	chl	chl	chl	chl	chl	chl	chl	ms	ms	ms	ms	ms	ms	ms
Spot number	56	58	1	3	5	16	21	29	31	34	35	37	38	43	44	47	50	51	53	57	59	60	61	62	63	64	65
OXIDES wt%																											
SiO_2	46.500	45.480	24.180	24.930	24.180	23.650	23.840	23.320	27.160	23.810	23.320	23.180	23.340	23.920	22.350	24.070	25.570	24.260	23.890	26.110	48.090	47.720	47.730	47.020	46.810	47.980	46.870
TiO_2	0.275	0.226	0.130	0.030	0.069	0.117	0.162	0.111	0.783	0.108	0.111	0.044	0.132	0.049	0.077	0.077	0.066	0.118	0.062	0.076	0.252	0.240	0.234	0.333	0.370	0.423	1.079
Al_2O_3	36.870	35.680	23.870	23.850	23.200	22.990	23.050	23.130	19.730	23.120	22.720	23.150	22.740	23.460	21.960	24.060	23.830	21.300	23.700	20.380	35.600	35.330	35.130	34.980	34.690	33.860	35.230
FeO	1.155	1.750	29.670	29.400	29.110	29.970	29.290	29.590	26.100	29.650	28.780	28.370	28.760	29.540	29.420	29.770	29.220	30.030	29.840	28.530	1.780	1.870	1.950	2.000	2.040	2.060	1.750
MnO	0.051	0.006	0.018	0.000	0.038	0.017	0.023	0.026	0.000	0.000	0.031	0.037	0.029	0.036	0.031	0.041	0.048	0.082	0.023	0.013	0.000	0.010	0.000	0.018	0.065	0.031	0.004
MgO	0.525	0.801	11.810	11.570	11.230	10.780	10.680	10.990	9.030	10.900	10.840	10.730	10.580	11.130	10.220	11.500	12.020	10.080	11.180	9.040	0.315	0.350	0.403	0.428	0.426	0.459	0.328
CaO	0.031	0.050	0.040	0.099	0.092	0.049	0.112	0.081	0.059	0.070	0.091	0.086	0.075	0.076	0.045	0.031	0.067	0.087	0.077	0.093	0.022	0.075	0.069	0.068	0.042	0.022	0.029
BaO	0.065	0.094	0.000	0.124	0.000	0.014	0.000	0.037	0.029	0.002	0.069	0.049	0.005	0.039	0.008	0.000	0.034	0.000	0.030	0.077	0.056	0.088	0.046	0.051	0.001	0.023	0.145
Na_2O	1.740	1.390	0.000	0.130	0.100	0.000	0.143	0.059	0.083	0.261	0.086	0.146	0.079	0.078	0.042	0.073	0.073	0.079	0.075	0.030	0.415	0.695	0.511	0.602	0.532	0.536	0.533
K_2O	8.310	8.610	0.027	0.076	0.148	0.064	0.204	0.053	3.060	0.193	0.079	0.044	0.113	0.044	0.038	0.067	0.078	0.456	0.041	0.130	10.570	10.300	10.310	10.230	10.250	10.190	10.360
F	0.000	0.000	0.000	0.000	0.060	0.000	0.000	0.000	0.201	0.000	0.000	0.000	0.000	0.000	0.000	0.000	0.025	0.000	0.000	0.000	0.097	0.000	0.145	0.058	0.000	0.000	0.000
Cl	0.013	0.025	0.000	0.033	0.060	0.025	0.047	0.011	0.050	0.038	0.037	0.047	0.076	0.024	0.024	0.034	0.019	0.026	0.015	0.027	0.017	0.021	0.000	0.006	0.011	0.000	0.015
tot	95.536	94.112	89.745	90.242	88.286	87.675	87.551	87.407	86.285	88.152	86.165	85.883	85.930	88.396	84.215	89.723	91.049	86.518	88.932	84.505	97.215	96.699	96.529	95.794	95.236	95.584	96.342
CATIONS apfu																											
Si	3.055	3.051	2.541	2.601	2.589	2.560	2.578	2.530	2.984	2.562	2.562	2.548	2.571	2.558	2.532	2.534	2.634	2.674	2.542	2.903	3.140	3.130	3.142	3.119	3.121	3.181	3.091
Ti	0.014	0.011	0.010	0.002	0.006	0.009	0.013	0.009	0.065	0.009	0.009	0.004	0.011	0.004	0.007	0.006	0.005	0.010	0.005	0.006	0.012	0.012	0.012	0.017	0.019	0.021	0.054
Al	2.855	2.821	2.956	2.932	2.928	2.933	2.938	2.958	2.555	2.932	2.941	3.000	2.952	2.957	2.932	2.985	2.893	2.767	2.972	2.670	2.739	2.731	2.726	2.735	2.726	2.645	2.738
Fe	0.063	0.098	2.607	2.565	2.607	2.713	2.649	2.685	2.398	2.668	2.644	2.608	2.649	2.642	2.787	2.621	2.517	2.768	2.655	2.653	0.097	0.103	0.107	0.111	0.114	0.114	0.097
Mn	0.003	0.000	0.002	0.000	0.003	0.002	0.002	0.002	0.000	0.000	0.003	0.003	0.003	0.003	0.003	0.004	0.004	0.008	0.002	0.001	0.000	0.001	0.000	0.001	0.004	0.002	0.000
Mg	0.051	0.080	1.850	1.799	1.792	1.739	1.722	1.777	1.479	1.748	1.775	1.758	1.737	1.774	1.725	1.805	1.846	1.656	1.773	1.498	0.031	0.034	0.040	0.042	0.042	0.045	0.032
Ca	0.002	0.004	0.004	0.011	0.011	0.006	0.013	0.009	0.007	0.008	0.011	0.010	0.009	0.009	0.006	0.004	0.007	0.010	0.009	0.011	0.002	0.005	0.005	0.005	0.003	0.002	0.002
Ba	0.002	0.002	0.000	0.005	0.000	0.001	0.000	0.002	0.001	0.000	0.003	0.002	0.000	0.002	0.000	0.000	0.001	0.000	0.001	0.003	0.001	0.002	0.001	0.001	0.000	0.001	0.004
Na	0.222	0.181	0.000	0.026	0.021	0.000	0.030	0.012	0.018	0.054	0.018	0.031	0.017	0.016	0.009	0.015	0.015	0.017	0.015	0.006	0.053	0.088	0.065	0.077	0.069	0.069	0.068
K	0.696	0.737	0.004	0.010	0.020	0.009	0.028	0.007	0.429	0.026	0.011	0.006	0.016	0.006	0.005	0.009	0.010	0.064	0.006	0.018	0.880	0.862	0.866	0.866	0.872	0.862	0.872
F	0.000	0.000	0.000	0.000	0.020	0.000	0.000	0.000	0.070	0.000	0.000	0.000	0.000	0.000	0.000	0.000	0.008	0.000	0.000	0.000	0.020	0.000	0.030	0.012	0.000	0.000	0.000
Cl	0.001	0.003	0.000	0.006	0.011	0.004	0.009	0.002	0.009	0.007	0.007	0.009	0.014	0.004	0.005	0.006	0.003	0.005	0.003	0.005	0.002	0.002	0.000	0.001	0.001	0.000	0.002
tot	6.965	6.990	9.973	9.958	10.008	9.975	9.982	9.995	10.016	10.014	9.984	9.980	9.980	9.977	10.010	9.988	9.944	9.980	9.982	9.776	6.977	6.971	6.994	6.987	6.970	6.941	6.959

SAMPLE	**UT15-40**																										
	ms	ms	ms	ms	ms	ms	ms	ms	ms	ms	ms	ms	ms	ms	ms	ms	ms	ms	ms	ms	ms	ms	ms	ms	ms	ms	ms
Spot number	66	67	68	69	70	71	72	73	74	75	76	77	78	79	80	81	82	83	84	85	86	87	88	89	90	91	92
OXIDES wt%																											
SiO_2	48.240	46.270	46.420	46.100	47.000	45.640	46.330	48.160	47.360	46.470	47.710	46.220	47.300	46.290	46.810	45.240	46.880	46.580	47.390	46.130	47.140	45.680	46.520	46.530	45.790	46.440	46.480
TiO_2	0.872	0.187	0.394	0.247	0.443	0.496	0.237	0.190	0.392	0.238	0.376	0.277	0.289	0.154	0.194	0.366	0.318	0.938	0.215	0.350	0.182	0.394	0.531	0.381	0.754	0.639	0.742
Al_2O_3	36.260	34.310	33.740	34.210	35.300	33.600	34.910	36.850	34.490	34.360	34.810	34.060	35.050	34.860	35.880	33.430	34.510	34.160	34.910	33.870	35.030	33.760	34.520	33.240	31.310	32.850	31.870
FeO	1.820	1.800	1.900	1.940	1.940	1.930	1.750	1.860	2.010	1.990	1.950	1.850	1.950	1.830	1.730	1.990	2.030	2.030	1.870	2.080	1.970	2.080	1.480	1.650	1.670	1.870	1.800
MnO	0.029	0.034	0.106	0.055	0.044	0.016	0.069	0.009	0.060	0.038	0.019	0.035	0.036	0.018	0.009	0.014	0.012	0.007	0.087	0.029	0.045	0.021	0.000	0.025	0.000	0.068	0.000
MgO	0.393	0.404	0.425	0.424	0.369	0.344	0.337	0.298	0.446	0.400	0.443	0.456	0.423	0.397	0.339	0.385	0.435	0.458	0.405	0.448	0.354	0.447	0.955	1.163	1.290	1.228	1.310
CaO	0.046	0.047	0.084	0.126	0.076	0.055	0.043	0.000	0.053	0.030	0.091	0.060	0.057	0.077	0.058	0.014	0.044	0.071	0.071	0.061	0.083	0.043	0.036	0.078	0.130	0.064	0.066
BaO	0.000	0.000	0.028	0.075	0.000	0.000	0.107	0.072	0.000	0.000	0.060	0.000	0.000	0.000	0.000	0.016	0.046	0.000	0.000	0.000	0.000	0.043	0.019	0.000	0.180	0.203	0.412
Na_2O	0.646	0.596	0.673	0.607	0.459	0.661	0.479	0.627	0.520	0.497	0.785	0.621	0.660	0.600	0.704	0.540	0.734	0.722	0.614	0.457	0.525	0.553	0.648	0.560	0.632	0.510	0.548
K_2O	10.270	10.280	9.840	10.040	10.340	10.410	10.610	10.190	10.190	10.200	10.340	10.440	10.180	10.100	10.100	10.490	10.090	10.080	10.040	10.460	10.240	10.210	10.260	10.260	10.070	10.120	10.290
F	0.000	0.122	0.000	0.126	0.035	0.068	0.023	0.026	0.192	0.192	0.058	0.000	0.058	0.047	0.054	0.046	0.077	0.034	0.065	0.141	0.116	0.055	0.021	0.023	0.065	0.245	0.215
Cl	0.014	0.026	0.036	0.034	0.036	0.023	0.008	0.024	0.003	0.001	0.148	0.098	0.000	0.006	0.000	0.094	0.013	0.011	0.000	0.021	0.067	0.007	0.056	0.077	0.069	0.042	0.027
tot	98.589	94.076	93.646	93.983	96.041	93.241	94.903	98.306	95.716	94.415	96.788	94.117	96.002	94.379	95.876	92.624	95.189	95.090	95.666	94.047	95.752	93.292	95.047	93.986	91.961	94.279	93.761
CATIONS apfu																											
Si	3.099	3.131	3.144	3.125	3.109	3.123	3.107	3.101	3.149	3.135	3.141	3.127	3.127	3.112	3.094	3.121	3.131	3.115	3.140	3.132	3.132	3.119	3.108	3.148	3.178	3.152	3.179
Ti	0.042	0.009	0.020	0.013	0.022	0.026	0.012	0.009	0.020	0.012	0.019	0.014	0.014	0.008	0.010	0.019	0.016	0.047	0.011	0.018	0.009	0.020	0.027	0.019	0.039	0.033	0.038
Al	2.745	2.736	2.694	2.733	2.752	2.709	2.759	2.797	2.703	2.732	2.701	2.716	2.731	2.762	2.795	2.718	2.717	2.692	2.726	2.710	2.743	2.717	2.718	2.650	2.561	2.628	2.569
Fe	0.098	0.102	0.108	0.110	0.107	0.110	0.098	0.100	0.112	0.112	0.107	0.105	0.108	0.103	0.096	0.115	0.113	0.114	0.104	0.118	0.109	0.119	0.083	0.093	0.097	0.106	0.103
Mn	0.002	0.002	0.006	0.003	0.002	0.001	0.004	0.001	0.003	0.002	0.001	0.002	0.002	0.001	0.000	0.001	0.001	0.000	0.005	0.002	0.003	0.001	0.000	0.001	0.000	0.004	0.000
Mg	0.038	0.041	0.043	0.043	0.036	0.035	0.034	0.029	0.044	0.040	0.043	0.046	0.042	0.040	0.033	0.040	0.043	0.046	0.040	0.045	0.035	0.045	0.095	0.117	0.134	0.124	0.134
Ca	0.003	0.003	0.006	0.009	0.005	0.004	0.003	0.000	0.004	0.002	0.006	0.004	0.004	0.006	0.004	0.001	0.003	0.005	0.005	0.004	0.006	0.003	0.003	0.006	0.010	0.005	0.005
Ba	0.000	0.000	0.001	0.002	0.000	0.000	0.003	0.002	0.000	0.000	0.002	0.000	0.000	0.000	0.000	0.000	0.001	0.000	0.000	0.000	0.000	0.001	0.000	0.000	0.005	0.005	0.011
Na	0.080	0.078	0.088	0.080	0.059	0.088	0.062	0.078	0.067	0.065	0.100	0.081	0.085	0.078	0.090	0.072	0.095	0.094	0.079	0.060	0.068	0.073	0.084	0.073	0.085	0.067	0.073
K	0.842	0.887	0.850	0.868	0.872	0.909	0.908	0.837	0.864	0.878	0.868	0.901	0.859	0.866	0.852	0.923	0.860	0.860	0.849	0.906	0.868	0.889	0.874	0.885	0.892	0.876	0.898
F	0.000	0.026	0.000	0.027	0.007	0.015	0.005	0.005	0.040	0.041	0.012	0.000	0.012	0.010	0.011	0.010	0.016	0.007	0.014	0.030	0.024	0.012	0.005	0.005	0.014	0.052	0.047
Cl	0.001	0.003	0.004	0.004	0.004	0.003	0.001	0.003	0.000	0.000	0.017	0.011	0.000	0.001	0.000	0.011	0.001	0.001	0.000	0.002	0.007	0.001	0.006	0.009	0.008	0.005	0.003
tot	6.950	7.018	6.964	7.016	6.976	7.021	6.995	6.961	7.007	7.020	7.017	7.009	6.983	6.987	6.986	7.031	6.998	6.981	6.971	7.028	7.004	7.002	7.002	7.008	7.023	7.059	7.058

SAMPLE	**UT15-40**																				**UT15-41**						
	ms	ms	ms	ms	ms	ms	ms	ms	ms	ms	bt	bt	bt	bt	bt	bt	bt	bt	bt	bt	ms	ms	ms	ms	ms	ms	ms
Spot number	93	95	97	99	100	102	107	108	111	112	94	96	98	101	103	104	105	106	109	110	1	2	3	4	5	6	7
OXIDES wt%																											
SiO_2	46.520	45.620	47.440	47.200	46.740	44.510	47.160	47.690	45.390	46.580	36.280	35.870	34.590	35.660	36.390	36.750	35.490	37.300	35.970	36.830	48.390	47.550	47.970	47.850	47.640	47.510	47.500
TiO_2	0.678	0.605	0.754	0.694	0.672	0.834	0.774	0.828	0.704	0.655	2.400	2.270	2.590	2.310	2.520	2.570	2.400	2.560	2.250	2.290	0.396	0.361	0.315	0.280	0.239	0.293	0.290
Al_2O_3	32.040	32.270	33.240	33.070	32.890	31.730	33.510	33.510	31.720	32.370	17.800	17.940	16.730	17.460	17.630	18.720	17.330	18.210	17.640	18.270	34.640	34.530	34.780	34.260	34.560	34.280	34.490
FeO	1.860	1.800	1.970	1.700	1.710	1.690	1.800	1.750	1.840	1.740	19.410	20.070	19.540	19.230	21.490	19.050	19.070	19.360	19.910	20.440	2.010	1.910	2.020	1.910	2.140	2.030	2.000
MnO	0.041	0.043	0.000	0.056	0.000	0.040	0.003	0.025	0.003	0.013	0.305	0.373	0.338	0.329	0.354	0.297	0.308	0.309	0.397	0.435	0.033	0.072	0.055	0.057	0.018	0.022	0.015
MgO	1.359	1.372	1.396	1.210	1.289	1.165	1.398	1.486	1.351	1.361	8.440	8.030	7.370	8.270	8.170	8.340	7.790	9.180	8.650	9.130	0.438	0.530	0.471	0.446	0.416	0.377	0.450
CaO	0.043	0.088	0.032	0.033	0.096	0.046	0.077	0.042	0.077	0.065	0.049	0.088	0.186	0.085	0.082	0.084	0.073	0.001	0.063	0.054	0.043	0.024	0.020	0.029	0.011	0.000	0.016
BaO	0.206	0.206	0.180	0.249	0.294	0.407	0.424	0.432	0.362	0.348	0.206	0.052	0.203	0.315	0.134	0.070	0.299	0.098	0.223	0.244	0.071	0.021	0.000	0.027	0.019	0.021	0.000
Na_2O	0.534	0.648	0.612	0.485	0.683	0.605	0.609	0.477	0.589	0.482	0.225	0.270	0.199	0.187	0.226	0.230	0.279	0.167	0.190	0.153	0.528	0.445	0.468	0.419	0.506	0.438	0.421
K_2O	10.300	9.970	10.130	10.230	10.260	10.190	10.220	10.280	10.040	10.030	9.010	8.870	9.040	9.010	8.950	8.910	8.780	9.210	8.980	9.040	10.450	10.660	10.600	10.490	10.390	10.550	10.580
F	0.143	0.121	0.180	0.199	0.175	0.140	0.218	0.101	0.170	0.109	1.360	1.020	1.150	1.250	1.040	1.300	1.120	1.120	1.320	0.882	0.027	0.049	0.110	0.000	0.000	0.026	0.001
Cl	0.036	0.129	0.063	0.028	0.079	0.084	0.089	0.021	0.040	0.019	0.010	0.038	0.058	0.019	0.066	0.000	0.027	0.023	0.022	0.016	0.007	0.014	0.000	0.000	0.000	0.000	0.000
tot	93.760	92.871	95.997	95.155	94.889	91.440	96.281	96.642	92.286	93.773	95.496	94.890	91.994	94.126	97.051	96.321	92.965	97.538	95.615	97.783	97.032	96.167	96.808	95.768	95.939	95.547	95.763
CATIONS apfu																											
Si	3.173	3.143	3.156	3.166	3.153	3.127	3.139	3.148	3.153	3.168	2.837	2.812	2.826	2.832	2.808	2.826	2.843	2.828	2.819	2.791	3.165	3.145	3.152	3.168	3.151	3.158	3.149
Ti	0.035	0.031	0.038	0.035	0.034	0.044	0.039	0.041	0.037	0.034	0.141	0.134	0.159	0.138	0.146	0.149	0.145	0.146	0.133	0.131	0.019	0.018	0.016	0.014	0.012	0.015	0.014
Al	2.576	2.621	2.607	2.615	2.615	2.628	2.629	2.607	2.597	2.594	1.641	1.657	1.611	1.634	1.603	1.697	1.636	1.627	1.629	1.632	2.670	2.692	2.694	2.673	2.694	2.686	2.695
Fe	0.106	0.104	0.110	0.095	0.096	0.099	0.100	0.097	0.107	0.099	1.270	1.316	1.335	1.277	1.387	1.225	1.278	1.228	1.305	1.296	0.110	0.106	0.111	0.106	0.118	0.113	0.111
Mn	0.002	0.003	0.000	0.003	0.000	0.002	0.000	0.001	0.000	0.001	0.020	0.025	0.023	0.022	0.023	0.019	0.021	0.020	0.026	0.028	0.002	0.004	0.003	0.003	0.001	0.001	0.001
Mg	0.138	0.141	0.138	0.121	0.130	0.122	0.139	0.146	0.140	0.138	0.984	0.938	0.898	0.979	0.940	0.956	0.930	1.038	1.010	1.031	0.043	0.052	0.046	0.044	0.041	0.037	0.044
Ca	0.003	0.007	0.002	0.002	0.007	0.003	0.005	0.003	0.006	0.005	0.004	0.007	0.016	0.007	0.007	0.007	0.006	0.000	0.005	0.004	0.003	0.002	0.001	0.002	0.001	0.000	0.001
Ba	0.006	0.006	0.005	0.007	0.008	0.011	0.011	0.011	0.010	0.009	0.006	0.002	0.007	0.010	0.004	0.002	0.009	0.003	0.007	0.007	0.002	0.001	0.000	0.001	0.000	0.001	0.000
Na	0.071	0.087	0.079	0.063	0.089	0.082	0.079	0.061	0.079	0.064	0.034	0.041	0.032	0.029	0.034	0.034	0.043	0.025	0.029	0.022	0.067	0.057	0.060	0.054	0.065	0.056	0.054
K	0.896	0.876	0.860	0.875	0.883	0.913	0.868	0.866	0.890	0.870	0.899	0.887	0.942	0.913	0.881	0.874	0.897	0.891	0.898	0.874	0.872	0.899	0.889	0.886	0.877	0.895	0.895
F	0.031	0.026	0.038	0.042	0.037	0.031	0.046	0.021	0.037	0.023	0.336	0.253	0.297	0.314	0.254	0.316	0.284	0.269	0.327	0.211	0.006	0.010	0.023	0.000	0.000	0.005	0.000
Cl	0.004	0.015	0.007	0.003	0.009	0.010	0.010	0.002	0.005	0.002	0.001	0.005	0.008	0.003	0.009	0.000	0.004	0.003	0.003	0.002	0.001	0.002	0.000	0.000	0.000	0.000	0.000
tot	7.040	7.058	7.039	7.029	7.061	7.074	7.065	7.005	7.060	7.007	8.174	8.076	8.154	8.158	8.095	8.105	8.096	8.077	8.192	8.030	6.959	6.987	6.994	6.951	6.961	6.968	6.964

SAMPLE	UT15-41																									UT15-51	
	ms	ms	ms	ms	ms	ms	ms	ms	ms	ms	ms	ms	ms	ms	ms	ms	ms	ms	ms	ms	ms	ms	ms	ms	ms	bt	bt
Spot number	8	9	10	11	12	13	14	15	16	17	18	19	20	21	22	23	24	25	26	27	28	29	30	31	32	33	34
OXIDES wt%																											
SiO_2	47.210	47.430	47.580	47.490	47.100	47.580	47.080	47.460	46.680	46.450	46.550	46.720	47.210	46.730	46.670	47.400	47.280	47.250	46.620	46.920	46.530	46.750	47.220	47.120	47.460	35.890	35.630
TiO_2	0.483	0.289	0.199	0.491	0.271	0.422	0.216	0.326	0.607	0.324	0.606	0.263	0.290	0.293	0.178	0.286	0.333	0.323	0.298	0.446	0.198	0.358	0.416	0.402	0.396	2.150	2.210
Al_2O_3	34.420	34.370	35.280	34.300	34.410	34.140	34.740	34.650	34.750	34.270	34.480	34.370	34.030	33.740	34.890	34.310	33.770	33.860	34.590	34.110	34.170	33.980	33.900	33.420	34.120	19.210	19.240
FeO	1.930	1.930	2.020	2.140	2.150	2.090	1.900	1.800	1.710	1.800	1.870	1.710	1.990	1.960	1.700	1.960	1.990	1.960	1.720	1.910	1.880	1.940	2.070	1.840	2.000	25.720	26.550
MnO	0.047	0.082	0.022	0.022	0.004	0.001	0.037	0.049	0.000	0.056	0.000	0.001	0.031	0.067	0.000	0.020	0.010	0.066	0.011	0.051	0.032	0.045	0.051	0.014	0.071	0.054	0.050
MgO	0.393	0.452	0.418	0.408	0.468	0.479	0.369	0.347	0.290	0.300	0.287	0.286	0.366	0.388	0.248	0.434	0.491	0.503	0.330	0.482	0.413	0.485	0.448	0.489	0.480	2.720	2.680
CaO	0.000	0.037	0.038	0.036	0.002	0.025	0.011	0.011	0.000	0.122	0.007	0.001	0.036	0.008	0.010	0.000	0.022	0.000	0.017	0.021	0.016	0.034	0.005	0.023	0.020	0.000	0.000
BaO	0.000	0.000	0.000	0.008	0.050	0.028	0.075	0.000	0.014	0.072	0.000	0.000	0.100	0.050	0.007	0.000	0.058	0.011	0.000	0.000	0.078	0.000	0.022	0.000	0.000	0.016	0.000
Na_2O	0.441	0.443	0.555	0.463	0.445	0.479	0.542	0.415	0.356	0.454	0.426	0.440	0.314	0.420	0.524	0.504	0.453	0.455	0.420	0.406	0.438	0.561	0.543	0.383	0.498	0.004	0.002
K_2O	10.660	10.570	10.390	10.570	10.550	10.480	10.520	10.680	10.780	10.820	10.770	10.680	10.710	10.640	10.620	10.490	10.420	10.660	10.650	10.510	10.800	10.510	10.410	10.610	10.640	9.090	9.120
F	0.000	0.000	0.122	0.052	0.066	0.041	0.138	0.000	0.030	0.000	0.000	0.039	0.000	0.045	0.000	0.000	0.074	0.021	0.000	0.107	0.014	0.054	0.060	0.050	0.078	1.240	1.100
Cl	0.000	0.000	0.000	0.000	0.018	0.000	0.032	0.022	0.011	0.018	0.014	0.014	0.014	0.000	0.011	0.000	0.014	0.007	0.025	0.011	0.000	0.000	0.000	0.000	0.018	0.000	0.000
tot	95.583	95.602	96.625	95.980	95.533	95.764	95.660	95.760	95.228	94.686	95.010	94.525	95.092	94.341	94.857	95.403	94.916	95.116	94.681	94.974	94.569	94.716	95.145	94.350	95.781	96.764	97.050
CATIONS apfu																											
Si	3.139	3.150	3.131	3.148	3.140	3.158	3.137	3.146	3.117	3.126	3.118	3.141	3.158	3.154	3.123	3.153	3.168	3.160	3.127	3.145	3.134	3.142	3.157	3.174	3.156	2.852	2.821
Ti	0.024	0.014	0.010	0.024	0.014	0.021	0.011	0.016	0.030	0.016	0.030	0.013	0.015	0.015	0.009	0.014	0.017	0.016	0.015	0.022	0.010	0.018	0.021	0.020	0.020	0.128	0.132
Al	2.697	2.690	2.736	2.680	2.704	2.671	2.728	2.707	2.735	2.718	2.722	2.723	2.683	2.684	2.752	2.690	2.667	2.669	2.735	2.695	2.712	2.691	2.671	2.653	2.674	1.799	1.796
Fe	0.107	0.107	0.111	0.119	0.120	0.116	0.106	0.100	0.095	0.101	0.105	0.096	0.111	0.111	0.095	0.109	0.112	0.110	0.096	0.107	0.106	0.109	0.116	0.104	0.111	1.709	1.758
Mn	0.003	0.005	0.001	0.001	0.000	0.000	0.002	0.003	0.000	0.003	0.000	0.000	0.002	0.004	0.000	0.001	0.001	0.004	0.001	0.003	0.002	0.003	0.003	0.001	0.004	0.004	0.003
Mg	0.039	0.045	0.041	0.040	0.046	0.047	0.037	0.034	0.029	0.030	0.029	0.029	0.037	0.039	0.025	0.043	0.049	0.050	0.033	0.048	0.041	0.049	0.045	0.049	0.048	0.322	0.316
Ca	0.000	0.003	0.003	0.003	0.000	0.002	0.001	0.001	0.000	0.009	0.000	0.000	0.003	0.001	0.001	0.000	0.002	0.000	0.001	0.002	0.001	0.002	0.000	0.002	0.001	0.000	0.000
Ba	0.000	0.000	0.000	0.000	0.001	0.001	0.002	0.000	0.000	0.002	0.000	0.000	0.003	0.001	0.000	0.000	0.002	0.000	0.000	0.000	0.002	0.000	0.001	0.000	0.000	0.001	0.000
Na	0.057	0.057	0.071	0.059	0.057	0.062	0.070	0.053	0.046	0.059	0.055	0.057	0.041	0.055	0.068	0.065	0.059	0.059	0.055	0.053	0.057	0.073	0.070	0.050	0.064	0.001	0.000
K	0.904	0.896	0.872	0.894	0.897	0.887	0.894	0.903	0.918	0.929	0.920	0.916	0.914	0.916	0.907	0.890	0.891	0.909	0.911	0.899	0.928	0.901	0.888	0.912	0.902	0.921	0.921
F	0.000	0.000	0.025	0.011	0.014	0.009	0.029	0.000	0.006	0.000	0.000	0.008	0.000	0.010	0.000	0.000	0.016	0.004	0.000	0.023	0.003	0.011	0.013	0.011	0.016	0.312	0.275
Cl	0.000	0.000	0.000	0.000	0.002	0.000	0.004	0.002	0.001	0.002	0.002	0.002	0.002	0.000	0.001	0.000	0.002	0.001	0.003	0.001	0.000	0.000	0.000	0.000	0.002	0.000	0.000
tot	6.969	6.967	7.001	6.980	6.996	6.973	7.020	6.966	6.979	6.996	6.981	6.986	6.966	6.989	6.981	6.965	6.983	6.982	6.977	6.997	6.997	6.999	6.984	6.975	6.999	8.049	8.023

SAMPLE	UT15-51																								
	bt	bt	bt	bt	bt	bt	bt	bt	bt	bt	bt	bt	bt	bt	bt	bt	bt	bt	bt	bt	bt	bt	bt	bt	bt
Spot number	35	36	37	38	39	40	41	42	43	44	45	46	47	48	49	50	51	52	53	54	55	56	57	58	59
OXIDES wt%																									
SiO_2	32.510	35.670	36.090	36.090	35.700	35.780	35.930	36.240	35.600	36.460	36.190	36.300	36.370	35.760	36.210	35.820	36.230	35.920	35.740	36.560	36.190	35.810	35.840	35.930	36.510
TiO_2	2.170	2.070	2.240	2.350	2.340	2.120	2.280	2.220	2.200	2.200	2.050	2.240	1.900	1.880	1.970	2.130	2.280	2.190	1.930	2.110	2.350	2.340	2.370	2.250	2.180
Al_2O_3	17.150	19.170	19.790	19.690	19.030	19.360	19.060	19.080	18.950	19.640	19.870	19.510	19.870	19.390	19.530	19.570	19.230	19.160	19.340	19.450	19.260	19.600	19.470	19.550	19.230
FeO	22.480	25.630	25.590	26.250	25.450	26.110	25.550	25.280	25.560	25.840	25.500	25.490	25.350	25.490	25.690	25.270	26.060	26.270	25.350	26.150	25.660	26.300	25.940	25.730	25.420
MnO	0.039	0.050	0.044	0.056	0.054	0.047	0.040	0.056	0.046	0.045	0.050	0.044	0.052	0.050	0.051	0.044	0.049	0.043	0.051	0.045	0.044	0.055	0.050	0.050	0.050
MgO	2.410	2.770	2.720	2.740	2.730	2.840	2.700	2.810	2.750	2.650	2.830	2.770	2.790	2.680	2.840	2.800	2.740	2.840	2.910	2.800	2.820	2.730	2.800	2.780	2.950
CaO	0.002	0.003	0.002	0.002	0.011	0.001	0.000	0.000	0.000	0.000	0.002	0.002	0.001	0.005	0.005	0.010	0.002	0.005	0.002	0.000	0.001	0.000	0.002	0.006	0.001
BaO	0.011	0.010	0.006	0.010	0.006	0.013	0.000	0.003	0.014	0.000	0.003	0.005	0.006	0.000	0.012	0.008	0.008	0.000	0.000	0.004	0.010	0.002	0.009	0.011	0.000
Na_2O	0.004	0.005	0.011	0.003	0.005	0.001	0.005	0.009	0.007	0.009	0.012	0.009	0.008	0.008	0.012	0.008	0.005	0.004	0.002	0.005	0.002	0.011	0.004	0.003	0.005
K_2O	7.990	9.090	9.050	9.050	8.880	9.130	9.040	9.030	9.010	9.150	8.970	9.240	9.030	9.120	8.860	8.870	9.110	8.980	8.970	9.130	9.020	9.050	9.230	8.930	9.150
F	0.095	1.140	1.440	1.100	1.140	1.370	1.170	1.350	1.450	1.120	1.060	1.150	1.360	1.070	1.320	1.280	1.320	1.250	1.330	1.340	1.390	1.220	1.310	1.220	1.450
Cl	0.009	0.000	0.000	0.000	0.000	0.000	0.000	0.000	0.000	0.001	0.005	0.001	0.003	0.000	0.003	0.004	0.000	0.001	0.003	0.003	0.003	0.003	0.000	0.002	0.001
tot	86.305	96.232	97.551	97.978	96.022	97.336	96.189	96.694	96.183	97.614	97.174	97.312	97.364	96.018	97.249	96.485	97.607	97.139	96.148	98.113	97.292	97.764	97.605	97.109	97.453
CATIONS apfu																									
Si	2.839	2.844	2.845	2.823	2.849	2.837	2.857	2.877	2.859	2.852	2.839	2.852	2.863	2.848	2.860	2.846	2.856	2.842	2.854	2.863	2.859	2.819	2.828	2.838	2.878
Ti	0.142	0.124	0.133	0.138	0.140	0.126	0.136	0.133	0.133	0.129	0.121	0.132	0.112	0.113	0.117	0.127	0.135	0.130	0.116	0.124	0.140	0.139	0.141	0.134	0.129
Al	1.765	1.801	1.839	1.815	1.790	1.809	1.786	1.785	1.793	1.811	1.837	1.806	1.843	1.820	1.818	1.833	1.787	1.787	1.820	1.795	1.793	1.818	1.811	1.820	1.787
Fe	1.642	1.709	1.687	1.717	1.698	1.731	1.699	1.678	1.716	1.690	1.673	1.675	1.669	1.698	1.697	1.679	1.718	1.739	1.693	1.713	1.695	1.731	1.712	1.699	1.676
Mn	0.003	0.003	0.003	0.004	0.004	0.003	0.003	0.004	0.003	0.003	0.003	0.003	0.003	0.003	0.003	0.003	0.003	0.003	0.003	0.003	0.003	0.004	0.003	0.003	0.003
Mg	0.314	0.329	0.320	0.319	0.325	0.336	0.320	0.333	0.329	0.309	0.331	0.324	0.327	0.318	0.334	0.332	0.322	0.335	0.346	0.327	0.332	0.320	0.329	0.327	0.347
Ca	0.000	0.000	0.000	0.000	0.001	0.000	0.000	0.000	0.000	0.000	0.000	0.000	0.000	0.000	0.000	0.001	0.000	0.000	0.000	0.000	0.000	0.000	0.000	0.000	0.000
Ba	0.000	0.000	0.000	0.000	0.000	0.000	0.000	0.000	0.000	0.000	0.000	0.000	0.000	0.000	0.000	0.000	0.000	0.000	0.000	0.000	0.000	0.000	0.000	0.000	0.000
Na	0.001	0.001	0.002	0.000	0.001	0.000	0.001	0.001	0.001	0.001	0.002	0.001	0.001	0.001	0.002	0.001	0.001	0.001	0.000	0.001	0.000	0.002	0.001	0.000	0.001
K	0.890	0.925	0.910	0.903	0.904	0.923	0.917	0.914	0.923	0.913	0.898	0.926	0.907	0.927	0.893	0.899	0.916	0.906	0.914	0.912	0.909	0.909	0.929	0.900	0.920
F	0.026	0.287	0.359	0.272	0.288	0.344	0.294	0.339	0.368	0.277	0.263	0.286	0.339	0.270	0.330	0.322	0.329	0.313	0.336	0.332	0.347	0.304	0.327	0.305	0.361
Cl	0.001	0.000	0.000	0.000	0.000	0.000	0.000	0.000	0.000	0.000	0.001	0.000	0.000	0.000	0.000	0.001	0.000	0.000	0.000	0.000	0.000	0.000	0.000	0.000	0.000
tot	7.623	8.025	8.097	7.992	8.000	8.110	8.014	8.064	8.126	7.986	7.967	8.005	8.065	7.998	8.056	8.044	8.068	8.057	8.082	8.070	8.081	8.045	8.081	8.027	8.102

SAMPLE	**AK18-5**																										
	tur	ms	ms	ms	ms	ms	ms	ms	ms	ms	ms	ms	ms	ms	ms	ms	ms	ms	ms	ms	ms	ms	ms	ms	ms	ms	ms
Spot number	75	76	77	78	79	80	81	82	83	84	85	86	87	88	89	90	91	92	93	94	95	96	97	98	99	100	101
OXIDES wt%																											
SiO_2	35.860	46.760	46.840	46.730	46.890	47.080	47.040	47.210	46.630	46.450	46.290	46.460	47.290	46.520	46.410	46.740	46.700	46.790	46.930	46.040	46.540	47.020	46.580	46.770	46.690	46.770	46.400
TiO_2	0.472	0.130	0.079	0.166	0.128	0.254	0.079	0.076	0.172	0.141	0.141	0.158	0.114	0.264	0.218	0.272	0.232	0.188	0.161	0.226	0.116	0.223	0.154	0.621	0.194	0.200	0.186
Al_2O_3	33.570	33.710	34.240	34.270	34.410	33.790	34.250	33.950	33.810	33.870	33.600	33.530	34.140	34.130	34.460	33.520	34.410	33.810	34.030	34.120	34.650	34.010	34.380	34.480	34.130	33.480	34.300
FeO	13.100	2.720	2.630	2.590	2.430	2.590	2.190	2.460	2.480	2.490	2.630	2.800	2.650	2.480	2.690	2.630	2.400	2.500	2.730	2.680	2.460	2.760	2.320	2.270	2.870	2.710	2.680
MnO	0.164	0.000	0.010	0.000	0.000	0.000	0.007	0.000	0.003	0.027	0.000	0.000	0.000	0.000	0.000	0.016	0.000	0.040	0.000	0.057	0.012	0.000	0.013	0.000	0.000	0.000	0.000
MgO	1.880	0.552	0.491	0.509	0.373	0.579	0.566	0.560	0.454	0.547	0.567	0.574	0.479	0.512	0.402	0.557	0.499	0.527	0.642	0.514	0.379	0.656	0.464	0.355	0.532	0.606	0.420
CaO	0.215	0.013	0.034	0.027	0.009	0.008	0.004	0.008	0.001	0.000	0.027	0.005	0.022	0.014	0.000	0.000	0.000	0.020	0.009	0.040	0.013	0.017	0.000	0.000	0.000	0.000	0.000
BaO	0.000	0.060	0.021	0.000	0.000	0.088	0.000	0.000	0.074	0.000	0.022	0.030	0.000	0.100	0.062	0.000	0.000	0.000	0.067	0.060	0.090	0.000	0.149	0.064	0.165	0.111	0.038
Na_2O	1.990	0.323	0.364	0.320	0.360	0.310	0.243	0.283	0.332	0.301	0.327	0.267	0.341	0.322	0.325	0.245	0.340	0.303	0.322	0.289	0.344	0.250	0.305	0.294	0.311	0.291	0.312
K_2O	0.054	10.860	10.850	10.830	10.770	10.860	10.640	10.680	10.780	10.770	10.790	10.680	10.840	10.840	10.780	10.890	10.760	10.750	10.840	10.810	10.890	10.720	10.930	10.800	10.870	10.880	10.840
F	0.459	0.000	0.000	0.000	0.000	0.000	0.000	0.000	0.000	0.000	0.000	0.000	0.000	0.000	0.000	0.000	0.000	0.000	0.000	0.000	0.000	0.000	0.000	0.000	0.000	0.000	0.000
Cl	0.004	0.018	0.000	0.000	0.004	0.000	0.018	0.000	0.014	0.007	0.000	0.000	0.029	0.000	0.000	0.000	0.014	0.000	0.014	0.004	0.014	0.000	0.000	0.000	0.007	0.000	0.000
tot	87.768	95.147	95.560	95.442	95.372	95.559	95.036	95.227	94.751	94.603	94.394	94.504	95.906	95.182	95.347	94.869	95.355	94.927	95.746	94.840	95.508	95.655	95.296	95.655	95.769	95.049	95.176
CATIONS apfu																											
Si	2.681	3.143	3.130	3.125	3.133	3.147	3.147	3.156	3.142	3.133	3.134	3.141	3.147	3.122	3.110	3.147	3.123	3.144	3.133	3.106	3.113	3.137	3.122	3.117	3.122	3.147	3.116
Ti	0.027	0.007	0.004	0.008	0.006	0.013	0.004	0.004	0.009	0.007	0.007	0.008	0.006	0.013	0.011	0.014	0.012	0.009	0.008	0.011	0.006	0.011	0.008	0.031	0.010	0.010	0.009
Al	2.958	2.670	2.697	2.701	2.710	2.662	2.700	2.675	2.685	2.693	2.681	2.671	2.678	2.700	2.722	2.660	2.712	2.677	2.678	2.713	2.731	2.674	2.715	2.708	2.690	2.655	2.714
Fe	0.819	0.153	0.147	0.145	0.136	0.145	0.123	0.138	0.140	0.140	0.149	0.158	0.147	0.139	0.151	0.148	0.134	0.140	0.152	0.151	0.138	0.154	0.130	0.127	0.161	0.153	0.150
Mn	0.010	0.000	0.001	0.000	0.000	0.000	0.000	0.000	0.000	0.002	0.000	0.000	0.000	0.000	0.000	0.001	0.000	0.002	0.000	0.003	0.001	0.000	0.001	0.000	0.000	0.000	0.000
Mg	0.209	0.055	0.049	0.051	0.037	0.058	0.056	0.056	0.046	0.055	0.057	0.058	0.048	0.051	0.040	0.056	0.050	0.053	0.064	0.052	0.038	0.065	0.046	0.035	0.053	0.061	0.042
Ca	0.017	0.001	0.002	0.002	0.001	0.001	0.000	0.001	0.000	0.000	0.002	0.000	0.002	0.001	0.000	0.000	0.000	0.001	0.001	0.003	0.001	0.001	0.000	0.000	0.000	0.000	0.000
Ba	0.000	0.002	0.001	0.000	0.000	0.002	0.000	0.000	0.002	0.000	0.001	0.001	0.000	0.003	0.002	0.000	0.000	0.000	0.002	0.002	0.002	0.000	0.004	0.002	0.004	0.003	0.001
Na	0.288	0.042	0.047	0.042	0.047	0.040	0.031	0.037	0.043	0.039	0.043	0.035	0.044	0.042	0.042	0.032	0.044	0.039	0.042	0.038	0.045	0.032	0.040	0.038	0.040	0.038	0.041
K	0.005	0.931	0.925	0.924	0.918	0.926	0.908	0.911	0.927	0.927	0.932	0.921	0.920	0.928	0.922	0.935	0.918	0.921	0.923	0.930	0.929	0.912	0.934	0.918	0.927	0.934	0.929
F	0.109	0.000	0.000	0.000	0.000	0.000	0.000	0.000	0.000	0.000	0.000	0.000	0.000	0.000	0.000	0.000	0.000	0.000	0.000	0.000	0.000	0.000	0.000	0.000	0.000	0.000	0.000
Cl	0.000	0.002	0.000	0.000	0.000	0.000	0.002	0.000	0.002	0.001	0.000	0.000	0.003	0.000	0.000	0.000	0.002	0.000	0.002	0.000	0.002	0.000	0.000	0.000	0.001	0.000	0.000
tot	7.124	7.005	7.003	6.998	6.988	6.993	6.972	6.976	6.995	6.997	7.006	6.994	6.995	7.000	7.000	6.993	6.993	6.988	7.005	7.010	7.005	6.987	7.000	6.976	7.008	7.001	7.002

SAMPLE	**AK18-5**																							**AK18-13**			
	ms	ms	ms	ms	ms	ms	ms	ms	ms	ms	ms	ms	ms	ms	ms	ms	ms	ms	ms	ms	ms	ms	ms	ms	ms	ms	ms
Spot number	102	103	104	105	106	107	108	109	110	111	112	113	114	115	116	117	118	119	120	121	122	123	124	60	61	62	63
OXIDES wt%																											
SiO_2	46.620	46.600	46.850	46.270	46.760	46.950	46.740	46.550	46.850	46.480	46.210	46.500	47.000	46.830	48.340	46.420	46.380	46.580	46.330	46.760	46.670	47.440	46.470	48.320	47.790	48.500	47.320
TiO_2	0.175	0.266	0.166	0.159	0.160	0.072	0.128	0.186	0.128	0.216	0.220	0.175	0.169	0.144	0.176	0.162	0.195	0.126	0.068	0.119	0.222	0.165	0.198	0.066	0.067	0.058	0.059
Al_2O_3	34.410	33.910	34.090	34.280	34.600	34.460	34.830	34.420	34.600	34.020	33.600	34.000	33.890	34.400	34.690	34.480	34.300	33.710	34.210	33.610	34.380	33.910	33.920	30.310	31.020	30.140	30.440
FeO	2.600	2.440	2.580	2.590	2.460	2.550	2.580	2.630	2.480	2.630	2.540	2.610	2.590	2.470	2.790	2.570	2.730	2.570	2.350	2.770	2.450	2.630	2.570	2.990	2.790	2.830	2.900
MnO	0.000	0.017	0.033	0.033	0.000	0.000	0.019	0.000	0.001	0.021	0.000	0.000	0.000	0.000	0.002	0.000	0.000	0.038	0.060	0.000	0.029	0.000	0.000	0.000	0.002	0.001	0.000
MgO	0.500	0.536	0.451	0.509	0.495	0.490	0.376	0.470	0.469	0.474	0.485	0.567	0.515	0.500	0.572	0.496	0.490	0.521	0.399	0.618	0.497	0.588	0.540	2.110	1.810	2.190	2.490
CaO	0.011	0.012	0.006	0.017	0.010	0.000	0.007	0.000	0.000	0.009	0.005	0.000	0.002	0.000	0.013	0.025	0.001	0.025	0.019	0.011	0.014	0.000	0.012	0.001	0.000	0.001	0.003
BaO	0.076	0.000	0.092	0.091	0.152	0.074	0.166	0.068	0.003	0.065	0.000	0.056	0.062	0.025	0.038	0.110	0.000	0.102	0.000	0.113	0.134	0.000	0.000	0.010	0.004	0.009	0.007
Na_2O	0.346	0.289	0.335	0.339	0.357	0.322	0.372	0.295	0.286	0.256	0.294	0.274	0.289	0.259	0.346	0.310	0.301	0.364	0.307	0.289	0.339	0.316	0.301	0.040	0.043	0.040	0.048
K_2O	10.820	10.810	10.860	10.820	10.830	10.750	10.820	10.800	10.760	10.770	10.770	10.850	10.860	10.760	10.690	10.920	10.820	10.700	10.730	10.820	10.850	10.940	10.810	10.760	10.560	10.610	10.620
F	0.000	0.000	0.000	0.000	0.000	0.000	0.000	0.000	0.000	0.000	0.000	0.000	0.000	0.000	0.000	0.000	0.000	0.000	0.000	0.000	0.000	0.000	0.000	0.000	0.000	0.000	0.000
Cl	0.000	0.025	0.007	0.014	0.000	0.022	0.000	0.000	0.000	0.004	0.004	0.000	0.022	0.007	0.029	0.000	0.000	0.022	0.000	0.011	0.000	0.004	0.004	0.001	0.001	0.001	0.001
tot	95.558	94.905	95.469	95.121	95.825	95.689	96.038	95.419	95.577	94.944	94.127	95.032	95.399	95.395	97.686	95.491	95.218	94.757	94.472	95.121	95.583	95.992	94.825	95.676	95.132	95.360	94.943
CATIONS apfu																											
Si	3.117	3.134	3.135	3.111	3.116	3.131	3.110	3.116	3.124	3.127	3.135	3.126	3.146	3.129	3.154	3.109	3.113	3.141	3.126	3.144	3.119	3.154	3.129	3.263	3.238	3.277	3.223
Ti	0.009	0.013	0.008	0.008	0.008	0.004	0.006	0.009	0.006	0.011	0.011	0.009	0.008	0.007	0.009	0.008	0.010	0.006	0.003	0.006	0.011	0.008	0.010	0.003	0.003	0.003	0.003
Al	2.711	2.688	2.689	2.716	2.718	2.708	2.731	2.715	2.719	2.698	2.686	2.694	2.674	2.709	2.667	2.721	2.713	2.679	2.721	2.664	2.708	2.657	2.692	2.413	2.477	2.400	2.443
Fe	0.145	0.137	0.144	0.146	0.137	0.142	0.144	0.147	0.138	0.148	0.144	0.147	0.145	0.138	0.152	0.144	0.153	0.145	0.133	0.156	0.137	0.146	0.145	0.169	0.158	0.160	0.165
Mn	0.000	0.001	0.002	0.002	0.000	0.000	0.001	0.000	0.000	0.001	0.000	0.000	0.000	0.000	0.000	0.000	0.000	0.002	0.003	0.000	0.002	0.000	0.000	0.000	0.000	0.000	0.000
Mg	0.050	0.054	0.045	0.051	0.049	0.049	0.037	0.047	0.047	0.048	0.049	0.057	0.051	0.050	0.056	0.049	0.049	0.052	0.040	0.062	0.049	0.058	0.054	0.212	0.183	0.221	0.253
Ca	0.001	0.001	0.000	0.001	0.001	0.000	0.001	0.000	0.000	0.001	0.000	0.000	0.000	0.000	0.001	0.002	0.000	0.002	0.001	0.001	0.001	0.000	0.001	0.000	0.000	0.000	0.000
Ba	0.002	0.000	0.002	0.002	0.004	0.002	0.004	0.002	0.000	0.002	0.000	0.001	0.002	0.001	0.001	0.003	0.000	0.003	0.000	0.003	0.004	0.000	0.000	0.000	0.000	0.000	0.000
Na	0.045	0.038	0.043	0.044	0.046	0.042	0.048	0.038	0.037	0.033	0.039	0.036	0.038	0.033	0.044	0.040	0.039	0.048	0.040	0.038	0.044	0.041	0.039	0.005	0.006	0.005	0.006
K	0.923	0.927	0.927	0.928	0.921	0.914	0.918	0.922	0.915	0.924	0.932	0.931	0.927	0.917	0.890	0.933	0.926	0.920	0.924	0.928	0.925	0.928	0.929	0.927	0.913	0.914	0.923
F	0.000	0.000	0.000	0.000	0.000	0.000	0.000	0.000	0.000	0.000	0.000	0.000	0.000	0.000	0.000	0.000	0.000	0.000	0.000	0.000	0.000	0.000	0.000	0.000	0.000	0.000	0.000
Cl	0.000	0.003	0.001	0.002	0.000	0.002	0.000	0.000	0.000	0.000	0.000	0.000	0.002	0.001	0.003	0.000	0.000	0.002	0.000	0.001	0.000	0.000	0.000	0.000	0.000	0.000	0.000
tot	7.003	6.996	6.998	7.011	7.000	6.993	7.001	6.997	6.986	6.993	6.997	7.001	6.994	6.986	6.976	7.009	7.004	7.001	6.992	7.003	7.000	6.994	6.999	6.993	6.979	6.980	7.017

SAMPLE	**AK18-13**																										
	ms	ms	ms	bt	bt	bt	ms	ms	ms	ms	ms	ms	ms	bt	ms	bt	ms	ms	ms	bt	ms	bt	ms	ms	ms	ms	bt
Spot number	64	65	66	67	68	69	70	71	72	73	74	75	76	77	78	79	80	81	82	83	84	85	86	87	88	89	90
OXIDES wt%																											
SiO_2	47.580	48.710	45.840	40.190	39.490	39.240	48.360	47.850	48.000	47.910	47.150	48.170	49.020	39.010	48.400	39.550	48.130	47.620	47.500	39.470	47.180	39.590	47.300	47.880	48.940	47.390	39.430
TiO_2	0.057	0.071	0.072	1.251	1.272	1.201	0.056	0.059	0.076	0.066	0.070	0.063	0.059	1.163	0.069	1.218	0.070	0.083	0.072	1.320	0.086	1.306	0.054	0.060	0.079	0.080	1.300
Al_2O_3	30.800	31.020	29.610	16.220	16.360	16.540	29.840	30.480	31.240	30.800	30.730	29.170	29.000	16.760	30.020	16.540	30.820	31.220	31.360	16.770	31.120	16.750	30.370	30.940	30.730	31.130	16.230
FeO	2.760	2.900	2.870	10.090	10.490	10.290	2.660	2.770	2.530	2.800	2.610	3.190	2.890	10.320	2.950	10.520	2.630	2.560	2.720	10.310	2.610	10.480	2.840	2.760	2.620	2.590	10.300
MnO	0.003	0.000	0.001	0.003	0.002	0.005	0.000	0.002	0.001	0.002	0.000	0.002	0.000	0.003	0.000	0.009	0.000	0.001	0.002	0.006	0.000	0.006	0.000	0.000	0.000	0.000	0.006
MgO	1.770	1.980	2.480	18.130	17.410	17.550	2.130	1.970	1.840	1.730	1.910	2.520	2.630	17.720	2.060	17.800	2.000	1.760	1.820	16.940	1.780	17.410	2.010	1.990	2.150	1.810	17.310
CaO	0.001	0.001	0.003	0.000	0.000	0.004	0.001	0.002	0.000	0.000	0.006	0.000	0.001	0.004	0.001	0.004	0.000	0.000	0.000	0.002	0.002	0.001	0.000	0.003	0.000	0.000	0.008
BaO	0.001	0.016	0.015	0.007	0.001	0.000	0.005	0.005	0.018	0.001	0.015	0.002	0.016	0.015	0.017	0.001	0.019	0.009	0.015	0.003	0.005	0.015	0.007	0.005	0.011	0.014	0.006
Na_2O	0.053	0.043	0.043	0.002	0.005	0.009	0.041	0.039	0.052	0.044	0.052	0.021	0.036	0.009	0.028	0.006	0.057	0.058	0.053	0.008	0.058	0.007	0.039	0.054	0.051	0.048	0.006
K_2O	10.620	10.700	10.600	10.300	10.280	10.190	10.710	10.750	10.540	10.710	10.560	10.970	10.860	10.100	10.760	10.120	10.530	10.480	10.590	10.240	10.480	10.050	10.880	10.490	10.600	10.550	10.150
F	0.000	0.000	0.000	0.063	0.064	0.065	0.000	0.000	0.000	0.000	0.000	0.000	0.000	0.053	0.000	0.053	0.000	0.000	0.000	0.044	0.000	0.049	0.000	0.000	0.000	0.000	0.052
Cl	0.000	0.000	0.000	0.000	0.002	0.003	0.000	0.000	0.001	0.003	0.000	0.000	0.001	0.000	0.000	0.002	0.000	0.000	0.001	0.000	0.000	0.000	0.000	0.000	0.000	0.000	0.002
tot	94.682	96.628	92.750	96.930	96.042	95.868	94.734	94.884	95.625	95.108	94.380	94.902	95.534	95.906	95.341	96.503	95.574	95.144	95.411	95.694	94.681	96.368	94.406	95.286	96.458	94.890	95.519
CATIONS apfu																											
Si	3.241	3.255	3.211	2.892	2.877	2.864	3.287	3.253	3.240	3.250	3.230	3.282	3.314	2.845	3.278	2.864	3.252	3.232	3.218	2.877	3.222	2.868	3.237	3.240	3.272	3.226	2.885
Ti	0.003	0.004	0.004	0.068	0.070	0.066	0.003	0.003	0.004	0.003	0.004	0.003	0.003	0.064	0.004	0.066	0.004	0.004	0.004	0.072	0.004	0.071	0.003	0.003	0.004	0.004	0.072
Al	2.473	2.443	2.444	1.376	1.405	1.423	2.390	2.442	2.485	2.462	2.481	2.342	2.311	1.441	2.396	1.412	2.454	2.497	2.504	1.441	2.505	1.430	2.450	2.467	2.421	2.498	1.400
Fe	0.157	0.162	0.168	0.607	0.639	0.628	0.151	0.157	0.143	0.159	0.150	0.182	0.163	0.629	0.167	0.637	0.149	0.145	0.154	0.628	0.149	0.635	0.163	0.156	0.146	0.147	0.630
Mn	0.000	0.000	0.000	0.000	0.000	0.000	0.000	0.000	0.000	0.000	0.000	0.000	0.000	0.000	0.000	0.001	0.000	0.000	0.000	0.000	0.000	0.000	0.000	0.000	0.000	0.000	0.000
Mg	0.180	0.197	0.259	1.944	1.890	1.909	0.216	0.200	0.185	0.175	0.195	0.256	0.265	1.926	0.208	1.921	0.201	0.178	0.184	1.840	0.181	1.880	0.205	0.201	0.214	0.184	1.888
Ca	0.000	0.000	0.000	0.000	0.000	0.000	0.000	0.000	0.000	0.000	0.000	0.000	0.000	0.000	0.000	0.000	0.000	0.000	0.000	0.000	0.000	0.000	0.000	0.000	0.000	0.000	0.001
Ba	0.000	0.000	0.000	0.000	0.000	0.000	0.000	0.000	0.000	0.000	0.000	0.000	0.000	0.000	0.000	0.000	0.001	0.000	0.000	0.000	0.000	0.000	0.000	0.000	0.000	0.000	0.000
Na	0.007	0.006	0.006	0.000	0.001	0.001	0.005	0.005	0.007	0.006	0.007	0.003	0.005	0.001	0.004	0.001	0.007	0.008	0.007	0.001	0.008	0.001	0.005	0.007	0.007	0.006	0.001
K	0.923	0.912	0.947	0.945	0.955	0.949	0.929	0.932	0.907	0.927	0.923	0.953	0.937	0.940	0.930	0.935	0.908	0.907	0.915	0.952	0.913	0.929	0.950	0.905	0.904	0.916	0.947
F	0.000	0.000	0.000	0.014	0.015	0.015	0.000	0.000	0.000	0.000	0.000	0.000	0.000	0.012	0.000	0.012	0.000	0.000	0.000	0.010	0.000	0.011	0.000	0.000	0.000	0.000	0.012
Cl	0.000	0.000	0.000	0.000	0.000	0.000	0.000	0.000	0.000	0.000	0.000	0.000	0.000	0.000	0.000	0.000	0.000	0.000	0.000	0.000	0.000	0.000	0.000	0.000	0.000	0.000	0.000
tot	6.984	6.979	7.040	7.847	7.852	7.857	6.982	6.992	6.971	6.982	6.990	7.022	6.998	7.860	6.987	7.850	6.975	6.972	6.987	7.823	6.982	7.827	7.013	6.980	6.969	6.982	7.836

SAMPLE	**AK18-13**																**AK18-23**										
	ms	ms	bt	ms	ms	ms	bt	bt	bt	bt	ms	ms	ms	ms	ms	ms	bt	ms	bt	ms	bt	bt	ms	bt	ms	ms	bt
Spot number	91	92	93	94	95	96	97	98	99	100	101	102	103	104	105	106	107	108	109	110	111	112	113	114	115	116	117
OXIDES wt%																											
SiO_2	48.370	48.170	45.940	47.650	48.180	47.520	39.610	39.700	39.730	39.660	45.620	46.920	46.880	48.250	48.530	48.640	39.100	48.640	38.970	48.260	39.050	39.470	48.780	39.420	47.760	48.580	39.340
TiO_2	0.076	0.060	0.075	0.073	0.057	0.068	1.308	1.418	1.042	1.391	1.049	0.078	0.073	0.079	0.057	0.064	0.095	0.028	0.081	0.047	0.075	0.072	0.034	0.084	0.031	0.021	0.072
Al_2O_3	30.400	29.760	29.230	30.340	31.000	31.900	16.880	16.500	16.450	16.790	25.880	26.700	29.250	30.850	30.220	30.450	17.310	31.840	17.430	32.010	17.670	17.670	31.930	17.240	32.220	31.500	17.730
FeO	3.450	2.910	3.840	3.210	2.690	2.640	10.310	10.390	10.210	10.100	6.120	5.000	3.490	2.340	2.830	2.740	11.820	1.390	11.520	1.258	11.720	11.390	1.360	11.130	1.520	1.340	11.910
MnO	0.000	0.000	0.000	0.000	0.002	0.004	0.004	0.006	0.006	0.008	0.000	0.002	0.002	0.000	0.000	0.003	0.011	0.002	0.011	0.000	0.005	0.010	0.000	0.010	0.003	0.001	0.009
MgO	3.890	2.260	3.650	2.380	1.970	1.680	17.520	17.350	17.770	17.130	8.470	6.920	3.080	2.010	2.180	2.230	16.000	1.950	16.540	2.020	16.110	16.290	2.180	16.620	2.230	2.230	16.280
CaO	0.006	0.000	0.000	0.003	0.001	0.004	0.001	0.000	0.003	0.005	0.009	0.012	0.002	0.001	0.004	0.002	0.001	0.003	0.002	0.000	0.000	0.003	0.004	0.002	0.001	0.000	0.000
BaO	0.014	0.009	0.013	0.018	0.008	0.013	0.011	0.013	0.006	0.013	0.000	0.012	0.016	0.025	0.012	0.012	0.000	0.015	0.013	0.010	0.010	0.002	0.006	0.012	0.010	0.015	0.012
Na_2O	0.039	0.038	0.041	0.044	0.052	0.055	0.012	0.007	0.008	0.015	0.031	0.038	0.039	0.056	0.043	0.045	0.016	0.034	0.006	0.042	0.011	0.011	0.034	0.012	0.043	0.026	0.018
K_2O	9.560	10.700	10.530	10.440	10.620	10.490	10.060	10.300	10.180	10.120	10.050	9.900	10.630	10.590	10.650	10.660	10.010	10.930	10.130	10.860	9.980	10.070	10.980	9.980	10.890	11.060	10.030
F	0.000	0.000	0.000	0.000	0.000	0.000	0.054	0.061	0.053	0.039	0.019	0.015	0.000	0.000	0.000	0.000	0.046	0.000	0.041	0.000	0.035	0.033	0.000	0.048	0.000	0.000	0.034
Cl	0.006	0.000	0.005	0.001	0.003	0.000	0.002	0.000	0.000	0.000	0.001	0.000	0.002	0.004	0.000	0.003	0.001	0.001	0.005	0.000	0.000	0.001	0.000	0.003	0.001	0.002	0.000
tot	97.071	94.872	94.539	95.404	95.693	95.678	96.531	96.524	96.142	95.983	97.788	97.018	94.674	95.700	95.570	96.015	95.931	95.572	96.167	95.400	95.898	96.211	96.019	96.099	95.500	95.353	96.738
CATIONS apfu																											
Si	3.216	3.277	3.177	3.236	3.246	3.207	2.864	2.878	2.883	2.880	3.084	3.186	3.225	3.258	3.274	3.269	2.886	3.249	2.866	3.233	2.871	2.885	3.242	2.894	3.201	3.250	2.871
Ti	0.004	0.003	0.004	0.004	0.003	0.003	0.071	0.077	0.057	0.076	0.053	0.004	0.004	0.004	0.003	0.003	0.005	0.001	0.004	0.002	0.004	0.004	0.002	0.005	0.002	0.001	0.004
Al	2.382	2.386	2.382	2.428	2.462	2.537	1.439	1.410	1.407	1.437	2.062	2.137	2.371	2.455	2.403	2.412	1.506	2.506	1.511	2.527	1.531	1.522	2.501	1.492	2.545	2.484	1.525
Fe	0.192	0.166	0.222	0.182	0.152	0.149	0.624	0.630	0.620	0.613	0.346	0.284	0.201	0.132	0.160	0.154	0.730	0.078	0.708	0.070	0.721	0.696	0.076	0.683	0.085	0.075	0.727
Mn	0.000	0.000	0.000	0.000	0.000	0.000	0.000	0.000	0.000	0.000	0.000	0.000	0.000	0.000	0.000	0.000	0.001	0.000	0.001	0.000	0.000	0.001	0.000	0.001	0.000	0.000	0.001
Mg	0.386	0.229	0.376	0.241	0.198	0.169	1.888	1.875	1.922	1.854	0.853	0.700	0.316	0.202	0.219	0.223	1.760	0.194	1.813	0.202	1.766	1.775	0.216	1.819	0.223	0.222	1.771
Ca	0.000	0.000	0.000	0.000	0.000	0.000	0.000	0.000	0.000	0.000	0.001	0.001	0.000	0.000	0.000	0.000	0.000	0.000	0.000	0.000	0.000	0.000	0.000	0.000	0.000	0.000	0.000
Ba	0.000	0.000	0.000	0.000	0.000	0.000	0.000	0.000	0.000	0.000	0.000	0.000	0.000	0.001	0.000	0.000	0.000	0.000	0.000	0.000	0.000	0.000	0.000	0.000	0.000	0.000	0.000
Na	0.005	0.005	0.006	0.006	0.007	0.007	0.002	0.001	0.001	0.002	0.004	0.005	0.005	0.007	0.006	0.006	0.002	0.004	0.001	0.005	0.002	0.002	0.004	0.002	0.006	0.003	0.003
K	0.811	0.928	0.929	0.904	0.913	0.903	0.928	0.952	0.942	0.937	0.867	0.858	0.933	0.912	0.917	0.914	0.943	0.931	0.950	0.928	0.936	0.939	0.931	0.935	0.931	0.944	0.934
F	0.000	0.000	0.000	0.000	0.000	0.000	0.012	0.014	0.012	0.009	0.004	0.003	0.000	0.000	0.000	0.000	0.011	0.000	0.010	0.000	0.008	0.008	0.000	0.011	0.000	0.000	0.008
Cl	0.001	0.000	0.001	0.000	0.000	0.000	0.000	0.000	0.000	0.000	0.000	0.000	0.000	0.000	0.000	0.000	0.000	0.000	0.001	0.000	0.000	0.000	0.000	0.000	0.000	0.000	0.000
tot	6.997	6.994	7.096	7.002	6.980	6.976	7.829	7.838	7.846	7.809	7.274	7.178	7.055	6.971	6.982	6.982	7.844	6.965	7.865	6.968	7.840	7.832	6.973	7.841	6.993	6.981	7.843

SAMPLE	**AK18-23**																										
	bt	bt	bt	bt	bt	bt	bt	bt	bt	bt	bt	bt	bt	bt	bt	bt	bt	ms	ms	ms	ms	ms	ms	ms	ms	bt	bt
Spot number	118	119	120	121	122	123	124	125	126	127	128	129	130	131	132	133	134	135	136	137	138	139	140	141	142	143	144
OXIDES wt%																											
SiO_2	39.470	48.190	39.620	49.450	39.810	39.050	47.560	39.480	47.480	49.270	39.350	39.880	39.610	49.130	39.130	39.350	39.390	48.750	46.940	47.700	39.520	48.690	39.280	47.180	48.680	48.160	38.950
TiO_2	0.100	0.023	0.073	0.023	0.056	0.062	0.027	0.074	0.026	0.025	0.087	0.081	0.094	0.028	0.049	0.062	0.072	0.044	0.031	0.020	0.069	0.015	0.060	0.030	0.024	0.023	0.070
Al_2O_3	17.470	33.350	17.010	30.260	17.310	17.460	31.880	17.470	33.640	31.760	16.540	17.260	16.690	32.230	17.710	17.450	17.530	31.360	32.530	33.240	17.540	31.500	17.400	33.560	32.110	31.840	17.640
FeO	11.410	1.350	11.040	1.390	11.090	11.210	1.370	11.190	1.199	1.410	11.350	11.520	10.930	1.263	10.730	10.890	10.960	1.380	1.560	1.072	10.720	1.199	11.230	1.219	1.269	1.310	10.960
MnO	0.009	0.000	0.006	0.000	0.009	0.007	0.000	0.005	0.001	0.002	0.011	0.008	0.010	0.000	0.011	0.008	0.007	0.001	0.001	0.002	0.001	0.002	0.011	0.001	0.001	0.002	0.012
MgO	15.940	1.850	16.520	2.660	16.770	16.440	2.060	16.340	1.548	2.200	16.040	16.930	16.430	2.220	16.610	16.570	16.620	2.350	2.190	1.563	16.690	2.250	17.040	1.660	2.250	2.300	16.880
CaO	0.001	0.000	0.000	0.011	0.003	0.006	0.007	0.003	0.002	0.001	0.003	0.006	0.000	0.005	0.001	0.000	0.000	0.001	0.000	0.001	0.002	0.003	0.001	0.001	0.001	0.000	0.000
BaO	0.008	0.000	0.000	0.011	0.005	0.002	0.004	0.006	0.020	0.002	0.005	0.014	0.000	0.009	0.000	0.001	0.003	0.007	0.005	0.007	0.000	0.014	0.002	0.009	0.011	0.012	0.000
Na_2O	0.007	0.032	0.009	0.020	0.006	0.013	0.026	0.014	0.034	0.026	0.002	0.010	0.005	0.043	0.012	0.000	0.009	0.034	0.033	0.042	0.015	0.034	0.006	0.034	0.035	0.039	0.008
K_2O	10.200	11.010	10.310	11.060	10.130	9.850	10.800	9.990	10.980	10.410	10.170	9.980	10.200	10.950	10.250	10.390	10.260	10.960	11.000	11.010	10.140	11.040	10.240	10.870	10.950	10.920	10.240
F	0.046	0.000	0.046	0.000	0.046	0.047	0.000	0.046	0.000	0.000	0.057	0.045	0.043	0.000	0.055	0.045	0.051	0.000	0.000	0.000	0.041	0.000	0.061	0.000	0.000	0.000	0.047
Cl	0.003	0.001	0.002	0.000	0.002	0.001	0.003	0.000	0.000	0.001	0.004	0.000	0.000	0.002	0.003	0.000	0.002	0.001	0.001	0.001	0.003	0.003	0.001	0.003	0.001	0.000	0.001
tot	96.228	96.312	95.862	95.482	96.380	95.410	94.349	95.952	95.663	95.620	95.144	97.201	95.376	96.670	95.741	95.805	96.186	95.678	94.938	95.310	95.919	95.375	96.610	95.261	95.987	95.291	96.051
CATIONS apfu																											
Si	2.900	3.187	2.910	3.304	2.900	2.880	3.216	2.895	3.169	3.268	2.927	2.894	2.925	3.242	2.873	2.885	2.883	3.256	3.167	3.190	2.890	3.255	2.868	3.161	3.234	3.227	2.857
Ti	0.006	0.001	0.004	0.001	0.003	0.003	0.001	0.004	0.001	0.001	0.005	0.004	0.005	0.001	0.003	0.003	0.004	0.002	0.002	0.001	0.004	0.001	0.003	0.002	0.001	0.001	0.004
Al	1.513	2.600	1.472	2.383	1.486	1.517	2.541	1.510	2.646	2.483	1.450	1.476	1.453	2.507	1.532	1.508	1.512	2.469	2.586	2.620	1.512	2.482	1.497	2.650	2.514	2.514	1.525
Fe	0.701	0.075	0.678	0.078	0.676	0.691	0.077	0.686	0.067	0.078	0.706	0.699	0.675	0.070	0.659	0.668	0.671	0.077	0.088	0.060	0.656	0.067	0.686	0.068	0.070	0.073	0.672
Mn	0.001	0.000	0.000	0.000	0.001	0.000	0.000	0.000	0.000	0.000	0.001	0.000	0.001	0.000	0.001	0.000	0.000	0.000	0.000	0.000	0.000	0.000	0.001	0.000	0.000	0.000	0.001
Mg	1.746	0.182	1.808	0.265	1.821	1.807	0.208	1.786	0.154	0.217	1.778	1.831	1.809	0.218	1.817	1.811	1.813	0.234	0.220	0.156	1.819	0.224	1.854	0.166	0.223	0.230	1.845
Ca	0.000	0.000	0.000	0.001	0.000	0.000	0.001	0.000	0.000	0.000	0.000	0.000	0.000	0.000	0.000	0.000	0.000	0.000	0.000	0.000	0.000	0.000	0.000	0.000	0.000	0.000	0.000
Ba	0.000	0.000	0.000	0.000	0.000	0.000	0.000	0.000	0.001	0.000	0.000	0.000	0.000	0.000	0.000	0.000	0.000	0.000	0.000	0.000	0.000	0.000	0.000	0.000	0.000	0.000	0.000
Na	0.001	0.004	0.001	0.003	0.001	0.002	0.003	0.002	0.004	0.003	0.000	0.001	0.001	0.006	0.002	0.000	0.001	0.004	0.004	0.005	0.002	0.004	0.001	0.004	0.004	0.005	0.001
K	0.956	0.929	0.966	0.943	0.941	0.927	0.932	0.935	0.935	0.881	0.965	0.924	0.961	0.922	0.960	0.972	0.958	0.934	0.947	0.939	0.946	0.942	0.954	0.929	0.928	0.933	0.958
F	0.011	0.000	0.011	0.000	0.011	0.011	0.000	0.011	0.000	0.000	0.013	0.010	0.010	0.000	0.013	0.010	0.012	0.000	0.000	0.000	0.009	0.000	0.014	0.000	0.000	0.000	0.011
Cl	0.000	0.000	0.000	0.000	0.000	0.000	0.000	0.000	0.000	0.000	0.001	0.000	0.000	0.000	0.000	0.000	0.000	0.000	0.000	0.000	0.000	0.000	0.000	0.000	0.000	0.000	0.000
tot	7.833	6.978	7.850	6.976	7.841	7.839	6.980	7.830	6.977	6.932	7.847	7.842	7.839	6.967	7.859	7.859	7.855	6.977	7.014	6.972	7.839	6.976	7.879	6.980	6.975	6.984	7.873

SAMPLE	**AK18-23**	**AK18-27**																									
	bt	anfib	bt	bt	bt	bt	bt	bt	bt	bt	bt	bt	bt	bt	bt	bt	bt	bt	bt	bt	bt	ms	ms	ms	bt	bt	bt
Spot number	146	33	34	35	36	37	38	39	40	41	42	43	44	45	46	47	48	49	50	51	52	53	54	55	56	57	58
OXIDES wt%																											
SiO_2	39.120	55.880	39.670	39.290	39.570	39.550	39.510	39.280	39.680	39.280	39.080	39.680	39.700	39.930	39.920	39.530	39.780	39.830	39.670	39.350	39.220	28.100	28.110	28.290	40.020	39.420	39.370
TiO_2	0.090	0.000	0.967	1.110	0.902	0.911	0.888	0.968	0.974	0.860	0.869	0.863	0.697	0.690	0.743	0.691	0.698	0.718	0.801	0.929	0.879	0.018	0.086	0.034	0.795	0.766	0.918
Al_2O_3	17.690	2.950	15.730	15.760	15.920	15.680	15.830	15.580	15.660	16.050	15.700	15.740	16.240	16.110	16.320	16.370	16.160	16.540	16.860	15.940	16.260	21.310	21.290	21.260	15.730	16.390	15.860
FeO	11.370	7.350	10.960	11.190	11.040	10.950	11.100	11.150	11.040	11.160	10.750	10.740	10.610	10.710	10.820	10.760	11.040	10.950	11.210	10.990	11.260	13.860	13.540	13.610	10.860	10.950	10.980
MnO	0.004	0.155	0.137	0.084	0.106	0.123	0.116	0.064	0.029	0.083	0.061	0.099	0.085	0.086	0.083	0.072	0.077	0.110	0.092	0.148	0.068	0.159	0.122	0.143	0.110	0.105	0.067
MgO	16.160	18.940	16.850	17.010	16.820	16.550	16.970	16.740	16.910	16.940	16.970	17.290	17.020	17.000	17.070	17.040	17.310	17.310	17.320	17.140	17.460	23.290	23.960	23.760	17.290	17.060	17.070
CaO	0.003	12.490	0.013	0.041	0.027	0.026	0.045	0.056	0.037	0.034	0.058	0.035	0.006	0.179	0.027	0.030	0.178	0.011	0.030	0.023	0.001	0.065	0.023	0.070	0.028	0.024	0.022
BaO	0.000	0.000	0.042	0.026	0.062	0.000	0.014	0.113	0.050	0.000	0.000	0.026	0.068	0.000	0.095	0.098	0.001	0.045	0.021	0.080	0.003	0.112	0.019	0.083	0.019	0.115	0.000
Na_2O	0.012	0.388	0.065	0.055	0.036	0.071	0.091	0.056	0.067	0.022	0.094	0.086	0.107	0.079	0.137	0.067	0.145	0.162	0.077	0.070	0.126	0.000	0.000	0.000	0.087	0.151	0.072
K_2O	9.990	0.070	9.950	10.200	10.010	10.020	10.140	10.050	10.130	10.060	9.910	9.940	9.790	9.690	9.760	9.770	9.090	9.880	9.820	9.980	9.860	0.023	0.094	0.082	9.990	9.860	10.010
F	0.041	0.000	0.212	0.213	0.196	0.133	0.197	0.294	0.180	0.228	0.258	0.127	0.170	0.277	0.139	0.203	0.073	0.179	0.238	0.256	0.273	0.000	0.000	0.000	0.257	0.207	0.218
Cl	0.000	0.000	0.018	0.018	0.004	0.057	0.039	0.000	0.011	0.000	0.011	0.014	0.000	0.018	0.000	0.004	0.004	0.000	0.000	0.007	0.011	0.000	0.000	0.043	0.021	0.000	0.036
tot	95.834	98.223	94.613	94.997	94.693	94.071	94.941	94.349	94.769	94.717	93.760	94.639	94.493	94.769	95.114	94.635	94.556	95.735	96.139	94.912	95.421	86.938	87.245	87.376	95.206	95.048	94.621
CATIONS apfu																											
Si	2.877	3.719	2.927	2.898	2.917	2.933	2.911	2.920	2.924	2.900	2.912	2.918	2.919	2.933	2.916	2.908	2.912	2.897	2.878	2.901	2.877	2.200	2.190	2.203	2.934	2.894	2.908
Ti	0.005	0.000	0.054	0.062	0.050	0.051	0.049	0.054	0.054	0.048	0.049	0.048	0.039	0.038	0.041	0.038	0.038	0.039	0.044	0.051	0.048	0.001	0.005	0.002	0.044	0.042	0.051
Al	1.533	0.231	1.368	1.370	1.383	1.370	1.375	1.365	1.360	1.397	1.379	1.364	1.408	1.395	1.405	1.419	1.394	1.418	1.442	1.385	1.406	1.967	1.954	1.951	1.359	1.418	1.380
Fe	0.699	0.409	0.676	0.690	0.681	0.679	0.684	0.693	0.680	0.689	0.670	0.661	0.653	0.658	0.661	0.662	0.676	0.666	0.680	0.678	0.691	0.908	0.882	0.886	0.666	0.672	0.678
Mn	0.000	0.009	0.009	0.005	0.007	0.008	0.007	0.004	0.002	0.005	0.004	0.006	0.005	0.005	0.005	0.005	0.005	0.007	0.006	0.009	0.004	0.011	0.008	0.009	0.007	0.007	0.004
Mg	1.771	1.879	1.853	1.870	1.848	1.829	1.864	1.855	1.857	1.864	1.885	1.895	1.866	1.861	1.859	1.868	1.888	1.877	1.873	1.883	1.909	2.718	2.782	2.758	1.889	1.867	1.879
Ca	0.000	0.891	0.001	0.003	0.002	0.002	0.004	0.004	0.003	0.003	0.005	0.003	0.000	0.014	0.002	0.002	0.014	0.001	0.002	0.002	0.000	0.005	0.002	0.006	0.002	0.002	0.002
Ba	0.000	0.000	0.001	0.001	0.002	0.000	0.000	0.003	0.001	0.000	0.000	0.001	0.002	0.000	0.003	0.003	0.000	0.001	0.001	0.002	0.000	0.003	0.001	0.003	0.001	0.003	0.000
Na	0.002	0.050	0.009	0.008	0.005	0.010	0.013	0.008	0.010	0.003	0.014	0.012	0.015	0.011	0.019	0.010	0.021	0.023	0.011	0.010	0.018	0.000	0.000	0.000	0.012	0.021	0.010
K	0.937	0.006	0.936	0.960	0.941	0.948	0.953	0.953	0.952	0.947	0.942	0.932	0.918	0.908	0.910	0.917	0.849	0.917	0.909	0.938	0.923	0.002	0.009	0.008	0.934	0.923	0.943
F	0.010	0.000	0.049	0.050	0.046	0.031	0.046	0.069	0.042	0.053	0.061	0.029	0.040	0.064	0.032	0.047	0.017	0.041	0.055	0.060	0.063	0.000	0.000	0.000	0.060	0.048	0.051
Cl	0.000	0.000	0.002	0.002	0.000	0.007	0.005	0.000	0.001	0.000	0.001	0.002	0.000	0.002	0.000	0.000	0.000	0.000	0.000	0.001	0.001	0.000	0.000	0.006	0.003	0.000	0.004
tot	7.835	7.193	7.886	7.918	7.883	7.868	7.911	7.928	7.888	7.909	7.921	7.871	7.864	7.891	7.853	7.879	7.814	7.886	7.899	7.920	7.940	7.816	7.833	7.832	7.910	7.899	7.911

SAMPLE	**AK18-27**																**AK18-42**										
	bt	bt	bt	bt	bt	bt	bt	bt	bt	bt	bt	bt	bt	bt	bt	bt	bt	bt	bt	ms	ms	bt	bt	bt	ms	bt	bt
Spot number	59	60	61	62	63	64	65	66	67	68	69	70	71	72	73	74	1	2	3	4	5	6	7	8	9	10	11
OXIDES wt%																											
SiO_2	39.480	39.560	39.390	39.360	39.630	39.640	39.940	39.820	39.520	39.810	39.570	39.730	39.980	39.080	39.450	39.650	34.580	34.740	34.640	47.100	46.090	34.510	34.570	34.540	46.620	34.440	33.630
TiO_2	0.710	0.817	0.864	0.719	0.921	0.923	0.868	0.926	0.940	0.954	0.886	0.901	0.993	0.966	0.991	0.958	4.030	3.810	3.600	1.068	1.057	3.390	3.680	3.720	1.041	4.090	3.580
Al_2O_3	16.520	16.000	16.270	16.370	15.900	16.200	16.200	16.290	16.190	16.150	16.400	16.070	15.930	15.890	16.000	16.110	17.280	17.250	17.850	32.900	34.400	17.230	17.530	17.090	34.480	17.660	17.410
FeO	10.830	10.570	10.820	10.540	11.010	11.000	10.900	11.190	11.370	10.990	11.020	10.990	11.010	11.020	11.250	10.940	28.290	27.960	28.550	2.710	2.500	28.730	28.380	28.300	2.510	28.650	28.230
MnO	0.042	0.072	0.074	0.057	0.071	0.169	0.084	0.153	0.107	0.107	0.128	0.119	0.069	0.052	0.115	0.048	0.018	0.024	0.017	0.000	0.001	0.022	0.016	0.018	0.000	0.014	0.022
MgO	17.310	17.250	17.300	17.040	16.470	16.700	17.050	16.910	17.130	16.730	16.700	17.040	16.910	16.640	16.960	16.650	4.030	4.170	4.140	0.069	0.044	4.070	4.130	4.140	0.040	3.930	4.440
CaO	0.030	0.023	0.034	0.006	0.086	0.024	0.029	0.026	0.029	0.034	0.029	0.057	0.019	0.021	0.036	0.030	0.000	0.000	0.002	0.001	0.002	0.002	0.000	0.000	0.002	0.001	0.004
BaO	0.003	0.061	0.000	0.000	0.056	0.044	0.033	0.049	0.000	0.086	0.000	0.074	0.057	0.098	0.079	0.042	0.017	0.007	0.007	0.000	0.006	0.002	0.012	0.021	0.015	0.012	0.012
Na_2O	0.143	0.050	0.069	0.094	0.148	0.163	0.138	0.128	0.099	0.086	0.105	0.053	0.037	0.072	0.131	0.121	0.007	0.000	0.008	0.048	0.053	0.007	0.004	0.005	0.051	0.006	0.002
K_2O	9.740	9.960	9.980	9.930	9.630	9.740	9.980	9.730	9.890	9.990	9.940	10.010	9.970	10.090	10.020	9.730	9.540	9.570	9.600	10.770	10.550	9.390	9.550	9.460	10.630	9.460	9.260
F	0.133	0.095	0.128	0.166	0.237	0.165	0.133	0.050	0.251	0.104	0.120	0.131	0.280	0.190	0.100	0.106	0.010	0.013	0.007	0.000	0.000	0.014	0.002	0.006	0.000	0.000	0.016
Cl	0.000	0.000	0.007	0.000	0.050	0.000	0.046	0.025	0.025	0.000	0.018	0.039	0.000	0.025	0.035	0.011	0.002	0.006	0.002	0.000	0.000	0.001	0.000	0.002	0.000	0.006	0.006
tot	94.941	94.459	94.937	94.283	94.209	94.769	95.400	95.297	95.551	95.043	94.915	95.215	95.255	94.144	95.168	94.397	98.300	97.991	98.802	95.725	95.661	97.778	98.183	97.769	96.367	98.620	97.164
CATIONS apfu																											
Si	2.889	2.910	2.889	2.902	2.935	2.913	2.915	2.905	2.894	2.916	2.903	2.910	2.930	2.904	2.896	2.919	2.688	2.702	2.675	3.174	3.100	2.699	2.684	2.699	3.113	2.666	2.651
Ti	0.039	0.045	0.048	0.040	0.051	0.051	0.048	0.051	0.052	0.053	0.049	0.050	0.055	0.054	0.055	0.053	0.236	0.223	0.209	0.054	0.053	0.199	0.215	0.219	0.052	0.238	0.212
Al	1.425	1.387	1.406	1.423	1.388	1.403	1.393	1.400	1.397	1.394	1.418	1.387	1.376	1.392	1.384	1.398	1.583	1.582	1.625	2.613	2.727	1.588	1.604	1.574	2.713	1.611	1.617
Fe	0.663	0.650	0.664	0.650	0.682	0.676	0.665	0.683	0.696	0.673	0.676	0.673	0.675	0.685	0.691	0.674	1.839	1.819	1.844	0.153	0.141	1.879	1.843	1.849	0.140	1.854	1.861
Mn	0.003	0.005	0.005	0.004	0.004	0.011	0.005	0.009	0.007	0.007	0.008	0.007	0.004	0.003	0.007	0.003	0.001	0.002	0.001	0.000	0.000	0.001	0.001	0.001	0.000	0.001	0.001
Mg	1.888	1.891	1.891	1.873	1.818	1.829	1.855	1.839	1.870	1.826	1.826	1.860	1.847	1.843	1.856	1.827	0.467	0.483	0.477	0.007	0.004	0.474	0.478	0.482	0.004	0.453	0.522
Ca	0.002	0.002	0.003	0.001	0.007	0.002	0.002	0.002	0.002	0.003	0.002	0.004	0.002	0.002	0.003	0.002	0.000	0.000	0.000	0.000	0.000	0.000	0.000	0.000	0.000	0.000	0.000
Ba	0.000	0.002	0.000	0.000	0.002	0.001	0.001	0.001	0.000	0.002	0.000	0.002	0.002	0.003	0.002	0.001	0.001	0.000	0.000	0.000	0.000	0.000	0.000	0.001	0.000	0.000	0.000
Na	0.020	0.007	0.010	0.013	0.021	0.023	0.020	0.018	0.014	0.012	0.015	0.008	0.005	0.010	0.019	0.017	0.001	0.000	0.001	0.006	0.007	0.001	0.001	0.001	0.007	0.001	0.000
K	0.909	0.935	0.934	0.934	0.910	0.913	0.929	0.905	0.924	0.933	0.930	0.935	0.932	0.957	0.938	0.914	0.946	0.950	0.946	0.926	0.905	0.937	0.946	0.943	0.905	0.934	0.931
F	0.031	0.022	0.030	0.039	0.056	0.038	0.031	0.011	0.058	0.024	0.028	0.030	0.065	0.045	0.023	0.025	0.003	0.003	0.002	0.000	0.000	0.003	0.001	0.002	0.000	0.000	0.004
Cl	0.000	0.000	0.001	0.000	0.006	0.000	0.006	0.003	0.003	0.000	0.002	0.005	0.000	0.003	0.004	0.001	0.000	0.001	0.000	0.000	0.000	0.000	0.000	0.000	0.000	0.001	0.001
tot	7.870	7.855	7.878	7.878	7.879	7.860	7.869	7.828	7.917	7.844	7.857	7.871	7.893	7.901	7.877	7.834	7.763	7.765	7.780	6.932	6.939	7.782	7.773	7.770	6.935	7.759	7.801

SAMPLE	**AK18-42**																				
	bt	bt	bt	bt	ms	ms	ms	bt	bt	ms	ms	bt	bt	bt	bt	bt	bt	bt	bt	bt	ms
Spot number	12	13	14	15	16	17	18	19	20	21	22	23	24	25	26	27	28	29	30	31	32
OXIDES wt%																					
SiO_2	34.920	34.300	34.410	33.750	46.430	47.820	46.260	35.390	34.230	46.840	47.110	34.690	34.070	34.930	34.430	34.830	34.730	34.810	33.300	35.010	46.140
TiO_2	3.490	3.860	4.220	3.830	0.092	0.095	0.085	4.060	4.410	1.147	1.036	4.120	4.200	3.820	3.730	3.110	4.100	3.190	4.000	3.210	1.214
Al_2O_3	17.460	17.450	17.570	17.480	34.190	31.210	33.960	16.590	16.980	33.110	33.320	17.530	17.010	17.630	17.150	17.900	17.540	17.720	17.460	17.600	33.870
FeO	28.700	28.300	28.060	28.140	2.340	3.030	2.510	27.600	28.380	2.630	2.750	28.640	28.630	27.480	28.730	28.670	28.150	28.800	28.710	28.220	2.470
MnO	0.016	0.021	0.020	0.016	0.000	0.000	0.001	0.015	0.017	0.002	0.000	0.019	0.017	0.014	0.010	0.019	0.006	0.019	0.013	0.017	0.001
MgO	4.190	4.360	4.120	4.100	0.048	1.073	0.048	4.580	3.960	0.063	0.066	4.010	3.810	4.120	4.050	4.240	3.980	4.310	4.080	4.230	0.044
CaO	0.000	0.003	0.007	0.004	0.000	0.000	0.002	0.003	0.001	0.001	0.000	0.002	0.003	0.000	0.005	0.002	0.000	0.002	0.002	0.002	0.000
BaO	0.012	0.007	0.012	0.015	0.008	0.011	0.007	0.017	0.008	0.010	0.009	0.007	0.019	0.013	0.007	0.009	0.007	0.003	0.008	0.008	0.011
Na_2O	0.003	0.004	0.009	0.006	0.045	0.038	0.054	0.005	0.007	0.041	0.045	0.010	0.004	0.013	0.008	0.000	0.005	0.006	0.008	0.006	0.056
K_2O	9.590	9.540	9.380	9.510	10.660	10.590	10.550	9.570	9.470	10.740	10.770	9.430	9.420	9.630	9.450	9.540	9.620	9.460	9.450	9.550	10.530
F	0.009	0.000	0.007	0.004	0.000	0.000	0.000	0.010	0.005	0.000	0.000	0.009	0.000	0.000	0.008	0.002	0.007	0.008	0.012	0.000	0.000
Cl	0.003	0.005	0.000	0.001	0.000	0.003	0.000	0.005	0.001	0.000	0.000	0.005	0.007	0.004	0.003	0.002	0.003	0.004	0.005	0.000	0.000
tot	98.782	98.197	98.308	97.260	95.549	95.192	95.234	98.339	97.815	95.628	96.193	98.935	97.641	98.057	97.947	98.637	98.404	98.701	97.473	98.145	95.349
CATIONS apfu																					
Si	2.699	2.666	2.668	2.654	3.147	3.249	3.148	2.737	2.674	3.159	3.160	2.677	2.673	2.705	2.688	2.691	2.686	2.691	2.624	2.712	3.116
Ti	0.203	0.226	0.246	0.226	0.005	0.005	0.004	0.236	0.259	0.058	0.052	0.239	0.248	0.222	0.219	0.181	0.238	0.185	0.237	0.187	0.062
Al	1.590	1.598	1.606	1.620	2.731	2.499	2.724	1.512	1.563	2.631	2.634	1.595	1.573	1.609	1.578	1.630	1.599	1.614	1.621	1.607	2.696
Fe	1.855	1.839	1.820	1.850	0.133	0.172	0.143	1.785	1.854	0.148	0.154	1.849	1.879	1.779	1.876	1.852	1.821	1.862	1.892	1.828	0.139
Mn	0.001	0.001	0.001	0.001	0.000	0.000	0.000	0.001	0.001	0.000	0.000	0.001	0.001	0.001	0.001	0.001	0.000	0.001	0.001	0.001	0.000
Mg	0.483	0.505	0.476	0.481	0.005	0.109	0.005	0.528	0.461	0.006	0.007	0.461	0.446	0.475	0.471	0.488	0.459	0.497	0.479	0.488	0.004
Ca	0.000	0.000	0.001	0.000	0.000	0.000	0.000	0.000	0.000	0.000	0.000	0.000	0.000	0.000	0.000	0.000	0.000	0.000	0.000	0.000	0.000
Ba	0.000	0.000	0.000	0.000	0.000	0.000	0.000	0.001	0.000	0.000	0.000	0.000	0.001	0.000	0.000	0.000	0.000	0.000	0.000	0.000	0.000
Na	0.000	0.001	0.001	0.001	0.006	0.005	0.007	0.001	0.001	0.005	0.006	0.001	0.001	0.002	0.001	0.000	0.001	0.001	0.001	0.001	0.007
K	0.945	0.946	0.928	0.954	0.922	0.918	0.916	0.944	0.944	0.924	0.921	0.928	0.943	0.951	0.941	0.940	0.949	0.933	0.950	0.944	0.907
F	0.002	0.000	0.002	0.001	0.000	0.000	0.000	0.002	0.001	0.000	0.000	0.002	0.000	0.000	0.002	0.001	0.002	0.002	0.003	0.000	0.000
Cl	0.000	0.001	0.000	0.000	0.000	0.000	0.000	0.001	0.000	0.000	0.000	0.001	0.001	0.001	0.000	0.000	0.000	0.000	0.001	0.000	0.000
tot	7.780	7.783	7.750	7.789	6.947	6.958	6.947	7.748	7.759	6.932	6.935	7.755	7.765	7.746	7.778	7.785	7.754	7.787	7.809	7.770	6.932

11. SUPPLEMENTARY MATERIAL APPENDIX 2: ^{40}Ar/^{39}Ar DATSET

SAMPLE	**40Ar Total**	**Err.40Ar**	**40Ar***	**Err.40Ar***	**39Ar**	**Err.39Ar**	**%39Ar**	**38Ar**	**Err.38Ar**	**38ArCl**	**Err.38Cl**	**37Ar**	**Err.37Ar**	**36Ar**	**Err.36Ar**	**Age**	**1 s Err Age**	**Ca/K**	**Error Ca/K**	**Cl/K**	**Error Cl/K**
GW13-28 bt																					
J= 0.002814	1.36E-08	2.86E-12	1.80E-09	4.55E-11	6.73E-11	3.47E-13	8.42E-01	1.49E-10	2.88E-13	1.40E-10	5.81E-14	2.10E-11	1.51E-12	3.95E-11	1.52E-13	130.82	3.38	0.60579	0.04370	0.37167	0.00192
m= 0.0088 g	3.72E-09	7.54E-13	4.91E-10	1.29E-11	2.27E-10	3.81E-13	2.84E+00	2.47E-11	5.02E-14	2.00E-11	5.37E-14	3.54E-11	1.51E-12	1.08E-11	4.31E-14	10.95	0.29	0.30276	0.01297	0.01567	0.00005
	5.33E-09	1.38E-12	8.16E-10	1.79E-11	4.31E-10	5.32E-13	5.39E+00	2.44E-11	5.03E-14	1.65E-11	5.51E-14	1.70E-11	1.51E-12	1.51E-11	5.97E-14	9.60	0.21	0.07655	0.00681	0.00683	0.00002
	8.03E-08	2.13E-11	6.52E-10	3.05E-10	6.39E-10	7.38E-13	8.00E+00	8.11E-11	1.59E-13	2.33E-11	1.99E-13	1.97E-11	1.51E-12	2.67E-10	1.02E-12	5.17	2.42	0.05978	0.00459	0.00649	0.00006
	5.16E-09	1.38E-12	1.36E-09	1.54E-11	6.37E-10	7.51E-13	7.97E+00	2.38E-11	4.93E-14	1.39E-11	5.56E-14	9.93E-12	1.51E-12	1.27E-11	5.14E-14	10.79	0.12	0.03027	0.00460	0.00388	0.00002
	6.95E-09	3.38E-12	3.70E-09	1.37E-11	1.59E-09	1.77E-12	2.00E+01	5.02E-11	1.01E-13	2.94E-11	5.72E-14	1.68E-11	1.51E-12	1.09E-11	4.45E-14	11.73	0.05	0.02049	0.00184	0.00328	0.00001
	2.79E-09	1.07E-12	1.24E-09	6.72E-12	5.19E-10	6.83E-13	6.50E+00	1.59E-11	3.29E-14	8.83E-12	5.46E-14	1.53E-11	1.51E-12	5.23E-12	2.22E-14	12.04	0.07	0.05718	0.00565	0.00303	0.00002
	3.14E-09	1.12E-12	1.24E-09	8.09E-12	5.04E-10	6.72E-13	6.31E+00	1.69E-11	3.52E-14	9.76E-12	5.49E-14	3.79E-11	1.52E-12	6.40E-12	2.68E-14	12.43	0.08	0.14613	0.00584	0.00345	0.00002
	7.86E-09	2.34E-12	1.90E-09	2.33E-11	6.28E-10	7.61E-13	7.87E+00	2.52E-11	5.18E-14	1.40E-11	5.62E-14	1.27E-10	1.56E-12	2.00E-11	7.76E-14	15.31	0.19	0.39334	0.00484	0.00397	0.00002
	1.30E-08	5.20E-12	3.11E-09	3.89E-11	9.75E-10	1.04E-12	1.22E+01	4.02E-11	8.40E-14	2.25E-11	6.07E-14	1.52E-10	1.58E-12	3.32E-11	1.29E-13	16.11	0.20	0.30331	0.00316	0.00410	0.00001
	1.27E-08	3.38E-12	2.86E-09	3.83E-11	1.21E-09	1.31E-12	1.51E+01	4.53E-11	8.98E-14	2.49E-11	5.89E-14	9.36E-11	1.54E-12	3.29E-11	1.28E-13	12.02	0.16	0.15060	0.00248	0.00368	0.00001
	1.37E-08	3.38E-12	1.91E-09	4.56E-11	5.63E-10	6.49E-13	7.04E+00	2.66E-11	5.35E-14	1.25E-11	6.01E-14	3.03E-10	1.75E-12	3.96E-11	1.52E-13	17.14	0.41	1.04541	0.00614	0.00394	0.00002
Conc (g/g)	**K**	**Cl**	**Ca**																		
	4.61E-02	3.45E-04	9.52E-03																		
GW13-28 ms																					
J= 0.002806	6.91E-08	2.86E-11	-5.63E-10	3.23E-10	1.45E-10	3.78E-13	2.64E+00	8.66E-11	2.05E-13	4.09E-11	2.12E-13	6.69E-12	2.30E-12	2.33E-10	1.08E-12	-19.80	-11.36	0.08968	0.03084	0.05035	0.00029
m= 0.0031 g	4.24E-09	4.42E-13	4.54E-11	1.98E-11	1.12E-10	3.38E-13	2.04E+00	4.90E-12	1.45E-14	9.29E-13	7.79E-14	2.27E-12	2.30E-12	1.41E-11	6.63E-14	2.05	0.90	0.03947	0.03993	0.00148	0.00012
	2.92E-09	4.68E-13	9.63E-10	9.98E-12	6.28E-10	8.09E-13	1.15E+01	9.10E-12	2.40E-14	4.82E-13	6.95E-14	2.54E-13	2.30E-12	6.57E-12	3.34E-14	7.75	0.08	0.00078	0.00711	0.00014	0.00002
	2.90E-09	4.94E-13	1.77E-09	6.08E-12	1.18E-09	1.42E-12	2.16E+01	1.52E-11	3.90E-14	5.83E-13	6.89E-14	1.43E-13	2.30E-12	3.79E-12	2.03E-14	7.54	0.03	0.00023	0.00377	0.00009	0.00001
	2.27E-09	4.94E-13	1.22E-09	5.73E-12	8.52E-10	1.06E-12	1.56E+01	1.11E-11	3.07E-14	4.15E-13	7.30E-14	6.83E-14	2.30E-12	3.52E-12	1.91E-14	7.26	0.04	0.00016	0.00524	0.00009	0.00002
	1.78E-09	4.68E-13	6.22E-10	6.06E-12	4.69E-10	6.51E-13	8.55E+00	6.54E-12	1.77E-14	2.94E-13	7.09E-14	3.22E-13	2.30E-12	3.89E-12	2.02E-14	6.70	0.07	0.00133	0.00952	0.00011	0.00003
	2.02E-09	5.20E-13	4.49E-10	7.89E-12	3.51E-10	5.11E-13	6.41E+00	5.36E-12	1.51E-14	2.38E-13	7.38E-14	3.89E-13	2.30E-12	5.27E-12	2.64E-14	6.46	0.11	0.00215	0.01271	0.00012	0.00004
	2.02E-09	5.46E-13	3.53E-10	8.39E-12	2.89E-10	4.75E-13	5.27E+00	4.68E-12	1.37E-14	2.31E-13	7.67E-14	3.59E-13	2.30E-12	5.57E-12	2.81E-14	6.17	0.15	0.00241	0.01545	0.00014	0.00005
	1.77E-08	4.16E-12	2.38E-10	8.11E-11	3.33E-10	5.11E-13	6.07E+00	1.55E-11	3.97E-14	5.07E-13	8.42E-14	9.68E-13	2.30E-12	5.86E-11	2.71E-13	3.62	1.23	0.00565	0.01342	0.00027	0.00005
	5.15E-09	1.04E-12	2.49E-10	2.30E-11	2.63E-10	4.54E-13	4.79E+00	6.42E-12	1.87E-14	2.38E-13	7.73E-14	4.77E-13	2.30E-12	1.64E-11	7.71E-14	4.79	0.44	0.00353	0.01700	0.00016	0.00005
	6.13E-09	1.40E-12	3.57E-10	2.71E-11	3.47E-10	5.24E-13	6.34E+00	8.00E-12	2.14E-14	2.68E-13	7.19E-14	5.64E-13	2.30E-12	1.93E-11	9.08E-14	5.20	0.39	0.00315	0.01285	0.00014	0.00004
	1.45E-08	3.38E-12	4.03E-10	6.56E-11	5.08E-10	6.89E-13	9.28E+00	1.52E-11	3.78E-14	2.66E-13	7.73E-14	1.04E-12	2.30E-12	4.73E-11	2.19E-13	4.01	0.65	0.00397	0.00878	0.00009	0.00003
Conc (g/g)	**K**	**Cl**	**Ca**																		
	9.01E-02	1.33E-04	4.32E-04																		
GW13-29 bt																					
J= 0.00284	9.51E-09	2.47E-12	2.90E-12	3.27E-11	2.56E-11	3.39E-13	3.21E-01	3.35E-11	6.08E-14	2.72E-11	5.16E-14	3.24E-13	1.43E-12	3.19E-11	1.09E-13	0.58	6.55	0.02460	0.10865	0.18941	0.00253
m= 0.005 g	4.97E-09	1.17E-12	2.02E-10	1.68E-11	1.53E-10	3.62E-13	1.92E+00	1.20E-11	2.51E-14	7.14E-12	5.57E-14	5.62E-13	1.43E-12	1.60E-11	5.61E-14	6.76	0.56	0.00714	0.01817	0.00832	0.00007
	6.99E-08	5.20E-11	2.20E-09	2.40E-10	9.94E-10	1.18E-12	1.25E+01	8.09E-11	1.54E-13	2.65E-11	1.56E-13	2.49E-12	1.43E-12	2.27E-10	7.84E-13	11.31	1.23	0.00486	0.00279	0.00474	0.00003
	1.03E-08	2.11E-12	2.54E-09	2.66E-11	1.44E-09	1.33E-12	1.81E+01	5.16E-11	9.39E-14	2.97E-11	5.26E-14	1.20E-12	1.43E-12	2.58E-11	8.90E-14	9.02	0.09	0.00161	0.00193	0.00367	0.00001
	9.95E-09	1.66E-12	2.50E-09	2.59E-11	1.42E-09	1.29E-12	1.78E+01	5.05E-11	9.11E-14	2.91E-11	5.20E-14	1.18E-12	1.43E-12	2.49E-11	8.65E-14	9.02	0.09	0.00161	0.00196	0.00365	0.00001
	6.58E-09	9.62E-13	1.49E-09	1.80E-11	8.50E-10	8.16E-13	1.07E+01	3.03E-11	5.57E-14	1.71E-11	5.00E-14	9.33E-13	1.43E-12	1.71E-11	6.00E-14	8.94	0.11	0.00213	0.00327	0.00359	0.00001
	6.72E-09	1.01E-12	1.14E-09	1.95E-11	6.50E-10	6.44E-13	8.16E+00	2.42E-11	4.55E-14	1.30E-11	5.10E-14	8.06E-13	1.43E-12	1.87E-11	6.53E-14	8.99	0.15	0.00241	0.00427	0.00356	0.00001
	7.41E-09	1.66E-12	8.79E-10	2.27E-11	5.23E-10	5.72E-13	6.57E+00	2.09E-11	3.84E-14	1.06E-11	5.04E-14	1.16E-12	1.43E-12	2.19E-11	7.58E-14	8.58	0.22	0.00430	0.00531	0.00360	0.00002
	1.26E-08	3.12E-12	1.24E-09	3.89E-11	7.19E-10	7.35E-13	9.03E+00	3.01E-11	5.45E-14	1.45E-11	5.37E-14	1.36E-12	1.43E-12	3.81E-11	1.30E-13	8.80	0.28	0.00366	0.00386	0.00359	0.00001
	1.76E-08	3.90E-12	1.08E-09	5.65E-11	6.05E-10	6.58E-13	7.60E+00	2.95E-11	5.43E-14	1.20E-11	6.01E-14	1.18E-12	1.43E-12	5.52E-11	1.89E-13	9.12	0.48	0.00379	0.00459	0.00353	0.00002
	6.93E-09	1.38E-12	5.10E-10	2.23E-11	3.18E-10	4.31E-13	3.99E+00	1.41E-11	2.77E-14	6.27E-12	5.34E-14	1.23E-12	1.43E-12	2.15E-11	7.45E-14	8.21	0.36	0.00751	0.00873	0.00351	0.00003
	7.92E-09	1.77E-12	2.49E-10	2.65E-11	1.80E-10	3.47E-13	2.27E+00	1.05E-11	2.14E-14	3.54E-12	5.56E-14	1.31E-12	1.43E-12	2.57E-11	8.86E-14	7.06	0.75	0.01404	0.01539	0.00349	0.00006
	8.06E-09	1.56E-12	1.19E-10	2.75E-11	8.53E-11	3.45E-13	1.07E+00	7.69E-12	1.69E-14	1.66E-12	6.00E-14	1.32E-12	1.43E-12	2.66E-11	9.19E-14	7.14	1.65	0.03011	0.03253	0.00347	0.00013
Conc (g/g)	**K**	**Cl**	**Ca**																		
	8.02E-02	3.55E-04	2.94E-04																		
GW13-29 ms																					
J= 0.002828	8.36E-08	2.86E-11	1.77E-09	2.80E-10	7.95E-10	8.03E-13	4.51E+00	1.54E-10	2.72E-13	9.35E-11	1.82E-13	2.82E-11	1.43E-12	2.74E-10	9.34E-13	11.30	1.79	0.06866	0.00350	0.02092	0.00005

m= 0.0096 g	2.77E-09	4.42E-13	5.94E-10	8.05E-12	4.80E-10	5.62E-13	2.72E+00	1.01E-11	2.08E-14	3.07E-12	5.43E-14	1.04E-11	1.43E-12	7.28E-12	2.69E-14	6.30	0.09	0.04207	0.00578	0.00114	0.00002
	2.99E-09	5.20E-13	1.09E-09	7.32E-12	8.54E-10	8.32E-13	4.85E+00	1.25E-11	2.49E-14	1.28E-12	5.27E-14	7.68E-12	1.43E-12	6.35E-12	2.45E-14	6.50	0.04	0.01744	0.00325	0.00027	0.00001
	9.02E-09	1.43E-12	4.79E-09	1.52E-11	3.58E-09	3.10E-12	2.03E+01	4.72E-11	8.33E-14	2.33E-12	5.94E-14	8.88E-12	1.43E-12	1.42E-11	5.06E-14	6.81	0.02	0.00481	0.00078	0.00012	0.00000
	1.80E-09	3.90E-13	8.04E-10	4.30E-12	6.50E-10	6.58E-13	3.69E+00	8.81E-12	1.88E-14	5.34E-13	5.60E-14	5.33E-12	1.43E-12	3.33E-12	1.43E-14	6.30	0.03	0.01592	0.00427	0.00015	0.00002
	1.75E-09	3.64E-13	7.92E-10	4.33E-12	6.35E-10	6.62E-13	3.60E+00	8.63E-12	1.79E-14	5.53E-13	5.45E-14	5.60E-12	1.43E-12	3.20E-12	1.44E-14	6.35	0.04	0.01709	0.00437	0.00016	0.00002
	2.77E-09	5.20E-13	1.35E-09	5.80E-12	1.07E-09	1.02E-12	6.06E+00	1.44E-11	2.91E-14	8.88E-13	5.41E-14	8.13E-12	1.43E-12	4.76E-12	1.94E-14	6.44	0.03	0.01476	0.00260	0.00015	0.00001
	3.43E-09	6.24E-13	1.57E-09	7.41E-12	1.27E-09	1.15E-12	7.19E+00	1.74E-11	3.49E-14	1.29E-12	5.41E-14	9.53E-12	1.43E-12	6.22E-12	2.47E-14	6.30	0.03	0.01458	0.00219	0.00018	0.00001
	3.72E-09	6.50E-13	1.58E-09	8.30E-12	1.28E-09	1.15E-12	7.25E+00	1.77E-11	3.52E-14	1.34E-12	5.36E-14	9.20E-12	1.43E-12	7.16E-12	2.77E-14	6.29	0.03	0.01396	0.00217	0.00019	0.00001
	1.04E-08	1.66E-12	2.78E-09	2.64E-11	2.17E-09	1.90E-12	1.23E+01	3.27E-11	6.05E-14	2.30E-12	5.56E-14	1.39E-11	1.43E-12	2.55E-11	8.83E-14	6.51	0.06	0.01238	0.00128	0.00019	0.00000
	1.89E-08	2.50E-12	3.96E-09	5.18E-11	2.92E-09	2.53E-12	1.66E+01	4.63E-11	8.26E-14	2.41E-12	6.41E-14	2.22E-11	1.43E-12	5.02E-11	1.73E-13	6.89	0.09	0.01469	0.00095	0.00015	0.00000
	1.70E-08	2.26E-12	2.74E-09	4.89E-11	1.92E-09	1.68E-12	1.09E+01	3.35E-11	6.04E-14	1.95E-12	5.95E-14	4.75E-11	1.44E-12	4.77E-11	1.63E-13	7.27	0.13	0.04806	0.00146	0.00018	0.00001
Conc (g/g)	**K**	**Cl**	**Ca**																		
	9.29E-02	1.04E-04	1.80E-03																		
GW13-29B bt																					
J= 0.002867	6.71E-09	1.56E-12	1.06E-10	2.29E-11	6.14E-12	3.64E-13	1.84E-01	1.87E-11	3.44E-14	1.44E-11	5.03E-14	4.21E-13	1.43E-12	2.21E-11	7.66E-14	87.33	19.57	0.13309	0.45312	0.41816	0.02484
m= 0.0022 g	2.10E-09	5.20E-13	7.57E-11	7.47E-12	3.35E-11	3.39E-13	1.00E+00	4.96E-12	1.14E-14	3.28E-12	6.02E-14	4.87E-13	1.43E-12	6.78E-12	2.49E-14	11.66	1.16	0.02824	0.08305	0.01746	0.00037
	4.86E-08	2.13E-11	8.66E-10	1.65E-10	2.46E-10	3.97E-13	7.36E+00	4.17E-11	7.66E-14	8.65E-12	1.14E-13	1.57E-12	1.43E-12	1.60E-10	5.46E-13	18.16	3.45	0.01241	0.01132	0.00627	0.00008
	1.41E-08	3.64E-12	1.09E-09	4.48E-11	5.29E-10	5.93E-13	1.58E+01	2.84E-11	5.24E-14	1.40E-11	5.61E-14	1.81E-12	1.43E-12	4.35E-11	1.50E-13	10.67	0.44	0.00665	0.00526	0.00471	0.00002
	3.30E-09	4.94E-13	1.54E-09	6.89E-12	8.47E-10	8.15E-13	2.54E+01	2.86E-11	5.30E-14	1.76E-11	4.93E-14	8.73E-13	1.43E-12	5.90E-12	2.30E-14	9.39	0.04	0.00200	0.00328	0.00369	0.00001
	2.63E-09	5.98E-13	1.01E-09	6.50E-12	5.86E-10	6.14E-13	1.76E+01	1.88E-11	3.56E-14	1.09E-11	4.98E-14	9.40E-13	1.43E-12	5.43E-12	2.17E-14	8.93	0.06	0.00311	0.00474	0.00331	0.00002
	3.59E-09	8.32E-13	6.54E-10	1.07E-11	3.75E-10	5.03E-13	1.12E+01	1.34E-11	2.71E-14	7.17E-12	5.33E-14	9.64E-13	1.43E-12	9.82E-12	3.57E-14	9.00	0.15	0.00499	0.00741	0.00340	0.00003
	3.77E-09	8.06E-13	2.67E-10	1.25E-11	1.26E-10	3.30E-13	3.79E+00	6.30E-12	1.50E-14	2.60E-12	6.27E-14	8.73E-13	1.43E-12	1.17E-11	4.18E-14	10.90	0.51	0.01340	0.02197	0.00366	0.00009
	6.13E-09	1.33E-12	3.34E-10	2.03E-11	1.36E-10	3.57E-13	4.07E+00	8.09E-12	1.70E-14	2.83E-12	5.63E-14	9.35E-13	1.43E-12	1.94E-11	6.79E-14	12.68	0.77	0.01337	0.02049	0.00372	0.00007
	5.71E-09	1.20E-12	3.58E-10	1.89E-11	1.65E-10	3.66E-13	4.95E+00	8.71E-12	1.79E-14	3.39E-12	5.48E-14	9.72E-13	1.43E-12	1.79E-11	6.31E-14	11.17	0.59	0.01143	0.01683	0.00365	0.00006
	1.61E-08	3.64E-12	5.55E-10	5.37E-11	1.76E-10	3.93E-13	5.27E+00	1.57E-11	3.03E-14	3.80E-12	6.07E-14	1.18E-12	1.43E-12	5.22E-11	1.79E-13	16.25	1.57	0.01297	0.01581	0.00384	0.00006
	6.09E-09	1.17E-12	2.42E-10	2.05E-11	1.11E-10	3.51E-13	3.34E+00	7.26E-12	1.64E-14	2.25E-12	6.03E-14	1.01E-12	1.43E-12	1.96E-11	6.84E-14	11.21	0.95	0.01762	0.02493	0.00360	0.00010
Conc (g/g)	**K**	**Cl**	**Ca**																		
	7.56E-02	3.67E-04	5.29E-04																		
GW13-29B ms																					
J= 0.002856	6.60E-08	2.86E-11	1.63E-08	2.02E-10	3.95E-10	5.93E-13	2.37E+00	8.59E-11	1.79E-13	4.98E-11	1.37E-13	9.39E-12	1.48E-12	1.67E-10	6.69E-13	200.42	2.50	0.04610	0.00726	0.02244	0.00007
m= 0.0096 g	3.99E-09	4.16E-13	6.63E-10	1.38E-11	5.47E-10	6.70E-13	3.27E+00	1.50E-11	3.35E-14	6.49E-12	5.91E-14	1.08E-11	1.48E-12	1.11E-11	4.60E-14	6.24	0.13	0.03816	0.00525	0.00211	0.00002
	8.83E-09	1.14E-12	4.48E-09	1.82E-11	3.76E-09	3.80E-12	2.25E+01	5.24E-11	1.09E-13	5.48E-12	7.09E-14	1.36E-11	1.48E-12	1.46E-11	6.07E-14	6.13	0.03	0.00700	0.00076	0.00026	0.00000
	2.49E-09	3.90E-13	1.38E-09	5.27E-12	1.16E-09	1.21E-12	6.93E+00	1.53E-11	3.47E-14	9.71E-13	6.08E-14	5.62E-12	1.48E-12	3.72E-12	1.76E-14	6.12	0.02	0.00942	0.00248	0.00015	0.00001
	1.50E-09	4.16E-13	7.01E-10	4.21E-12	6.16E-10	7.26E-13	3.68E+00	8.23E-12	2.10E-14	4.80E-13	6.70E-14	5.37E-12	1.48E-12	2.69E-12	1.40E-14	5.86	0.04	0.01693	0.00466	0.00014	0.00002
	1.72E-09	4.16E-13	7.43E-10	5.00E-12	6.48E-10	7.41E-13	3.88E+00	8.81E-12	2.13E-14	5.64E-13	6.35E-14	5.53E-12	1.48E-12	3.26E-12	1.67E-14	5.89	0.04	0.01655	0.00442	0.00015	0.00002
	2.11E-09	4.16E-13	8.49E-10	5.77E-12	7.39E-10	8.32E-13	4.42E+00	1.01E-11	2.39E-14	6.49E-13	6.22E-14	5.80E-12	1.48E-12	4.22E-12	1.93E-14	5.91	0.04	0.01521	0.00388	0.00016	0.00001
	2.89E-09	4.94E-13	1.05E-09	8.22E-12	9.16E-10	9.91E-13	5.48E+00	1.29E-11	2.97E-14	9.34E-13	6.13E-14	6.83E-12	1.48E-12	6.19E-12	2.75E-14	5.88	0.05	0.01447	0.00313	0.00018	0.00001
	4.87E-09	7.80E-13	1.31E-09	1.50E-11	1.14E-09	1.22E-12	6.81E+00	1.70E-11	3.87E-14	1.41E-12	6.15E-14	7.41E-12	1.48E-12	1.19E-11	5.02E-14	5.92	0.07	0.01263	0.00252	0.00022	0.00001
	4.07E-09	7.02E-13	1.78E-09	9.96E-12	1.50E-09	1.57E-12	8.96E+00	2.10E-11	4.55E-14	1.88E-12	5.98E-14	8.55E-12	1.48E-12	7.68E-12	3.33E-14	6.10	0.03	0.01108	0.00192	0.00022	0.00001
	5.60E-09	8.32E-13	3.04E-09	1.09E-11	2.51E-09	2.55E-12	1.50E+01	3.38E-11	7.15E-14	2.69E-12	6.29E-14	9.92E-12	1.48E-12	8.57E-12	3.64E-14	6.23	0.02	0.00766	0.00114	0.00019	0.00000
	1.19E-08	1.79E-12	3.57E-09	3.35E-11	2.78E-09	2.83E-12	1.67E+01	4.12E-11	8.59E-14	3.21E-12	6.70E-14	2.08E-11	1.48E-12	2.78E-11	1.12E-13	6.60	0.06	0.01451	0.00103	0.00021	0.00000
Conc (g/g)	**K**	**Cl**	**Ca**																		
	8.71E-02	6.93E-05	1.11E-03																		
GW13-39 ms																					
J= 0.000879	8.13E-08	6.05E-11	1.13E-09	2.58E-10	8.95E-11	5.06E-13	2.70E+00	5.30E-11	9.34E-14	1.34E-12	1.69E-13	8.46E-12	1.01E-12	2.69E-10	8.40E-13	19.91	4.55	0.18335	0.02193	0.00267	0.00034
m= 0.0066 g	1.22E-08	6.72E-12	2.66E-09	3.14E-11	2.77E-10	5.44E-13	8.37E+00	9.57E-12	2.28E-14	2.87E-13	8.28E-14	2.64E-12	1.01E-12	3.19E-11	1.03E-13	15.16	0.18	0.01846	0.00704	0.00018	0.00005
	1.26E-08	4.70E-12	9.07E-09	1.32E-11	9.82E-10	9.99E-13	2.97E+01	1.45E-11	3.10E-14	7.19E-13	7.33E-14	1.50E-12	1.01E-12	1.19E-11	4.14E-14	14.60	0.03	0.00297	0.00199	0.00013	0.00001
	8.25E-09	7.39E-12	5.49E-09	1.26E-11	6.05E-10	7.83E-13	1.83E+01	9.23E-12	2.03E-14	3.73E-13	7.47E-14	1.72E-12	1.01E-12	9.25E-12	3.41E-14	14.34	0.04	0.00551	0.00323	0.00011	0.00002

	5.03E-09	2.96E-12	2.60E-09	9.29E-12	2.87E-10	5.46E-13	8.66E+00	5.12E-12	1.41E-14	2.11E-13	9.28E-14	1.63E-12	1.01E-12	8.13E-12	2.95E-14	14.32	0.06	0.01102	0.00680	0.00013	0.00006
	5.01E-09	2.89E-12	2.12E-09	1.10E-11	2.31E-10	5.63E-13	6.99E+00	4.72E-12	1.45E-14	1.80E-13	1.03E-13	1.43E-12	1.01E-12	9.66E-12	3.55E-14	14.48	0.08	0.01199	0.00844	0.00014	0.00008
	5.62E-09	2.86E-12	1.83E-09	1.32E-11	2.01E-10	4.92E-13	6.07E+00	4.90E-12	1.36E-14	1.43E-13	9.35E-14	1.31E-12	1.01E-12	1.27E-11	4.30E-14	14.43	0.11	0.01267	0.00971	0.00013	0.00008
	6.17E-09	2.96E-12	1.39E-09	1.61E-11	1.52E-10	5.47E-13	4.61E+00	4.91E-12	1.29E-14	9.78E-14	8.89E-14	1.48E-12	1.01E-12	1.60E-11	5.29E-14	14.41	0.17	0.01889	0.01280	0.00011	0.00010
	5.65E-09	2.15E-12	8.92E-10	1.61E-11	9.56E-11	6.06E-13	2.89E+00	4.19E-12	1.26E-14	6.18E-14	1.02E-13	1.77E-12	1.01E-12	1.59E-11	5.33E-14	14.73	0.28	0.03593	0.02046	0.00012	0.00019
	1.97E-09	7.39E-13	5.06E-10	6.11E-12	5.99E-11	5.37E-13	1.81E+00	1.59E-12	7.33E-15	-3.94E-14	1.55E-13	5.02E-15	1.01E-12	4.90E-12	2.03E-14	13.36	0.20	0.00016	0.03257	-0.00012	-0.00046
	6.85E-09	3.36E-12	1.51E-09	1.76E-11	1.55E-10	5.15E-13	4.69E+00	5.37E-12	1.43E-14	1.69E-13	9.03E-14	7.53E-13	1.01E-12	1.79E-11	5.79E-14	15.35	0.19	0.00941	0.01257	0.00019	0.00010
	1.17E-08	6.38E-12	1.60E-09	3.26E-11	1.75E-10	5.51E-13	5.28E+00	8.45E-12	1.86E-14	1.02E-14	7.67E-14	1.01E-12	1.01E-12	3.39E-11	1.07E-13	14.48	0.30	0.01124	0.01116	0.00001	0.00008
Conc (g/g)	**K**	**Cl**	**Ca**																		
	8.16E-02	1.56E-05	1.13E-03																		
GW13-51 ms	4.21E-08	1.92E-11	4.28E-10	9.98E-11	9.35E-11	3.94E-13	3.31E+00	2.83E-11	4.13E-14	8.71E-13	7.27E-14	1.00E-11	2.22E-13	1.40E-10	3.28E-13	7.25	1.69	0.20784	0.00469	0.00166	0.00014
J= 0.000881	1.16E-08	2.86E-12	9.82E-10	2.54E-11	1.00E-10	3.69E-13	3.54E+00	8.11E-12	1.57E-14	2.40E-13	5.28E-14	3.52E-12	2.21E-13	3.55E-11	8.45E-14	15.54	0.41	0.06837	0.00429	0.00043	0.00009
m= 0.0051 g	4.73E-09	1.01E-12	1.99E-09	7.68E-12	1.72E-10	4.28E-13	6.10E+00	3.88E-12	1.05E-14	1.24E-13	7.09E-14	1.28E-12	2.20E-13	9.19E-12	2.55E-14	18.25	0.08	0.01448	0.00248	0.00013	0.00007
	2.72E-09	5.72E-13	1.76E-09	3.64E-12	1.61E-10	4.01E-13	5.70E+00	2.55E-12	9.03E-15	4.61E-14	9.22E-14	5.10E-13	2.20E-13	3.24E-12	1.20E-14	17.25	0.06	0.00615	0.00265	0.00005	0.00010
	2.14E-09	5.72E-13	1.46E-09	3.11E-12	1.37E-10	3.99E-13	4.86E+00	2.09E-12	8.16E-15	4.87E-14	1.02E-13	2.98E-13	2.20E-13	2.27E-12	1.03E-14	16.85	0.06	0.00421	0.00311	0.00006	0.00013
	2.63E-09	9.10E-13	1.89E-09	3.37E-12	1.79E-10	3.79E-13	6.33E+00	2.62E-12	9.06E-15	5.22E-14	8.99E-14	3.88E-13	2.20E-13	2.48E-12	1.09E-14	16.73	0.05	0.00421	0.00239	0.00005	0.00009
	5.91E-09	1.77E-12	4.37E-09	5.28E-12	4.19E-10	4.59E-13	1.49E+01	5.99E-12	1.22E-14	8.04E-14	5.32E-14	9.95E-13	2.20E-13	5.15E-12	1.67E-14	16.48	0.03	0.00460	0.00102	0.00003	0.00002
	3.62E-09	1.12E-12	2.60E-09	4.25E-12	2.49E-10	3.92E-13	8.82E+00	3.63E-12	9.50E-15	5.97E-14	6.82E-14	1.61E-13	2.20E-13	3.41E-12	1.37E-14	16.51	0.04	0.00125	0.00171	0.00004	0.00005
	4.79E-09	1.14E-12	3.37E-09	4.58E-12	3.26E-10	3.87E-13	1.15E+01	4.81E-12	1.17E-14	8.10E-14	6.34E-14	1.05E-13	2.20E-13	4.74E-12	1.49E-14	16.37	0.03	0.00063	0.00131	0.00004	0.00003
	5.40E-09	1.38E-12	3.84E-09	5.10E-12	3.68E-10	4.44E-13	1.31E+01	5.40E-12	1.29E-14	8.20E-14	6.24E-14	1.82E-13	2.20E-13	5.23E-12	1.65E-14	16.50	0.03	0.00096	0.00116	0.00004	0.00003
	6.36E-09	1.43E-12	4.26E-09	6.24E-12	3.99E-10	4.30E-13	1.41E+01	6.10E-12	1.33E-14	8.06E-14	5.71E-14	-2.24E-13	-2.20E-13	7.01E-12	2.03E-14	16.90	0.03	-0.00109	-0.00107	0.00004	0.00003
	1.12E-08	2.37E-12	2.19E-09	2.19E-11	2.18E-10	3.37E-13	7.74E+00	8.33E-12	1.58E-14	4.31E-14	5.14E-14	1.72E-13	2.20E-13	3.03E-11	7.31E-14	15.89	0.16	0.00153	0.00195	0.00004	0.00004
Conc (g/g)	**K**	**Cl**	**Ca**																		
	8.98E-02	1.02E-05	1.08E-03																		
GW13-57 ms																					
J= 0.000879	4.71E-08	3.24E-11	1.27E-09	1.45E-10	5.08E-11	5.71E-13	1.78E+00	3.00E-11	5.55E-14	4.25E-13	1.09E-13	5.48E-12	1.19E-12	1.54E-10	4.74E-13	39.25	4.50	0.20897	0.04564	0.00149	0.00038
m= 0.0057 g	1.15E-08	6.07E-12	1.24E-09	3.25E-11	1.06E-10	4.76E-13	3.71E+00	7.89E-12	1.76E-14	1.65E-13	7.79E-14	9.19E-13	1.19E-12	3.44E-11	1.07E-13	18.52	0.49	0.01682	0.02184	0.00028	0.00013
	1.62E-08	8.09E-12	7.28E-09	2.94E-11	7.10E-10	8.54E-13	2.48E+01	1.42E-11	2.75E-14	2.31E-13	6.83E-14	2.13E-13	1.19E-12	3.00E-11	9.47E-14	16.19	0.07	0.00058	0.00326	0.00006	0.00002
	9.94E-09	8.09E-12	4.54E-09	1.94E-11	4.52E-10	7.50E-13	1.58E+01	8.83E-12	1.91E-14	1.08E-13	7.43E-14	2.22E-13	1.19E-12	1.81E-11	5.89E-14	15.87	0.07	0.00095	0.00512	0.00004	0.00003
	8.22E-09	5.06E-12	3.01E-09	1.73E-11	3.00E-10	5.50E-13	1.05E+01	6.93E-12	1.80E-14	1.08E-13	8.82E-14	5.09E-13	1.19E-12	1.74E-11	5.55E-14	15.81	0.10	0.00329	0.00771	0.00006	0.00005
	7.48E-09	3.71E-12	2.18E-09	1.72E-11	2.14E-10	5.28E-13	7.49E+00	5.97E-12	1.58E-14	9.75E-14	9.01E-14	5.05E-13	1.19E-12	1.78E-11	5.61E-14	16.06	0.13	0.00458	0.01081	0.00008	0.00007
	8.40E-09	4.72E-12	2.15E-09	2.04E-11	2.09E-10	5.26E-13	7.29E+00	6.49E-12	1.62E-14	8.41E-14	8.55E-14	4.88E-13	1.19E-12	2.09E-11	6.65E-14	16.27	0.16	0.00454	0.01110	0.00007	0.00007
	1.01E-08	5.73E-12	1.89E-09	2.65E-11	1.78E-10	5.20E-13	6.23E+00	7.37E-12	1.68E-14	6.73E-14	7.85E-14	3.40E-13	1.19E-12	2.76E-11	8.67E-14	16.75	0.24	0.00370	0.01300	0.00007	0.00008
	1.20E-08	6.74E-12	1.57E-09	3.30E-11	1.42E-10	4.48E-13	4.96E+00	8.31E-12	1.95E-14	3.88E-14	8.19E-14	6.31E-13	1.19E-12	3.50E-11	1.08E-13	17.45	0.37	0.00864	0.01633	0.00005	0.00010
	2.50E-08	1.52E-11	2.24E-09	7.28E-11	1.98E-10	5.24E-13	6.93E+00	1.66E-11	3.27E-14	-1.06E-13	8.03E-14	1.12E-12	1.19E-12	7.63E-11	2.38E-13	17.86	0.58	0.01097	0.01169	-0.00010	-0.00007
	1.83E-08	1.11E-11	1.20E-09	5.42E-11	9.56E-11	5.41E-13	3.34E+00	1.19E-11	2.59E-14	6.04E-15	8.07E-14	1.08E-12	1.19E-12	5.71E-11	1.78E-13	19.84	0.90	0.02197	0.02422	0.00001	0.00015
	3.43E-08	1.79E-11	2.39E-09	1.00E-10	2.05E-10	4.94E-13	7.17E+00	2.23E-11	4.29E-14	-2.44E-13	9.02E-14	2.63E-12	1.19E-12	1.07E-10	3.31E-13	18.35	0.77	0.02486	0.01130	-0.00021	-0.00008
Conc (g/g)	**K**	**Cl**	**Ca**																		
	8.16E-02	4.97E-06	7.83E-04																		

SAMPLE	40Ar Total	Err.40Ar	40Ar*	Err.40Ar*	39Ar	Err.39Ar	%39Ar	38Ar	Err.38Ar	38ArCl	Err.38Cl	37Ar	Err.37Ar	36Ar	Err.36Ar	Age	1 s Err Age	Ca/K	Error Ca/K	Cl/K	Error Cl/K
UT15-5 bt	3.035E-08	2.797E-11	5.293E-09	7.466E-11	1.509E-09	1.788E-12	1.735E+01	4.976E-11	8.069E-14	1.715E-11	7.308E-14	4.621E-11	2.175E-13	8.394E-11	2.319E-13	6.12	0.09	0.05940	0.00029	0.00202	0.00001
J= 0.000969	4.717E-09	8.762E-13	3.916E-09	4.128E-12	1.427E-09	1.088E-12	1.640E+01	3.090E-11	5.073E-14	1.453E-11	5.686E-14	3.055E-11	2.053E-13	2.692E-12	1.351E-14	4.79	0.01	0.04153	0.00028	0.00181	0.00001
m= 0.01605 g	1.651E-09	5.729E-13	1.352E-09	2.830E-12	4.884E-10	6.000E-13	5.614E+00	1.080E-11	2.108E-14	5.186E-12	6.614E-14	9.757E-12	1.857E-13	1.003E-12	9.283E-15	4.83	0.01	0.03876	0.00074	0.00189	0.00002
	1.381E-09	5.392E-13	1.095E-09	2.887E-12	3.954E-10	5.395E-13	4.545E+00	8.783E-12	1.936E-14	4.207E-12	7.458E-14	7.248E-12	1.848E-13	9.613E-13	9.500E-15	4.83	0.01	0.03557	0.00091	0.00189	0.00003
	1.795E-09	5.392E-13	1.363E-09	3.011E-12	4.924E-10	6.015E-13	5.660E+00	1.093E-11	2.175E-14	5.180E-12	6.747E-14	8.872E-12	1.861E-13	1.447E-12	9.922E-15	4.83	0.01	0.03495	0.00073	0.00187	0.00002
	1.722E-09	5.055E-13	1.168E-09	3.142E-12	4.145E-10	5.458E-13	4.764E+00	9.347E-12	1.895E-14	4.390E-12	6.864E-14	7.656E-12	1.853E-13	1.856E-12	1.039E-14	4.92	0.01	0.03584	0.00087	0.00189	0.00003
	1.579E-09	5.055E-13	9.582E-10	3.367E-12	3.194E-10	5.479E-13	3.672E+00	7.331E-12	1.610E-14	3.388E-12	7.433E-14	6.625E-12	1.834E-13	2.081E-12	1.115E-14	5.24	0.02	0.04024	0.00112	0.00189	0.00004
	2.682E-09	7.077E-13	1.661E-09	4.283E-12	4.379E-10	4.976E-13	5.033E+00	1.049E-11	2.108E-14	4.975E-12	6.802E-14	1.922E-11	1.930E-13	3.425E-12	1.415E-14	6.62	0.02	0.08517	0.00086	0.00202	0.00003
	3.640E-09	1.011E-12	2.547E-09	4.673E-12	5.915E-10	6.394E-13	6.799E+00	1.473E-11	2.637E-14	7.458E-12	6.087E-14	2.938E-11	2.028E-13	3.669E-12	1.528E-14	7.51	0.02	0.09636	0.00067	0.00224	0.00002
	1.110E-08	2.191E-12	7.477E-09	1.137E-11	2.305E-09	1.711E-12	2.650E+01	5.250E-11	7.817E-14	2.458E-11	5.453E-14	4.833E-11	2.253E-13	1.214E-11	3.736E-14	5.66	0.01	0.04067	0.00019	0.00190	0.00000
	1.060E-08	2.426E-12	1.481E-09	2.527E-11	3.187E-10	5.168E-13	3.663E+00	1.300E-11	2.445E-14	3.675E-12	6.565E-14	7.665E-11	2.574E-13	3.057E-11	8.426E-14	8.11	0.14	0.46669	0.00174	0.00205	0.00004
Conc (g/g)	**K**	**Cl**	**Ca**																		
	8.00E-02	1.55E-04	5.18E-03																		
UT15-5 bt+ms	3.565E-08	6.740E-12	4.389E-09	8.645E-11	7.807E-10	7.533E-13	1.513E+01	4.028E-11	6.540E-14	1.185E-11	7.768E-14	5.441E-11	2.421E-13	1.047E-10	2.887E-13	9.79	0.19	0.13520	0.00062	0.00270	0.00002
J= 0.000968	4.669E-09	6.066E-13	2.147E-09	8.733E-12	7.619E-10	6.751E-13	1.476E+01	1.808E-11	3.253E-14	8.007E-12	6.141E-14	4.726E-11	2.222E-13	8.459E-12	2.918E-14	4.92	0.02	0.12033	0.00058	0.00187	0.00001
m= 0.01234 g	1.604E-09	1.314E-12	1.025E-09	4.098E-12	3.657E-10	4.734E-13	7.087E+00	8.320E-12	1.721E-14	3.884E-12	6.997E-14	2.367E-11	2.005E-13	1.944E-12	1.300E-14	4.89	0.02	0.12555	0.00108	0.00189	0.00003
	1.286E-09	1.078E-12	8.044E-10	3.442E-12	2.844E-10	5.089E-13	5.511E+00	6.460E-12	1.475E-14	2.991E-12	7.723E-14	1.703E-11	1.960E-13	1.619E-12	1.095E-14	4.93	0.02	0.11615	0.00135	0.00187	0.00005
	2.139E-09	6.066E-13	1.188E-09	4.130E-12	4.193E-10	5.497E-13	8.125E+00	9.674E-12	1.928E-14	4.410E-12	6.752E-14	2.151E-11	1.955E-13	3.190E-12	1.368E-14	4.94	0.02	0.09955	0.00091	0.00187	0.00003
	1.060E-09	7.414E-13	5.636E-10	3.366E-12	1.786E-10	5.192E-13	3.460E+00	4.176E-12	1.118E-14	1.876E-12	9.049E-14	8.798E-12	1.878E-13	1.663E-12	1.100E-14	5.50	0.04	0.09558	0.00206	0.00187	0.00009
	1.391E-09	6.066E-13	6.840E-10	3.605E-12	1.912E-10	4.887E-13	3.705E+00	4.625E-12	1.150E-14	2.051E-12	8.403E-14	1.036E-11	1.886E-13	2.370E-12	1.190E-14	6.24	0.04	0.10515	0.00193	0.00191	0.00008
	2.141E-09	5.055E-13	1.090E-09	4.502E-12	2.157E-10	4.933E-13	4.180E+00	5.679E-12	1.546E-14	2.612E-12	9.195E-14	2.119E-11	1.969E-13	3.527E-12	1.498E-14	8.80	0.04	0.19054	0.00182	0.00216	0.00008
	4.072E-09	9.436E-13	2.642E-09	5.471E-12	2.774E-10	4.760E-13	5.376E+00	9.083E-12	1.762E-14	5.083E-12	6.571E-14	5.638E-11	2.298E-13	4.806E-12	1.805E-14	16.56	0.04	0.39432	0.00174	0.00326	0.00004
	6.669E-09	1.415E-12	4.985E-09	6.611E-12	7.837E-10	7.791E-13	1.519E+01	2.095E-11	3.908E-14	1.115E-11	6.366E-14	8.983E-11	2.865E-13	5.664E-12	2.163E-14	11.07	0.02	0.22238	0.00074	0.00253	0.00001
	5.865E-09	1.786E-12	1.959E-09	1.199E-11	5.679E-10	6.339E-13	1.101E+01	1.509E-11	2.772E-14	6.307E-12	6.280E-14	2.720E-11	2.023E-13	1.309E-11	3.972E-14	6.01	0.04	0.09290	0.00070	0.00198	0.00002
	1.256E-08	3.134E-12	1.769E-09	3.061E-11	3.339E-10	5.224E-13	6.470E+00	1.439E-11	2.731E-14	3.849E-12	6.705E-14	7.890E-11	2.650E-13	3.615E-11	1.020E-13	9.23	0.16	0.45849	0.00170	0.00205	0.00004
Conc (g/g)	**K**	**Cl**	**Ca**																		
	6.18E-02	1.37E-04	1.06E-02																		
UT15-6 bt	2.912E-08	5.392E-12	4.805E-09	7.271E-11	1.066E-09	9.813E-13	1.401E+01	4.348E-11	7.590E-14	1.625E-11	7.543E-14	1.005E-10	3.116E-13	8.147E-11	2.428E-13	7.89	0.12	0.18286	0.00059	0.00271	0.00001
J= 0.000973	4.409E-09	1.449E-12	2.686E-09	6.882E-12	9.816E-10	9.340E-13	1.290E+01	2.420E-11	4.317E-14	1.219E-11	6.124E-14	8.694E-11	2.862E-13	5.795E-12	2.253E-14	4.80	0.01	0.17184	0.00059	0.00221	0.00001
m= 0.0162 g	1.980E-09	6.066E-13	1.393E-09	3.405E-12	5.155E-10	6.014E-13	6.774E+00	1.273E-11	2.499E-14	6.624E-12	6.655E-14	4.423E-11	2.147E-13	1.976E-12	1.122E-14	4.74	0.01	0.16648	0.00083	0.00229	0.00002
	1.455E-09	5.055E-13	9.863E-10	2.956E-12	3.636E-10	5.402E-13	4.778E+00	9.054E-12	1.855E-14	4.711E-12	6.936E-14	2.816E-11	2.006E-13	1.577E-12	9.753E-15	4.76	0.02	0.15024	0.00109	0.00231	0.00003
	1.508E-09	5.055E-13	9.979E-10	3.210E-12	3.676E-10	5.416E-13	4.830E+00	9.165E-12	1.893E-14	4.751E-12	6.992E-14	2.594E-11	1.951E-13	1.716E-12	1.062E-14	4.76	0.02	0.13692	0.00105	0.00230	0.00003
	1.560E-09	5.729E-13	9.720E-10	3.330E-12	3.581E-10	5.090E-13	4.706E+00	8.914E-12	1.789E-14	4.558E-12	6.792E-14	2.288E-11	1.925E-13	1.974E-12	1.099E-14	4.76	0.02	0.12394	0.00106	0.00227	0.00003
	1.518E-09	5.055E-13	9.008E-10	3.363E-12	3.256E-10	5.273E-13	4.279E+00	8.131E-12	1.709E-14	4.118E-12	7.112E-14	1.711E-11	1.869E-13	2.073E-12	1.114E-14	4.85	0.02	0.10193	0.00113	0.00225	0.00004
	2.122E-09	6.403E-13	1.246E-09	4.088E-12	4.356E-10	5.397E-13	5.724E+00	1.073E-11	2.009E-14	5.326E-12	6.350E-14	2.277E-11	1.925E-13	2.939E-12	1.352E-14	5.02	0.02	0.10143	0.00087	0.00218	0.00003
	3.309E-09	9.099E-13	2.063E-09	4.992E-12	6.458E-10	6.884E-13	8.487E+00	1.590E-11	2.969E-14	7.926E-12	6.353E-14	4.806E-11	2.177E-13	4.186E-12	1.644E-14	5.60	0.01	0.14437	0.00067	0.00218	0.00002
	6.021E-09	1.314E-12	4.250E-09	7.228E-12	1.451E-09	1.247E-12	1.906E+01	3.568E-11	5.962E-14	1.843E-11	5.836E-14	6.902E-11	2.544E-13	5.950E-12	2.381E-14	5.14	0.01	0.09230	0.00035	0.00226	0.00001
	4.423E-09	1.011E-12	2.526E-09	7.302E-12	8.379E-10	7.894E-13	1.101E+01	2.110E-11	3.545E-14	1.058E-11	5.756E-14	2.930E-11	1.997E-13	6.362E-12	2.422E-14	5.28	0.02	0.06784	0.00047	0.00225	0.00001
	7.925E-09	1.988E-12	1.430E-09	2.008E-11	2.617E-10	5.084E-13	3.439E+00	1.036E-11	2.147E-14	3.325E-12	7.125E-14	8.205E-11	2.692E-13	2.177E-11	6.693E-14	9.57	0.14	0.60843	0.00232	0.00226	0.00005
Conc (g/g)	**K**	**Cl**	**Ca**																		
	6.90E-02	1.60E-04	1.02E-02																		
UT15-6 bt+ms	2.102E-08	5.729E-12	3.171E-09	4.459E-11	8.093E-11	4.408E-13	7.485E+00	1.426E-11	2.509E-14	2.073E-12	6.575E-14	4.804E-11	2.332E-13	5.980E-11	1.481E-13	67.40	1.02	1.152	0.008	0.005	0.00015
J= 0.000971	1.067E-08	2.460E-12	4.141E-10	2.594E-11	1.211E-10	4.441E-13	1.120E+01	9.416E-12	1.759E-14	1.565E-12	6.524E-14	9.992E-11	2.883E-13	3.439E-11	8.648E-14	5.98	0.38	1.601	0.007	0.002	0.00010
m= 0.00886 g	1.117E-09	5.055E-13	2.123E-10	3.853E-12	6.795E-11	4.736E-13	6.285E+00	2.091E-12	7.135E-15	7.506E-13	1.152E-13	5.095E-11	2.360E-13	3.045E-12	1.279E-14	5.47	0.11	1.456	0.012	0.002	0.00030
	9.645E-10	5.055E-13	1.638E-10	3.502E-12	5.251E-11	4.729E-13	4.857E+00	1.660E-12	6.349E-15	5.619E-13	1.291E-13	3.221E-11	2.174E-13	2.690E-12	1.161E-14	5.46	0.13	1.191	0.013	0.002	0.00044
	9.441E-10	7.414E-13	1.597E-10	3.456E-12	4.647E-11	4.390E-13	4.298E+00	1.534E-12	6.304E-15	5.166E-13	1.386E-13	2.313E-11	2.117E-13	2.633E-12	1.130E-14	6.01	0.14	0.966	0.013	0.002	0.00053
	1.044E-09	4.045E-13	1.858E-10	3.703E-12	5.198E-11	4.392E-13	4.808E+00	1.674E-12	7.958E-15	5.490E-13	1.603E-13	1.983E-11	2.101E-13	2.879E-12	1.233E-14	6.25	0.14	0.740	0.010	0.002	0.00055
	1.375E-09	5.392E-13	3.028E-10	3.899E-12	6.987E-11	4.737E-13	6.463E+00	2.208E-12	8.472E-15	7.501E-13	1.294E-13	1.843E-11	2.102E-13	3.595E-12	1.293E-14	7.58	0.11	0.512	0.007	0.002	0.00033
	4.764E-09	1.517E-12	7.119E-10	1.128E-11	1.851E-10	4.519E-13	1.712E+01	6.486E-12	1.370E-14	1.862E-12	7.172E-14	3.254E-11	2.196E-13	1.358E-11	3.743E-14	6.73	0.11	0.341	0.002	0.002	0.00007
	1.670E-09	5.729E-13	2.894E-10	4.595E-12	5.546E-11	4.394E-13	5.129E+00	2.035E-12	7.428E-15	5.431E-13	1.231E-13	1.532E-11	2.078E-13	4.628E-12	1.527E-14	9.12	0.16	0.536	0.008	0.002	0.00040
	3.344E-09	1.011E-12	9.694E-10	7.197E-12	1.274E-10	4.447E-13	1.178E+01	4.251E-12	1.012E-14	1.323E-12	8.056E-14	4.887E-11	2.329E-13	7.965E-12	2.387E-14	13.29	0.11	0.745	0.004	0.002	0.00011
	9.047E-09	2.393E-12	6.341E-10	2.170E-11	1.233E-10	4.443E-13	1.141E+01	8.029E-12	1.627E-14	1.332E-12	6.985E-14	5.297E-11	2.392E-13	2.819E-11	7.225E-14	8.99	0.31	0.834	0.005	0.002	0.00010
	4.846E-09	1.314E-12	6.251E-10	1.171E-11	7.437E-11	4.404E-13	6.878E+00	4.241E-12	1.171E-14	7.395E-13	9.350E-14	3.596E-11	2.193E-13	1.415E-11	3.896E-14	14.67	0.29	0.938	0.008	0.002	0.00022

	5.955E-09	1.719E-12	7.590E-10	1.420E-11	1.927E-11	4.720E-13	1.783E+00	3.651E-12	1.010E-14	1.456E-13	9.385E-14	3.730E-11	2.243E-13	1.741E-11	4.721E-14	67.79	2.09	3.760	0.095	0.001	0.00087
	8.532E-09	2.191E-12	5.235E-10	2.055E-11	5.474E-12	4.381E-13	5.063E-01	5.107E-12	1.382E-14	-1.888E-14	9.224E-14	2.601E-11	2.168E-13	2.683E-11	6.842E-14	160.69	14.36	9.247	0.747	-0.001	-0.00300
Conc (g/g)	**K**	**Cl**	**Ca**																		
	1.80E-02	3.76E-05	1.75E-02																		
UT15-9 ms	1.225E-08	3.707E-12	6.082E-10	3.297E-11	5.488E-11	4.732E-13	1.986E+00	4.135E-11	6.457E-14	3.339E-11	5.681E-14	6.890E-12	1.321E-13	3.900E-11	1.097E-13	19.39	1.06	0.244	0.005	0.10829	0.00095
J= 0.000975	2.005E-08	5.055E-12	3.627E-10	5.478E-11	6.824E-11	4.405E-13	2.469E+00	1.476E-11	2.638E-14	1.566E-12	6.958E-14	1.171E-11	1.363E-13	6.594E-11	1.827E-13	9.33	1.41	0.333	0.004	0.00409	0.00018
m= 0.00721 g	2.862E-09	6.403E-13	4.164E-10	7.727E-12	9.686E-11	4.097E-13	3.505E+00	4.083E-12	1.078E-14	1.460E-12	8.921E-14	9.845E-12	1.347E-13	8.194E-12	2.579E-14	7.55	0.14	0.197	0.003	0.00268	0.00016
	9.638E-10	4.718E-13	3.502E-10	3.198E-12	8.461E-11	4.752E-13	3.062E+00	2.405E-12	9.154E-15	1.076E-12	1.284E-13	7.912E-12	1.334E-13	2.057E-12	1.059E-14	7.27	0.08	0.181	0.003	0.00226	0.00027
	8.136E-10	4.718E-13	2.761E-10	3.032E-12	7.542E-11	4.745E-13	2.729E+00	1.972E-12	7.374E-15	7.926E-13	1.262E-13	6.850E-12	1.324E-13	1.802E-12	1.003E-14	6.43	0.08	0.176	0.004	0.00187	0.00030
	7.570E-10	5.055E-13	2.628E-10	3.047E-12	7.703E-11	4.746E-13	2.787E+00	1.824E-12	7.000E-15	6.544E-13	1.295E-13	6.470E-12	1.323E-13	1.657E-12	1.006E-14	5.99	0.08	0.163	0.003	0.00151	0.00030
	1.014E-09	4.718E-13	4.390E-10	3.145E-12	1.378E-10	4.479E-13	4.985E+00	2.738E-12	9.011E-15	8.424E-13	1.110E-13	8.013E-12	1.327E-13	1.927E-12	1.041E-14	5.60	0.04	0.113	0.002	0.00109	0.00014
	1.561E-09	6.066E-13	8.737E-10	3.520E-12	3.082E-10	5.159E-13	1.115E+01	4.812E-12	1.249E-14	9.516E-13	8.774E-14	8.043E-12	1.338E-13	2.304E-12	1.161E-14	4.98	0.02	0.051	0.001	0.00055	0.00005
	4.876E-09	1.213E-12	2.043E-09	9.539E-12	7.864E-10	7.582E-13	2.846E+01	1.200E-11	2.212E-14	1.467E-12	6.305E-14	1.003E-11	1.352E-13	9.493E-12	3.169E-14	4.56	0.02	0.025	0.000	0.00033	0.00001
	1.396E-09	5.392E-13	4.771E-10	4.072E-12	1.703E-10	4.856E-13	6.161E+00	2.925E-12	9.118E-15	4.519E-13	1.052E-13	3.382E-12	1.307E-13	3.080E-12	1.352E-14	4.92	0.04	0.039	0.001	0.00047	0.00011
	1.835E-09	6.403E-13	6.927E-10	4.545E-12	2.200E-10	4.627E-13	7.960E+00	4.192E-12	1.085E-14	1.025E-12	8.747E-14	6.802E-12	1.331E-13	3.828E-12	1.507E-14	5.53	0.04	0.060	0.001	0.00083	0.00007
	3.155E-09	9.099E-13	1.269E-09	6.390E-12	2.864E-10	4.791E-13	1.036E+01	6.828E-12	1.494E-14	2.453E-12	7.406E-14	8.357E-12	1.335E-13	6.319E-12	2.118E-14	7.78	0.04	0.057	0.001	0.00152	0.00005
	4.214E-09	1.213E-12	1.156E-09	9.513E-12	2.015E-10	4.268E-13	7.290E+00	5.416E-12	1.237E-14	1.244E-12	7.733E-14	1.185E-11	1.358E-13	1.024E-11	3.160E-14	10.07	0.09	0.114	0.001	0.00110	0.00007
	1.597E-08	4.718E-12	1.633E-09	4.058E-11	1.916E-10	4.247E-13	6.933E+00	1.222E-11	2.361E-14	1.035E-12	7.007E-14	2.570E-11	1.470E-13	4.802E-11	1.350E-13	14.94	0.37	0.260	0.002	0.00096	0.00007
	1.030E-08	2.426E-12	9.166E-11	2.892E-11	4.462E-12	4.380E-13	1.615E-01	6.557E-12	1.443E-14	5.895E-14	7.655E-14	4.339E-12	1.313E-13	3.420E-11	9.651E-14	35.80	11.83	1.888	0.194	0.00235	0.00306
Conc (g/g)	**K**	**Cl**	**Ca**																		
	5.62E-02	1.75E-04	5.37E-03																		
UT15-9 ms+chl	2.419E-08	6.403E-12	9.609E-10	6.349E-11	4.941E-11	4.059E-13	3.310E+00	3.750E-11	5.660E-14	2.227E-11	6.482E-14	5.333E-12	8.628E-14	7.781E-11	2.116E-13	34.06	2.27	0.209	0.004	0.08024	0.00070
J= 0.000980	5.095E-09	1.011E-12	3.499E-10	1.389E-11	5.574E-11	4.735E-13	3.734E+00	4.705E-12	1.179E-14	1.088E-12	8.509E-14	5.338E-12	8.652E-14	1.589E-11	4.640E-14	11.07	0.45	0.186	0.003	0.00347	0.00027
m= 0.00472 g	1.056E-09	5.055E-13	2.705E-10	3.637E-12	5.406E-11	4.398E-13	3.621E+00	1.832E-12	7.634E-15	7.343E-13	1.405E-13	4.745E-12	8.638E-14	2.631E-12	1.206E-14	8.83	0.14	0.170	0.003	0.00242	0.00046
	8.325E-10	4.718E-13	1.791E-10	3.515E-12	3.920E-11	4.391E-13	2.626E+00	1.261E-12	6.479E-15	4.120E-13	1.732E-13	3.148E-12	8.525E-14	2.189E-12	1.167E-14	8.06	0.18	0.156	0.005	0.00187	0.00079
	9.003E-10	4.382E-13	2.271E-10	3.398E-12	4.614E-11	4.730E-13	3.091E+00	1.294E-12	6.188E-15	3.552E-13	1.613E-13	2.902E-12	8.541E-14	2.256E-12	1.129E-14	8.68	0.16	0.122	0.004	0.00137	0.00062
	1.221E-09	5.055E-13	4.411E-10	3.697E-12	1.341E-10	4.473E-13	8.985E+00	2.548E-12	8.292E-15	5.635E-13	1.098E-13	3.993E-12	8.578E-14	2.614E-12	1.227E-14	5.80	0.05	0.058	0.001	0.00075	0.00015
	1.786E-09	1.078E-12	7.949E-10	4.623E-12	2.544E-10	5.013E-13	1.704E+01	4.080E-12	1.046E-14	6.266E-13	8.662E-14	4.150E-12	8.581E-14	3.321E-12	1.506E-14	5.52	0.03	0.032	0.001	0.00044	0.00006
	1.799E-09	6.066E-13	6.047E-10	4.602E-12	2.216E-10	4.944E-13	1.484E+01	3.659E-12	9.875E-15	4.422E-13	9.118E-14	2.609E-12	8.579E-14	4.001E-12	1.528E-14	4.82	0.04	0.023	0.001	0.00036	0.00007
	2.666E-09	7.751E-13	7.020E-10	6.463E-12	2.264E-10	4.954E-13	1.516E+01	4.336E-12	1.093E-14	5.797E-13	8.527E-14	3.193E-12	8.545E-14	6.578E-12	2.149E-14	5.47	0.05	0.027	0.001	0.00046	0.00007
	2.385E-09	7.414E-13	5.162E-10	6.374E-12	1.380E-10	4.808E-13	9.242E+00	3.407E-12	9.411E-15	6.933E-13	9.334E-14	2.417E-12	8.516E-14	6.261E-12	2.120E-14	6.60	0.08	0.034	0.001	0.00089	0.00012
	4.392E-09	1.213E-12	8.459E-10	1.094E-11	1.424E-10	4.814E-13	9.542E+00	4.848E-12	1.160E-14	1.024E-12	8.111E-14	5.037E-12	8.695E-14	1.188E-11	3.643E-14	10.47	0.14	0.069	0.001	0.00128	0.00010
	4.507E-09	1.180E-12	6.121E-10	1.175E-11	6.931E-11	5.078E-13	4.643E+00	3.593E-12	1.076E-14	3.624E-13	1.014E-13	3.863E-12	8.597E-14	1.305E-11	3.915E-14	15.55	0.32	0.108	0.003	0.00093	0.00026
	6.785E-09	1.854E-12	7.996E-10	1.719E-11	5.382E-11	4.734E-13	3.605E+00	4.647E-12	1.145E-14	2.666E-13	8.393E-14	6.433E-12	8.681E-14	2.005E-11	5.725E-14	26.08	0.61	0.232	0.004	0.00088	0.00028
	2.007E-08	5.729E-12	6.516E-10	5.336E-11	8.249E-12	4.384E-13	5.525E-01	1.240E-11	2.232E-14	4.270E-14	6.948E-14	4.761E-12	8.689E-14	6.504E-11	1.777E-13	134.58	13.14	1.120	0.063	0.00092	0.00150
Conc (g/g)	**K**	**Cl**	**Ca**																		
	4.61E-02	1.62E-04	3.47E-03																		
UT15-9 chl	3.341E-08	7.751E-12	2.866E-09	8.243E-11	3.502E-10	4.957E-13	8.659E+00	5.006E-11	7.442E-14	2.688E-11	7.232E-14	1.536E-11	1.902E-13	1.023E-10	2.749E-13	14.38	0.41	0.085	0.001	0.01366	0.00004
J= 0.000978	5.682E-09	8.088E-13	4.535E-09	4.454E-12	5.584E-10	5.732E-13	1.381E+01	2.272E-11	3.679E-14	1.579E-11	5.506E-14	1.075E-11	1.865E-13	3.847E-12	1.467E-14	14.27	0.02	0.037	0.001	0.00503	0.00002
m= 0.01238 g	1.502E-09	7.751E-13	1.165E-09	2.775E-12	1.491E-10	4.820E-13	3.685E+00	5.784E-12	1.370E-14	3.914E-12	8.003E-14	3.617E-12	1.827E-13	1.131E-12	8.926E-15	13.73	0.06	0.047	0.002	0.00467	0.00010
	1.201E-09	4.718E-13	8.564E-10	2.651E-12	1.176E-10	3.788E-13	2.907E+00	4.638E-12	1.291E-14	3.112E-12	9.395E-14	3.437E-12	1.828E-13	1.156E-12	8.736E-15	12.81	0.06	0.057	0.003	0.00471	0.00014
	1.173E-09	4.718E-13	8.093E-10	2.795E-12	1.331E-10	4.469E-13	3.290E+00	5.421E-12	1.344E-14	3.712E-12	8.371E-14	4.611E-12	1.836E-13	1.218E-12	9.228E-15	10.70	0.05	0.067	0.003	0.00497	0.00011
	1.567E-09	5.055E-13	1.085E-09	3.058E-12	2.284E-10	5.276E-13	5.648E+00	6.541E-12	1.342E-14	3.697E-12	6.945E-14	5.867E-12	1.841E-13	1.615E-12	1.010E-14	8.36	0.03	0.050	0.002	0.00288	0.00005
	2.231E-09	7.751E-13	1.597E-09	3.506E-12	3.073E-10	5.138E-13	7.598E+00	8.025E-12	1.583E-14	4.209E-12	6.677E-14	4.938E-12	1.831E-13	2.125E-12	1.145E-14	9.15	0.03	0.031	0.001	0.00244	0.00004
	2.299E-09	6.740E-13	1.535E-09	3.664E-12	2.836E-10	4.459E-13	7.011E+00	7.637E-12	1.694E-14	4.003E-12	7.498E-14	3.945E-12	1.831E-13	2.561E-12	1.206E-14	9.52	0.03	0.027	0.001	0.00251	0.00005
	3.408E-09	8.762E-13	2.191E-09	4.855E-12	3.583E-10	5.281E-13	8.859E+00	1.165E-11	2.352E-14	6.894E-12	6.840E-14	5.809E-12	1.837E-13	4.080E-12	1.599E-14	10.76	0.03	0.031	0.001	0.00342	0.00003
	9.225E-09	2.089E-12	7.053E-09	7.929E-12	8.302E-10	7.698E-13	2.052E+01	3.265E-11	5.135E-14	2.206E-11	5.398E-14	6.083E-12	1.841E-13	7.275E-12	2.562E-14	14.93	0.02	0.014	0.000	0.00473	0.00001
	7.331E-09	1.820E-12	4.996E-09	7.872E-12	5.515E-10	5.703E-13	1.363E+01	2.146E-11	3.454E-14	1.385E-11	5.488E-14	9.527E-12	1.852E-13	7.824E-12	2.565E-14	15.91	0.03	0.034	0.001	0.00447	0.00002
	6.240E-09	1.584E-12	1.820E-09	1.320E-11	1.770E-10	4.862E-13	4.377E+00	8.883E-12	1.742E-14	4.121E-12	6.683E-14	1.686E-11	1.914E-13	1.481E-11	4.391E-14	18.05	0.14	0.185	0.002	0.00414	0.00007
Conc (g/g)	**K**	**Cl**	**Ca**																		
	4.78E-02	2.36E-04	2.08E-03																		
UT15-10 ms2	3.380E-08	8.762E-12	1.501E-08	8.087E-11	1.574E-10	4.677E-13	2.055E+00	1.860E-11	4.577E-14	4.987E-12	9.737E-14	2.940E-12	9.523E-14	6.294E-11	2.693E-13	162.35	1.00	0.0362	0.0012	0.00564	0.00011
J= 0.000987	2.242E-08	6.066E-12	1.126E-09	9.112E-11	2.122E-10	5.520E-13	2.772E+00	1.724E-11	4.168E-14	1.437E-12	9.987E-14	3.725E-12	9.569E-14	7.132E-11	3.045E-13	9.42	0.76	0.0341	0.0009	0.00121	0.00008

m= 0.03252 g	4.633E-09	1.011E-12	1.411E-09	1.455E-11	3.214E-10	5.806E-13	4.198E+00	6.450E-12	1.832E-14	8.443E-13	9.642E-14	1.837E-12	9.477E-14	1.079E-11	4.863E-14	7.80	0.08	0.0111	0.0006	0.00047	0.00005
	3.052E-09	9.099E-13	1.207E-09	8.690E-12	2.787E-10	6.134E-13	3.640E+00	4.661E-12	1.454E-14	3.998E-13	1.055E-13	1.038E-12	9.427E-14	6.178E-12	2.895E-14	7.70	0.06	0.0072	0.0007	0.00026	0.00007
	3.101E-09	9.099E-13	1.088E-09	9.556E-12	2.621E-10	6.352E-13	3.424E+00	4.486E-12	1.372E-14	3.019E-13	1.035E-13	7.975E-13	9.411E-14	6.743E-12	3.186E-14	7.37	0.07	0.0059	0.0007	0.00021	0.00007
	3.070E-09	9.099E-13	1.104E-09	9.379E-12	2.555E-10	6.020E-13	3.337E+00	4.315E-12	1.405E-14	2.342E-13	1.101E-13	6.549E-13	9.407E-14	6.586E-12	3.127E-14	7.68	0.07	0.0050	0.0007	0.00016	0.00008
	6.083E-09	1.786E-12	3.085E-09	1.363E-11	6.244E-10	8.519E-13	8.157E+00	9.366E-12	2.460E-14	5.342E-13	8.950E-14	7.850E-13	9.404E-14	1.004E-11	4.527E-14	8.78	0.04	0.0024	0.0003	0.00015	0.00003
	8.511E-09	2.258E-12	5.287E-09	1.494E-11	1.150E-09	1.358E-12	1.502E+01	1.537E-11	3.804E-14	5.577E-13	8.545E-14	9.523E-13	9.438E-14	1.080E-11	4.947E-14	8.17	0.03	0.0016	0.0002	0.00009	0.00001
	7.796E-09	4.044E-12	4.623E-09	1.492E-11	1.029E-09	1.316E-12	1.344E+01	1.378E-11	3.499E-14	3.417E-13	8.744E-14	8.169E-13	9.440E-14	1.063E-11	4.811E-14	7.98	0.03	0.0015	0.0002	0.00006	0.00002
	6.335E-09	1.820E-12	3.640E-09	1.250E-11	7.583E-10	9.850E-13	9.905E+00	1.044E-11	2.810E-14	3.160E-13	9.174E-14	1.768E-12	9.494E-14	9.027E-12	4.141E-14	8.53	0.03	0.0045	0.0002	0.00007	0.00002
	7.652E-09	2.393E-12	2.741E-09	2.170E-11	4.959E-10	7.758E-13	6.478E+00	9.200E-12	2.363E-14	5.873E-13	8.811E-14	7.275E-12	9.861E-14	1.645E-11	7.224E-14	9.82	0.08	0.0285	0.0004	0.00021	0.00003
	6.661E-09	1.921E-12	2.090E-09	2.021E-11	3.973E-10	7.094E-13	5.189E+00	7.637E-12	2.026E-14	3.357E-13	9.070E-14	3.581E-12	9.584E-14	1.531E-11	6.739E-14	9.34	0.09	0.0175	0.0005	0.00015	0.00004
	2.688E-08	5.729E-12	8.535E-09	7.898E-11	1.607E-09	1.841E-12	2.099E+01	3.003E-11	7.001E-14	5.876E-13	9.547E-14	8.134E-12	1.010E-13	6.145E-11	2.639E-13	9.43	0.09	0.0098	0.0001	0.00007	0.00001
	2.413E-08	6.740E-12	2.393E-09	9.336E-11	1.067E-10	4.514E-13	1.393E+00	1.496E-11	3.649E-14	4.964E-14	1.012E-13	3.383E-12	9.577E-14	7.280E-11	3.119E-13	39.51	1.55	0.0615	0.0018	0.00008	0.00017
Conc (g/g)	**K**	**Cl**	**Ca**																		
	3.41E-02	9.13E-06	3.26E-04																		
UT15-10 ms3	9.460E-09	6.066E-12	7.434E-10	3.422E-11	1.008E-10	4.817E-13	2.185E+00	2.206E-11	4.698E-14	1.543E-11	7.508E-14	2.359E-11	1.220E-13	2.920E-11	1.128E-13	13.12	0.61	0.454	0.003	0.02724	0.00019
J= 0.000990	2.097E-08	5.729E-12	7.251E-10	7.734E-11	1.464E-10	5.243E-13	3.173E+00	1.534E-11	3.432E-14	9.164E-13	8.999E-14	1.694E-11	1.089E-13	6.783E-11	2.583E-13	8.83	0.94	0.225	0.002	0.00111	0.00011
m= 0.00916 g	5.487E-09	1.348E-12	9.303E-10	1.805E-11	2.135E-10	5.130E-13	4.626E+00	5.947E-12	1.617E-14	6.960E-13	9.252E-14	3.512E-12	9.589E-14	1.526E-11	6.029E-14	7.77	0.15	0.032	0.001	0.00058	0.00008
	2.202E-09	6.740E-13	7.239E-10	6.707E-12	1.760E-10	5.323E-13	3.814E+00	3.176E-12	1.115E-14	2.864E-13	1.186E-13	1.587E-12	9.457E-14	4.953E-12	2.235E-14	7.33	0.07	0.017	0.001	0.00029	0.00012
	1.952E-09	6.403E-13	5.867E-10	6.416E-12	1.483E-10	4.924E-13	3.215E+00	2.681E-12	1.004E-14	1.701E-13	1.264E-13	1.116E-12	9.429E-14	4.573E-12	2.138E-14	7.05	0.08	0.015	0.001	0.00020	0.00015
	2.066E-09	8.088E-13	6.685E-10	6.416E-12	1.590E-10	4.632E-13	3.445E+00	2.792E-12	9.830E-15	1.425E-13	1.189E-13	1.040E-12	9.432E-14	4.681E-12	2.132E-14	7.50	0.08	0.013	0.001	0.00016	0.00013
	8.640E-09	2.494E-12	3.008E-09	2.236E-11	7.208E-10	8.651E-13	1.562E+01	1.217E-11	2.854E-14	6.007E-13	8.094E-14	2.608E-12	9.507E-14	1.886E-11	7.443E-14	7.44	0.06	0.007	0.000	0.00015	0.00002
	2.723E-09	8.425E-13	1.145E-09	6.986E-12	2.678E-10	5.649E-13	5.803E+00	4.197E-12	1.200E-14	2.248E-13	9.668E-14	8.896E-13	9.435E-14	5.287E-12	2.323E-14	7.62	0.05	0.006	0.001	0.00015	0.00006
	3.550E-09	1.112E-12	1.589E-09	8.609E-12	3.769E-10	5.899E-13	8.167E+00	5.680E-12	1.554E-14	2.536E-13	9.265E-14	1.223E-12	9.431E-14	6.569E-12	2.859E-14	7.51	0.04	0.006	0.000	0.00012	0.00004
	5.381E-09	1.449E-12	2.054E-09	1.340E-11	4.697E-10	6.458E-13	1.018E+01	7.685E-12	1.833E-14	3.637E-13	8.117E-14	3.064E-12	9.536E-14	1.115E-11	4.462E-14	7.79	0.05	0.013	0.000	0.00014	0.00003
	9.774E-09	2.865E-12	2.048E-09	2.996E-11	4.710E-10	6.717E-13	1.021E+01	1.050E-11	2.394E-14	3.814E-13	7.955E-14	5.950E-12	9.729E-14	2.588E-11	9.987E-14	7.75	0.11	0.025	0.000	0.00014	0.00003
	4.560E-09	1.348E-12	1.140E-09	1.387E-11	2.693E-10	5.655E-13	5.836E+00	5.318E-12	1.452E-14	1.651E-13	9.270E-14	3.340E-12	9.543E-14	1.146E-11	4.623E-14	7.55	0.09	0.024	0.001	0.00011	0.00006
	1.474E-08	3.707E-12	4.370E-09	4.044E-11	1.016E-09	1.112E-12	2.201E+01	1.817E-11	4.072E-14	3.341E-13	8.074E-14	1.370E-11	1.066E-13	3.474E-11	1.349E-13	7.67	0.07	0.026	0.000	0.00006	0.00001
	1.653E-08	4.381E-12	4.531E-10	6.139E-11	7.910E-11	5.114E-13	1.714E+00	1.094E-11	2.625E-14	-9.170E-14	8.981E-14	2.119E-12	9.497E-14	5.386E-11	2.051E-13	10.20	1.38	0.052	0.002	-0.00021	-0.00020
Conc (g/g)	**K**	**Cl**	**Ca**																		
	7.28E-02	5.58E-05	2.47E-03																		
UT15-10 ms+chl	4.794E-09	1.180E-12	4.424E-10	1.502E-11	2.602E-11	4.718E-13	2.269E+00	4.910E-12	1.255E-14	1.871E-12	8.683E-14	2.437E-12	1.202E-13	1.458E-11	5.016E-14	29.96	1.15	0.182	0.010	0.012802	0.000638
J= 0.000985	1.806E-08	4.718E-12	5.406E-10	5.654E-11	3.945E-11	5.060E-13	3.441E+00	1.232E-11	2.383E-14	8.205E-13	7.449E-14	2.287E-12	1.204E-13	5.868E-11	1.887E-13	24.18	2.55	0.112	0.006	0.003702	0.000339
m= 0.00287 g	3.311E-09	6.740E-13	3.992E-10	1.019E-11	4.858E-11	4.394E-13	4.237E+00	2.887E-12	9.339E-15	5.083E-13	1.093E-13	1.124E-12	1.197E-13	9.753E-12	3.405E-14	14.54	0.39	0.045	0.005	0.001862	0.000401
	9.093E-10	5.729E-13	2.360E-10	3.580E-12	3.706E-11	4.051E-13	3.232E+00	1.027E-12	6.103E-15	1.903E-13	2.003E-13	3.084E-13	1.193E-13	2.255E-12	1.184E-14	11.28	0.21	0.016	0.006	0.000914	0.000962
	7.711E-10	4.718E-13	2.013E-10	3.256E-12	3.121E-11	4.384E-13	2.722E+00	8.602E-13	5.462E-15	1.536E-13	2.141E-13	2.697E-13	1.194E-13	1.909E-12	1.079E-14	11.43	0.24	0.017	0.007	0.000876	0.001221
	7.967E-10	5.055E-13	1.968E-10	3.437E-12	3.453E-11	4.722E-13	3.011E+00	8.858E-13	5.755E-15	1.233E-13	2.190E-13	2.432E-13	1.194E-13	2.009E-12	1.139E-14	10.10	0.22	0.014	0.007	0.000636	0.001129
	1.019E-09	5.055E-13	2.800E-10	3.822E-12	5.900E-11	4.067E-13	5.146E+00	1.259E-12	6.210E-15	1.360E-13	1.664E-13	2.852E-13	1.194E-13	2.477E-12	1.269E-14	8.41	0.13	0.009	0.004	0.000410	0.000502
	1.546E-09	5.392E-13	6.279E-10	4.377E-12	1.391E-10	4.513E-13	1.213E+01	2.337E-12	8.047E-15	2.119E-13	1.162E-13	3.151E-13	1.193E-13	3.074E-12	1.455E-14	8.00	0.06	0.004	0.002	0.000271	0.000149
	1.773E-09	5.729E-13	7.344E-10	4.525E-12	1.661E-10	4.569E-13	1.448E+01	2.738E-12	9.227E-15	2.367E-13	1.137E-13	3.437E-13	1.194E-13	3.480E-12	1.504E-14	7.84	0.05	0.004	0.001	0.000254	0.000122
	2.039E-09	7.077E-13	7.169E-10	5.382E-12	1.587E-10	4.877E-13	1.384E+01	2.820E-12	8.994E-15	2.213E-13	1.077E-13	5.567E-13	1.194E-13	4.429E-12	1.787E-14	8.01	0.06	0.007	0.001	0.000248	0.000121
	5.085E-09	1.247E-12	5.992E-10	1.515E-11	1.220E-10	4.482E-13	1.064E+01	4.538E-12	1.164E-14	3.493E-13	8.713E-14	1.588E-12	1.200E-13	1.503E-11	5.057E-14	8.71	0.22	0.025	0.002	0.000510	0.000127
	2.199E-09	6.740E-13	2.458E-10	7.260E-12	4.915E-11	4.394E-13	4.286E+00	1.863E-12	7.140E-15	8.320E-14	1.294E-13	7.097E-13	1.195E-13	6.541E-12	2.421E-14	8.87	0.27	0.028	0.005	0.000301	0.000469
	3.066E-09	7.751E-13	3.858E-10	9.499E-12	9.383E-11	4.439E-13	8.183E+00	2.775E-12	8.669E-15	4.011E-14	1.056E-13	7.918E-13	1.196E-13	8.977E-12	3.171E-14	7.29	0.18	0.016	0.002	0.000076	0.000200
	1.511E-08	4.381E-12	5.576E-10	4.701E-11	1.374E-10	4.837E-13	1.198E+01	1.078E-11	2.189E-14	5.657E-14	7.476E-14	1.849E-12	1.200E-13	4.876E-11	1.568E-13	7.20	0.61	0.026	0.002	0.000073	0.000097
	7.197E-09	1.955E-12	5.532E-11	2.345E-11	4.569E-12	4.041E-13	3.985E-01	4.523E-12	1.163E-14	-3.868E-14	8.800E-14	5.848E-13	1.194E-13	2.392E-11	7.826E-14	21.39	9.26	0.248	0.055	-0.001507	-0.003431
Conc (g/g)	**K**	**Cl**	**Ca**																		
	5.80E-02	4.47E-05	1.34E-03																		
UT15-41 ms	1.770E-08	1.078E-11	3.961E-09	3.528E-11	7.304E-11	4.394E-13	1.059E+00	1.167E-11	1.985E-14	2.180E-12	6.133E-14	1.889E-12	9.126E-14	4.602E-11	1.125E-13	92.03	0.99	0.050	0.002	0.00531	0.00015
J= 0.000965	1.588E-08	4.381E-12	5.319E-10	3.746E-11	4.675E-11	4.046E-13	6.778E-01	1.051E-11	1.983E-14	2.926E-13	6.798E-14	3.357E-12	9.173E-14	5.142E-11	1.246E-13	19.70	1.40	0.139	0.004	0.00111	0.00026
m= 0.01154 g	3.395E-09	7.414E-13	6.505E-10	8.016E-12	6.940E-11	4.058E-13	1.006E+00	2.569E-12	8.486E-15	6.424E-14	1.115E-13	1.200E-12	9.094E-14	9.194E-12	2.673E-14	16.25	0.22	0.034	0.003	0.00016	0.00029
	2.413E-09	7.414E-13	6.486E-10	5.585E-12	5.782E-11	4.722E-13	8.383E-01	1.778E-12	7.513E-15	2.079E-14	1.426E-13	5.756E-13	9.069E-14	5.910E-12	1.854E-14	19.42	0.23	0.019	0.003	0.00006	0.00044
	2.589E-09	7.077E-13	8.452E-10	5.680E-12	5.695E-11	4.721E-13	8.256E-01	1.759E-12	7.170E-15	2.481E-14	1.375E-13	4.501E-13	9.066E-14	5.840E-12	1.888E-14	25.66	0.27	0.015	0.003	0.00008	0.00043
	3.569E-09	1.112E-12	1.511E-09	6.485E-12	1.139E-10	4.424E-13	1.652E+00	2.611E-12	7.840E-15	4.590E-14	1.014E-13	4.853E-13	9.070E-14	6.891E-12	2.140E-14	22.95	0.13	0.008	0.002	0.00007	0.00016
	8.043E-09	2.359E-12	5.489E-09	7.858E-12	5.086E-10	5.293E-13	7.374E+00	7.472E-12	1.491E-14	2.079E-13	6.768E-14	5.221E-13	9.072E-14	8.557E-12	2.511E-14	18.69	0.03	0.002	0.000	0.00007	0.00002

	2.078E-08	4.381E-12	1.752E-08	9.836E-12	1.672E-09	1.170E-12	2.424E+01	2.105E-11	3.485E-14	4.203E-13	5.772E-14	6.114E-13	9.094E-14	1.089E-11	2.950E-14	18.15	0.02	0.001	0.000	0.00004	0.00001
	1.641E-08	4.381E-12	1.389E-08	8.864E-12	1.323E-09	1.027E-12	1.918E+01	1.646E-11	2.826E-14	1.671E-13	5.931E-14	6.170E-13	9.076E-14	8.453E-12	2.581E-14	18.19	0.02	0.001	0.000	0.00002	0.00001
	1.208E-08	2.696E-12	9.255E-09	8.699E-12	8.745E-10	7.681E-13	1.268E+01	1.156E-11	2.062E-14	5.413E-14	6.103E-14	9.093E-13	9.101E-14	9.480E-12	2.770E-14	18.33	0.02	0.002	0.000	0.00001	0.00001
	9.925E-09	2.662E-12	6.605E-09	9.652E-12	6.136E-10	6.756E-13	8.896E+00	9.179E-12	1.891E-14	2.639E-13	7.011E-14	1.379E-12	9.108E-14	1.112E-11	3.107E-14	18.64	0.03	0.004	0.000	0.00008	0.00002
	1.113E-08	3.168E-12	6.813E-09	1.194E-11	6.019E-10	6.158E-13	8.727E+00	9.707E-12	1.834E-14	2.938E-13	6.448E-14	2.309E-12	9.129E-14	1.445E-11	3.855E-14	19.60	0.04	0.007	0.000	0.00009	0.00002
	2.199E-08	4.381E-12	9.010E-09	3.221E-11	7.873E-10	7.614E-13	1.141E+01	1.713E-11	3.055E-14	1.879E-13	6.401E-14	7.278E-12	9.462E-14	4.346E-11	1.069E-13	19.82	0.07	0.018	0.000	0.00004	0.00001
	2.824E-08	8.425E-12	1.303E-09	6.510E-11	9.865E-11	5.413E-13	1.430E+00	1.811E-11	2.828E-14	-3.773E-15	6.688E-14	4.005E-12	9.200E-14	9.023E-11	2.162E-13	22.85	1.15	0.079	0.002	-0.00001	-0.00012
Conc (g/g)	**K**	**Cl**	**Ca**																		
	8.86E-02	9.65E-06	6.37E-04																		
UT15-51 bt	8.487E-08	1.483E-11	2.081E-08	1.896E-10	1.964E-09	1.573E-12	2.356E+01	7.029E-11	1.118E-13	8.003E-12	1.321E-13	2.834E-11	1.990E-13	2.146E-10	6.331E-13	18.31	0.17	0.0280	0.0002	0.00073	0.00001
J= 0.000963	1.908E-08	2.898E-12	1.793E-08	5.876E-12	1.638E-09	1.317E-12	1.966E+01	2.372E-11	4.087E-14	4.793E-12	6.018E-14	2.561E-12	1.791E-13	3.839E-12	1.712E-14	18.92	0.02	0.0030	0.0002	0.00052	0.00001
m= 0.01576 g	5.246E-09	8.425E-13	4.626E-09	3.639E-12	4.215E-10	5.904E-13	5.057E+00	6.379E-12	1.322E-14	1.304E-12	7.023E-14	1.409E-12	1.787E-13	2.077E-12	1.186E-14	18.97	0.03	0.0065	0.0008	0.00055	0.00003
	2.128E-09	6.066E-13	1.638E-09	3.064E-12	1.496E-10	4.840E-13	1.794E+00	2.439E-12	8.787E-15	4.671E-13	1.216E-13	1.080E-12	1.783E-13	1.643E-12	1.006E-14	18.92	0.07	0.0140	0.0023	0.00056	0.00014
	2.357E-09	1.281E-12	1.611E-09	3.761E-12	1.509E-10	4.515E-13	1.811E+00	2.578E-12	9.842E-15	4.303E-13	1.288E-13	1.505E-12	1.783E-13	2.496E-12	1.184E-14	18.45	0.07	0.0193	0.0023	0.00051	0.00015
	2.174E-09	5.729E-13	1.322E-09	3.900E-12	1.256E-10	4.474E-13	1.506E+00	2.269E-12	8.370E-15	3.352E-13	1.245E-13	1.552E-12	1.784E-13	2.854E-12	1.292E-14	18.19	0.08	0.0240	0.0028	0.00048	0.00018
	3.317E-09	7.751E-13	2.111E-09	4.700E-12	2.025E-10	4.620E-13	2.430E+00	3.539E-12	9.836E-15	5.262E-13	9.388E-14	1.793E-12	1.785E-13	4.039E-12	1.553E-14	18.02	0.06	0.0172	0.0017	0.00046	0.00008
	9.971E-09	1.854E-12	8.189E-09	6.835E-12	7.629E-10	7.716E-13	9.152E+00	1.164E-11	2.332E-14	2.037E-12	6.825E-14	2.692E-12	1.794E-13	5.967E-12	2.204E-14	18.55	0.02	0.0068	0.0005	0.00048	0.00002
	2.152E-08	4.381E-12	1.941E-08	8.926E-12	1.781E-09	1.454E-12	2.136E+01	2.610E-11	4.521E-14	4.976E-12	6.103E-14	3.509E-12	1.806E-13	7.079E-12	2.605E-14	18.83	0.02	0.0038	0.0002	0.00050	0.00001
	1.141E-08	2.191E-12	9.080E-09	8.508E-12	8.275E-10	8.057E-13	9.927E+00	1.287E-11	2.726E-14	2.201E-12	7.219E-14	1.001E-11	1.839E-13	7.807E-12	2.754E-14	18.96	0.03	0.0235	0.0004	0.00047	0.00002
	5.402E-09	1.281E-12	2.596E-09	9.381E-12	2.382E-10	4.396E-13	2.858E+00	5.048E-12	1.196E-14	6.132E-13	8.021E-14	5.977E-11	2.400E-13	9.414E-12	3.112E-14	18.84	0.08	0.4869	0.0022	0.00046	0.00006
	7.967E-09	1.820E-12	8.287E-10	2.188E-11	7.352E-11	4.413E-13	8.819E-01	5.481E-12	1.349E-14	1.429E-13	8.427E-14	5.090E-11	2.261E-13	2.392E-11	7.305E-14	19.49	0.53	1.3438	0.0100	0.00035	0.00020
Conc (g/g)	**K**	**Cl**	**Ca**																		
	7.85E-02	4.33E-05	3.02E-03																		

SAMPLE	40Ar Total	Err.40Ar	40Ar*	Err.40Ar*	39Ar	Err.39Ar	%39Ar	38Ar	Err.38Ar	38ArCl	Err.38Cl	37Ar	Err.37Ar	36Ar	Err.36Ar	Age	1 s Err Age	Ca/K	Error Ca/K	Cl/K	Error Cl/K
AK18-5 ms	5.288E-08	1.147E-11	1.789E-08	9.692E-11	4.745E-09	3.303E-12	1.416E+01	7.865E-11	1.307E-13	6.593E-12	8.865E-14	3.095E-11	9.496E-14	1.172E-10	3.223E-13	7.44	0.04	0.01265	0.00004	0.00025	0.00000
J= 0.0010961	9.811E-09	6.510E-13	6.490E-09	1.015E-11	2.358E-09	1.680E-12	7.037E+00	2.771E-11	4.967E-14	7.899E-13	5.932E-14	2.680E-12	5.349E-14	1.112E-11	3.391E-14	5.43	0.01	0.00220	0.00004	0.00006	0.00000
m= 0.06516 g	8.378E-09	7.130E-13	5.179E-09	9.872E-12	1.835E-09	1.336E-12	5.474E+00	2.178E-11	4.129E-14	4.498E-13	6.115E-14	1.241E-12	5.217E-14	1.072E-11	3.298E-14	5.57	0.01	0.00131	0.00006	0.00004	0.00001
	1.060E-08	1.395E-12	7.296E-09	1.009E-11	2.496E-09	1.764E-12	7.447E+00	2.898E-11	5.359E-14	6.155E-13	6.130E-14	1.476E-12	5.201E-14	1.107E-11	3.347E-14	5.77	0.01	0.00115	0.00004	0.00004	0.00000
	1.741E-08	2.046E-12	1.320E-08	1.254E-11	4.291E-09	2.998E-12	1.280E+01	4.960E-11	9.301E-14	1.769E-12	6.844E-14	1.875E-12	5.264E-14	1.413E-11	4.143E-14	6.07	0.01	0.00085	0.00002	0.00007	0.00000
	1.997E-08	2.263E-12	1.417E-08	1.690E-11	4.495E-09	3.117E-12	1.341E+01	5.337E-11	9.085E-14	2.393E-12	6.512E-14	1.812E-12	5.223E-14	1.944E-11	5.609E-14	6.22	0.01	0.00078	0.00002	0.00009	0.00000
	1.093E-08	1.302E-12	7.502E-09	1.019E-11	2.309E-09	1.649E-12	6.888E+00	2.734E-11	4.814E-14	8.734E-13	5.827E-14	8.876E-13	5.163E-14	1.150E-11	3.385E-14	6.41	0.01	0.00075	0.00004	0.00007	0.00000
	1.645E-08	2.077E-12	1.212E-08	1.302E-11	3.620E-09	2.570E-12	1.080E+01	4.268E-11	7.437E-14	1.844E-12	6.243E-14	1.302E-12	5.199E-14	1.448E-11	4.305E-14	6.61	0.01	0.00070	0.00003	0.00009	0.00000
	1.559E-08	2.108E-12	1.095E-08	1.372E-11	3.052E-09	2.164E-12	9.107E+00	3.650E-11	6.388E-14	1.435E-12	6.054E-14	1.473E-12	5.219E-14	1.554E-11	4.539E-14	7.08	0.01	0.00094	0.00003	0.00008	0.00000
	1.646E-08	1.984E-12	1.015E-08	1.847E-11	2.460E-09	1.765E-12	7.340E+00	3.113E-11	5.365E-14	1.245E-12	5.849E-14	1.301E-12	5.199E-14	2.114E-11	6.150E-14	8.14	0.02	0.00103	0.00004	0.00009	0.00000
	1.259E-08	1.457E-12	5.765E-09	1.942E-11	1.173E-09	9.382E-13	3.499E+00	1.712E-11	3.389E-14	4.627E-13	6.354E-14	8.840E-13	5.178E-14	2.286E-11	6.488E-14	9.70	0.03	0.00146	0.00009	0.00007	0.00001
	2.369E-08	3.410E-12	4.148E-09	5.407E-11	6.827E-10	6.266E-13	2.037E+00	1.974E-11	3.753E-14	2.047E-13	6.849E-14	1.443E-12	5.238E-14	6.547E-11	1.808E-13	11.98	0.16	0.00410	0.00015	0.00005	0.00002
Conc (g/g)	**K**	**Cl**	**Ca**																		
	6.71E-02	6.66E-06	1.84E-04																		
AK18-13 ms	4.399E-08	9.300E-12	1.381E-08	7.877E-11	2.508E-09	1.715E-12	9.957E+00	5.504E-11	8.921E-14	9.576E-12	7.330E-14	2.517E-11	8.208E-14	1.011E-10	2.620E-13	10.89	0.06	0.01947	0.00006	0.00068	0.00001
J= 0.0010994	1.326E-08	1.736E-12	9.022E-09	1.215E-11	2.864E-09	1.943E-12	1.137E+01	3.369E-11	7.089E-14	8.622E-13	6.954E-14	5.995E-12	6.032E-14	1.421E-11	4.027E-14	6.24	0.01	0.00406	0.00004	0.00005	0.00000
m= 0.03571 g	3.910E-09	4.960E-13	2.403E-09	5.539E-12	8.723E-10	6.950E-13	3.464E+00	1.020E-11	2.085E-14	6.608E-14	6.398E-14	1.578E-12	5.437E-14	5.046E-12	1.848E-14	5.46	0.01	0.00351	0.00012	0.00001	0.00001
	5.142E-09	7.130E-13	3.503E-09	5.593E-12	1.353E-09	9.774E-13	5.374E+00	1.534E-11	3.026E-14	6.024E-14	6.231E-14	2.154E-12	5.486E-14	5.491E-12	1.858E-14	5.13	0.01	0.00309	0.00008	0.00001	0.00001
	7.584E-09	1.147E-12	5.693E-09	6.439E-12	2.219E-09	1.513E-12	8.809E+00	2.493E-11	4.317E-14	3.795E-13	5.670E-14	2.914E-12	5.522E-14	6.336E-12	2.122E-14	5.08	0.01	0.00255	0.00005	0.00003	0.00000
	8.122E-09	9.610E-13	6.221E-09	6.061E-12	2.372E-09	1.626E-12	9.419E+00	2.665E-11	4.684E-14	4.760E-13	5.787E-14	2.564E-12	5.492E-14	6.368E-12	2.004E-14	5.19	0.01	0.00210	0.00004	0.00004	0.00000
	7.726E-09	1.147E-12	5.864E-09	6.386E-12	2.187E-09	1.495E-12	8.683E+00	2.457E-11	4.254E-14	3.703E-13	5.663E-14	2.229E-12	5.426E-14	6.238E-12	2.104E-14	5.31	0.01	0.00198	0.00005	0.00003	0.00000
	1.291E-08	1.829E-12	1.028E-08	8.001E-12	3.697E-09	2.448E-12	1.468E+01	4.186E-11	6.819E-14	1.287E-12	5.835E-14	6.203E-12	5.751E-14	8.792E-12	2.609E-14	5.51	0.01	0.00326	0.00003	0.00006	0.00000
	1.386E-08	1.953E-12	1.067E-08	9.938E-12	3.478E-09	2.298E-12	1.381E+01	4.007E-11	6.651E-14	1.447E-12	5.845E-14	2.271E-11	7.721E-14	1.068E-11	3.264E-14	6.08	0.01	0.01267	0.00004	0.00007	0.00000
	1.117E-08	1.581E-12	7.796E-09	1.014E-11	2.183E-09	1.480E-12	8.666E+00	2.599E-11	4.412E-14	8.776E-13	5.580E-14	1.743E-11	6.957E-14	1.130E-11	3.353E-14	7.07	0.01	0.01549	0.00006	0.00007	0.00000
	7.423E-09	9.300E-13	3.694E-09	1.085E-11	9.834E-10	7.686E-13	3.905E+00	1.294E-11	2.636E-14	2.296E-13	6.416E-14	1.334E-11	6.508E-14	1.249E-11	3.622E-14	7.44	0.02	0.02631	0.00013	0.00004	0.00001
	9.251E-09	1.705E-12	2.141E-09	1.872E-11	4.702E-10	4.982E-13	1.867E+00	9.983E-12	1.967E-14	5.367E-13	6.247E-14	2.400E-11	7.688E-14	2.382E-11	6.244E-14	9.01	0.08	0.09903	0.00033	0.00020	0.00002
Conc (g/g)	**K**	**Cl**	**Ca**																		
	9.17E-02	1.05E-05	8.92E-04																		
AK18-13 bt	3.241E-08	4.650E-12	1.124E-08	5.540E-11	6.868E-10	6.092E-13	7.759E+00	2.433E-11	5.164E-14	3.720E-12	7.480E-14	5.051E-11	1.368E-13	7.092E-11	1.849E-13	32.23	0.16	0.14270	0.00041	0.00096	0.00002
J= 0.0011016	2.041E-08	2.728E-12	1.337E-08	1.925E-11	1.100E-09	8.455E-13	1.243E+01	1.843E-11	3.918E-14	2.406E-12	6.772E-14	1.595E-11	6.876E-14	2.356E-11	6.384E-14	23.99	0.04	0.02813	0.00012	0.00039	0.00001
m= 0.01496 g	5.215E-09	7.750E-13	3.710E-09	5.232E-12	3.119E-10	4.756E-13	3.523E+00	5.222E-12	1.425E-14	9.881E-13	8.483E-14	2.331E-12	5.467E-14	5.041E-12	1.733E-14	23.49	0.05	0.01450	0.00034	0.00056	0.00005
	5.213E-09	9.300E-13	3.644E-09	5.251E-12	3.122E-10	4.198E-13	3.527E+00	5.280E-12	1.390E-14	1.002E-12	8.185E-14	2.372E-12	5.429E-14	5.254E-12	1.731E-14	23.05	0.05	0.01474	0.00034	0.00057	0.00005
	7.165E-09	1.395E-12	5.134E-09	6.452E-12	4.595E-10	5.199E-13	5.191E+00	7.597E-12	1.686E-14	1.477E-12	6.918E-14	3.754E-12	5.516E-14	6.804E-12	2.110E-14	22.07	0.04	0.01585	0.00023	0.00057	0.00003
	6.703E-09	1.209E-12	4.488E-09	6.945E-12	4.618E-10	5.206E-13	5.217E+00	7.622E-12	1.653E-14	1.360E-12	6.763E-14	4.153E-12	5.549E-14	7.421E-12	2.291E-14	19.21	0.04	0.01745	0.00023	0.00052	0.00003
	6.080E-09	1.085E-12	3.710E-09	7.236E-12	4.626E-10	5.209E-13	5.227E+00	7.608E-12	1.687E-14	1.240E-12	6.915E-14	4.025E-12	5.570E-14	7.941E-12	2.396E-14	15.87	0.04	0.01688	0.00023	0.00048	0.00003
	7.712E-09	1.178E-12	4.971E-09	8.389E-12	6.922E-10	6.116E-13	7.821E+00	1.010E-11	2.253E-14	1.080E-12	6.973E-14	4.420E-12	5.634E-14	9.181E-12	2.782E-14	14.22	0.03	0.01239	0.00016	0.00028	0.00002
	1.018E-08	1.519E-12	6.902E-09	9.566E-12	8.694E-10	7.340E-13	9.822E+00	1.245E-11	2.530E-14	1.227E-12	6.385E-14	5.869E-12	5.838E-14	1.100E-11	3.163E-14	15.71	0.03	0.01310	0.00013	0.00025	0.00001
	1.755E-08	2.449E-12	1.359E-08	1.146E-11	1.238E-09	9.333E-13	1.398E+01	1.808E-11	3.546E-14	2.555E-12	6.217E-14	8.783E-12	6.190E-14	1.324E-11	3.751E-14	21.70	0.02	0.01377	0.00010	0.00037	0.00001
	1.756E-08	2.418E-12	1.432E-08	9.804E-12	1.151E-09	8.893E-13	1.300E+01	1.694E-11	3.254E-14	2.782E-12	6.074E-14	6.453E-12	5.825E-14	1.084E-11	3.182E-14	24.56	0.03	0.01088	0.00010	0.00043	0.00001
	1.912E-08	2.759E-12	1.452E-08	1.320E-11	1.106E-09	8.482E-13	1.249E+01	1.724E-11	3.311E-14	2.697E-12	6.091E-14	1.122E-11	6.367E-14	1.540E-11	4.322E-14	25.92	0.03	0.01969	0.00011	0.00043	0.00001
Conc (g/g)	**K**	**Cl**	**Ca**																		
	7.68E-02	3.48E-05	2.02E-03																		
AK18-23 bt	8.218E-08	1.457E-11	4.147E-08	1.091E-10	2.079E-09	1.472E-12	8.406E+00	6.993E-11	1.197E-13	2.234E-11	8.818E-14	1.992E-11	7.160E-14	1.364E-10	3.621E-13	39.29	0.11	0.01859	0.00007	0.00191	0.00001
J= 0.0011038	5.876E-08	8.990E-12	5.269E-08	1.924E-11	2.933E-09	2.015E-12	1.186E+01	4.622E-11	7.339E-14	1.151E-11	5.568E-14	7.216E-12	5.676E-14	2.033E-11	5.697E-14	35.42	0.03	0.00477	0.00004	0.00070	0.00000
m= 0.04021 g	4.076E-08	4.030E-12	3.721E-08	1.121E-11	2.113E-09	1.492E-12	8.543E+00	3.263E-11	5.366E-14	8.144E-12	5.432E-14	3.375E-12	5.337E-14	1.189E-11	3.505E-14	34.74	0.03	0.00310	0.00005	0.00069	0.00000
	3.261E-08	3.410E-12	2.939E-08	1.027E-11	1.679E-09	1.229E-12	6.787E+00	2.612E-11	4.590E-14	6.419E-12	5.668E-14	2.341E-12	5.271E-14	1.079E-11	3.244E-14	34.53	0.03	0.00271	0.00006	0.00068	0.00001
	3.587E-08	4.030E-12	3.228E-08	1.168E-11	1.860E-09	1.319E-12	7.521E+00	2.886E-11	5.176E-14	7.016E-12	5.814E-14	2.498E-12	5.319E-14	1.201E-11	3.673E-14	34.23	0.03	0.00261	0.00006	0.00067	0.00001

	3.275E-08	4.030E-12	2.838E-08	1.321E-11	1.679E-09	1.229E-12	6.790E+00	2.695E-11	4.878E-14	6.508E-12	5.849E-14	2.515E-12	5.296E-14	1.466E-11	4.213E-14	33.34	0.03	0.00291	0.00006	0.00069	0.00001
	1.874E-08	2.108E-12	1.485E-08	1.130E-11	9.174E-10	7.704E-13	3.710E+00	1.560E-11	2.800E-14	3.485E-12	5.681E-14	1.832E-12	5.223E-14	1.304E-11	3.719E-14	31.94	0.04	0.00387	0.00011	0.00068	0.00001
	1.556E-08	1.891E-12	1.172E-08	1.132E-11	8.178E-10	7.017E-13	3.307E+00	1.363E-11	2.592E-14	2.592E-12	5.997E-14	2.226E-12	5.228E-14	1.286E-11	3.739E-14	28.32	0.04	0.00528	0.00012	0.00056	0.00001
	2.149E-08	2.573E-12	1.691E-08	1.363E-11	1.224E-09	9.468E-13	4.950E+00	1.947E-11	3.551E-14	3.690E-12	5.824E-14	4.719E-12	5.426E-14	1.534E-11	4.482E-14	27.30	0.03	0.00748	0.00009	0.00054	0.00001
	3.887E-08	5.270E-12	3.312E-08	1.763E-11	2.150E-09	1.490E-12	8.693E+00	3.407E-11	5.703E-14	7.811E-12	5.579E-14	9.257E-12	5.785E-14	1.926E-11	5.634E-14	30.42	0.03	0.00835	0.00005	0.00065	0.00000
	5.190E-08	6.820E-12	4.586E-08	1.825E-11	2.827E-09	1.963E-12	1.143E+01	4.551E-11	7.317E-14	1.194E-11	5.596E-14	4.303E-12	5.413E-14	2.022E-11	5.670E-14	32.02	0.03	0.00295	0.00004	0.00075	0.00000
	7.803E-08	1.147E-11	7.049E-08	2.395E-11	4.452E-09	3.038E-12	1.800E+01	7.153E-11	1.184E-13	1.991E-11	6.393E-14	6.112E-12	5.628E-14	2.526E-11	7.041E-14	31.26	0.02	0.00266	0.00002	0.00080	0.00000

Conc (g/g)	**K**	**Cl**	**Ca**
	7.97E-02	6.39E-05	4.14E-04

AK18-26 bt	5.169E-08	1.271E-11	2.044E-08	8.050E-11	6.063E-10	5.752E-13	5.110E+00	3.754E-11	5.460E-14	1.141E-11	6.782E-14	4.768E-11	1.137E-13	1.047E-10	2.662E-13	66.19	0.27	0.15259	0.00039	0.00335	0.00002
J= 0.0011061	3.444E-08	4.340E-12	2.909E-08	1.572E-11	1.057E-09	8.429E-13	8.910E+00	2.331E-11	4.703E-14	8.802E-12	6.403E-14	1.310E-11	6.735E-14	1.794E-11	5.061E-14	54.19	0.05	0.02405	0.00013	0.00148	0.00001
m= 0.02539 g	4.209E-08	5.270E-12	3.696E-08	1.491E-11	1.420E-09	1.013E-12	1.197E+01	2.988E-11	5.035E-14	1.170E-11	5.430E-14	9.595E-12	6.121E-14	1.716E-11	4.673E-14	51.31	0.04	0.01311	0.00008	0.00147	0.00001
	1.532E-08	2.232E-12	1.320E-08	6.901E-12	5.152E-10	5.397E-13	4.342E+00	1.156E-11	2.292E-14	4.803E-12	6.190E-14	2.861E-12	5.391E-14	7.094E-12	2.187E-14	50.52	0.06	0.01077	0.00020	0.00166	0.00002
	1.906E-08	3.410E-12	1.675E-08	7.826E-12	6.592E-10	5.973E-13	5.556E+00	1.465E-11	2.611E-14	6.243E-12	5.589E-14	3.334E-12	5.400E-14	7.760E-12	2.359E-14	50.09	0.05	0.00981	0.00016	0.00169	0.00002
	1.844E-08	2.325E-12	1.543E-08	9.394E-12	6.066E-10	5.523E-13	5.113E+00	1.338E-11	2.408E-14	5.086E-12	5.648E-14	2.926E-12	5.439E-14	1.011E-11	3.049E-14	50.14	0.06	0.00936	0.00017	0.00149	0.00002
	1.140E-08	1.860E-12	8.118E-09	9.778E-12	3.106E-10	4.471E-13	2.618E+00	8.327E-12	1.844E-14	2.984E-12	6.910E-14	2.557E-12	5.364E-14	1.100E-11	3.215E-14	51.52	0.10	0.01597	0.00034	0.00171	0.00004
	1.061E-08	1.922E-12	7.233E-09	9.941E-12	2.670E-10	4.649E-13	2.251E+00	7.534E-12	1.577E-14	2.588E-12	6.541E-14	3.773E-12	5.389E-14	1.132E-11	3.267E-14	53.36	0.12	0.02741	0.00039	0.00172	0.00004
	1.895E-08	4.030E-12	1.374E-08	1.451E-11	5.062E-10	5.618E-13	4.266E+00	1.368E-11	2.465E-14	5.060E-12	5.695E-14	1.309E-11	6.231E-14	1.743E-11	4.668E-14	53.49	0.08	0.05017	0.00025	0.00178	0.00002
	3.956E-08	4.960E-12	3.293E-08	1.857E-11	1.220E-09	9.239E-13	1.028E+01	2.875E-11	4.727E-14	1.166E-11	5.332E-14	2.636E-10	5.346E-13	2.227E-11	5.991E-14	53.21	0.05	0.41932	0.00091	0.00170	0.00001
	5.767E-08	7.130E-12	5.076E-08	2.044E-11	1.996E-09	1.375E-12	1.682E+01	4.528E-11	6.940E-14	1.971E-11	5.163E-14	7.256E-10	1.629E-12	2.336E-11	6.409E-14	50.15	0.04	0.70538	0.00166	0.00176	0.00000
	7.386E-08	1.116E-11	6.685E-08	2.206E-11	2.701E-09	1.802E-12	2.276E+01	5.845E-11	8.736E-14	2.549E-11	5.235E-14	3.816E-10	7.726E-13	2.357E-11	6.371E-14	48.83	0.04	0.27413	0.00058	0.00168	0.00000

Conc (g/g)	**K**	**Cl**	**Ca**
	6.03E-02	1.05E-04	1.45E-02

AK18-42 bt	2.889E-08	6.510E-12	1.765E-09	7.062E-11	2.704E-10	4.369E-13	1.332E+01	4.229E-10	6.854E-13	4.029E-10	6.725E-14	8.029E-12	5.697E-14	9.084E-11	2.355E-13	13.01	0.52	0.05761	0.00042	0.26529	0.00043
J= 0.0011083	4.591E-09	4.960E-13	1.519E-09	9.062E-12	3.182E-10	4.216E-13	1.568E+01	1.329E-11	2.529E-14	8.001E-12	5.947E-14	1.563E-12	5.295E-14	1.029E-11	3.031E-14	9.52	0.06	0.00953	0.00032	0.00448	0.00003
m= 0.00365 g	4.350E-09	7.440E-13	1.406E-09	8.403E-12	2.866E-10	4.694E-13	1.412E+01	1.173E-11	2.111E-14	6.858E-12	5.630E-14	9.423E-13	5.247E-14	9.861E-12	2.804E-14	9.78	0.06	0.00638	0.00036	0.00426	0.00004
	3.511E-09	6.510E-13	8.872E-10	7.814E-12	1.683E-10	4.466E-13	8.291E+00	7.162E-12	1.693E-14	3.734E-12	7.361E-14	6.635E-13	5.264E-14	8.788E-12	2.608E-14	10.51	0.10	0.00765	0.00061	0.00395	0.00008
	4.094E-09	7.750E-13	1.096E-09	8.717E-12	2.057E-10	4.526E-13	1.013E+01	8.444E-12	1.782E-14	4.385E-12	6.586E-14	8.415E-13	5.265E-14	1.004E-11	2.908E-14	10.62	0.09	0.00794	0.00050	0.00380	0.00006
	5.534E-09	1.023E-12	1.414E-09	1.156E-11	2.697E-10	4.367E-13	1.329E+01	1.149E-11	2.121E-14	6.044E-12	5.795E-14	1.242E-12	5.280E-14	1.380E-11	3.858E-14	10.45	0.09	0.00893	0.00038	0.00399	0.00004
	3.513E-09	5.890E-13	6.078E-10	8.402E-12	9.987E-11	4.386E-13	4.921E+00	5.093E-12	1.232E-14	2.207E-12	7.535E-14	8.899E-13	5.252E-14	9.730E-12	2.807E-14	12.13	0.18	0.01729	0.00102	0.00393	0.00014
	4.267E-09	9.300E-13	6.249E-10	1.041E-11	9.592E-11	4.383E-13	4.726E+00	5.369E-12	1.396E-14	2.059E-12	8.102E-14	1.203E-12	5.279E-14	1.220E-11	3.473E-14	12.98	0.22	0.02434	0.00107	0.00382	0.00015
	4.720E-09	8.680E-13	6.257E-10	1.145E-11	9.477E-11	4.075E-13	4.669E+00	5.621E-12	1.486E-14	2.037E-12	8.239E-14	1.172E-12	5.259E-14	1.371E-11	3.823E-14	13.15	0.25	0.02400	0.00108	0.00383	0.00016
	5.114E-09	9.300E-13	7.063E-10	1.215E-11	1.022E-10	4.082E-13	5.036E+00	6.009E-12	1.546E-14	2.149E-12	8.028E-14	1.255E-12	5.266E-14	1.476E-11	4.058E-14	13.76	0.24	0.02381	0.00100	0.00374	0.00014
	6.021E-09	1.178E-12	5.088E-10	1.513E-11	6.590E-11	3.744E-13	3.247E+00	5.386E-12	1.397E-14	1.211E-12	8.108E-14	8.607E-13	5.253E-14	1.846E-11	5.052E-14	15.37	0.47	0.02534	0.00155	0.00327	0.00022
	1.525E-08	3.410E-12	4.495E-10	3.851E-11	5.224E-11	4.045E-13	2.574E+00	1.083E-11	2.167E-14	9.353E-13	6.676E-14	1.204E-12	5.259E-14	4.956E-11	1.285E-13	17.12	1.47	0.04473	0.00198	0.00319	0.00023

Conc (g/g)	**K**	**Cl**	**Ca**
	7.17E-02	2.78E-03	1.36E-03